Tampere University

HANNU VÄLIMÄKI

Surface-selective Luminescence Methods

Enabling technologies for rapid immunoassays and chemical sensing in cell cultures

Tampere University Dissertations 282

Tampere University Dissertations 282

HANNU VÄLIMÄKI

Surface-selective Luminescence Methods

Enabling technologies for rapid immunoassays and chemical sensing in cell cultures

ACADEMIC DISSERTATION
To be presented, with the permission of
the Faculty of Medicine and Health Technology
of Tampere University
for public discussion in the auditorium SA203
of the Sähkötalo, Korkeakoulunkatu 3, Tampere,
on August 28, 2020, at 12 o'clock.

ACADEMIC DISSERTATION
Tampere University, Faculty of Medicine and Health Technology
Finland

Responsible supervisor and Custos
Professor Emeritus
Jukka Lekkala
Tampere University
Finland

Supervisor
Docent
Kirsi Tappura
Tampere University
Finland

Pre-examiners
Professor Emeritus
Colette McDonagh
Dublin City University
Ireland

Professor
Pekka Hänninen
University of Turku
Finland

Opponent
Professor
Carl-Fredrik Mandenius
Linköping University
Sweden

Cover design: Roihu Inc.

ISBN 978-952-03-1632-7 (print)
ISBN 978-952-03-1633-4 (pdf)
ISSN 2489-9860 (print)
ISSN 2490-0028 (pdf)
http://urn.fi/URN:ISBN:978-952-03-1633-4

PunaMusta Oy – Yliopistopaino
Tampere 2020

To my father

PREFACE

This work started about 15 years ago at VTT, Technical Research Center of Finland, where I remember glancing through scientific papers about the surface-sensitive fluorescence detection for the first time. The papers used fascinating concepts such as *forbidden light* and *supercritical angle fluorescence* that stayed in my mind even though our research group "Biosensors" did not work on the topic at the time. However, soon thereafter we received a funding from TEKES (Business Finland) for a project called "Fastdiag", which aimed for novel technologies in the rapid on-site drug screening. In a few years, we constructed an immunoassay platform that utilized exactly those fascinating concepts and performed well in practice. The work resulted in three publications, which would years later comprise the first part my thesis. However, businesses at VTT took a sudden turn in 2013, and as I left VTT together with many colleagues, I laid down all plans to ever complete a dissertation.

After two busy years of teaching at schools, completing courses in physics, playing music and doing gigs, I got a second chance with the dissertation. Prof. Jukka Lekkala, who knew me from his own years at VTT, offered me an opportunity to join the multidisciplinary research at the BioMediTech ─ a joint institute of Tampere University of Technology and Tampere University at the time. I happily accepted the offer in May 2015. In the TEKES-funded project "Human Spare Parts", our research group "Sensor Technology and Biomeasurements" focused on the chemical measurements in miniaturized cell cultures, and my task was to develop methods for the oxygen sensing. As it happens, the best option we could consider was to apply surface-selective luminescence methods. This work on the oxygen sensing and the related two publications comprise the second part of thesis.

My path with the dissertation has been a long one, and so is the list of people I owe a thank you. I am grateful to Dr. Janusz Sadowski, with whom I started the research on surface-selective fluorescence at VTT and who introduced me to the art of optics. The work continued with Dr. Kirsi Tappura, who became my thesis supervisor and whom I cannot thank enough. In addition, I want to express my gratitude to all my former workmates at VTT. Especially, to Timo Flyktman for the read-out electronics; to Jussi Tuppurainen for the help in optics; to Sanna Auer and Inger Vikholm-Lundin for the help in the immunoassay practices; to Tony Munter

and Martin Albers for the help in surface chemistries and to Hannu Helle and Janne Saijets for their friendship and support. I also want to thank Timo Pulli (VTT) and Ann-Charlotte Hellgren (Biosensors Application AB) for providing the antibodies and assistance for the important drug immunoassays.

Likewise, I wish to thank all my current colleagues at BioMediTech at Tampere University. I am especially grateful to Prof. Emeritus Jukka Lekkala for providing the opportunity to complete my dissertation, as well as for the guidance and a long friendship. I wish to thank my current group leader Prof. Pasi Kallio for the patience and continuous support. I thank Dhanesh Rajan and Joose Kreutzer for many busy hours around the modular cell culturing system; Jarmo Verho for the read-out electronics; Tomi Ryynänen for the help in clean room practices; Joni Leivo and Haider Iftikhar for the important indicator chemistry work. I also wish to thank everybody else who have been collaborating with me, either at the office or at the laboratories. Especially grateful I am to Jouni Niemelä, whose versatile skills has solved many practical problems. In addition, I wish to thank Heimo Ihalainen and Markus Karjalainen for many inspiring discussions on and off the topic.

I have had a precious opportunity to collaborate closely with the stem cell researchers at BioMediTech and learn constantly about the foundations of life and the amazing prospects of the regenerative medicine. I am grateful to Prof. Susanna Narkilahti (Neuro group) and Prof. Katriina Aalto-Setälä (Heart group) and their groups for the close cooperation. Especially, I wish to express my gratitude to Tanja Hyvärinen and Mari Pekkanen-Mattila, who have greatly contributed to the thesis with numerous cytotoxicity and oxygen sensing tests.

I wish to express my gratitude to the pre-examiners, Prof. Pekka Hänninen and Prof. Emeritus Colette McDonagh for the thorough examination and excellent recommendations. Likewise, I am grateful to Prof. Carl-Fredrik Mandenius for acting as the opponent and taking the time to examine the thesis as well. The financial support of the Academy of Finland and Business Finland is greatly acknowledged.

Lastly, I thank my parents Jukka and Vilma, my sister Susanna and her husband Juha Torvinen for their warm support. My wife Elina and my daughters Vilja, Maija and Liisa I thank deeply for providing a life full of love and meaning. I also thank our Border Terrier Tove for many shared kilometers in the woods.

"*Work is a blessing that looks like a curse.*" - Lawrence Durrell

Tampere, June 2020

ABSTRACT

Luminescence is the most widely used technology in chemical and biochemical assays and sensor applications. It is used extensively in the fields of biotechnology, medical diagnostics, DNA sequencing, genetic research, forensic analysis as well as in various on-site diagnostic, screening and safety applications. Luminescence technology is attractive, since it provides high sensitivity, a wide variety of sensing schemes and several measurable parameters. The technology is based on the use of luminescent labels or indicator molecules, whose radiation in the detector is modulated by the analyte in terms of emission intensity, lifetime, anisotropy, energy transfer or spectroscopic properties.

Typically, the luminescent molecules to be detected are located at interfaces. There is a myriad of fluorescent immunoassays, where the fluorescently labelled biomolecules bind on transparent surfaces. Similarly, a typical sensing element a luminescence-based chemical sensor is composed of a thin dielectric layer embedded with analyte-sensitive indicators. In these common sensing geometries, the dielectric interfaces create discontinuities in the refractive index, which has substantial effects on the local electric field and the spatial radiation distribution of the adjacent molecular emitters. With appropriate optical arrangements, these effects can be exploited in the luminescence detection. Indeed, both the luminescence excitation and emission collection can be transformed into surface-selective or layer-selective modes, which significantly enhances the detected emission and suppresses the background signals.

The surface-selective fluorescence detection is an excellent technological choice for rapid fluorescent immunoassays. The technique gives highly sensitive means to monitor biochemical binding processes in real time and thus generate estimates for the analyte concentrations as soon as the assay begins. The technique is also relatively insensitive to many bulk matrix effects, which makes it especially well-suited for rapid on-site applications with challenging sample matrices, such as point-of-care diagnostics and rapid on-site screening of many small but important molecules, including steroids, hormones, toxins and abused drugs.

In this thesis, a fluorescent measurement platform with surface-selective techniques is developed for rapid immunoassays. For maximal surface-selectivity,

the platform incorporates both the technique of total internal reflection excitation (TIR) and supercritical angle fluorescence (SAF). The key element of the platform is a parabolic lens, designed in the thesis and custom-manufactured from polystyrene, which facilitates the simultaneous application of TIR and SAF. The relatively high refractive index of polystyrene is advantageous in terms of the SAF collection efficiency and, in addition, polystyrene lens makes the platform compatible with standard flat-bottom microtiter plates. The thesis reports on the design, construction and characterization of the platform, as well as on its application to rapid immunoassays of two abused drug molecules: morphine and cocaine.

The morphine assay is based on a noncompetitive immunoassay utilizing two antibodies. The fluorescent detection antibodies bind on the sensing surface, which is monitored with the developed platform in real time. As a result, morphine concentrations below one tenth of the typical screening cutoff concentration of the authorities (40 ng/mL) can be detected in 30 sec. The cocaine assay is based on a displacement-type immunoassay. The developed platform makes it possible to follow the displacement process in real time. The results show that cocaine concentrations down to 10 ng/mL, comparable to the common cutoff values of the authorities (8 - 20 ng/mL), can be detected in untreated saliva samples in 30 sec.

Chemical sensing in *in vitro* cell cultures represents another key application for the surface-selective luminescence technology. In a widely applied chemical sensing geometry, analyte-specific indicators are embedded in an analyte-permeable thin film on the culturing substrate, and the analyte molecules modulate the luminescence properties of the indicator. To this geometry, the surface-selective (or layer-selective) detection techniques bring certain advantages, especially in terms of minimizing the invasiveness and the disruptions the cells experience. Firstly, compared to conventional luminescence collection set-ups, the surface-selective methods enhance the signal multiple times, thus allowing the use of low indicator concentrations and excitation power. Secondly, the surface-selective excitation protects the cells from a direct illumination. Especially in sensitive cell cultures, such as based on human induced pluripotent stem cell-derived (hiPSC-derived) cells, these features can be significant.

In the thesis, luminescence-based oxygen sensors with surface-selective TIR and SAF techniques are developed for *in vitro* cell cultures. The key factors in the designs are the minimal invasiveness and the integrability to the modular cell culture platform with numerous other functionalities, including temperature and gas control, microelectrode arrays and microscopy. The optical read-outs are based on custom-manufactured parabolic lenses. The developed oxygen sensors are characterized and

applied in experiments, where the functionality of hiPSC-derived cardiomyocytes is monitored under varying oxygen conditions. Finally, the thesis demonstrates how the luminescent sensing material itself can be made significantly more biocompatible by linking of the indicators covalently into the supporting matrix, that is, by preventing the leaching of the indicators.

TIIVISTELMÄ

Luminesenssiin perustuvia mittaustekniikoita hyödynnetään laajasti kemiallisissa ja biokemiallisissa määrityksissä, anturisovelluksissa ja kuvantamisessa, ja ne ovat vakiinnuttaneet paikkansa erityisesti biotekniikan ja lääketieteellisen diagnostiikan alalla. Lisäksi tekniikkaa käytetään hyödyksi monissa ympäristö- ja turvallisuus-sovelluksissa kuten viranomaisten tekemissä kenttätesteissä. Luminesenssitekniikan etuja ovat sen herkkyys ja sen tarjoamat monipuoliset mittaustavat ja -parametrit. Luminesenssitekniikka perustuu luminoivan eli valoa säteilevän molekyylin käyttöön. Tyypillisesti luminoiva molekyyli toimii mitattavaan yhdisteeseen eli analyyttiin kiinnittyvänä leimamolekyylinä tai analyytille herkkänä indikaattorina. Sopivan mittausjärjestelyn avulla analyytin pitoisuusmuutokset voidaan havaita muutoksina mitatussa luminesenssiemissiossa, joko sen intensiteetissä, elinajassa, anisotropiassa, energiansiirrossa tai spektroskooppisissa ominaisuuksissa.

Mitattavat luminesenssimolekyylit sijaitsevat useimmiten jollakin rajapinnalla. Esimerkiksi tavallisessa fluoroimmunomäärityksessä leimatut vasta-ainemolekyylit sitoutuvat funktionalisoidulle mittauspinnalle, joka on usein läpinäkyvää dielektristä ainetta. Vastaavasti kemiallisessa anturoinnissa hyödynnetään usein järjestelyä, jossa analyytille herkät luminesenssi-indikaattorit sijaitsevat mittauspinnalla ohuen dielektrisen kalvon sisällä. Nämä dielektriset rajapinnat luovat optiseen taitekerroinavaruuteen epäjatkuvuuskohtia, jotka vaikuttavat merkittävästi sekä virittävän sähkökentän ominaisuuksiin että luminesenssiemission intensiteettiin ja avaruudelliseen säteilyjakaumaan rajapintojen lähellä. Sopivilla järjestelyillä näitä ilmiöitä voidaan hyödyntää luminesenssin mittaamisessa. Rajapintojen avulla sekä luminesenssin viritys että emission keräystekniikka voidaan tehdä pintaselektiivisesti. Tämä lisää merkittävästi pinnasta kerätyn luminesenssin intensiteettiä ja vaimentaa pinnan ulkopuolelta tulevia taustasignaaleja.

Pintaselektiivinen fluoresenssitekniikka soveltuu erinomaisesti nopeisiin immunomäärityksiin. Tekniikan avulla immunologisia sitoutumisreaktioita voidaan seurata reaaliaikaisesti, mikä mahdollistaa analyyttipitoisuuden ennustamisen jo testin varhaisessa vaiheessa. Erityisen hyvin tekniikka soveltuu pienten analyyttien, kuten steroidien, hormonien ja huumeiden pikadiagnostiikkaan haastavissa biologisissa näytematriiseissa. Tämän väitöskirjan keskeisen osan muodostaakin

pintaselektiivisen mittausalustan kehittäminen nopean fluoroimmunomäärityksen tarpeisiin. Maksimaalisen pintaselektiivisyyden saavuttamiseksi kehitetyssä mittausalustassa hyödynnetään yhtä aikaa sekä sisäiseen kokonaisheijastukseen perustuvaa fluoresenssiviritystä (engl. total internal reflection, TIR) että ylikriittiseen kulman fluoresenssiin (engl. supercritical angle fluorescence, SAF) perustuvaa emission keräämistä. Mittausalustan keskeisenä komponenttina toimii mittatilaustyönä valmistettu paraboloidinen linssi, jonka avulla TIR ja SAF tekniikat voidaan yhdistää. Linssi on valmistettu polystyreenistä, jonka suhteellisen korkea taitekertoimen arvo parantaa SAF fluoresenssin keräystehokkuutta. Lisäksi näytealustana voidaan käyttää tavallisia polystyreenistä valmistettuja suorapohjaisia mikrokuoppalevyjä. Mittausalustan toiminta ja pintaselektiivisyys karakterisoidaan kokeellisesti, ja sen käyttöä tutkitaan kahden huumausaineen, morfiinin ja kokaiinin immunomäärityksessä.

Morfiinimääritys perustuu ei-kompetitiiviseen, kahta vasta-ainetta hyödyntävään immunomääritykseen. Merkkiaineilla leimattujen vasta-aineiden sitoutumista mittauspinnalle seurataan kehitetyllä mittausalustalla reaaliaikaisesti. Tulosten mukaan 30 sekunnin testissä voidaan määrittää morfiinipitoisuuksia, jotka ovat alle kymmenesosan viranomaisten morfiinille määrittämistä seulontarajoista (40 ng/mL). Kokaiinimääritys perustuu syrjäytys-tyyppiseen (engl. displacement-type) immunomääritykseen, jossa leimattujen vasta-aineiden irtoamista mittauspinnalta seurataan reaaliaikaisesti. Tulosten perusteella viranomaisten seulontarajoja vastaavien kokaiinipitoisuuksien (8 – 20 ng/mL) määrittäminen sylkinäytteistä on mahdollista 30 sekunnissa.

Toinen pintaselektiivistä luminesenssimenetelmistä hyötyvä sovellus on *in vitro* soluviljelmien kemiallinen anturointi. Tyypillisessä mittausjärjestelyssä analyytille herkät indikaattorimolekyylit on upotettu ohueen dielektriseen mittauskalvoon, joka on kiinnitetty soluviljelmän kasvatusalustaan. Pintaselektiivisten menetelmien käyttö tehostaa tällaista mittausta, sillä menetelmien avulla emissiovaloa saadaan kerättyä moninkertainen määrä verrattuna tavanomaisiin optisiin järjestelyihin. Tämä antaa mahdollisuuden käyttää alhaisempaa indikaattoripitoisuutta ja luminesenssin viritystehoa ja vähentää näin mittauksen invasiivisuutta ja solujen kokemaa häiriötä. Lisäksi pintaselektiivinen virityksessä solut eivät altistu suoralle viritysvalolle. Erityisesti herkkien, ihmisperäisistä kantasoluista johdettujen (engl. human induced pluripotent cell-derived, hiPSC-derived) solumallien yhteydessä nämä tekijät voivat olla merkittäviä.

Työssä kehitetään kaksi pintaselektiiviseen TIR ja SAF tekniikkaan perustuvaa happianturia *in vitro* soluviljelmien ja -mallien monitoroimiseen. Anturiratkaisujen

lähtökohtana on minimoida niiden invasiivisuus ja toteuttaa optinen ratkaisu siten, että integroimien osaksi laajempaa solunkasvatusjärjestelmää on mahdollista. Molempien anturien keskeisenä optisena komponentti toimii mittatilaustyönä valmistetuttu paraboloidinen linssi. Kehitetyt happianturit karakterisoidaan, ja niitä käytetään ihmisperäisistä kantasoluista johdettujen sydänsolumallien happikonsentraation mittaamiseen yhdessä lämpötila- ja kaasunohjauksen, mikroelektrodi-matriisimittausten ja mikroskopian kanssa. Lopuksi työssä osoitetaan, että indikaattorien kovalenttinen kiinnittäminen mittauskalvoon parantaa ratkaisevasti mittauskalvon materiaalista bioyhteensopivuutta.

CONTENTS

ABBREVIATIONS AND SYMBOLS

BSA	Bovine serum albumin
CM	Cardiomyocyte
CMOS	Complementary metal oxide semiconductor
DMD	Digital mirror device
ELISA	Enzyme linked immunosorbent assay
FRET	Fluorescence resonance energy transfer
FWHM	Full width at half maximum
GC-MS	Gas chromatography - mass spectrometry
hiPSC	Human induced pluripotent stem cell
IC	Immunocomplex
IgG	Immunoglobulin G
ISFET	Ion-sensitive field-effect transistors
LAPS	Light addressable potentiometric sensors
LD	Laser diode
LED	Light emitting diode
Lipa-DEA	A diaminomethanol derivative of lipoic-acid
LOD	Limit of detection
MEA	Microelectrode array
NSB	Non-specific binding
PBS	Phosphate-buffered saline
PDMS	Polydimethylsiloxane
PMT	Photomultiplier tube
PMMA	Poly(methylmethacrylate)
pO_2	Partial pressure of oxygen
POM	Polyoxymethylene
PS	Polystyrene
PtOEPK	Platinum(II) octaethylporphyrinketone
PtTFPP	Platinum(II)-5,10,15,20-tetrakis-(2,3,4,5,6-pentafluorphenyl)-porphyrin
PPFS	Poly(pentafluorostyrene)

QCM	Quartz crystal microbalance
RMS	Root mean square
SAF	Supercritical angle fluorescence
SERS	Surface enhanced Raman spectroscopy
SPR	Surface plasmon resonance
TCSPC	Time correlated single photon counting
TIR	Total internal reflection
TIRF	Total internal reflection fluorescence
TSM	Thickness-shear mode
2D	Two-dimensional
3D	Three-dimensional

d	the thickness of the parabolic lens
d_p	penetration depth
$E_{p,s}^{(+,-)}(z)$	*p*- or *s*-polarized electric field propagating in positive or negative direction
f	frequency; or the focal length of the parabolic lens
I	intensity
k	free space wavenumber
k_i	wavenumber in material *i*
K_{sv}	Stern-Volmer constant
n	refractive index
n_i	the refractive index of material *i*
L_i	the thickness of layer *i*
$P_{\perp}^{p}(\theta)$	*p*-polarized emission power of a vertical dipole
$P_{\parallel}^{p,s}(\theta)$	*p*- or *s*-polarized emission power of a horizontal dipole
r_{bot}	the bottom radius of the parabolic lens
r_{up}	the upper radius of the parabolic lens
r_{ij}	Fresnel reflection coefficient (light is incident in material *i*)
t_{ij}	Fresnel transmission coefficient (light is incident in material *i*)
z	z-coordinate

θ	angle of incidence or polar emission angel
θ_c	critical angle

θ_c^{ij}	the critical angle between the materials *i* and *j*
λ	wavelength
λ_0	free space wavelength
τ	luminescence lifetime
τ_0	unquenched luminescence lifetime
ϕ	phase angle

ORIGINAL PUBLICATIONS

Publication I **H. Välimäki** and K. Tappura, A novel platform for highly surface-sensitive fluorescent measurements applying simultaneous total internal reflection excitation and super critical angle detection. Chemical Physics Letters 473 (2009) 358-362.

Publication II **H. Välimäki**, T. Pulli, K. Tappura, Applying total internal reflection excitation and super critical angle fluorescence detection to a morphine assay. Journal of Fluorescence 20:5 (2010) 1003-1008.

Publication III **H. Välimäki**, S. Auer, A-C Hellgren, K. Tappura, Applying a surface sensitive fluorescence method to fast on-site detection of cocaine in saliva. Procedia Engineering 25 (2011) 968-971. Proceedings of Eurosensors XXV, September 4-7, 2011, Athens, Greece.

Publication IV **H. Välimäki**, J. Verho, J. Kreutzer, D. Rajan, T. Ryynänen, M. Pekkanen-Mattila, A. Ahola, K. Tappura, P. Kallio, J. Lekkala, Fluorimetric oxygen sensor with an efficient optical read-out for in vitro cell models. Sensors and Actuators B Chemical (2017) 738-746

Manuscript 1 **H. Välimäki**, T. Hyvärinen, J. Leivo, H. Iftikhar, M. Pekkanen-Mattila, J. Verho, J. Kreutzer, T. Ryynänen, D. K. Rajan, J. Pirhonen, K. Aalto-Setälä, P. Kallio, S. Narkilahti, J. Lekkala, Covalently linked indicators enhance the biocompatibility of the luminescent oxygen sensing material with hiPSC-derived neurons and cardiomyocytes (unpublished manuscript)[1]

[1] A revised version of the manuscript is published under the title "Covalent immobilization of luminescent oxygen indicators reduces cytotoxicity", Biomedical Microdevices (2020) 22:41 https://doi.org/10.1007/s10544-020-00495-3

AUTHOR'S CONTRIBUTION

Publication I This paper introduces the surface-selective fluoroimmunoassay platform. The author carried out the modelling and simulations and designed the platform together with Kirsi Tappura. The author constructed and tuned the platform. The immunoassay experiments were designed together with Kirsi Tappura. The author functionalized the sensing surfaces, carried out the measurements, analyzed the results and wrote most of the publication.

Publication II In this paper, the immunoassay platform is applied to the morphine detection. The author functionalized the sensing surfaces, carried out the measurements, analyzed the results and wrote most of the publication. Kirsi Tappura and Timo Pulli participated in the design of the experiments, as well as in the final editing of the publication.

Publication III In this paper, the immunoassay platform is applied to the cocaine detection. The author functionalized the sensing surfaces together with Sanna Auer, who also carried out the labelling of the antibodies. The author carried out the measurements, analyzed the results and wrote most of the publication. All co-authors participated in the design of the experiments, as well as in the final editing of the publication.

Publication IV This paper introduces the luminescence-based oxygen sensor with surface-selective characteristic. The author carried out the modelling and simulations and designed and constructed the optics and mechanics for the oxygen sensor. Jarmo Verho designed and manufactured the sensor read-out hardware. Cell culturing chambers were made by Joose Kreutzer. Dhanesh Rajan designed and constructed most of the modular cell culturing platform. Mari Pekkanen-Mattila cultured cardiomyocytes, and Antti Ahola carried out the beating analysis for the recorded microscopy videos. The author prepared the oxygen sensing films, made the laboratory measurements, analyzed the results and wrote most of the publication. The rest of the authors participated in the experimental design and final editing of the publication.

Manuscript 1 This paper focuses on the development and testing of biocompatible oxygen sensing material. The author planned the material

development work together with Joni Leivo and Haider Iftikhar, who prepared the material with covalently linked indicators. The author prepared all sensing films and spots and carried out the measurements to characterize the oxygen sensing properties of the individual materials. Tanja Hyvärinen carried out the biocompatibility tests with neurons and made the respective statistical analysis. Mari Pekkanen-Mattila carried out the biocompatibility tests with cardiomyocytes and designed the hypoxia tests together with the author. The author carried out the statistical analysis for the cardiomyocytes. Joose Kreutzer, Dhanesh Rajan, and Tomi Ryynänen worked together with the author in the instrument integration for the hypoxia tests, and Jonatan Pirhonen carried out the hypoxia tests. The author compiled the results and wrote most of the manuscript. Susanna Narkilahti participated in the design of the biocompatibility tests and provided support for the analysis and manuscript writing. The rest of the authors participated in the experimental design and final editing of the publication. In addition, the work in M1 includes a further design and realization of the oxygen sensor introduced in the paper IV. Here, the author designed the new parabolic lens as well as the improved optical read-out. The author constructed the optics and the sensor set-up. Jarmo Verho designed and constructed the read-out electronics.

1 INTRODUCTION

Many optical spectroscopic techniques are enhanced on surfaces. The surfaces can intensify local electromagnetic fields and strengthen the radiative properties of the adjacent molecular emitters. Today, the surface-enhanced optical spectroscopies comprise an active research field with rapidly developing techniques dedicated to a highly sensitive and selective chemical and biochemical sensing. The techniques include surface-enhanced Raman scattering (SERS), surface-enhanced infrared absorption, surface-enhanced chiroptical spectroscopy and surface-enhanced luminescence, to name a few (Mun et al. 2019).

Surface-enhanced luminescence utilizes the optical near-field interaction between molecular emitters and adjacent surfaces. The surfaces can be planar or highly patterned sub-wavelength plasmonic structures, resulting in the enhancements of orders of magnitude (Fort and Grésillon 2008). In essence, metallic surfaces and structures significantly shorten the radiative decay time of the molecular emitters at suitable distances, thus intensifying the emitted power (Aslan et al. 2005). In addition, a metal film of appropriate thickness can transform the emission into a highly directed, surface plasmon coupled mode (Gryczynski et al. 2004).

However, even the presence of plain transparent dielectric materials, such as glass and optical polymers, can greatly modify the luminescence (Chance et al. 1978; Lukosz 1978; Courtois et al. 1996). The material interfaces generate discontinuities in the refractive index, which has a large effect on the local electric fields and the spatial radiation distribution of the adjacent molecular emitters. This is important to realize, since many luminescent sensing schemes apply such sensing surfaces, layers and waveguides (Polerecký et al. 2000). While the luminescence decay rate change at a dielectric sample-substrate interface is much more modest than at a metallic interface (Drexhage 1970), the angular emission pattern is nevertheless substantially modified. The emission pattern becomes highly anisotropic and very dependent on the sub-wavelength proximity of the emitters. This opens up possibilities for enhanced, surface-selective luminescence sensing methods (Enderlein et al. 1999). Indeed, both the luminescence excitation and emission collection can be transformed in surface-selective or layer-selective modes, which significantly

enhances the detected emission and suppresses the background. In this thesis, these methods are exploited in two important sensing applications:

i) rapid fluorescent immunoassays
ii) luminescence-based chemical sensing in cell cultures

The surface-selective fluorescence technology is a well-grounded choice for rapid heterogeneous immunoassays, especially in biological sample matrices. The technology is relatively insensitive to many bulk matrix effects and other interfering influences, which often become more serious issues for label-free techniques such as surface plasmon resonance (SPR) (Sapsford and Ligler 2004). Moreover, the surface-selective fluorescence methods enhance the collection efficiency and provide highly sensitive means to monitor the immunological binding processes in real time. Indeed, with a strong surface-selectivity, no washing steps are necessary after the injection of the sample, and sound estimates for the analyte concentration can be generated already at the early stages of the binding process.

Chemical sensing in *in vitro* cell cultures represents another application, where the surface-selective luminescence methods may prove advantageous. The methods provide means to enhance the collection efficiency of thin, solid, luminescently doped sensing films on transparent cell culturing substrates, which are often utilized in chemical sensing in cell culture applications. The enhanced collection efficiency allows the use of low indicator concentration and excitation power, which can significantly limit the invasiveness of the sensing. Especially luminescence-based oxygen sensing – prone to generate toxic oxygen radicals as an unwanted by-product – in sensitive cell cultures may benefit from the increased detection efficiency.

1.1 The aim and the scope of the work

This thesis aims for a surface-selective luminescence detection in

a) fluorescent immunoassays, where the target molecules bind to or dissociate from the sensing surface. Emphasis is given on the rapid detection (in 30 sec) of small analytes in challenging sample matrices, in particular on the abused drugs in oral fluids.

b) luminescence-based chemical sensing, where the analyte-specific indicators are embedded in a thin sensing layer deposited on a transparent, solid substrate.

Emphasis is given on the minimally invasive monitoring of the oxygen tension in sensitive cell culture applications.

1.2 Research questions

The outlined aims can be formulated as a set of research questions:

- How to apply the surface-selective fluorescence methods effectively to immunoassays?
- Are the surface-selective fluorescence methods beneficial in terms of assay sensitivity and speed?
- Can the surface-selective fluorescence methods provide means to create rapid on-site assays for small molecules in biological sample matrices? Can drug molecules be detected in concentrations below the recommended cutoff levels in 30 sec in oral fluids?
- How to integrate surface-selective luminescence detection into a miniaturized or microfluidic cell culturing platform?
- Can the surface-selective luminescence methods make the chemical sensing less invasive in sensitive cell cultures?
- Can the covalent linking of the indicators enhance the biocompatibility of luminescent sensing material?

These research questions are studied in the publications P1 – P4 and M1 with theoretical calculations and experimental set-ups.

1.3 The structure of the thesis

This thesis outlines the work carried out in publications P1 – P4 and manuscript M1. Chapter 2 provides an introduction to surface-selective luminescence techniques at dielectric interfaces, as well as introductions to immunoassays and chemical sensing in cell cultures. Chapter 3 presents the optical set-ups and measurement platforms developed in this thesis. Chapter 4 recapitulates and discusses the results when the developed platforms were applied in specific immunoassays and luminescence-based oxygen sensing in cell-cultures. Finally, Chapter 5 draws conclusions and gives a future outlook.

2 BACKGROUND

This thesis brings together several research areas, technologies and application fields, including chemical sensor and immunoassay technologies, optics, physics of luminescence, drug screening with on-site challenges and miniaturized cell models with instrumentation and biocompatibility issues. The diverse technological landscape makes it challenging to provide a background section that is general enough and, on the other hand, specific enough. In addition, the thesis aims to compact work and publications spanning over a decade. As the best effort to meet these challenges, this chapter aims to give both general overviews of the research fields as well as more in-depth discussions on the key topics. The chapter is organized as follows:

- Section 2.1 discusses the luminescence at dielectric interfaces, in the geometries relevant to the thesis. The discussion is divided into sub-sections covering total internal reflection fluorescence, supercritical angle fluorescence, and emission stemming from a thin luminescent film deposited on a solid, transparent substrate. The physics behind the simulations is reviewed in the final subsection.
- Section 2.2 provides an introduction to immunoassay technologies. A subsection is dedicated to fluoroimmunoassays exploiting the surface-selective detection.
- Section 2.3 reviews the chemical sensing technologies applied in *in vitro* cell cultures. A subsection focuses on the luminescence-based chemical sensing technologies.

2.1 Luminescence at dielectric interfaces

Solid dielectric interfaces modify the luminescence of adjacent molecular emitters in a substantial way. The local excitation field, angular emission distribution as well as the luminescence decay time can significantly change near the interfaces.

2.1.1 Total internal reflection fluorescence (TIRF)

Total internal reflection fluorescence (TIRF) is a widely applied technique for a surface-selective excitation of luminescent molecules. The technique was first introduced by Hirschfeld (1965), who applied it to the selective fluorescence excitation at liquid-solid interfaces. The surface-selectivity of the TIRF excitation is based on an exponentially decaying evanescent electromagnetic field that a totally reflected light generates. In 1975, the evanescent field was used for the first time in a fluorescence immunoassay by Kronick and Little (1975).

In TIRF, the sample-substrate interface is illuminated from the substrate side at angles exceeding the critical angle between the sample and substrate. The critical angle is defined as $\theta_c = \sin^{-1}(n_1/n_3)$, where n_1 denotes the refractive index of the sample and n_3 the refractive index of the substrate, where $n_3 > n_1$. As shown schematically in Fig. 1, the excitation wave is totally reflected from the interface, but an evanescent electromagnetic field penetrates the interface and probes the sample in the very vicinity of the interface. The luminescent molecules located within the depth of the evanescent field become selectively excited.

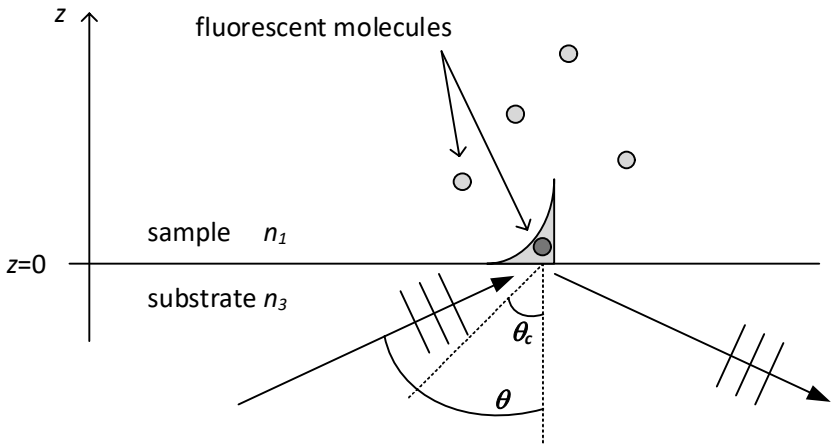

Figure 1. The principle of the total internal reflection fluorescence (TIRF), a surface-selective technique for luminescence excitation.

The intensity of the evanescent field $I(z)$ decays exponentially along the distance z from the surface into the sample:

$$I(z) = I_0 \exp(-z/d_p) \qquad (2.1)$$

where I_0 is the field intensity at the interface, and d_p is the penetration depth. The penetration depth depends on the wavelength, illumination angle and the refractive indices as (Axelrod et al. 1984)

$$d_p = \frac{\lambda_0}{4\pi}(n_3^2\, sin^2\, \theta - \, n_1^2)^{-1/2} \qquad (2.2)$$

for all angles of incidence $\theta > \theta_c$ and free space wavelengths λ_0. The depth is independent of polarization, and it decreases with increasing θ. The nature of the equation (2.2) is illustrated in Fig. 2, where the penetration depth is plotted against the angle of incidence for the water-glass and water-polystyrene interfaces. The figure shows that the penetration depth is of order λ_0 at the angles just above the critical angle, and then it drops down to values close to $\lambda_0/10$ at large incident angles.

The exponential decay of the field intensity restricts the sensing to the very vicinity of the surface. The phenomenon has led to the development of the TIRF microscopy devices, which have become invaluable tools especially in biomedical sciences. Due to the surface-selective excitation, TIRF microscopy can generate images with a low background fluorescence, minimal out-of-focus fluorescence, and importantly, with a minimal exposure of cells to light (Axelrod 2001).

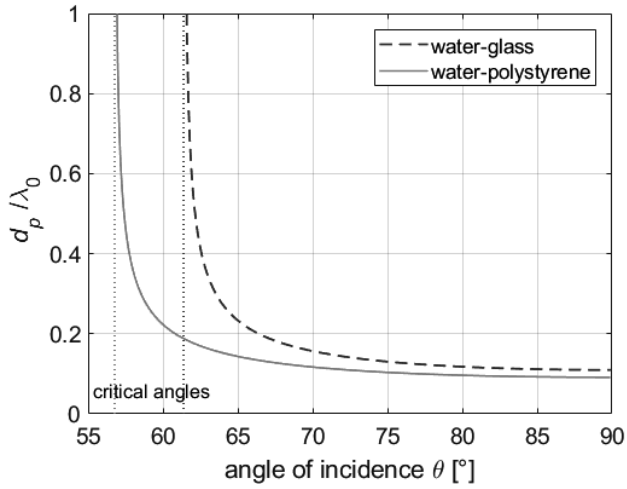

Figure 2. Calculated evanescent wave penetration depths for water-glass and water-polystyrene interfaces as a function of the angle of incidence. Here, n_1 = 1.33 (water); n_3 = 1.515 (glass) or n_3 = 1.59 (polystyrene). The respective critical angles are marked with dashed lines in the graph. The y-axis is scaled by the free space wavelength λ_0.

The surface-selectivity of the evanescent field has also been utilized in many chemical sensors, biosensors and immunoassay set-ups, including fiber optic and planar waveguides (see e.g. Taitt et al. 2005; McDonagh et al. 2008; Taitt et al. 2016), interferometers (Lechuga et al. 1995) and surface plasmon resonance (SPR) sensors (Olaru et al. 2015), to name a few.

2.1.2 Supercritical angle fluorescence (SAF)

A randomly oriented molecular emitter in a homogeneous medium radiates isotropically. However, when the emitter is located in the vicinity of a dielectric interface, such as a sample-substrate interface, the emission distribution becomes anisotropic, and more power radiates towards the medium of the higher refractive index (see e.g. Lukosz 1979; Courtois et al. 1996; Enderlein 1999; Polerecký et al 2000). Moreover, substantial power is radiated into a range of angles exceeding the critical angle of the interface, that is, into supercritical angles. As schematically illustrated in Fig. 3, the emission into the supercritical angles can be generated only by emitters within the optical near field to the interface, as the emitters outside of the near field can radiate into the substrate only in angles below the critical angle. This forms the basis for a highly surface-selective luminescence detection mode, called supercritical angle fluorescence (SAF) (Ruckstuhl and Verdes 2004).

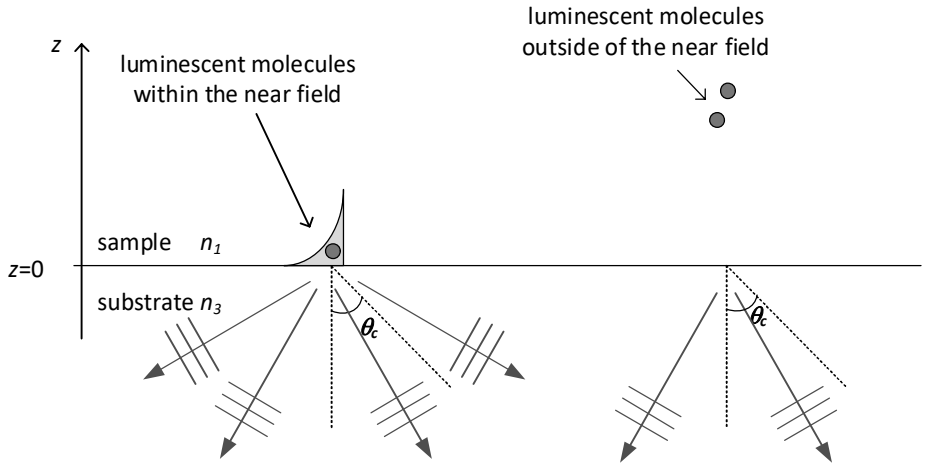

Figure 3. The principle of supercritical angle fluorescence (SAF), a surface-selective detection mode of luminescence.

Fig. 4A shows a simulated angular emission distribution of a randomly oriented molecular emitter located exactly at the substrate-sample interface, where an aqueous solution (n_1 = 1.33) and polystyrene (n_3 = 1.59) represent the sample and substrate materials, respectively. The figure illustrates the highly anisotropic nature of the radiation. Overall, 75.5% of the power is radiated towards the substrate, and the highest power radiates exactly towards the critical angle (marked with a dashed line). With given materials, SAF power equals to 41.3% of total radiation.

Fig. 4B shows the corresponding distribution, when the emitting molecule is moved a distance of $\lambda_0/3$ away from the interface in the sample. The power towards the substrate is decreased, and more importantly, the SAF emission has almost vanished. This rapid decay of SAF has important consequences in luminescent sensing: by restricting the detection to SAF angles, surface-selective fluorescence sensing can be realized.

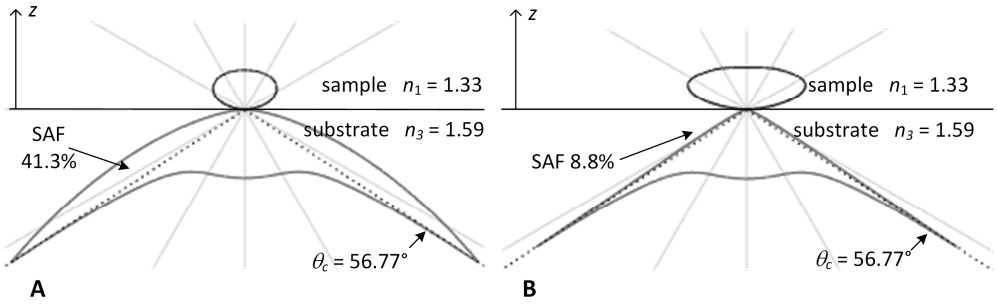

Figure 4. Calculated angular emission distributions for a randomly oriented molecular emitter in the vicinity of the sample-substrate interface. (A) The emitting molecule at the interface; (B) the emitting molecule in the sample at a distance of $z = \lambda_0/3$ from the surface.

Fig. 5 shows the decay of the SAF emission for a length of one wavelength away from surface of the substrate in the sample. The shape of the decay is very exponential, close to $\sim\exp\left(-z/\left(\frac{\lambda_0}{5}\right)\right)$. Compared to the emitters at the PS-water interface, the emitters at one λ_0 away radiate only 1/30 of the power into SAF angles. The figure also shows that a substrate with a slightly higher refractive index (PS) makes the surface-selectivity slightly higher as well.

The exponentially decaying SAF emission provides a powerful alternative, called SAF microscopy, to the widely used TIRF microscopy (Ruckstuhl and Verdes 2004). The key idea in SAF microscopy is to detect both the SAF emission and the under critical angle fluorescence at the same time. This gives means to calculate the z-coordinate of the fluorescence emitter with a nanometer resolution, thus breaking

the diffraction limit in one dimension (Winterflood et al. 2010). The surface-selectivity of the SAF has also been utilized in immunoassays, but with much less popularity than TIRF-based devices, and contrary to many excellent reviews on TIRF based immunoassays and biosensors, no review focusing solely on SAF-type immunoassays has been published to this day. Selected SAF immunoassay platforms will be reviewed in the sub-section 2.2.3

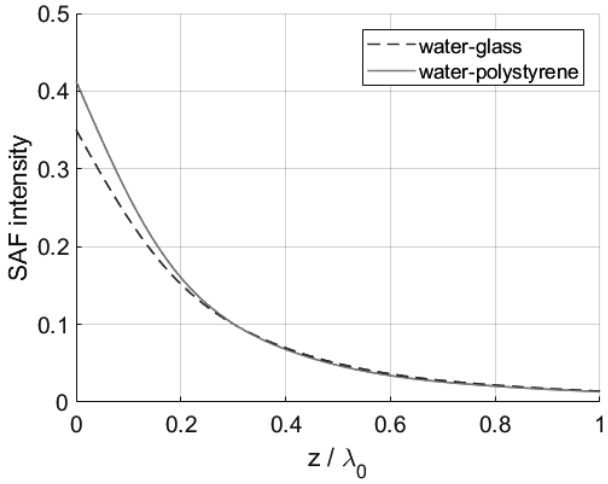

Figure 5. Simulated decays of the supercritical angle fluorescence as a function of the distance z into the sample from the water-glass and water-polystyrene interfaces. Here, n_1 = 1.33 (water); n_3 = 1.515 (glass) or n_3 = 1.59 (polystyrene).

2.1.3 A luminescent thin film at the sample-substrate interface

Striking emission anisotropies can also be observed when a luminescent thin film is located at the substrate-sample interface (Courtois et al. 1996; Polerecký et al. 2000). The geometry is popular in the luminescence-based sensing of oxygen, pH and temperature, to name a few, and the geometry can display itself both in planar and non-planar waveguides, such as optical fibers or capillaries. Fig. 6 shows a simulated emission pattern of a luminescent film having a thickness of $1.5\lambda_0$ and a refractive index between the refractive indices of the sample and the substrate. The figure demonstrates that the emission power to distinct supercritical angles can exceed the direct radiation power multiple times. Here, the film is assumed to contain a homogenous distribution of randomly oriented mutually incoherent molecular emitters.

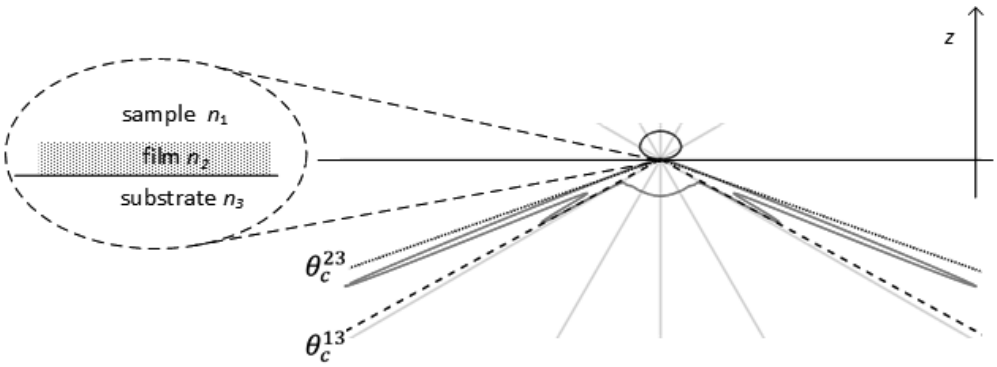

Figure 6. A luminescent thin film at the sample-substrate interface. The radiation pattern is calculated with following parameters: n_1 = 1.33 (water); n_2 = 1.43 (film); n_3 = 1.515 (glass); film thickness $1.5\lambda_0$, where λ_0 is the free space emission wavelength. The molecular emitters in the film are assumed to be homogeneously distributed, randomly orientated and mutually incoherent. The critical angles for the sample-substrate and film-substrate interfaces are denoted by θ_c^{13} and θ_c^{23}, respectively.

Fig. 7 shows in more detail how the emission pattern depends on the refractive index and the thickness of the film. There are two technically relevant cases that apply to chemical sensing. The refractive index of the film (n_2) is usually higher than that of sample (n_1), but the value can be either smaller or greater than the refractive index of the substrate (n_3). Therefore, we have either

(A) $n_1 < n_2 < n_3$ or
(B) $n_1 < n_3 < n_2$

Case (A) corresponds to a typical sol-gel- or silicone-based luminescently doped sensing film on a glassy substrate material, applied to gas or liquid phase sensing. The respective angular emission distribution (Fig. 7A) shows intense peaking between the angle values corresponding to the critical angle θ_c^{13} between the substrate and the sample, and the critical angle θ_c^{23} between the substrate and the sensing film. The thicker the film, the more peaks the film generates through the multiple reflections of the high angle modes. Polerecký et al. (2000) called these modes as [e_1 p_2 p_3] modes, because the corresponding field is evanescent in the medium of refractive index n_1 (sample), but propagating in the media of refractive indices of n_2 (film) and n_3 (substrate).

Case (B) corresponds to, for example, a luminescently doped polystyrene film on a glassy substrate material. The angular emission distribution (Fig. 7B) shows peaking at angle values exceeding the critical angle between the sample and substrate, but as

no critical angle between film and substrate can be defined ($n_2 > n_3$), the peaks are wider and lower in shape compared to case (A). Moreover, the peaks can locate very close to 90° (Fig. 7B).

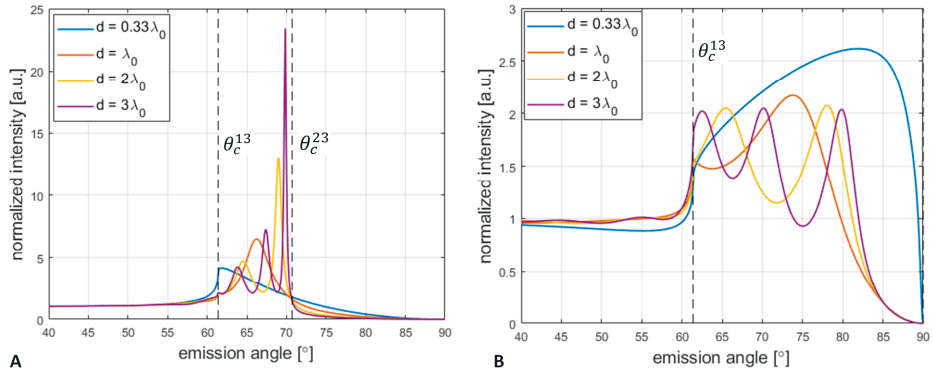

Figure 7. The angular emission distribution of luminescent thin films with various thicknesses at the sample-substrate interface. Following parameter values are used: sample n_1 = 1.33 (water); substrate n_3 = 1.515 (glass); (A) film n_2 = 1.43 (sol-gel); (B) film n_2 = 1.59 (polystyrene). Four film thicknesses are used: 1/3λ0, λ0, 2λ0, 3λ0, where λ0 is the free space emission wavelength. The critical angles for the sample-substrate and film-substrate interfaces are denoted by θ_c^{13} and θ_c^{23}, respectively.

These simulations show that the efficient luminescence detection in this configuration is not a trivial task but requires knowledge and control with respect the material parameters such as the refractive index and thickness of the film. In particular, the placement of the detector with conventional optics underneath the substrate leads to the loss of the main emission contribution. Either optical wave guiding structures (e.g. Burke et al. 2005), detection on the edges of the substrate (e.g. Gouin et al. 1998; Polerecký et al. 2000), specially shaped substrates (e.g. Blue et al. 2005) or in-contact optics should be applied in order to collect the main emission contribution radiated into the supercritical angles.

2.1.4 Modelling of the luminescence at interfaces

While TIRF-based methods are more popular than SAF-based, the first theoretical studies related to SAF date back a hundred years to Sommerfeld, who confronted the problem of dipole radiation close to a dielectric interface, albeit in larger physical dimensions, while studying the properties of antennas and radio waves above the

surface of the earth (Sommerfeld 1909). Since then, the theory has evolved and, as Novotny and Hecht (2012) in their summary say, "many things have been reinvented". However, the theory of SAF is more complex than the theory of TIRF, and an effective SAF instrumentation typically demands more case-specific designs than TIRF instrumentation, in which only a supercritical illumination is required. These facts have probably slowed down the progress of SAF applications.

Twenty years ago, several authors published theoretical studies on the dipole emitters within an arbitrary multilayer system. Courtois et al. (1996) elegantly applied Lorentz's reciprocity theorem and derived a transfer matrix model based on a propagating plane wave from outside towards the position of the dipole. A few years later, Benisty et al. (1998) and Polerecky et al. (2000) also constructed transfer matrix models, but for a wave propagating outwards from the dipole position. About the same time, Enderlein et al. treated the case of a single interface without the transfer matrix formalism (Enderlein 1999, Enderlein et al. 1999).

In the following, we follow Courtois et al. (1996) and apply the Lorenz reciprocity theorem together the with optical transfer matrix method (Katsidis and Sipakas 2002). We consider a single classical molecular emitter inside a planar, dielectric layer on the substrate (Fig. 8). The results can easily be extended for a homogeneous layer of emitters assumed to be mutually incoherent and randomly orientated. This corresponds to the simulations shown in the sections 2.1.3 and 3.1, as well as those in P4. Moreover, the model can be reduced for the case of a single interface by simply setting the refractive index of the molecule layer as equal to the refractive index of the sample (i.e. $n_2 = n_1$). This corresponds to the simulations in the sections 2.1.2 and 3.1, as well as those in P1. The notation comes from Luan et al. (2006).

The radiation pattern of a classical, oscillating electric dipole, oriented either parallel (horizontal, $\parallel$) or perpendicular (vertical, $\perp$) to the dielectric interface, can be expressed with three power distributions: $P_{\parallel}^{p}(\theta)$, $P_{\parallel}^{s}(\theta)$, $P_{\perp}^{p}(\theta)$, where the subscripts denote the dipole orientation, superscripts denote the polarization of the emission, and θ denotes the polar emission angle.

Due to the planar geometry, these expressions are independent of the azimuthal emission angle. Now, according to Lorentz reciprocity principle, these expressions can be calculated directly from the incoming "coupling efficiencies", i.e. by finding out the field strength at dipole positions induced by an incoming wave.

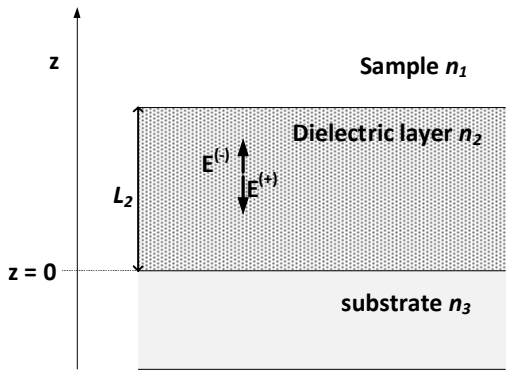

Figure 8. The starting point for the modelling of the radiation pattern of a dipole emitter inside a dielectric layer on a transparent substrate. The forward and backward propagating electric fields inside the dielectric layer are shown for the sample-side incoming wave. For the substrate-side incoming wave, opposite directions for the propagating fields apply. The single interface can be modelled as a special case, where $n_2 = n_1$. Adapted from Luan et al. (2006).

The electric field strength at the dipole position

$$\boldsymbol{E}_{p,s}(z) = \begin{bmatrix} E_{p,s}^{(+)}(z) \\ E_{p,s}^{(-)}(z) \end{bmatrix} \tag{2.3}$$

can be derived using transfer matrix formalism. Here the subscript denotes polarization and superscripts the propagation direction. Setting the field magnitude of the incoming wave to unity, we get for the sample-side incoming wave

$$E_{p,s}^{(+)}(z) = \frac{(1-r_{21}^2)\exp\left[jk_2(L_2-z)\right]}{t_{21}[1+r_{21}r_{32}\exp(2jk_2L_2)]} \tag{2.4a}$$

$$E_{p,s}^{(-)}(z) = \frac{(r_{21}^2-1)r_{32}\exp\left[jk_2(L_2+z)\right]}{t_{21}[1+r_{21}r_{32}\exp(2jk_2L_2)]} \tag{2.4b}$$

Similarly, for the substrate-side incoming wave

$$E_{p,s}^{(+)}(z) = \frac{(1-r_{23}^2)\exp\left(jk_2z\right)}{t_{23}[1+r_{12}r_{23}\exp(2jk_2L_2)]} \tag{2.4c}$$

$$E_{p,s}^{(-)}(z) = \frac{r_{12}(r_{23}^2-1)\exp\left(2jk_2L_2-jk_2z\right)}{t_{23}[1+r_{12}r_{23}\exp(2jk_2L_2)]} \tag{2.4d}$$

Here, $k_2 = n_2 k \cos(\theta_2)$ is the magnitude of the normal component of the wave vector in the dielectric layer, where k is the free space wavenumber; L_2 is the thickness of the dielectric layer; n_2 is the refractive index of the layer; θ_2 is the polar angle in the layer, and r_{ij} and t_{ij} denote the Fresnel reflection and transmission coefficients when light enters the medium *j* from the medium *i*. Finally, the three power distributions are given by

$$P_{\parallel}^{s}(\theta) = \frac{3}{8\pi} n(\theta) \left| E_s^{(+)}(z) + E_s^{(-)}(z) \right|^2 \tag{2.5a}$$

$$P_{\parallel}^{p}(\theta) = \frac{3}{8\pi} n(\theta) \left| E_p^{(+)}(z) - E_p^{(-)}(z) \right|^2 |cos\theta_2|^2 \tag{2.5b}$$

$$P_{\perp}^{p}(\theta) = \frac{3}{8\pi} n(\theta) \left| E_p^{(+)}(z) + E_p^{(-)}(z) \right|^2 |sin\ \theta_2|^2 \tag{2.5c}$$

where $n(\theta) = n_1$ and $n(\theta) = n_3$ for the sample side and the substrate side radiation, respectively. The three power distributions (2.5) describe the radiation of three orthogonal dipole orientations; therefore, summing the distributions yields the distribution of a randomly orientated dipole.

All the simulations in this thesis, as well as those in (P4), have been carried out with the described methodology. To ensure the correctness of the method, the corresponding simulations in (Polerecký et al. 2000) have been reproduced. The original calculations in (P1), however, were carried out according to Enderlein et al. (1999).

2.2 Immunoassays

This section provides a brief introduction to immunoassay technologies. Common molecular assay formats and detection technologies are reviewed. A sub-section is dedicated for the surface-selective fluoroimmunoassays, and selected devices relevant to the thesis are discussed in more detail.

Immunoassays utilize the highly specific antibody-antigen immunoreaction in the analyte recognition. The technology was introduced in clinical chemistry in late 1950s by Yalov and Berson (1959), and independently, by Ekins (1960). They both developed first generation radioimmunoassays, Yalov and Berson for insulin and Ekins for thyroxine, but only the first mentioned work was rewarded with Nobel Prize in medicine 18 years later. Since then, immunoassay technologies have evolved

rapidly, and they play a significant role in the many fields, including medical diagnostics, environmental monitoring, food analysis and security, to name a few (Vashist and Luong 2018). Today, antibodies have been engineered against thousands of analytes (Wu 2006), including disease biomarkers, pathogens, contaminants, allergens and abused drugs. In addition, the radioimmunoassays have been replaced by other technologies, of which the enzyme linked immunosorbent assay (ELISA) has become the gold standard. However, the progress in biosensor technologies has resulted in the development of many other immunoanalytical sensing systems, including mass-sensitive devices (Fogel 2016), electrochemical systems (Warsinke et al. 2000), and especially SPR-based immunoassay platforms (Mullet et al. 2000; Nguyen et al. 2015). In addition, advances in microfluidics and lab-on-a-chip technologies have led to novel immunoassay systems applying lower sample and reagent volumes and often a reduced number of test steps. The most widely used microfluidic immunoassays are based on the lateral flow technology, which enables both the cost-effective single analyte qualitative assays, such as pregnancy tests, as well as more sophisticated, quantitative assays for multiple analytes with a separate read-out device (Anfossi et al. 2019).

2.2.1 Immunoassay formats

There is a wide variety of molecular immunoassay formats. Depending on the properties of the analyte (i.e. the antigen), the complexity of the sample matrix, the features of available antibodies and the read-out device, one molecular format can outperform the others in terms of sensitivity and specificity. Generally, the formats occur in two basic types: noncompetitive (or direct, immunometric) and competitive (indirect) immunoassays (Sapsford et al. 2002). In a noncompetitive immunoassay, the analyte binds to the immobilized capture antibody on the sensing surface. With large antigens at a high enough concentration the binding can be directly measured, but most often a labelled detection antibody is applied. This configuration is frequently called a sandwich assay, and the format is schemed in Fig. 9A. The sandwich-type immunoassays are typically very sensitive and highly specific, but when the same antibody operates both as the capture and detection antibody, they require relatively large size antigens containing more than one epitope for the antibody binding. The measured signal is proportional to the analyte concentration.

In a competitive immunoassay, a known concentration of labelled antigen molecules competes with the antigen molecules in the sample for the limited number

of available binding sites (Fig. 9B). This format is especially useful in the detection of small molecules, not possessing two distinct epitopes for antibody binding. In the competitive format, the measured signal is conversely proportional to the analyte concentration. A variant of the competitive immunoassay is the so-called displacement immunoassay, where the binding sites are initially saturated with labelled antigens (or antibodies, depending on the configuration), and upon the injection of the sample, the unlabelled antigens begin the displacement of the labelled antigens (or antibodies) (Ngo 2007).

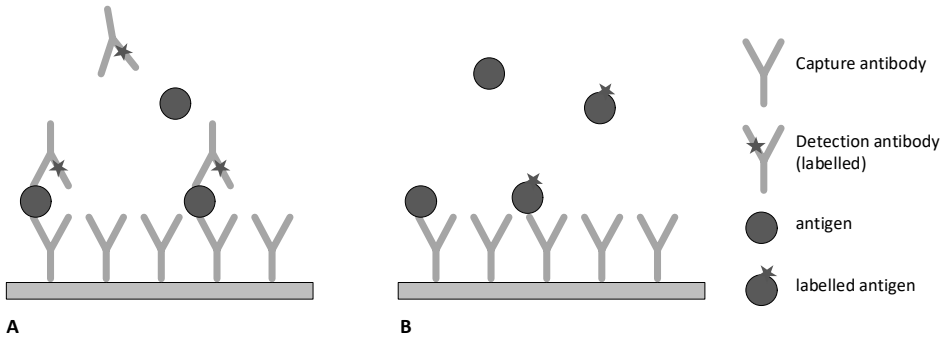

Figure 9. The basic molecular formats of immunoassays: a noncompetitive sandwich assay (A); a competitive assay (B).

2.2.2 Label and label-free technologies

There are many transducer technologies available for the detection of the immunochemical binding event on the sensing surface. Generally, the technologies are divided into two classes: label-free and label-based technologies.

The label-free technologies rely on the sensitive detection of the analyte-induced changes in the inherent properties of the molecular sensing layer, such as changes in the accumulated mass or refractive index. The mass-based methods include microcantilevers and acoustic resonators, typically operating in shear modes to avoid excessive energy dissipation into liquid medium (Voiculescua and Nordin 2012). As an example of such a device, Fig. 10A shows the principle of a thickness-shear mode resonator (also called as quartz crystal microbalance, QCM) applied to the immunosensing. Analogically to the optical evanescent field, the acoustic shear wave decays rapidly in liquids; the decay length of a 10 MHz shear wave is 180 nm in water (Välimäki et al. 1997), which makes the sensing very surface-sensitive. The changes in the biological layer on the sensing surface affect the effective mass (and often the

quality factor of the resonator), which results in a change in the electrical characteristics of the device (Fig. 10B). The mass resolution of the TSM-resonators in liquid is of order 0.1 ngcm^{-2} (Rodríguez-Padro et al. 2005).

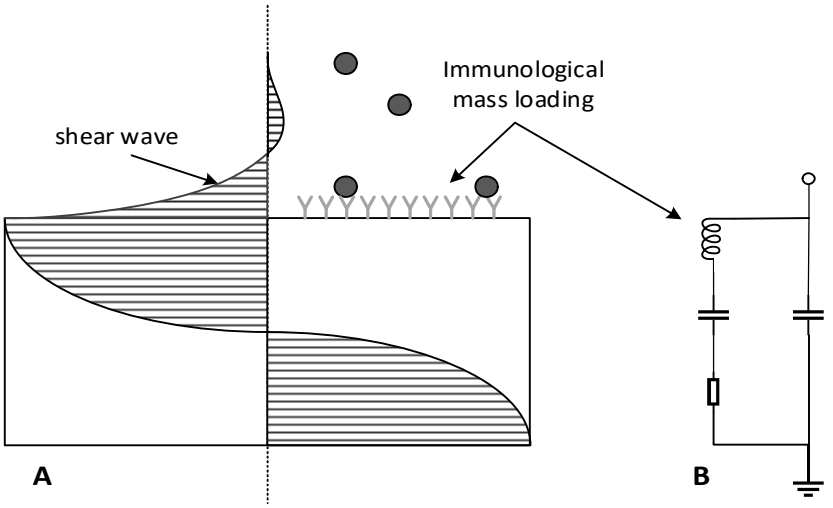

Figure 10. The principle of a thickness-shear mode resonator in mass-sensitive detection. (A) The schematics of the shear wave inside the resonator and coupled liquid; (B) An electrical equivalent circuit of the resonator.

The most established and widely used label-free immunoassay technique is probably SPR (Olaru et al. 2015). The technique relies on the detection of minute changes in the refractive index of the sensing layer immobilized on a thin metallic film, most commonly of gold, manufactured on a transparent substrate. A beam of p-polarized monochromatic light is used to illuminate the film through a prism, and the intensity of the reflected light is measured, as Fig. 11A shows. At certain angle of incidence, the excitation light becomes coupled to surface plasmons at the metallic interface and the reflected power strongly decreases (Fig. 11B). The condition for the coupling is highly sensitive for the refractive index of the molecular layer. With the best commercial devices, a resolution of 10^{-7} in the refractive index is achieved (Ho et al. 2015), which transposes to a typical SPR mass resolution of order 10 pgcm^{-2} and detection limit of order 10 pg/mL (Nguyen et al. 2015).

Recently, advances in integrated optics have brought up optical microring resonators as another option for the detection of immunologically induced minute changes in the refractive index. While small in the actual physical sizes, the ring resonators yet provide large effective path lengths due to circulation of the light in the structure, which forms the basis for the reported high sensitivity with detection

limits of order 10 pM for DNA (Kindt and Bailey 2013). The changes in the biological layer affect the effective refractive index of the guided mode of the resonator, which can be detected with interferometric means. The structure also offers possibilities for multiplexed sensing and interesting signal enhancements through enzymatic labelling (Kindt et al. 2013).

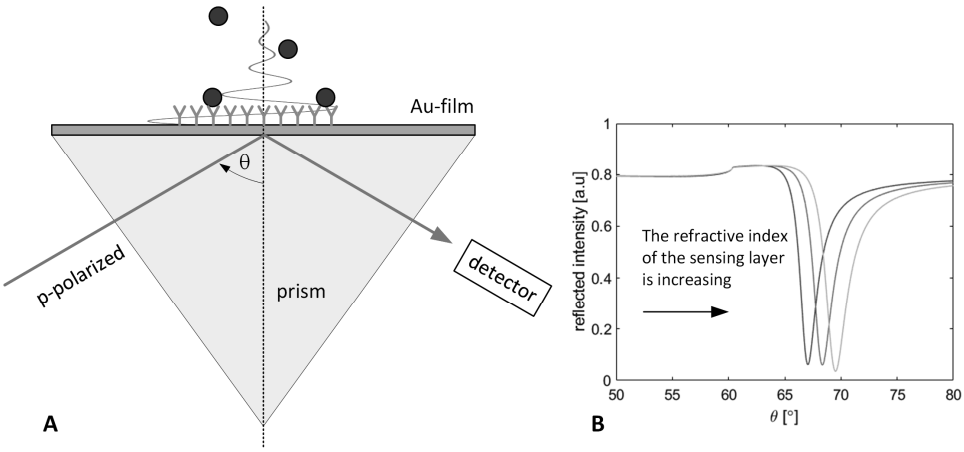

Figure 11. The principle of the surface-plasmon-resonance (SPR) immunosensor. (A) The scheme of a typical measurement set-up; (B) Illustrative SPR-responses.

While the label-free technologies are based on the sensitive detection of the intrinsic properties of the binding molecules, the label-based technologies rely on the detection of the engineered properties of the labelled molecules, which most often are of fluorescent or enzymatic nature. The use of the label can greatly enhance the sensitivity of the assay, as the label is particularly designed to deliver a maximal signal upon interrogation. On the other hand, the labels can have detrimental effects on the affinity of an antigen-antibody interaction (Sun et al. 2008). The chemical properties of the recognition molecule can change and its specificity decrease. In addition, the labelling procedure inevitably adds to the cost and complexity of the assay.

Surface-selective fluorescent immunoassay technologies, exploiting the sample-substrate interface in the fluorescent detection, form an interesting sub-set of the label-based technologies. The technologies have benefited greatly from the advances in optical telecommunication technology, as new waveguide materials, high performing LEDs and laser diodes and integrated optics have pushed the surface-selective fluorescent sensing towards new limits in sensing performance while decreasing the costs at the same time (Taitt et al. 2016). The special feature of

surface-selective fluorescent technologies is the rejection of the bulk fluorescence effects, which makes it possible to monitor binding processes in real time. This can result in an enhanced functionality in challenging matrices and the elimination of certain assay steps such as washing. In addition, the early binding rates can be utilized in rapid assays.

Li et al. (2014) have reported on an interesting fiber-optic set-up for α-Fetoprotein that utilizes the sample-substrate interface for evanescent wave interaction with Au-labels. The set-up is schemed in Fig. 12. The capture antibodies are immobilized on the core of the fiber, and the detection antibodies are conjugated on the Au-nanoparticles that act as signal amplifying labels. The presence of the analyte brings Au-nanoparticles within the penetration depth of the evanescent field, and the transmitted power in the fiber is attenuated in proportion to the analyte concentration through the plasmonic coupling.

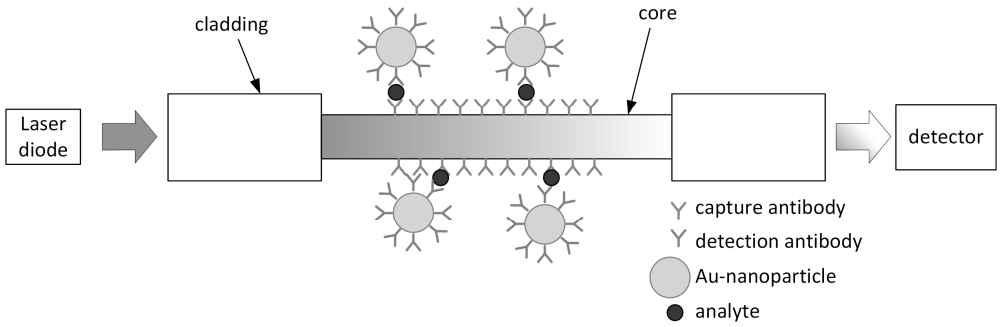

Figure 12. A cross-sectional scheme of the fiber-optic set-up utilizing the evanescent wave and Au-nanoparticles in sensing of α-Fetoprotein (Li et al. 2014). The capture antibodies are immobilized on the core of the fiber. The presence of the analyte initiates the binding of Au-nanoparticles through the conjugated detection antibodies. An analyte-concentration-dependent attenuation of the transmitted signal is observed in the detector.

Zero-mode waveguides represent a unique TIR-based, highly confined mode of fluorescence detection (Leven et al. 2003). An array of zero-mode waveguides can be realized by manufacturing holes with subwavelength diameter on a thin metal film deposited on a glassy substrate. The core of these waveguides is formed by the sample liquid and the cladding by the metal. No propagating modes exist (thus the word zero-mode), and the excitation intensity in the waveguide decays exponentially away from the substrate.

2.2.3 SAF immunoassays

During the last two decades, novel SAF-based immunoassay platforms have been developed. The groups of Stefan Seeger (University of Zurich) and Brian MacCraith (Dublin City University) have been the leading figures in the field. The key feature of the platforms is their optical sensing geometry aimed for an efficient and exclusive collection the SAF emission. To this end, several tailored structures have been designed, and especially parabolic shapes have been popular. The optical schemes of some SAF devices, developed between 2003 and 2013, are shown in Fig. 13.

Parabolic surfaces provide practical means to collect radiation from a point source and transform it into a highly directed beam. In connection with SAF, the parabolic emission collector was first proposed by Enderlein et al. (1999). In the arrangement, the fluorescent emitters were located on the focal point of the parabolic lens, and the SAF emission was reflected by the parabolic surface through total internal reflection, resulting in a collimated, ring-shaped output beam. The idea was quickly applied to the detection of a single fluorescent molecule (Ruckstuhl et al. 2000) as well as in the online monitoring of binding kinetics of a model immunoassay, with the optical scheme shown in Fig. 13A (Ruckstuhl et al. 2003). Similar systems were also applied to real-time studies of DNA (Krieg et al. 2004; Krieg at al. 2006; Laib et al. 2006).

In 2009, Kurzbuch et al. (2009) developed a SAF-based reader for multiplexed assays on plastic biochip. In the set-up, shown in Fig. 13B, a parabolic lens was manufactured from Zeonex 480R (high transmission moldable plastics), and the lens incorporated an aspheric surface for the focusing the excitation beam as well. A motorized xy-stage scanned the multiassay plastic biochips.

Two years later, Hill et al. (2011) presented a first report on a low-cost disposable plastic biochip array (Fig. 13C), where paraboloid elements were integrated into the chip. A nine-element chip was made of Zeonex, and each element contained an integrated parabolic lens that was used for both the TIRF excitation and the SAF collection. At the same year, Ruckstuhl et al. (2011) reported on a novel SAF immunoassay platform as well. The authors presented disposable polymer test tubes (Zeonex) with integrated parabolic collection optics (Fig. 13D) and a compact SAF reader. Experimental results with a one-step immunoassay for interleukin-2 demonstrated a detection limit below 4.5 pg/mL with 13 min test time. The same device has been later applied to an interferon-α assay (Winterflood et al. 2013). In 2013, Kurzbuch et al. (2013) presented a polymer biochip with embedded SAF collection optics.

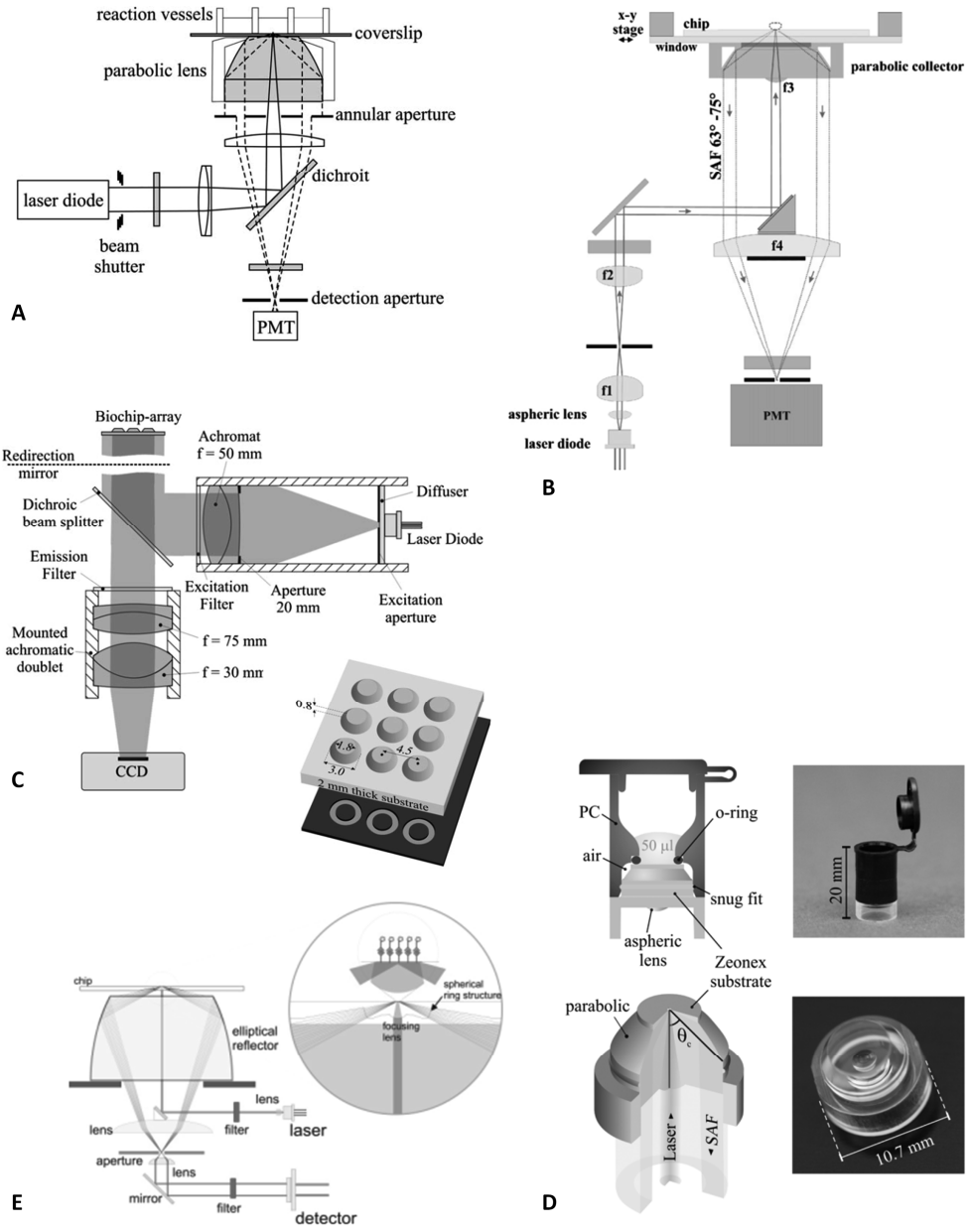

Figure 13. Optical schemes of selected immunoassay platforms utilizing supercritical angle fluorescence. (A) Ruckstuhl et al. 2003; (B) Kurzbuch et al. 2009; (C) Hill et al. 2011; (D) Ruckstuhl et al. 2011; (E) Kurzbuch et al 2013.

This time no parabolic element was present, but an integrated ring-lens together with a separate elliptical mirror were applied (Fig. 13E). Test results with human IgG assays yielded detection limits below 10 pg/mL. The idea to separate the polymer chip and reflecting surface was also presented in a letter by O'Driscoll et al. (2012). In addition, Hung et al. (2015) have recently presented an integration of plastic microlens array in a microfluidic system for a solid phase PCR and later applied the device to pathogen detection (Hung et al. 2017).

An alternative SAF approach utilizing the waveguiding properties of capillary tubes has been reported by several authors (Weigl et al. 1994; Ligler et al. 2002; Baldini et al. 2008). In this approach, the inner surface of a glass or polymer tubing is used as the sensing surface. The structure serves as a well-defined sample volume with a large area-to-volume ratio and represents an optical waveguide providing means for enhanced SAF detection. One possible sensing geometry is depicted in Fig. 14, where orthogonal excitation is used along the whole sample length of the capillary. The SAF emission is coupled to guided modes in the capillary structure. The integrated SAF emission, originating from a large sensing area, can be efficiently collected at the end(s) of the capillary. As the collected emission is exclusively of SAF origin, the background fluorescence is powerfully suppressed. The capillary structures have been used to detect several chemical and biochemical compounds, including pH and C-reactive protein, to name a few (Baldini et al. 2008; Baldini et al. 2009). More recently, Balsam et al. (2013) demonstrated a cost-effective multi-analyte device based on glass capillary arrays using smartphone as the detector.

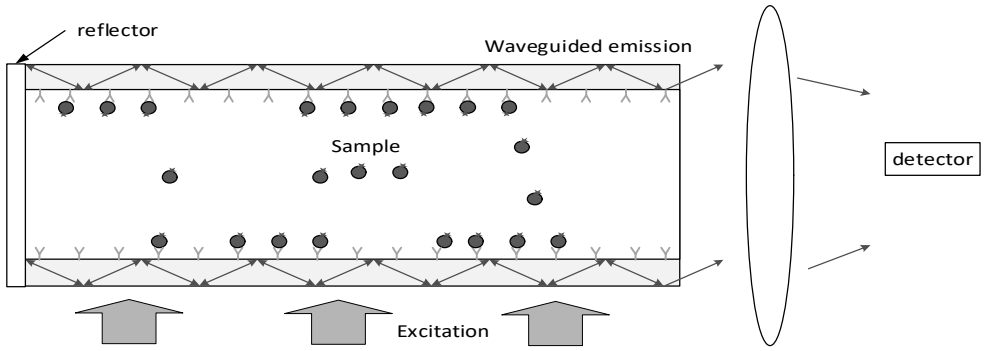

Figure 14. One possible geometry of a capillary immunoassay. Orthogonal excitation is applied on the total sample length and the integrated SAF-emission is efficiently collected at the end of the structure.

Finally, an interesting approach was recently introduced by Sandeau et al. (2015), who applied a novel large area CMOS array for multiplexed chemiluminescent

biosensing. Due to the high refractive index contrast between aqueous samples and silicon, the chemiluminescent SAF emission of the biomolecules bound on the CMOS pixels can be efficiently collected without any collection optics. The authors demonstrated the power of the device with simultaneous assays for three cytokines with detection limits at low pg/mL.

2.3 Chemical sensing in cell cultures

This section provides an overview of the chemical sensing in cell cultures. A sub-section is dedicated to the luminescence-based sensing and imaging.

Technological progress in microfabrication, microfluidic systems, sensor technology, biomaterials and cell and tissue engineering has resulted in the development of sophisticated *in vitro* cell and tissue models, which are physiologically relevant in many aspects (Modena et al. 2018). These models are providing new experimental platforms for studying the functioning and operation of cells and tissues. Studying such models not only contributes to the fundamental understanding of the basic units of life, but also provides new possibilities for disease studies (Schlachetzki et al. 2013; Kim et al. 2004) and drug testing (Astashkina et al. 2012; Horvath et al. 2016). For example, experiments with advanced neuronal models can shed light on how epilepsy develops, what triggers seizures and what halts. Moreover, if such neuronal models are constructed of the human induced pluripotent stem cell-derived (hiPSC-derived) neuronal cells of the patient, then even personalized *in vitro* drug tests and therapies are possible (Gurwitz 2016).

In a proper physiological *in vitro* cell model, the environmental conditions should mimic the actual conditions of the corresponding tissue *in vivo*. This means that temperature, pH, oxygen tension and nutrient supplies should be kept within certain, typically narrow limits (Wilson 2008). Therefore, integrating chemical monitoring devices to the cell models is important. In addition, the monitoring devices can generate valuable information on the metabolic status of the cells. The following section gives a survey on the most important analytes in cell culturing and the related measurement technologies. The focus is, however, on oxygen and on the luminescence-based sensing technologies.

2.3.1 Overview

Oxygen. Molecular oxygen is vital for living cells, and it plays a key role in their metabolism. The oxygen partial pressure in tissues and organs results from a fine balance between oxygen delivery and consumption, and its optimal value is highly tissue-specific, ranging from approximately 13 kPa in arterial blood to values below 4 kPa in muscles, brain and skin (Carreau et al. 2011). Therefore, a physiological *in vitro* cell model should be studied in the tissue-specific pO_2 conditions rather than in the ambient oxygen tension, which is many times considered as "normoxic" (Mohyeldin et al. 2010)

Controlling and measuring the oxygen level is challenging in miniaturized or microfluidic cell models, where the volumes are low and the available space for instrumentation limited. The limited space excludes bulky and expensive laboratory scale measurement methods, such as Winkler titration or magnetic resonance imaging (MRI), and the choice is to be made between the electrochemical oxygen electrodes and optical devices based on the oxygen induced quenching of luminescence (Papkovsky and Dmitriev 2013).

The electrochemical oxygen sensors are based on the reduction of oxygen on the noble metal sensing electrode. Two basic types of the sensors are i) direct amperometric sensors, where the sensing electrode is in direct contact with the medium, and ii) Clark-type sensors, where the sensing electrode is separated from the medium by a gas-permeable membrane (Kieninger et al. 2018). The Clark-type is more complex to realize but interfering and possibly harmful interactions between the sensing electrode and the culture are much less an issue. Clark-type oxygen sensors were introduced already in 1956, and it is one of the earliest chemical sensors (Clark 1956). The principle of a Clark-type is illustrated in Fig. 15. Oxygen molecules can diffuse through the membrane into the sensing electrode, where they become reduced. Applying a constant voltage between the sensing and reference electrodes creates an output current that is directly proportional to the oxygen concentration. The linear behavior and typically a one-point calibration procedure are the advantages of a Clark-type oxygen sensor, and they are applied in some commercial cell culture monitoring systems, such as Bionas devices (Thedinga et al. 2007). However, the electrochemical reaction consumes oxygen, which can become an issue in miniaturized or microfluidic cell cultures. In addition, imaging or scanning set-ups are challenging to realize (Wolfbeis 2015).

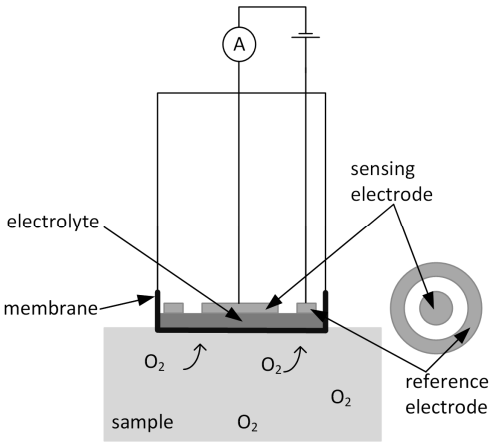

Figure 15. The principle of Clark's oxygen electrode.

The optical oxygen sensors based on the oxygen-dependent quenching of luminescence provide an attractive alternative for the electrochemical sensors. In principle, optical oxygen sensors are minimally invasive and do not consume oxygen, their sensitivity and dynamical range can be tuned (Mills 1997, Lehner et al. 2014), they enable remote sensing by using optical fibers, they are relatively easy to miniaturize, insensitive to electromagnetic disturbances and compatible with imaging set-ups (Wolfbeis 2015). Furthermore, multiple luminescence sensing is possible by combining oxygen sensitive indicators in the same matrix with other indicators, such as temperature- and/or pH-sensitive indicators (Liebsch et al. 2000). In recent decades, significant progress has been made in the development of oxygen indicators, matrix materials and the measurement set-ups. Many commercial devices exist, and excellent technology reviews are available (Grist 2010; Quaranta 2012; Papkovsky and Dmitriev 2013; Wang and Wolfbeis 2014).

pH. Biological processes are very sensitive to pH, and a stable pH is a strict requirement for any viable cell model (Michl et al. 2019). A large variety of pH sensing methods exist. Overall, the most widely used pH sensors are potentiometric pH glass electrodes, but their size restricts the application in cell culturing (Kieninger et al. 2018). Therefore, the available options for miniaturized cell culture monitoring are light addressable potentiometric sensors (LAPS), ion-sensitive field-effect transistors (ISFETs), metal oxide-based potentiometric devices or optical methods based on pH-sensitive indicators, either as dissolved in the medium (see for example Rajan et al. 2016) or as embedded in solid layers or particles (Wencel at al. 2014; Kieninger et al. 2018).

Glucose and lactate. Glucose is the main source of energy and lactate a crucial metabolite in cultured mammalian cell cultures (Ozturk et al. 1997). Monitoring the concentration of these two compounds can therefore be of great significance. Because of the large clinical importance, glucose sensors are by far the most studied and developed biosensors (Wang 2008). The enzyme-based electrochemical biosensors dominate glucose sensing both in general and in cell culture applications (Kieninger et al. 2018). In a typical configuration, an enzyme is immobilized in a matrix on the sensing electrode, and through an enzymatic reaction, the analyte is converted to a by-product that is oxidized or reduced in the sensing electrode. Often, oxidase enzymes (glucose oxidase, lactate oxidase) are used. Also reports on enzyme-based optical devices exist (Koman et al. 2015), but the electrochemical devices dominate.

2.3.2 Luminescent chemical sensing and imaging

Many features make luminescence one of the most powerful and widely applied transduction mechanism in chemical sensing (Basabe-Desmonds et al. 2007). Luminescent transduction provides high sensitivity, a wide variety of sensing schemes and several measurable parameters, including fluorescence microscopy and spectroscopy techniques in luminescence intensity, lifetime, energy transfer or anisotropy modes. The progress in the development of optical components such as LEDs, laser diodes and sensitive detectors and cameras has paved the way for the dominance of luminescence-based sensing, particularly in life sciences. Especially options for spatially resolving imaging set-ups even in miniaturized platforms gives luminescence-based technology an advantage that can hardly be met by any other technology (Pfeiffer and Nagl 2015).

A luminescence-based chemical sensor is typically composed of a luminescent sensing element, light source, optics, detector and read-out electronics. If the aim is to locate the sensing surface inside a miniaturized cell culture well and not to rely on any sampling procedures or on the outlet stream in a perfusion system, great effort in the design of the sensing element, geometry and the whole instrumentation ensemble is needed (Wu and Gu 2011). The design must consider not only the factors that effect on the performance of the sensor, but also consider the manufacturing feasibility, biocompatibility, invasiveness and functioning of other sensors and instrumentation. Today, most luminescent sensors applied in cell

culturing measure oxygen, pH and or temperature, while the reports on the monitoring of any other compounds are rare (Pfeiffer and Nagl 2015).

2.3.2.1 Luminescent sensing element

A luminescent sensing element is typically composed of the analyte-sensitive indicators in a suitable solid matrix, which is most often of polymer nature in cell culture applications. The matrix material must be selected carefully, as it must be soluble enough for the indicator, permeable for the analyte, transparent, mechanically stable, biocompatible, and it must possess strong enough adhesion to the used substrate. In addition, in miniaturized or microfluidic devices, the choice of the matrix material affects directly the use of other materials. In particular, various solvents or temperatures required in the manufacturing processes, or inadequate adhesion properties may create issues (Pfeiffer and Nagl 2015). Most widely applied polymeric matrices include PS, PMMA, PDMS, and some fluorinated co-polymers.

Sol-gel chemistry offers another option for the matrix material manufacturing (Gareth et al. 2016; Owens et al. 2016). The sol-gel films are typically microporous, and the versatile processes provides possibilities to control the structure and the physicochemical properties to optimize the sensor performance (MacCraith and McDonagh 2002). Excellent reviews on different indicators and matrix materials are available (see for example Pfeiffer and Nagl 2015; Wang and Wolfbeis 2014; Wang and Wolfbeis 2013; Quaranta et al. 2012; McDonagh et al. 2008; Basabe-Desmonds et al. 2007; Amao 2003).

The sensing element can be in the form of a thin film or a sensing spot, and most often it is deposited on a glassy substrate, planar waveguide, well plate or optical fiber. Spin- or blade-coating is often used to ensure homogeneous indicator distribution, especially in imaging set-ups. A successful integration of the sensing element may also require patterning procedures. For example, when working with luminescent sensing layers in connection with microelectrode arrays (MEAs), the electrodes cannot be covered with the dielectric layers. Also, with regard to bonding or imaging issues, it can be beneficial to have the sensing layer on rather restricted areas and not on the whole substrate. Possible solutions for the patterning include lithographic procedures (Nock et al. 2008; Nock et al. 2010), laser ablation (Grist et al. 2014) and inkjet printing (Moya et al. 2018).

The luminescence-based chemical sensing and imaging lend to 3D cell cultures as well. Distributed sensing beads (Wang et al. 2013), or smart scaffold structures (Jenkins et al. 2015), composed of the indicators and a suitable matrix material can

be applied in the 3D cell cultures. Imaging such structures can be carried-out by various microscopy technologies and combined with optical tomographies (Graf and Boppart 2010; Gualda et al. 2014).

2.3.2.2 Optical read-out

Most optical read-outs for luminescence-based sensors in miniaturized or microfluidic cell culturing devices are based on microscopic set-ups (Pfeiffer and Nagl 2015). This is obvious, since the microscopy of living cultures and the analysis of stained cells are widely applied technologies in cell research, and additional devices such as heater plates are available for long-term monitoring under standard microscopes. Another option is to apply commercial measurement devices or tailored optical read-outs. In any case, the read-out system typically comes in one of the three sensing modalities: luminescence intensity sensing, ratiometric (wavelength referenced) intensity sensing or luminescence lifetime sensing. The unreferenced intensity measurement is the simplest to carry out, but prone to be disturbed by many factors, including a fluctuating or spatially uneven excitation, fluctuating background, photo bleaching, an inhomogeneous distribution of indicators, to name a few. The situation is improved in the ratiometric sensing, where an inert reference dye, not sensitive to the analyte, is introduced. The dye must be excitable with the same source as the indicator but radiate into a different band of wavelengths. The lifetime-based sensing represents another technique to overcome most of the listed issues with an intensity-based read-out.

The luminescence lifetime can be determined with so-called frequency-domain or time-domain methods. In the frequency-domain method, a sinusoidal excitation signal is typically applied, and the phase shift between the emission and excitation signal is recorded (Fig. 16A). Assuming one dominating luminescence lifetime, the measured phase shift $\emptyset$ and luminescence lifetime τ are related as (Lakowicz 2006)

$$\tan(\emptyset) = 2\pi f\tau \qquad (2.6)$$

where f is the modulation frequency. The frequency-domain read-out is usually relatively cost-effective to realize, and it is popular among many commercial devices.

In the time-domain method, a high-speed detector is accurately gated, and the lifetime is calculated either by two integrated time windows (Fig. 16B) or by fitting a decay function into time-correlated intensity data (Fig. 16C), as in so-called time-correlated single photon counting (TCSPC). The time-domain methods are typically

used in imaging instruments, such as fluorescence lifetime microscopes. Fig. 16D shows the principle of the ratiometric read-out.

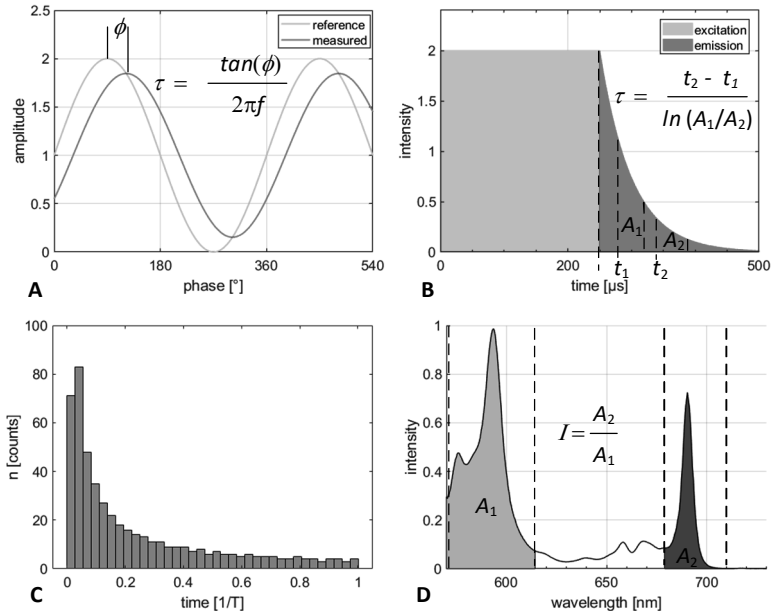

Figure 16. The common optical read-out methods of luminescent sensors. (A) The frequency-domain luminescence lifetime method; (B) A time-domain luminescence lifetime method based on two integrated time windows; (C) A time-domain luminescence lifetime method based on time-correlated single photon counting; (D) The ratiometric luminescence intensity method. Adapted from (Pfeiffer and Nagl 2015).

2.3.2.3 On the non-invasiveness and the biocompatibility

Applications requiring full material biocompatibility, such as sensitive cell cultures, possess additional challenges for the luminescence-based sensing. Even a minor leaching of the indicators may prove harmful. The leaching can be mitigated with an additional, indicator-free but analyte permeable shielding layer (Thomas et al. 2009) or prevented by bonding the indicators covalently into the matrix, as in M1 and in some other reports (Koren et al. 2012; Tian 2010). The covalent linking typically improves the stability of the sensing material as well.

A special issue with luminescence-based oxygen sensing is the generation of an unwanted by-product, singlet oxygen $^1O_2$ (Ogilby 2010). The oxygen-induced

quenching of the luminescence takes place through energy transfer from the excited indicator molecule to the oxygen molecule. The ground state of oxygen is a triplet state $^3O_2$, but through the energy uptake, the excited state can be $^1O_2$. Exposure to singlet oxygen can be irreversibly damaging or even lethally toxic to cells (Dahl 1993). Indeed, nanoparticles based on metalloporphyrins have been designed for photodynamic cancer therapy, where singlet oxygen is produced inside the cells (Wang et al. 2016). However, Wang et al. conjugated the nanoparticles to enter the cells, and high-level excitation was used. Otherwise the very limited lifetime ($\tau \approx 3.5$ μs in water) and the mean diffusion distance (of order 200 nm for 5τ) of $^1O_2$ makes the treatment ineffective.

It is also important to protect the sensitive cells from unnecessary illumination. Light can activate phototoxic compounds in culture or be directly harmful at high levels. In addition, light can unwantedly stimulate neurons and change their behavior (Mahmoudi et al. 2017). It is also known that hiPSC-derived cardiomyocytes (CMs) can temporally cease beating after exposures to light (Singh 2019 et al.).

In conclusion, indicators with maximal brightness, preferably excitable with long-wavelengths, firmly embedded or preferably covalently linked in a biocompatible matrix material with an appropriate permeability for the analyte form the basis for minimally invasive luminescence-based chemical sensing. However, an efficient luminescence detection scheme is equally important. Together with an appropriate sensing element, it provides means to minimize the used indicator concentration and applied excitation power.

3 DEVELOPED OPTICAL SET-UPS AND PLATFORMS

Based on the discussions and simulations in the previous chapter, surface-selective optical set-ups and measurement platforms were designed and constructed for fluorescent immunoassays (P1-P3) and luminescence-based oxygen sensing in cell cultures (P4, M1). The central element in all the set-ups is an in-contact parabolic lens, an idea first introduced in connection with the collection of SAF by Enderlein (1999).

In the designed immunoassay platform, the parabolic lens efficiently collects the SAF emission, and with a proper spatial filtering (i.e. with an annular aperture below the parabolic lens), the collection is restricted to a range of supercritical angles, resulting in a surface-selective fluorescence detection (P1). In addition, the parabolic lens facilitates a well-focused evanescent excitation into the focal point of the system, which further increases the degree of the surface-selectivity of the system. The high surface-selectivity enables the real time detection of the bound fluorescent molecules against a high concentration of unbound fluorescent molecules, which is the key feature of the platform.

In the designed oxygen sensor set-ups, the parabolic lens collects the emission of thin luminescent oxygen sensing films with a high efficiency (P4, M1). In particular, the collected luminescence includes the peak radiation in the supercritical angles, which cannot be collected by conventional lens systems. In addition, the parabolic lens is utilized in TIR-type excitation, because such an arrangement minimizes the optical power radiated into the cell culture. Both the high detection efficiency and minimized direct radiation contribute to the non-invasiveness of the sensing method, which is essential in sensitive cell cultures and one of the driving factors of the design.

3.1 TIR-SAF immunoassay platform

3.1.1 Motivation

An important group of analytes consists of small compounds such as hormones, steroids, toxins, pollutants, pharmaceuticals and abused drugs, which need to be frequently tested by the authorities. The molecular weight of these compounds is typically less than 5 kDa, and the on-site detection at low concentrations is a great challenge (Li et al. 2018). Analytical devices such as Gas Chromatography-Mass Spectrometry (GC-MS), possessing high sensitivity and specificity, carry out analysis in laboratories. However, as such instruments are bulky, expensive and their use time-consuming, they apply poorly to rapid on-site detection (Gandhi et al. 2015).

An obvious on-site alternative for the analytical devices is the immunoassay technology, which provides high specificity through the unique immunoreactions. When the most suitable molecular sensing scheme is combined with the most suitable transducer technology, rapid and sensitive tests can be created. For the small analytes, the most developed and studied on-site immunoassays are based on competitive scheme in a lateral flow format (Stano-Rossi et al. 2012). While the sensitivity and specificity of these assays are often sufficient, their use in rapid on-site safety and drug screening applications is hampered by their assay time, which typically is over five minutes. Usually five or ten minutes assay time does not create issues at a doctor's office, but many on-site safety and drug screening applications should be carried out in less than a minute, preferably in 30 sec (Frisk et al. 2008).

The need for the rapid on-site detection of small molecules in challenging sample matrices – in particular the need for rapid saliva-based drug screening assays – motivated the development of the immunoassay platform in this thesis. As for this task, the surface-selective fluorescence technique provides advantages. The fluorescent transduction is highly sensitive, and importantly, the surface-selective techniques make the transduction less vulnerable to the matrix effects that can seriously hamper the performance in challenging matrices (Sapsford and Ligler 2004). More precisely, autofluorescent, quenching or fluorescence-altering sample constituents outside the reach of the evanescent field do not interfere with the surface-selective detection, even if spectrally overlapping. Furthermore, fluorescently non-interacting sample constituents that may bind non-specifically onto the sensing surface create far less issues for the fluorescent transduction than for the label-free techniques. In fact, for surface-selective fluorescence detection, the

labelled detection antibodies binding non-specifically onto the sensing surface represent probably the strongest problem related to the non-specific binding (NSB). However, a short base-line measurement can reveal such a process, although with a cost of increased assay complexity and time. Finally, as with all immunoassay techniques, the sample constituents interacting non-specifically with the analyte and assay components may self-evidently create problems (Chiu et al. 2010).

As a starting point of the platform design, the immunoassay platform was supposed to fulfill the following requirements:

1. to enable fluorescent measurements with maximal surface-selectivity
2. to enable the real time monitoring of fluorescent binding processes in samples containing a large bulk concentration of fluorescent molecules
3. to be compatible with standard flat-bottom polystyrene well plates
4. to enable rapid on-site immunoassays for drugs of abuse with a target assay time of 30 sec.

In practice, the requirement of maximal surface-selectivity means that the platform should apply both TIR excitation and SAF detection (Axelrod 2013). Moreover, if the design results in a high enough surface-selectivity, the second requirement of real time monitoring will be fulfilled, even in large bulk fluorescence concentrations.

The third requirement of the compatibility with standard well plates originates from practicalities. As immunoassays are routinely carried out in PS well plates, the standard practices and immunoassay surface chemistries can be transferred as such into the system. In addition, the well plates and arrays can facilitate sample batching and motor-based scanning in future designs. As for lens material, PS provides good optical and mechanical properties, and it is relatively easy to machine or cast. Finally, yet importantly, PS possesses a relatively high refractive index ($n = 1.59$). This is advantageous, as the ratio of the refractive indices over the sample-substrate interface defines the share of SAF emission. In aqueous samples, 41.3% of the total emission power is directed towards SAF angles with PS. This is approximately 20% more than with optical glass substrates ($n = 1.515$, SAF 35%). Moreover, the decay length of the SAF emission is slightly shorter with PS (Fig. 5).

Lastly, the final requirement of enabling rapid drug immunoassays in 30 sec testing time depends self-evidently not only on the platform, but on many other factors, including the applied antibodies, assay scheme, surface functionalization practices and sample matrix complexity, to name a few. Nevertheless, it demands for a high-sensitivity detector, stable excitation source, high quality optical components, as well as for an appropriate optical design and a careful platform construction.

3.1.2 Technical considerations

General. Surface-selective platforms can be divided in two basic classes according to whether they apply i) a separate front-end optics and a separate sample well or ii) front-end optics as integrated into the body of the sample well. Of the five examples reviewed in Fig. 13, three (A, B, E) belong the first class and two (C, D) in the second. Both classes have their advantages and shortcomings. Separate front-end optics can be manufactured with high precision from more expensive high-quality materials and have larger dimensions. Therefore, their optical performance can be of highest quality. As a downside, the optical contact between the front-end optical element and the sample well must be usually ensured with optical contact oil or similar. In addition, multianalyte assays demand for a scanning mechanism. On the other hand, optical elements integrated into the sample well must be disposable, and therefore, they generally are of a lower optical quality. However, the advantage of the integrated optics is the simplicity of the system and assay protocol, as no contact oil nor complicated scanning is necessary even for multianalyte assays.

At the early stages of the immunoassay platform development, we decided to design a platform with a separate front-end parabolic lens made of PS. A parabolic lens can be efficiently utilized both for TIR and SAF, and it makes the platform compatible with flat-bottom well plates. In addition, a separate parabolic lens allows a fluent experimenting with other optical components and dimensional factors, such as the range of the collected SAF angles. Nevertheless, later the cumulative experimental knowledge could lead to more integrated solutions[2].

Parabolic lens. Fig. 17 shows the operation and calculated key parameter of various parabolic lenses with individual focal lengths: f = 3.00 mm (A), f = 2.78 mm (B) and f = 2.30 mm (C). The lenses are truncated in such a way that the focal point of the paraboloid is at the top-surface of the substrate (substrate thickness 1.00 mm), where the fluorescent molecules to be detected are located. The parabolic surface collects the emission radiated from the focal point and reflects the radiation through total internal reflection at the lens-air interface as a collimated annular beam from the bottom surface of the lens. The range of detectable emission angles depends on the dimensions of the lens. We decided to fix the bottom radius r_{bot} = 12.45 mm, which facilitates a smooth integration into standard optical set-ups of 25.00 mm diameter.

[2] In addition, the prototype manufacturing processes were much more limited at that time (2007-2009) than today, when especially high precision 3D printing of optical polymers can greatly assist prototyping and accelerate the development of integrated solutions.

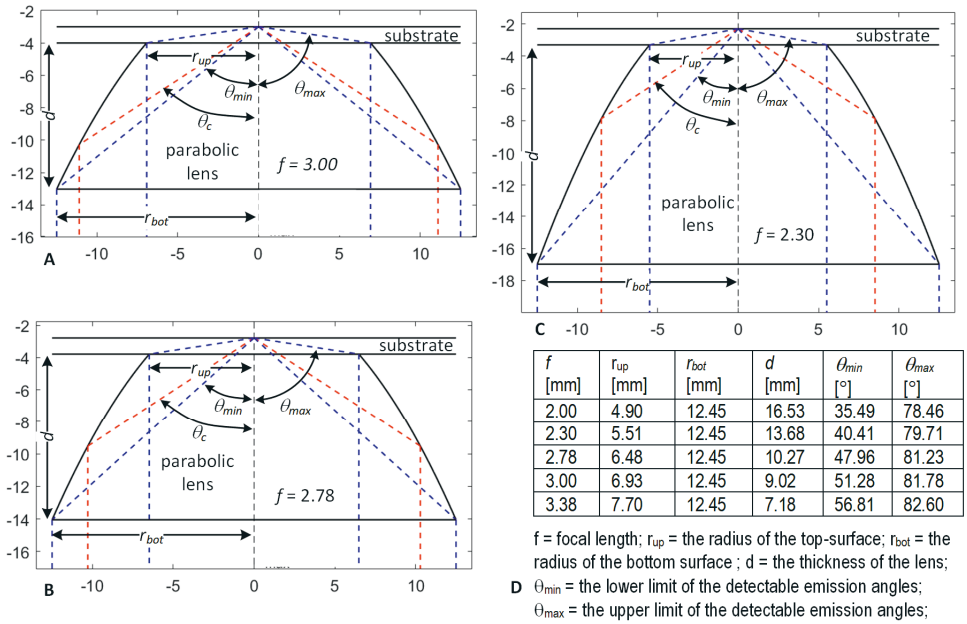

f [mm]	r_{up} [mm]	r_{bot} [mm]	d [mm]	θ_{min} [°]	θ_{max} [°]
2.00	4.90	12.45	16.53	35.49	78.46
2.30	5.51	12.45	13.68	40.41	79.71
2.78	6.48	12.45	10.27	47.96	81.23
3.00	6.93	12.45	9.02	51.28	81.78
3.38	7.70	12.45	7.18	56.81	82.60

D

f = focal length; r_{up} = the radius of the top-surface; r_{bot} = the radius of the bottom surface ; d = the thickness of the lens; θ_{min} = the lower limit of the detectable emission angles; θ_{max} = the upper limit of the detectable emission angles;

Figure 17. Cross-sectional schemes of polystyrene parabolic lenses with individual focal lengths *f* but a fixed bottom radius r_{bot} = 12.45 mm. (A) *f* = 3.00 mm; (B) *f* = 2.78 mm; (C) *f* = 2.30 mm. A polystyrene substrate with a thickness of 1.00 mm is in optical contact with the lens. The corresponding dimensional parameters are summarized in (D). The critical angle between polystyrene and water θ_c = 56.8° is shown as a dashed red line.

When the bottom radius is fixed, the focal length of the lens determines all the other parameters, and representative values for individual focal lengths are collected into a table in Fig. 17D. The table illustrates how shortening the focal length increases the thickness of the lens (d), decreases the upper radius (r_{up}) and extends the range of detectable angles in the lower end of the emission angles. Increasing the focal length produces changes in the opposite direction.

The range of the detectable angles is one of the key parameters defining the immunoassay performance. The emission above the critical angle θ_c (θ_c = 56.8° for polystyrene-water interface, shown as dashed red line in Fig. 17) originates from the sensing surface and should be exclusively detected by the system. Therefore, in this respect, f = 3.38 mm represents an optimal solution, as the lower limit of the detectable angles equals with the critical angle. However, we decided to construct the platform with a 0.5 mm shorter focal length (f = 2.78 mm) to make the system feasible for extended studies, where the ability to collect a limited range of under critical emission could be useful. As the actual range of the collected emission angles can be accurately adjusted through straightforward spatial filtering of the collimated

annular beam, the only disadvantage of f = 2.78 mm compared to f = 3.38 mm is the 3.1mm increased thickness of the lens and the respective optical losses.

3.1.3 The platform design

Fig. 18A shows the optical scheme of the developed TIR-SAF immunoassay platform (P1). The parabolic lens (f = 2.78 mm) is manufactured from PS (by Jenoptik, Germany). The upper and lower diameters of the lens are 13.00 and 24.90 mm, respectively. The lens is truncated in such a way that the focal point of the lens is located 1.00 mm above the top-surface. This makes the platform compatible with PS substrates with 1.00 mm thickness, provided that the optical contact is ensured with index-matching oil.

Excitation. A laser diode (LD, 650 nm, 0.8 mW, from Photonic Products) is used for the excitation purposes (targeted for Alexa-647). The optical output of the LD is connected to an optical fiber (4 μm core diameter) equipped with a pigtailed collimator lens. The excitation beam (beam waist < 0.5 mm) is orthogonally directed to the bottom surface of the lens, and the parabolic shape focuses the beam into the focal point of the system, located at the bottom of the sample well. The set-up allows a smooth adjustment of the TIR-excitation angle by adjusting the lateral position of the collimator. For a maximal surface-selectivity, it is preferable to have a maximal excitation angle. However, at very large angles, the outer edge of the excitation beam generates unwanted reflections from the upper edges of the lens. Therefore, the lateral distance was fixed to 8.4 mm, which corresponds to an excitation beam with a mean angle of incidence of 67.0°. The selected value has a high enough tolerance for the unwanted reflections and is well above the critical angle θ_c = 56.8°.

Selecting SAF angles. The range of detected SAF angles can be selected through spatial filtering, that is, by placing an annular ring with appropriate dimensions under the parabolic lens. Ideally, to maximize the detected emission, the whole range of SAF angles should be collected. In practice, however, some tolerance is required between the critical angle and the smallest collected emission angle. We had a set of different annular rings manufactured from polyoxymethylene (POM) by a local company specialized in water-cutting, which allowed us to do experimental optimization of the annular ring in terms of the signal-to-noise ratio and surface-selectivity. The experiments resulted in the use of an annular ring with an inner and

outer diameter of 13.0 mm and 20.0 mm, respectively, which restricts the detection to the SAF angles between 58.1° and 81.1°.

Lenses and filters. The collected SAF emission is focused to the detector by a plano-convex lens with a focal length of $f = 80$ mm. The relatively long focal length allows a precise tuning of the distance between the lens and the detector to maximize the detected signal. The fiber lens support bar (made of POM) efficiently blocks the excitation beam, but nevertheless, as the LD wavelength (650 nm) and Alexa-647 emission maximum (670 nm) are relatively close to each other, efficient filtering is needed to maximize the performance. After experimenting with a set of individual bandpass and longpass filters, we decided to apply two optical filters in succession: IF665 (bandpass, center wavelength 665 nm, FWHM 10 nm) and RDG665 (longpass, cut-off at 665 nm), which produced the best signal-to-background ratio.

Detector and controller. A low-noise photon counter (PMT, Hamamatsu 7421-40) is used as a detector. The system is controlled with NI-USB-6251 hardware and a tailored Labview software. A photograph of the constructed platform is shown in the Fig. 18B.

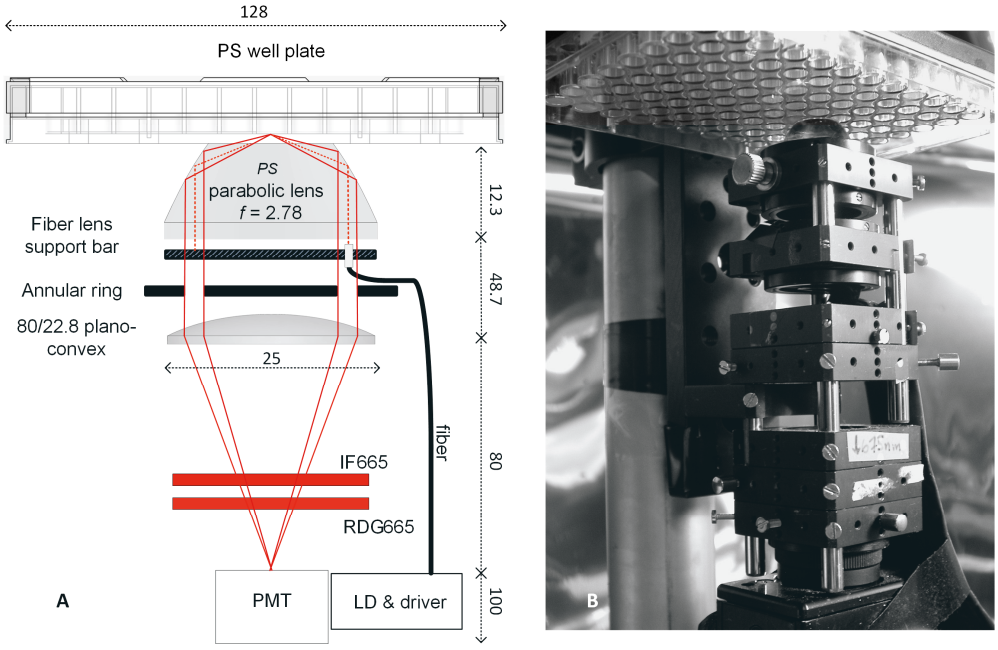

Figure 18. (A) The optical scheme of the TIR-SAF immunoassay platform (P1). The dimensions are in mm, but the scheme is not drawn in scale; (B) A photograph of the constructed device.

The degree of the surface-selectivity of the platform can be estimated with the help of Fig. 19. Here, the relative intensity of the TIR excitation (650 nm at 67.0°) is plotted with the dotted blue line as a function of the distance from the sensing surface into the sample. The dashed red line shows the corresponding decay curve for the SAF intensity (670 nm) into the collected emission angles. The solid curve shows the combined effect, calculated as the product of the TIR and SAF curves. In (P1), the combined curves, illustrating the surface-selectivity, were referred to as the relative fluorescence detection function values. The figure shows that at the distance of one quarter of the emission wavelength from the interface, the detection function value of the platform has already decreased below 4% of the value at the interface. Note that the SAF decay curve in Fig. 1C in (P1) is plotted for a slightly larger range of SAF angles. The performance of the platform is demonstrated in Chapter 4 with the model (P1), morphine (P2) and cocaine (P3) immunoassays.

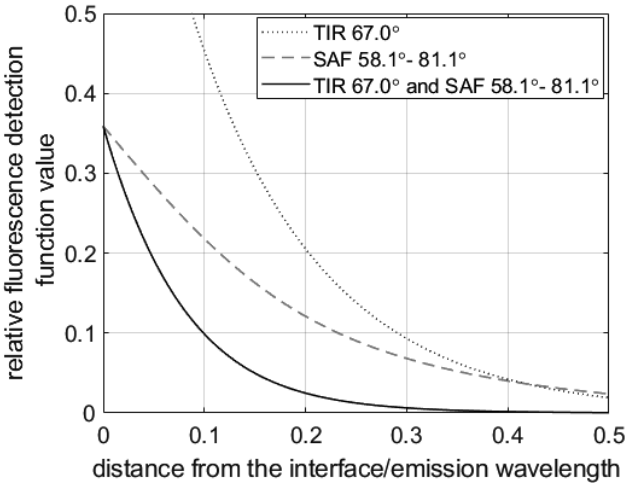

Figure 19. The calculated surface-selectivity of the developed TIR-SAF platform. The dotted and dashed lines show the relative intensity of the TIR excitation and SAF emission as a function of the distance from the sample-substrate interface into the sample, respectively. The solid line illustrates the combined effect, when both methods are applied at the same time. Note that the Fig. 1C in (P1) is plotted for a slightly larger range of SAF angles.

3.2 Oxygen sensors

The starting point for the oxygen sensor development was the need to combine oxygen monitoring with the cell culturing devices developed in our research group. In particular, the oxygen sensor technology was supposed to fulfill the following requirements:

1. to be integrable with customized, in-house manufactured MEA plates (Ryynänen et al. 2018 and 2019)
2. to be integrable with customized, in-house manufactured cell wells and gas-exchange chamber structures, as well as with microfluidic devices (Kreutzer et al. 2012 and 2017)
3. to be minimally invasive
4. to be compatible with customized live microscopy (Rajan et al. 2018)
5. to enable 2D scanning/or imaging options for the oxygen sensing.

The first requirement practically ruled out most of the available commercial options, including available sensor spots and foils (such as developed by PreSens)[3], which are practically impossible to attach to MEA plates due to dimensional restrictions. The fiber-optic oxygen sensors provided an interesting option, integrable with MEAs, but the mounting of the devices would require gas- and water-proof inlets in the structure, which complicates the set-up and easily creates issues with gas-exchange structures. In addition, the fiber-optic devices do not provide a real scanning option. Therefore, customized, in-house spin-coated luminescent sensing films provided the most promising and versatile starting point. In principle, the patterning technologies (Nock et al. 2010; Grist et al. 2014; Moya 2018) make the spin-coated films fully compatible with MEAs, PDMS structures and microfluidic devices, and simultaneous microscopy should be feasible as well as the scanning and imagining oxygen sensing set-ups. Therefore, the key factor in the design was to minimize the invasiveness of the luminescent sensing technology.

Interestingly, a measurement platform with a basic scheme and surface-selective characteristics similar to the immunoassay platform offers a very appropriate solution for minimally invasive luminescence-based oxygen sensing. In essence, the surface-selective detection substantially increases the detection efficiency of luminescent thin films, and a high detection efficiency in turn makes it possible to use low indicator concentration and low excitation power without compromising the

[3] http://www.presens.de/

quality of the measurements. In addition, TIR-type excitation does not directly illuminate the sample, and therefore it greatly reduces the radiated power into the cell culture. Finally, since the emission power into supercritical angles is multiple times higher than the power directed straight towards the substrate (see Fig. 7), the technique provides also an option to detect the SAF emission only, and yet direct most of the emission power into the detector. This arrangement results in improved robustness against ambient light and background signals and, in addition, provides free space directly under the cells for other purposes such as optical microscopy. Thus, the surface-selective optical set-ups can also facilitate smooth integration with other instrumentation.

This thesis reports on two set-ups for luminescence-based oxygen sensors with surface-selective detection characteristics. The set-up A, developed in P4, is a straight-forward modification of the immunoassay platform. The excitation source, filters and the detector are changed, but otherwise the optical geometry remains relatively similar. This is well-grounded, because the set-up is very effective with regard to the angular emission distribution of luminescently doped films of certain thicknesses. The set-up B, developed in connection with the development of the biocompatible oxygen sensing material (M1), is a modification of the set-up A, where the parabolic lens, detector and excitation devices and geometry are all updated.

3.2.1 Oxygen sensing elements

In recent years, many oxygen indicators have been developed, and quite a few are commercially available. The luminescence lifetime of the indicator and the oxygen permeability of the matrix material define the limits for the sensitivity and the measurement range of the sensor (Mills 1997). A combination of a highly oxygen permeable matrix and an indicator with a long luminescence lifetime results in a strong quenching even at low oxygen concentrations, thus making the device ultra-sensitive, but suitable only applications at very low oxygen concentrations (Lehner et al. 2014). On the other hand, a low oxygen permeability and short luminescence lifetime lead to a sensor with a low sensitivity, but it can nevertheless represent a feasible solution for the oxygen monitoring at a high range of oxygen concentrations. Importantly, most Pt(II) porphyrins have luminescence lifetimes of 40-80 μs, and when embedded in PS or other material with an oxygen permeability of the same range, well performing oxygen sensors can be realized for the physiologically relevant range of oxygen tensions (Quaranta et al. 2012). Table 1 lists some of the most

popular metalloporphyrins and their photophysical properties. The indicators used in this thesis are bolded.

Table 1. Photophysical properties of the most common metalloporphyrins oxygen indicators (Quaranta et al. 2012).

Indicator	λ_{max}^{abs}(nm) (ε×10^{-3}M^{-1}cm^{-1})	λ_{max}^{em} (nm)	Medium	Quantum yield	Lifetime (μs)
PtOEP	382/536	649	Toluene	0.41	75
PdOEP	546	670	PS	0.20	990
PtTFPP[1]	**390(323)/504(23.2)/538(29.4)**	**647/710**	**CH_2Cl_2**	**0.088**	**60**
PdTFPP	406(192)/519(18.2)/552(15.5)	738	CH_2Cl_2	0.21	1650
PtOEPK[2]	**398(86.2)/592(55.1)**	**758**	**$CHCl_3$**	**0.12**	**60**
PdOEPK	410(82.6)/603(53.5)	789	$CHCl_3$	0.01	455
PtTPTBP	430(205)/614(136)	770	Toluene	0.51	47
PdTPTBP	443(416)/628(173)	800	Toluene	0.21	286

[1] used in M1; [2] used in P4.

As a matrix material, PS have many desirable properties in oxygen sensing in cell cultures, including high optical transparency, mechanical stability in aqueous solutions, sterilization with ethanol and general compatibility with many cell culture practices (Wang and Wolfbeis 2014). It is no surprise that PS combined with Pt(II) porphyrins, in particular Pt(II) octaethylporphyrinketone (PtOEPK), have gained popularity in biomedical applications. PtOEPK has a strong absorption band at 591 nm – accurately matching a standard LED wavelength – and it is a photostable indicator. In addition, the leaching of PtOEPK from polymer matrices into most aqueous solutions has been reported as low or even non-detectable (O'Riordan et al. 2005), and reports exist on the biocompatibility with certain mammalian cells such as canine kidney cells in week-long tests (Sinkala and Eddington 2010). Therefore, PtOEPK in PS was chosen as the indicator-matrix combination in the development of the set-up A (P4).

However, later it became evident that the biocompatibility of PtOEPK physically entrapped in PS is not sufficient for hiPSC-derived neurons and CMs, at least in experiments taking days or even weeks to complete. This finding led to the preparation and biocompatibility testing of the sensing material based on covalently linked PtTFPP in PS-PPFS-blend, reported in M1, in connection with the set-up B.

3.2.2 Oxygen sensor set-up A

Optical scheme. Fig. 20A shows the set-up A for the luminescence-based oxygen sensing (P4). An in-contact parabolic lens is applied with the same dimensions as in

the immunoassay platform. An excitation LED (590 nm) is mounted in a tailored structure that directs the LED output vertically to the bottom surface of the lens. The parabolic shape concentrates the LED light into the focal point, which is located on the top surface of the cell culturing substrate. In the set-up, the excitation angle has the value of 66.0°, which exceeds the critical angle between glass and cell culture medium. This way the excitation beam is totally reflected, and minimum amount of the optical power is radiated into the cell chamber. Fig. 20B shows the ray-tracing simulation of the excitation optics with the parameters of the LED and mechanics.

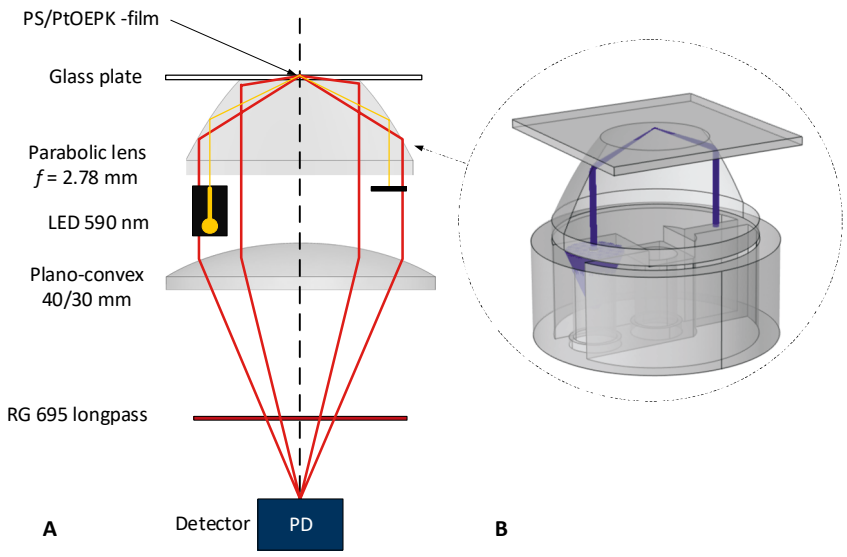

Figure 20. (A) The optical scheme of the luminescence-based oxygen sensor set-up A P4); (B) a ray-tracing simulation showing the excitation beam focusing with the actual parameters.

Fig. 21 shows simulated emission distributions for homogeneously PtOEPK-doped PS films (λ_{em} = 750 nm) with thicknesses between 100 nm and 900 nm. As in Fig. 7, each film thickness has a unique angle of maximum radiation, corresponding to a strong evanescent mode coupling between certain high-angle wave vectors and radiation dipole locations inside the film. The effect becomes even more pronounced at larger film thicknesses, as the reflection of these modes interferes either constructively or destructively with the field. The dashed lines in the graphs indicate the maximum and minimum angles that the parabolic shape of the applied parabolic lens can collect. In addition, the direct radiation from the lens bottom can be detected with normal optics. Generally, with the applied parabolic lens, PtOEPK-doped PS films having thickness of approximately of 100 nm or 400-700 nm are well

compatible with the set-up. However, it is important to notice that with a poor choice of film thickness, a significant part of the radiation power can be lost. For example, with the applied parabolic lens, PtOEPK-doped PS films with a thickness close to 300 nm or 1000 nm would be poor choices.

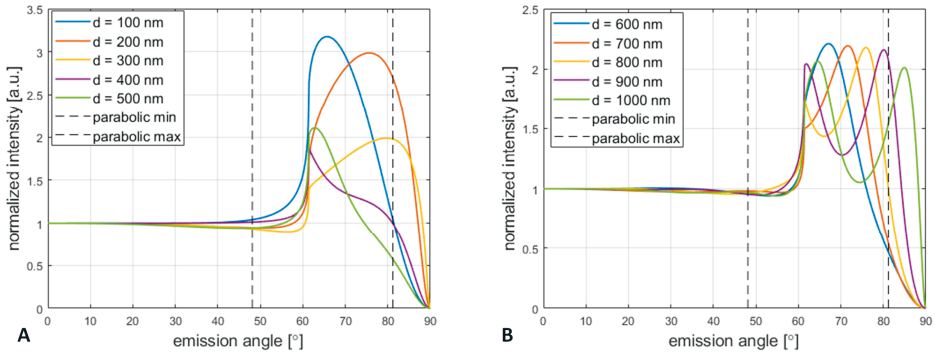

Figure 21. Angular emission distributions of oxygen sensing films composed of PtOEPK (λ_{em} = 750 nm) in PS. The curves are normalized so that unity power is being radiated at zero angle. (A) film thicknesses between 100 – 500 nm (P4); (B) film thicknesses 600 – 1000 nm. The dashed lines mark minimum and maximum angles of detection with the parabolic lens applied in the set-up A.

Luminescence lifetime read-out. As stated in the section 2.3, the luminescence lifetime is a preferred parameter to the luminescence intensity when measuring a dynamically quenched emission (Lakowicz 2006). This is because, contrary to luminescence intensity, the luminescence lifetime is insensitive to the many gain-type noise components, including photobleaching and excitation power fluctuations. Assuming that the emission is dominated by a single luminescence lifetime τ,the emission intensity can be written as

$$I(t) = I(0)e^{-t/\tau} \tag{3.1}$$

Then the luminescence intensity and lifetime under oxygen-induced quenching can be modelled with the so-called Stern-Volmer equation (Lakowicz 2006)

$$\frac{I_0}{I} = \frac{\tau_0}{\tau} = 1 + K_{sv}\, pO_2 \tag{3.2}$$

where I and τ are the measured luminescence intensity and lifetime at oxygen partial pressure pO_2, respectively; I_0 and τ_0 are the unquenched fluorescence intensity and

lifetime, respectively, and K_{sv} is the so-called Stern-Volmer constant. However, the supporting polymer matrices are often heterogeneous on a microscopic scale, which gives rise to different microenvironments and more complex decay kinetics, leading to some deviation from (3.2). In addition, at low oxygen concentrations, very high quantum efficiency indicators close to the sample-film interface can have different decay rates than the indicators in the bulk matrix, further adding to complexity of the decay kinetics. More complex models, such as two-site Stern-Volmer equations, or other linearizing techniques can be useful with highly non-linear Stern-Volmer plots (Carraway et al. 1991).

The frequency-domain lifetime detection typically uses sinusoidal excitation, and the phase of the emission is measured with respect to the excitation signal (Fig. 22A). In this configuration, assuming one dominating luminescence lifetime, the measured phase and luminescence lifetime are related according to Eq. (2.6).

Another option is to apply square wave excitation (Fig. 22B). Here, the duty cycle can be adjusted so that the excitation is powered only for a time equal or less than the luminescence lifetime. Using longer exposure times gives no benefit, as the size of the excited population cannot increase further. A square wave signal is very simple to produce, while a well-defined sinusoidal excitation usually requires a more complicated circuitry. A drawback with the square wave excitation is that the phase difference typically depends also on the duty cycle and that the equation (2.6) does not necessary hold anymore (Booth and Wilson 2004).

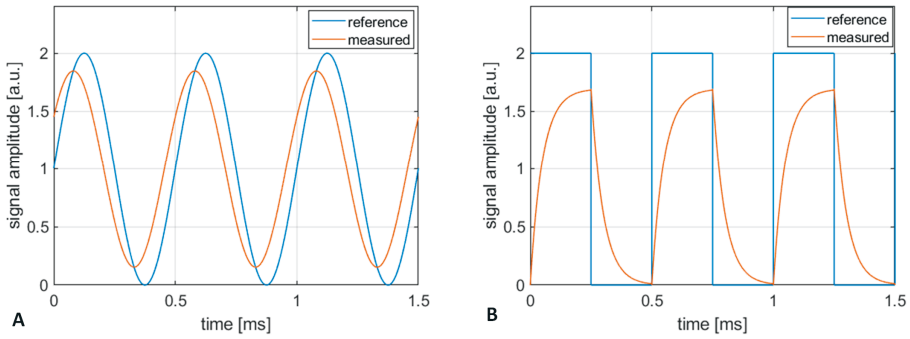

Figure 22. The principle of the frequency-domain method in the luminescence lifetime measurements. (A) sinusoidal and (B) a square wave reference signal.

Hardware (P4). Fig. 23A shows a photo of the constructed hardware and optical components of the set-up A. The luminescence emission is detected with a photodiode connected to a transimpedance amplifier (cut-off at 10 kHz). The square

wave excitation is carried out at 2 kHz frequency, and quadrature synchronous detection is applied for the phase measurement. The synchronous detection has a bandwidth of 23 Hz and its I/Q outputs are sampled at a data rate of 10 Hz. The 2 kHz driving frequency was chosen after experimenting with different driving frequencies and the related cut-off frequencies of the transimpedance amplifier. The signal to noise-ratio of the device was at the local optimum with the chosen value. Interestingly, the 2 kHz driving frequency is about one half of the theoretical optimal modulation frequency for sinusoidal excitation and monoexponential decay (Holst et al. 1997)

$$f = \frac{1}{2\pi\sqrt{\tau_0 \tau_1}} \tag{3.3}$$

where τ_0 and τ_1 are the unquenched and maximally quenched lifetimes. Assuming τ_0 = 60 µs and τ_1 = 27 µs (O'Donovan et al. 2005) results in f = 3.95 kHz as the optimal excitation frequency.

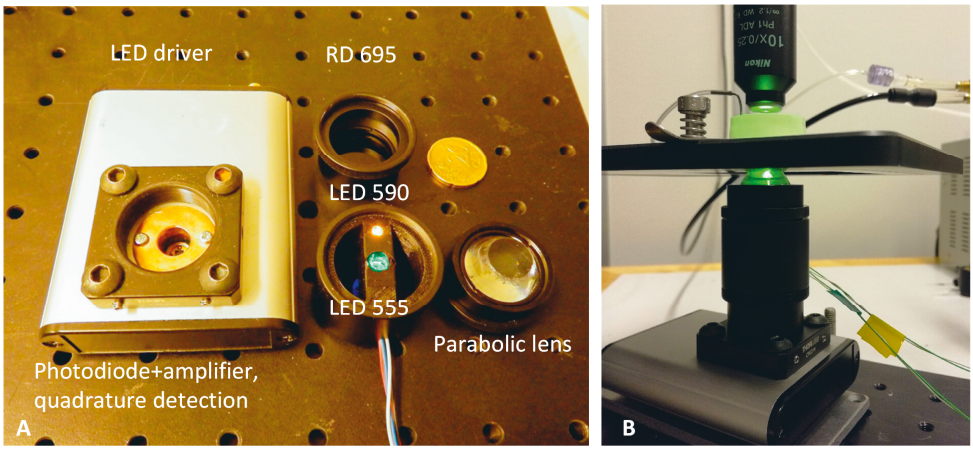

Figure 23. (A) The hardware and the optical components of the oxygen sensor set-up A. The amber LED (590 nm) is used for the PtOEPK excitation, and the green LED (555 nm) is used for upright microscopy illumination as shown in (B).

In addition, Fig. 23A shows that two LEDs are mounted under the parabolic lens: an amber LED (590 nm) used in the PtOEPK excitation, and a green LED (555 nm) used in the microscopy illumination. The excitation LED output is focused into the focal point of the system by the parabolic lens. The green wavelength is well outside of the excitation band of PtOEPK, and the LED is located in the optical axis. The LED illuminates the cell culture through a diffuser (not shown) at the center part of

the parabolic lens. Fig. 23B shows the assembled sensor used in connection with a heater plate and an upright microscope.

3.2.3 Oxygen sensor set-up B

The set-up B of the oxygen sensor was developed in connection with the development of the biocompatible sensing material (M1). With respect to set-up A, the key changes where: a new parabolic lens, the replacement of the photodiode with a photomultiplier tube, a new excitation unit based on laser diode (505 nm) and a fluorescence microscope-type optical arrangement based on a dichroic mirror.

Parabolic lens. The parabolic lens for set-up B (manufactured from BK-7 optical glass by Sanghai Optics) was designed to have the same bottom radius r_{bot}= 12.45 as in set-up (A). However, in order to facilitate the integration with heating plates of the MEA amplifiers (Multichannel Systems), the upper radius r_{up} was designed as smaller by shortening the focal length of the lens. The MEA amplifier provides metallic heating plates, on top of which the MEA substrates can be placed. The heating plates have a customized circular opening in the center for imaging purposes, and this opening can be utilized for the oxygen sensing as well. The parabolic lens can reach the MEA substrate through the opening (a typical opening diameter is 17 mm), but some tolerance for lateral adjusting is needed so that the active cell area can always be brought in the center of the system. As a downside, the decrease in the upper radius results in an increase of the thickness of the lens (d), which results in increased optical losses. However, as it is not necessary to restrict the detection to the SAF angles, the losses can be compensated by the increased collection at under critical range of angles. We chose f = 2.30, which results in d =13.68 and r_{up}= 5.51 mm (Fig. 24).

PMT vs PD. Compared to the PD utilized in set-up A, the application of a PMT significantly increases the detection efficiency, thus allowing the use of a lower excitation power. In addition, a fast PMT-based detection makes it possible to apply, if needed, TCSPC to the luminescence lifetime detection.

Modified excitation scheme. The excitation scheme was modified as well (Fig. 24). While the excitation scheme in set-up (A) performed well in terms of oxygen sensing parameters, the amount of stray radiation and a slightly blurred excitation focus

motivated the modifications. These issues were solved with a collimated LD output and proper optical design.

In the scheme (Fig. 24), the excitation laser diode (LD, Single Mode Sharp GH05035A2G, 505 nm, 35 mW) is from BeamQ. The output of the laser is collimated with a set of lenses, attenuated with a neutral density filter (NE10A) and directed through an annular aperture defined by the diameters of 12.8 mm and 14.2 mm. The aperture was 3D printed out of photoactive resin (Formlabs, Form 2, nominal resolution 0.02 mm). The resulting annular beam is reflected by a dichroic mirror (DMLP550R) to the parabolic surface that focuses the beam into the focal point, located on the optical axis on the top surface of the glass plate. The chosen parameters correspond to a range of excitation angles between 65.9° and 71.4°, which is notably larger than the critical angle between glass and water (61.4°).

The modified excitation scheme provides a better control of the excitation beam both in terms of sharper focus and reduced amount of stray radiation into the culture well. In addition, the scheme facilitates smoothly integrated illumination for microscopy in upright configuration. A single LED, with the nominal wavelength outside of the excitation bands of the PtTFPP, such as LED591nm (from Thorlabs), can be mounted in the center of the annular ring. The dichroic mirror partially reflects and transmits the LED radiation, which results in a diffusive, uniform illumination of the culture.

Emission collection. The parabolic lens can collect emission power radiated into range of angles between 40.4° and 79.7°. Fig. 25 shows simulated emission distributions for the homogeneously PtTFPP-doped PS films (λ_{em} = 650 nm) with thicknesses between 100 nm and 1000 nm. Comparing the distributions with the PtOEPK distributions in Fig. 21 shows that the peak angles are shifted due to the change in the emission wavelength. As before, certain film thicknesses, such as 100 nm and 400 nm – 700 nm, are well compatible with the set-up, and certain thicknesses, such as 200 nm or 800 nm – 900 nm, are only poorly compatible with the set-up.

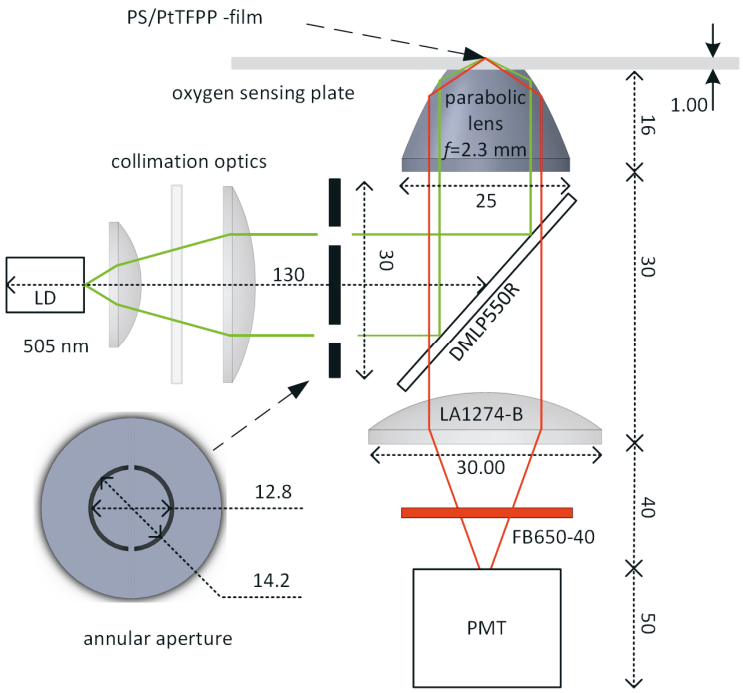

Figure 24. The optical scheme of the luminescence-based oxygen sensor set-up B. The dimensions are in mm, but the scheme is not in scale. Adapted from the published version of (M1)[4].

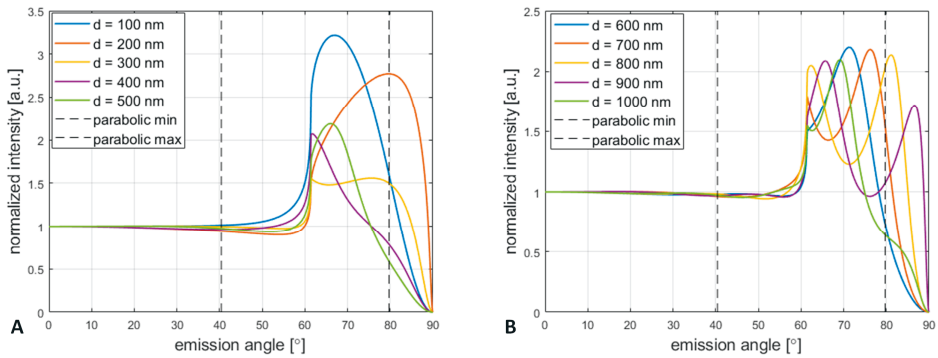

Figure 25. Angular emission distributions (λ_{em} = 650 nm) of oxygen sensing films composed of PtTFPP in PS. The curves are normalized so that unity power is being radiated at zero angle. (A) Film thicknesses between 100 – 500 nm; (B) Film thicknesses 600 – 1000 nm. The dashed lines mark minimum and maximum angles of detection with the applied parabolic lens in the set-up B.

[4] "Covalent immobilization of luminescent oxygen indicators reduces cytotoxicity", Biomedical Microdevices (2020) 22:41 https://doi.org/10.1007/s10544-020-00495-3

Luminescence lifetime readout. The principle of the read-out in the set-up B of the oxygen sensor was essentially same as in the set-up A: square wave excitation and quadrature synchronous detection for the phase measurements.

Hardware. Fig. 26 shows a photo of the constructed hardware. The luminescence emission is detected with a current-output photomultiplier tube (Hamamatsu H12056) connected to a tailored transimpedance amplifier. The square wave excitation is carried out at 2 kHz frequency, and a quadrature synchronous detection is applied for the phase measurement. The synchronous detection has a bandwidth of 23 Hz and the I/Q outputs are sampled at a data rate of 10 Hz.

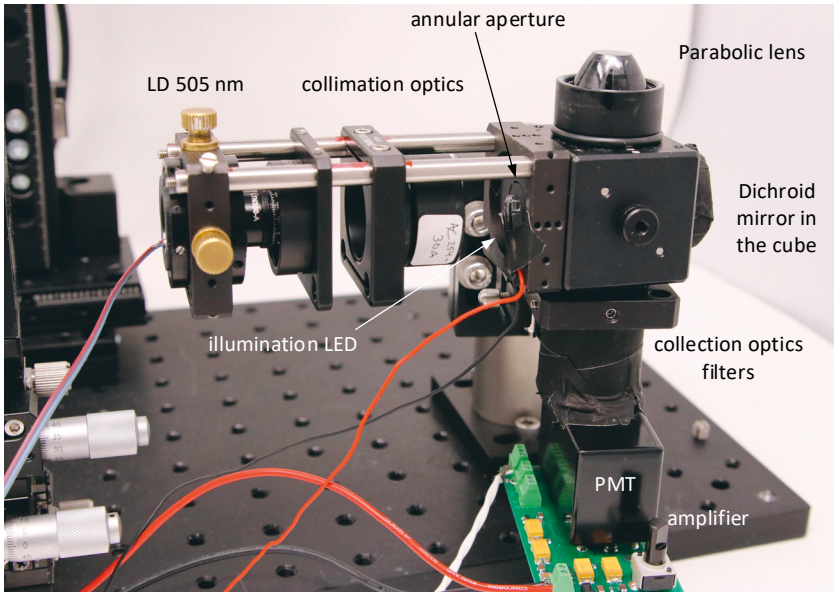

Figure 26. The hardware and the optical components of the oxygen sensor set-up B.

3.2.4 Modular cell culturing platform

The developed oxygen sensors are targeted for long-term cell culturing applications outside of incubator and, in particular, they are designed to operate as an integral part in a portable, modular cell culturing and measurement platform shown in Fig. 27, developed by our group (Rajan et al. 2018). The platform is centered on a transparent heater plate, where tailored, miniaturized cell culture wells with

integrated gas-exchange structures (Kreutzer et al. 2012) can be positioned. In addition, the system can accommodate simultaneous microscopy either in the upright or inversed configuration, either of the developed oxygen sensors, a MEA amplifier and temperature sensors. The system has been successfully used in hypoxia (P4) and temperature stressing of CMs (Mäki et al. 2018).

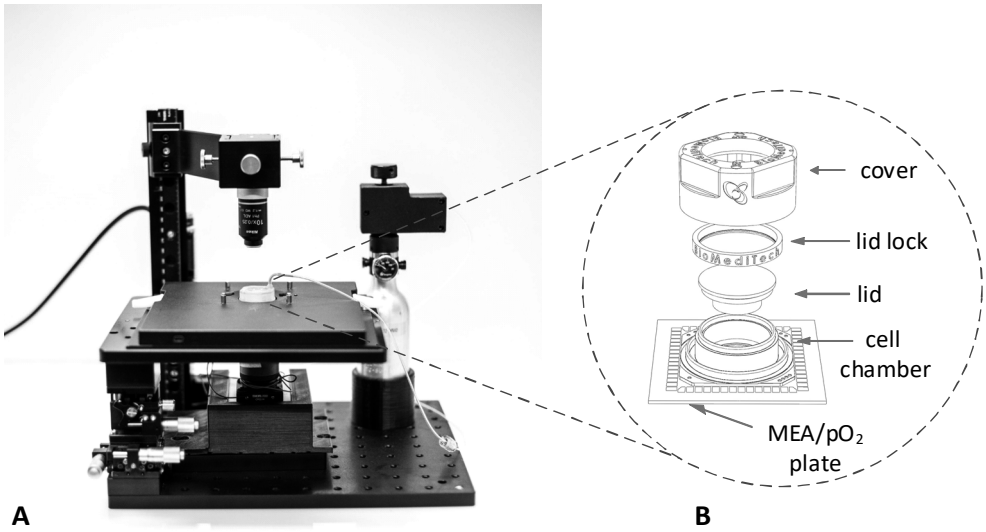

Figure 27. (A) The modular cell culture system composed of a tailored PDMS cell culture bonded on a MEA plate with oxygen sensing film, transparent heating plate, temperature sensing and control, gas control, oxygen sensor (set-up A), upright microscopy and a pre-amplifier unit for MEAs (Rajan et al. 2018). (B) details of the PDMS cell culture well. The well provides a sealed, sterilized environment for the cells surrounded by a gas-exchange chamber, so that the partial pressure of the gases can be adjusted in the culture.

4 SENSING APPLICATIONS

This chapter summarizes the experimental results when the developed surface-selective set-ups and platforms were applied to fluoroimmunoassays and luminescence-based oxygen sensing in cell cultures. First, the performance of the developed immunoassay platform was studied with a model immunoassay (P1). Then the platform was applied to the rapid immunoassays for two important abused drugs: morphine (P2) and cocaine (P3). In (P4, M1), the developed oxygen sensors were characterized in terms of sensitivity and noise properties. Finally, the oxygen sensors were used – as a part of the modular cell culture platform – in the hypoxic tests of hiPSC-derived cardiac cells (P4, M1). The chapter is concluded with a summary of performed biocompatibility tests of the selected oxygen sensing materials (M1).

4.1 Rapid on-site immunoassays for small molecules

Rapid noncompetitive fluoroimmunoassays require a relatively high concentration of the detection antibodies and a reliable method to monitor the binding processes in real time. Therefore, the critical feature of the platform is the degree of surface-selectivity. The detection must be sensitive to the surface-generated emission while suppressing the signal from the unbound detection antibodies in the sample. In the following, the sensitivity and the degree of the surface-selectivity of the developed immunoassay platform are experimentally examined with a model assay utilizing well-established, commercial human IgG antibodies (P1).

4.1.1 Model immunoassay

A noncompetitive model immunoassay shown in Fig. 28 was used for the platform characterization (P1). Briefly, microtiter plates were coated with non-labelled anti-human IgG antibody Fab_2 fragments (FC-specific) and blocked against NSB, resulting in sensing surface that is specific for whole human IgG molecules. Alexa

647 labelled whole human IgG molecules and Alexa 647 labelled Fab-specific anti-human IgG antibody Fab_2 fragments, were used as the specific and non-specific analytes (antigens) in the tests, respectively. For all details, see P1.

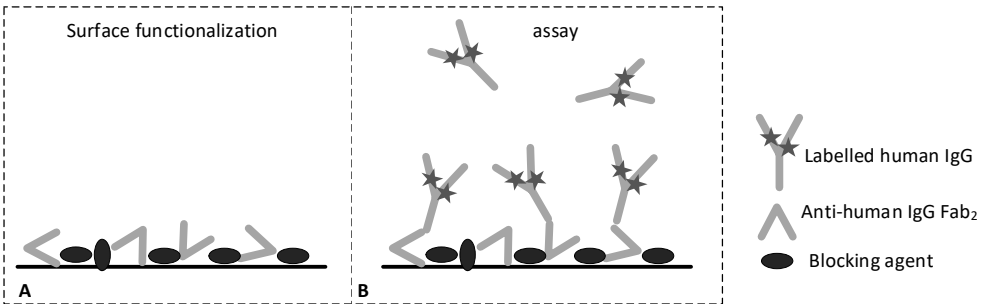

Figure 28. The scheme of the model IgG immunoassay used for the immunoassay platform characterization in (P1). (A) The functionalization of the surface with anti-human IgG Fab_2 fragments; (B) the labelled human IgG acting as the specific analyte.

To assess the performance of the immunoassay platform, the responses to the specific and non-specific antigens were recorded (Fig. 29). The injection of 20 nM of the non-specific antigen (marked as A) triggered a step-like response that remained on a constant level until the rinsing took place (at B). This step corresponds to the fluorescent background generated by unbound fluorophores in the sample solution. The injection of 20 nM of the specific antigen (at C) triggered a rapidly increasing response, which corresponds to the binding of the labelled antigen molecules to the free binding sites on the surface. After 25 min after the injection, the surface was rinsed, and the response stabilized to a constant level. By comparing the responses, the specific sensitivity is approximately 1200 times higher than the sensitivity to the non-specific antigens. This demonstrates the great rejection of background fluorescence, in other words, the great degree of the surface-selectivity in the fluorescence detection.

Fig. 30A shows the system responses to more diluted concentrations of the specific antigen, and Fig. 30B summarizes the saturation levels of 11 different specific analyte concentrations. It is evident that the limit of detection (LOD) is below the lowest measured concentration of 5 pM, where LOD is calculated as the concentration corresponding the mean of response in buffer plus three times its standard deviation (Armbruster and Pry 2008). The dynamic range is more than three decades, where the upper limit stems from the saturation of the binding sites.

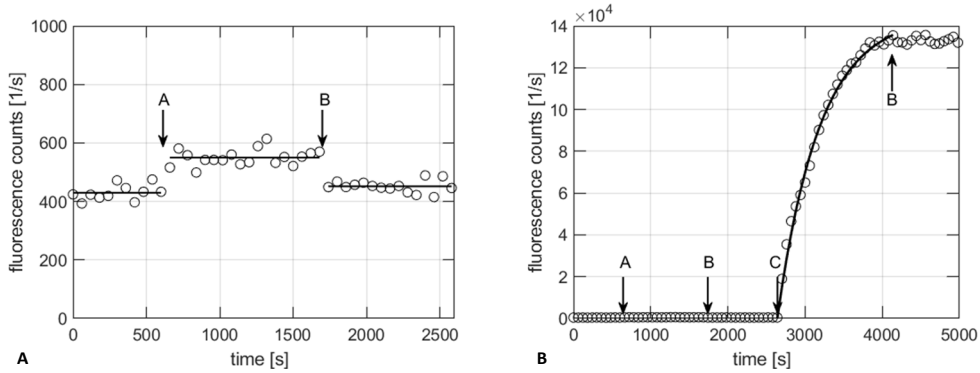

Figure 29. The response of the system to (A) 20 nM of the non-specific analyte; (B) 20 nM of the specific analyte. The letter A marks the injection of the non-specific analyte, B washing and C the injection of specific analyte. The figures are from P1.

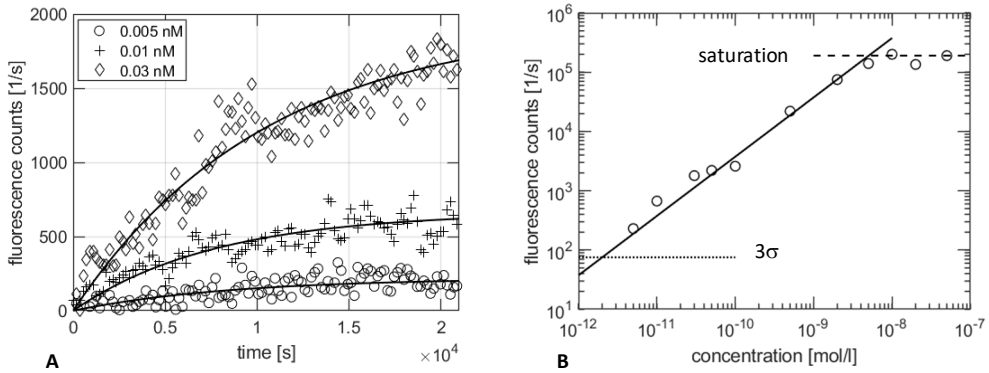

Figure 30. (A) The response of the immunoassay platform to three different specific analyte concentrations. (B) The final fluorescence intensity levels against the specific analyte concentration. The saturation level is shown with a dashed line, and the mean intensity of a blank sample plus 3 times its standard deviation with a dotted line. The figures are from P1.

4.1.2 Morphine immunoassay

Morphine (C17H19NO3; M = 285.34 gmol-1) belongs to the group of opiates, and it is widely used as a pain medication. While an effective pain reliever, morphine, as well as the other opiates, heroine and opium, is a strongly harmful drug when abused. According to World Drug Report (2018), more than 75% of drug-related deaths among older people are caused by the abused opiates.

Most commercial on-site opiate tests are based on competitive immunoassays in a lateral flow format, see e.g. the tested devices in (Stano-Rossi et al. 2012). These tests, however, are usually relatively time-consuming – typical response times are between 5 and 13 minutes. In addition, the competitive morphine and heroine assays typically cross-react with codeine, commonly used in cough medicaments. Generally, these tests are considered only as opiate-specific, and the positive test results must be confirmed using standard laboratory techniques such as gas chromatography - mass spectrometry (GC-MS) (Langel et al. 2011).

The scheme of the morphine assay (P2). In P2, the starting point for the morphine assay was a previously developed, homogeneous noncompetitive morphine assay scheme (Pulli 2005 et al.), shown in Fig. 31A. In the assay, two engineered antibody Fab fragments are utilized: (i) antibody M1 against morphine; (ii) and antibody K11 against the immunocomplex (IC) formed by the morphine molecule and antibody M1. In this scheme, the presence of morphine binds the antibodies together. If the antibodies are labelled with a suitable pair of fluorescent dyes, the binding can be measured with fluorescence resonance energy transfer (FRET) technology (Bajar et al. 2016). In FRET, the excited donor molecule (here Europium) non-radiatively transfers the excitation energy to the acceptor molecule (Cy5). The more there are morphine in the sample, the stronger the FRET signal. With this assay, morphine concentrations down to 5 ng/mL were successfully detected in two minutes (Pulli et al. 2005). As the cutoff level for morphine in drug testing is 40 ng/mL (Dams et al. 2007), the achieved detection limit was very satisfactory. However, compared with the target assay time of 30 sec, two minutes still leaves room for improvement.

The surface-selective fluorescence detection provides means to transfer the homogeneous FRET-based immunoassay into a heterogeneous format exploiting the binding processes on a sample-substrate interface (P2). This scheme is shown in Fig. 31B, where the non-labelled anti-morphine antibody Fab fragments (M1), used as the capture antibodies, are immobilized on polystyrene surface, and the free surface sites are blocked against NSB with bovine serum albumin (BSA). Labelled anti-IC antibody Fab fragments (K11) operate as the detection antibodies, and they are set free in a known concentration in phosphate-buffered saline buffer (PBS) into the sample well. Then the injection of the sample initiates the assay. The presence of morphine induces the binding of the detection antibodies on the sensing surface. The morphine concentration can be rapidly determined by monitoring the binding process in real time. For labelling and immobilization details, see P2.

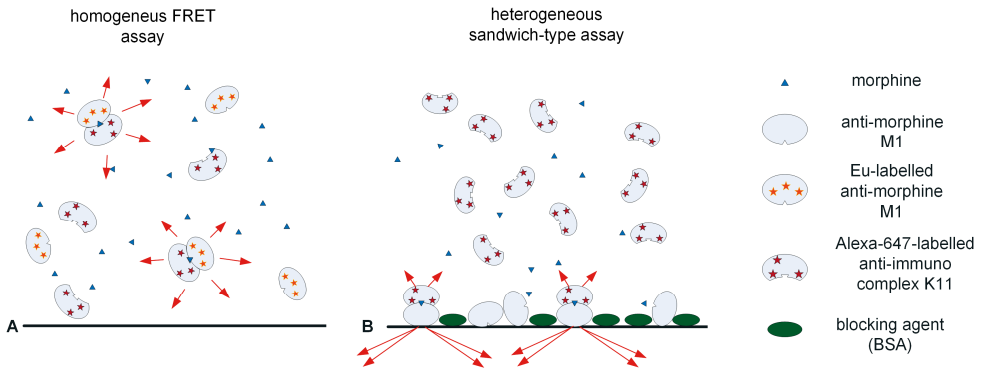

Figure 31. (A) The starting point for the morphine immunoassays development: the homogeneous morphine assay with labelled antibodies utilizing FRET (Pulli et al. 2005); (B) the scheme of the heterogeneous morphine assay with the same antibodies (P2). In this format, only the anti-immunocomplex antibody K11 is labelled.

Experimental results (P2). Fig. 32A demonstrates the functioning of the antibodies and the measurement platform according to the described heterogeneous scheme. After the injection of the labelled K11-antibodies at a high concentration (50 μg/mL or 100 μM), marked as K11 in the figure, a step-like shift in the baseline value can be seen. As with the model assay, the signal remains at a constant level after the shift. This means that the shift is due to the increased background signal, originating from the unbound K11-antibodies fluctuating in the sample. Only the injection of morphine (here at a concentration of 5.8 ng/mL) starts the binding process. Fig. 32B shows the binding curve in a wider time scale.

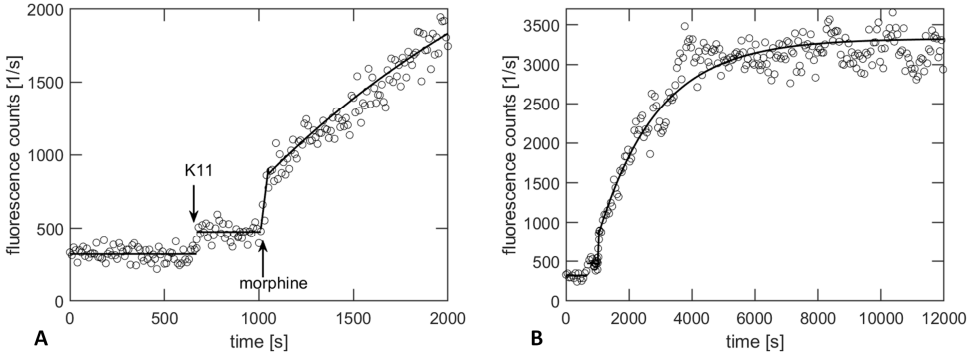

Figure 32. (A) Demonstration of the functioning of the antibodies and the TIR-SAF immunoassay platform in the morphine assay: responses to the injection of the labelled detection antibody K11 (no morphine) and to the injection of 5.8 ng/mL morphine; (B) the binding curve in its entire length. The figures are from P2.

The responses to different morphine concentrations are shown in Fig. 33A. The background fluorescence levels, measured after the injection of the K11 antibodies, are subtracted from the curves. The responses show that the fluorescence intensity values depend logically on the morphine concentration at all time points; that is, the higher the morphine concentration, the higher is the fluorescence intensity.

Fig. 33B shows the corresponding signals at three different time spots after the analyte injection as a function of the morphine concentration. In P2 (Fig. 6 in P2), the shortest analyzed time point was 20 sec, but here the same data set is reanalyzed in accordance with the outlined goal of the thesis of 30 sec assay time. Thus, the data at t = 60 sec and 120 sec is as in P2, but the data at the first time point t = 30 sec is different from P2. Evidently, the shift in the first time point increases the fluorescence intensity values at the first time point and shifts the corresponding slope towards the slopes at later time points; thus, distinguishing the responses at t = 30 sec more clearly from the noise floor.

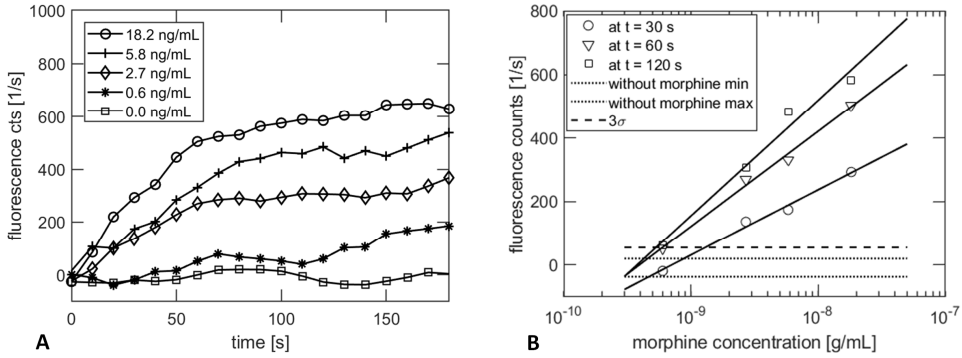

Figure 33. (A) The fluorescence recordings for different concentrations of morphine in PBS. The figure is from P2; (B) The respective fluorescence intensities at three time points after the morphine injection as a function of the morphine concentration. The open markers denote the mean value of the measurements, the solid lines (-) the linear fits and the dotted lines the minimum and maximum values of a blank response. The dashed line denotes to the mean intensity of the blank sample plus 3 times its standard deviation. The data set is the same as in P2, but the figure is replotted so that the shortest analyzed time point value is t = 30 s.

Overall, the figure shows that, at each time point, the dependence between the logarithmic morphine concentration and the fluorescence intensity value is approximately linear, and that the slope of the respective fit increases along with the time point value. The value of the lowest measured morphine concentration of 0.6 ng/mL remains below the LOD level at all time points. However, morphine

concentrations of 2.7 ng/mL and above exceeds the LOD level with some margin already in 30 sec. Although the repeatability of the results was not thoroughly studied in P2, the results suggest, albeit with a limited data set, that morphine concentrations down to 2.7 ng/mL could be detected in 30 sec, and concentrations close 1.0 ng/mL in 120 sec.

Comparing the performance with the performance of the homogeneous assay (Pulli et al. 2005), the results indicate that the assay time could be reduced from 120 sec to 30 sec by transferring the assay to a heterogeneous scheme and applying surface- selective measurement platform. In addition, the results show a LOD enhanced approximately by a factor of five for the two minutes assay time. Due to the stricter performance criteria, these numbers are slightly more cautious than the respective numbers in the original publication (P2).

4.1.3 Cocaine assay

Cocaine (C17H21NO4; M = 303.35 gmol-1) is a strongly addictive drug, made of the leaves of coca plants. It is the most often found drug in traffic, usually in connection with ethanol (Stano-Rossi et al. 2012). Therefore, a reliable, rapid on-site detection of cocaine is of great importance. As with other drugs, most often the on-site devices are based on lateral flow immunoassays, typically in a competitive form. While the sensitivity and specificity of the devices are often remarkably high, the on-site tests are hampered by the lengthy test times of 5-13 minutes.

The scheme of the cocaine assay (P3). A displacement immunoassay schemed in Fig. 34 was used for the cocaine detection (P3). The sensing surface is functionalized with the BSA-cocaine-conjugate molecules and the free surface sites are blocked with a diaminomethanol derivative of lipoic-acid (Lipa-DEA) (Tappura 2007 et al.). The labelled anti-cocaine antibodies are added in PBS buffer and they bind onto the functionalized surface. After rinsing the well, the system is ready for the tests.

The sample injection starts the assay. If the sample contains cocaine molecules, a displacement of the anti-cocaine antibodies from the surface begins. This displacement of antibodies can be monitored in real time with the surface-selective fluorescence detection. The higher the cocaine concentration, the more rapidly the emission intensity decreases.

The anti-cocaine antibodies and BSA-conjugated cocaine were obtained from Biosensors Applications AB. For the details of the surface functionalization and measurement procedure, see P3.

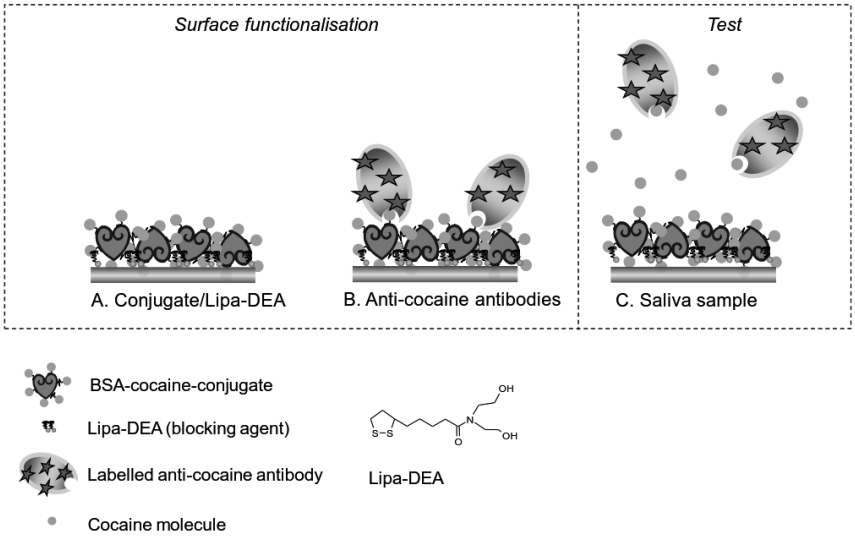

Figure 34. The scheme of the displacement immunoassay used for cocaine detection in P3. During the surface functionalization BSA-cocaine-conjugates and blocking agents (Lipa-DEA) are first immobilized (A). Then the labelled anti-cocaine antibodies are let to saturate the surface in buffer (B). In the assay, cocaine molecules displace the antibodies off from the surface (C).

Experimental results (P3). Fig. 35A shows the system response during the functionalization phase. When the labelled anti-cocaine antibodies are injected into the sample well, they rapidly bind onto the functionalized surface (blue line). After the surface is saturated, a rinsing step is taking place. The rinsing results in a small step-like decrease in the emission intensity (red line) due to the removal of free and loosely bound labelled antibodies. Finally, the injection of cocaine (here 50 ng/mL) induces the displacement process, where the bound antibodies leave the sensing surface and the emission intensity rapidly decreases.

Fig. 35B shows the representative responses to non-treated saliva samples, spiked with different cocaine concentrations. The shown data represents a larger data set than in the original publication P3, where only the representative data set was used for a rapid proof of concept. The responses are normalized with respect to the initial intensity levels. The normalized response curves show a logical behavior; the higher the cocaine concentration, the more rapid is the decrease. There is also a clear difference between the zero sample and the lowest cocaine concentration of 1.0 ng/mL. In addition, the repeatability of the responses is acceptable, especially at high concentrations and at later time points. Evidently, the early binding rates at lower

concentrations are more influenced by such experimental factors as variations in the manual sample injection and the resulting degree of initial mixing.

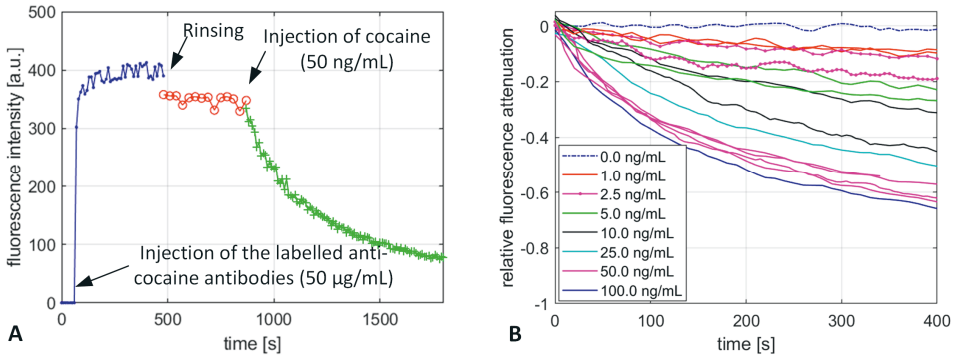

Figure 35. (A) The sensor response during the surface functionalization and after the injection of cocaine. The figure is from P3. (B) The normalized responses for different cocaine concentrations. The figure is constructed with a help of new data sets acquired after the publication of P3.

Fig. 36 shows the mean responses as a function of the cocaine concentration at four different time spots: 30, 60, 90 and 120 sec. The figure illustrates a clear correlation between the responses and the cocaine concentration. According to the Fig. 36A, the responses of the cocaine concentration down to 2.5 ng/mL can be detected within 60 sec. Shortening the assay time to 30 sec decreases the magnitude of the responses, and the responses for the concentration of 5 ng/mL and below may remain indistinguishable from the background. The results suggest, albeit with a relatively small data set, a LOD of 10 ng/mL in saliva for 30 sec test time, which is in accordance with P3. The performance in untreated saliva is very acceptable, as the recommended cutoff values for cocaine screening and confirmation varies between 8 and 20 ng/mL (Bosker and Huestis 2009).

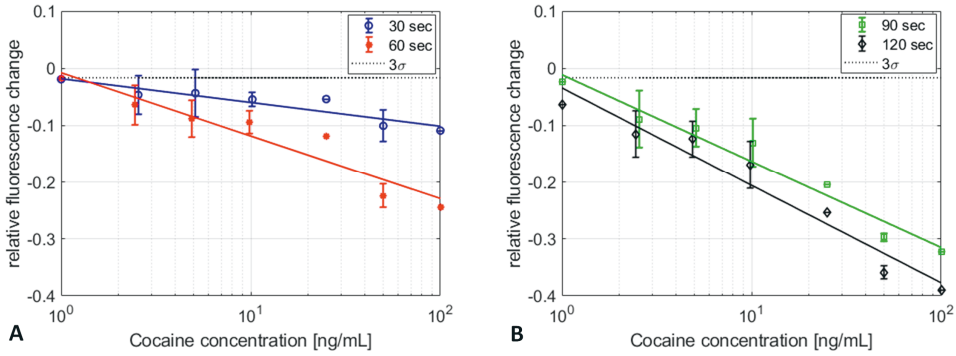

Figure 36. The fluorescence intensities at four time points after the cocaine injection as a function of the cocaine concentration. The open markers denote the actual measurements, error bars the standard deviation (1 - 4 repetitions per concentration), and the dotted line corresponds to the mean intensity of the blank sample plus 3 times its standard deviation. The figures are constructed with a help of new data sets acquired after the publication of P3.

4.1.4 Discussion on immunoassays

Platform performance. The previous sections have shown the performance of the developed TIR-SAF immunoassay platform with three different immunoassays (P1, P2, P3). The achieved results are summarized in Table 2 in terms of the analyte properties, limits of detection and assay details.

Table 2. The summary of the results with the TIR-SAF immunoassay platform (P1,P2,P3)

Analyte	M_w (kDa)	LOD (ng/mL)	Assay form	Assay time (min)	Sample matrix	Function-alization method	NSB rejection method	Wash-ing	ref
IgG	150	0.75	nonc[1]	160	buffer	physisorption	BSA	No[3]	P1
morphine	0.285	2.7	nonc	0.5	buffer	physisorption	BSA	No	P2
cocaine	0.303	10.0	disp[2]	0.5	saliva	physisorption	Lipa-DEA	No	P3

[1]noncompetitive; [2]displacement; [3]Not washed after analyte/detection antibody binding

In order to assess the performance of the platform in the model immunoassay, the achieved results with IgG are shown together with other reported SAF-based IgG immunoassays in Table 3. The table shows that while all assays were performed in a buffer and within comparable timescales, the applied immunoassay methods differ significantly, which makes the comparison challenging. Overall, the lowest LOD of

0.01 ng/mL has been generated by Kurzbuch et al. (2013), but the measurements were carried out only after washing the unbound capture antibodies, which can substantially improve the results. O'Mahony et al. (2012) studied novel PEG-COOH-like films in surface functionalization and achieved a LOD of 0.11 ng/mL but washed away the unbound capture antibodies before the actual measurements as well. However, Ruckstuhl et al. (2003) demonstrated real time monitoring of the binding kinetics of labelled IgG molecules, and the results are very comparable with the results of P1 in terms of LOD. Interestingly, the authors reported a ratio of 50 between the response to the specific and non-specific analyte, which is significantly lower than the value reported in P1. The lower degree of surface-selectivity can be due to various factors, such as the non-TIR excitation, a higher degree of NSB and different degrees of labelling, to name a few.

Overall, the functionalization and NSB rejection method have a substantial effect on the assay performance. Usually covalent functionalization methods should yield enhanced results compared to the physisorption methods due to higher degree of antibody orientation and stability (Welch 2017).

Table 3. Summarized results of immunoassay platforms applying SAF to the detection of IgG

LOD (pmol/ L)	LOD (ng/ mL)	Assay time (min)	Sample matrix	Function-alization method	NSB rejection method	Washing	ref
5	0.75	160	buffer	physisorption	BSA	No	P1
2	0.3	170	buffer	covalent	Cellulose	No	Ruckstuhl et al. 2003
246	36.9	60	buffer	covalent	BSA	Yes	O'Mahony et al. 2012
0.73	0.11	60	buffer	covalent	PEG	Yes	O'Mahony et al. 2012
0.067	0.01	60	buffer	covalent	BSA	Yes	Kurzbuch et al. 2013

No reports exist - other than P2 and P3 – on the SAF-based detection of abused drugs. Therefore, for comparison, Table 4 shows the results achieved with the morphine and cocaine assay together with selected reported SAF immunoassays for analytes of lower molecular weight.

As before, a comparison between the results is challenging as many assay parameters are different. However, the results of Ruckstuhl et al. (2011) and Winterflood et al. (2013) in the detection of interleukin-2 and interferon-γ, as well as the results of Kurzbuch et al. (2009) in the detection of biotin are remarkably high in terms of the two decades smaller LODs. However, at least a part of the difference can be explained with longer assay times and covalent functionalization techniques.

Table 4. Selected results of SAF-based immunoassay platforms in the detection of various analytes

Analyte	M_w (kDa)	LOD (ng/mL)	Assay time (min)	Assay form	Sample matrix	Functionalization method	NSB rejection method	Washing	ref
morphine	0.285	2.7	0.5	nonc	buffer	physi-sorption	BSA	No	P2
cocaine	0.303	10	0.5	displ	saliva	physi-sorption	Lipa-Dea	No	P3
CRP	25	7.6	60	nonc	serum	covalent	BSA	Yes	1
Interleukin-2	16	0.0046	12	nonc	buffer	covalent	BSA	No	2
Interferon-γ	16	0.03	12	nonc	buffer	covalent	BSA	No	3
Biotin	0.24	0.01	3.5	nonc	buffer	covalent	BSA	No	4

[1] Hill et al. 2011; [2] Ruckstuhl et al. 2011; [3] Winterflood et al. 2013; [4] Kurzbuch et al. 2009

Morphine assay (P2). Compared to the homogeneous FRET-based morphine assay, improvements with respect to the assay speed and sensitivity were achieved by transforming the assay into a heterogeneous format and applying the TIR-SAF platform in the real time monitoring of the fluorescent binding process. The results suggest - albeit with a small sample size – that the change in the sensing scheme may increase the sensitivity by a factor of five and decrease the assay time from 120 sec to 30 sec. The increase in assay speed can be significant, as in many on-site applications fields, a response time below 30 sec is considered as acceptable (Frisk et al. 2008). The achieved improvements are probably mainly due to the significantly enhanced emission collection and elimination of FRET-based signal losses.

However, there are possibilities for further improvements in the morphine assay by:

- limiting the active sensing area through patterned immobilization
- applying site-directed antibody immobilization through more advanced surface chemistries
- optimizing the anti-immune complex antibodies (K11) concentration
- including a controlled sample mixing procedure

Indeed, in all immunoassays (P1, P2, P3), the bottom surface of the sample well, as well as the wall surfaces up to a certain height, were functionalized. The 60 μL sample volume, applied in the morphine assay, results in a total functionalized area of ~70 mm^2 in the sample well. Assuming a circular SAF detection area with a diameter of 200 μm - limited mainly by the focusing of the excitation light - leads to an estimate that more than 99.95% of the available binding sites for morphine remained outside of the detection area. Whether or not this matters, depends according to Ekins (1998), on the total number of available binding sites, affinity constant and sample

volume. More precisely, the maximum number of binding sites producing a negligible disturbance (<1%) to the analyte concentration in the sample can be estimated as $N = 10^{-5}\ VN_a/K$, where V is the sample volume (mL), K is the affinity constant (M^{-1}) and N_a is the Avogadro number. Assuming a typical $K = 10^9\ M^{-1}$ for the morphine antibody (Jun-ichi et al. 1988), V = 60 µL yields $N = 3.6 \times 10^9$. Furthermore, assuming a surface density of $10^4/\mu m^2$ for the capture antibodies, a circular area with a diameter of 390 µm can be estimated as the maximum functionalized area causing still negligible disturbances for the ambient analyte concentration. Therefore, the morphine concentration is very likely disturbed by the assay set-up, and reducing the active area of capture antibodies could improve the assay performance. However, the detection area should remain large enough to create a large enough signal, as well as to provide some lateral tolerance for the adjustment of the detection position. With the developed platform, a functionalized spot with a diameter of 500 – 800 µm should fulfill both requirements.

How much the reduction of the functionalized area would affect to the LOD of morphine assay at the later stages of the assay can be discussed, but it is straightforward to assume that at least the early binding kinetics should speed up (Ekins 1998). Indeed, along with the removal of most of the excess binding sites, the initial depletion rate of the analyte and/or the detection antibody concentration near the detection area should considerably decrease. This in turn should lead to increased binding rate and enhanced signal levels at the early stages of the assay. In rapid on-site screening, this would be beneficial.

Another potential way to enhance the assay is to apply site-directed immobilization techniques (Welch 2017). The physical adsorption of the capture antibodies on the PS surfaces, used in this thesis, is the simplest method, but it results in randomly orientated antibodies with less activity and an increased probability of denaturation. In addition, the concentration of the detection antibody K11 could be optimized by experimenting systematically with different K11 concentrations. Finally, a controlled procedure for the mixing of the sample would possibly speed up the assay, as the transport of target molecules always play a critical role in the immunoassay performance (Squires et al. 2008).

Interestingly, the same pair of antibodies has later been applied in a paper-based lateral flow immunoassay by Teerinen et al. (2014). Here, the anti-morphine antibodies were immobilized in the test line, and the sample liquid dissolved the gold-conjugated anti-immunocomplex antibodies into the channel. The authors used diluted (1:20) oral fluid samples and applied an in-house developed test strip reader (Mannila et al. 2007) for the quantitative analysis. Morphine concentrations as low

as 0.05 ng/mL were detectable in the sample buffer, but the assay time were 5-20 minutes.

In conclusion, the results with morphine demonstrate the power of surface-selective fluorescent detection in rapid on-site drug detection. The achieved results are satisfactory with respect to the recommend cutoff values of 40 ng/mL and the test speed of 30 sec. In addition, the system performs well when comparing with other reported morphine immunoassays, recently summarized by Gandhi et al. (2015).

Cocaine assay (P3). The results with cocaine assay demonstrated the applicability of the immunoassay platform to operate in biological sample matrices, which is undoubtedly one the key features of the surface-selective fluorescence detection. The matrix effects outside the reach of the evanescent field can only limitedly interfere with the detection. Moreover, as the propagating light and fluorophores interact only through evanescent effects, scattering, absorption, or sample matrix opacity should not affect to the detection. In the cocaine assay, no sample pretreatment took place, but the untreated saliva samples were spiked with cocaine. Nevertheless, the early responses of the antibody displacement proved to be correlated with the morphine concentrations. The size of the data set is relatively compact, but the results suggest that the displacement type immunoassay could detect cocaine concentrations comparable to the recommended cutoff values (8 – 20 ng/mL) for oral fluids in 30 sec.

For further cocaine assay improvements, the arguments for morphine assay apply well. The reduction of the active sensing area, covalent functionalization procedures and the mixing of the sample would probably improve the speed of the cocaine assay as well.

Finally, in typical security or health care applications, there are more than one interesting analyte that should be screened on-site at the same time. SAF-based immunoassays apply well for the task, and several authors have already reported on multiplexed assays based on mechanical scanning (Kurzbuch et al. 2009) or multielement chips (Hill et al. 2011).

4.2 Oxygen sensing in cell cultures

This section presents the experimental results with the developed oxygen sensors, introduced in Section 3.2. The section starts by assessing the sensing characteristics of the devices (P4, M1). Then the section summarizes the experiments, where the sensors were used for oxygen monitoring in hypoxia tests of hiPSC-derived CMs (P4, M1). Finally, the results of the sensing material biocompatibility tests with hiPSC-derived cells are summarized (M1), and the overall performance of the oxygen sensing set-ups is discussed.

4.2.1 Characterization of the oxygen sensors

Oxygen sensing films

Set-up A (P4): PS films with physically embedded PtOEPK were prepared. PS pellets and PtOEPK in three different concentrations were dissolved in toluene and spin-coated on glass substrates (1 mm thickness), used in cell culturing. The resulted average oxygen sensing film thickness was 480 nm, which is well compatible with the set-up A (see Fig. 21). For full details of the film manufacturing, see P4.

Set-up B (M1): Three different films were prepared, named as Cov1, Ref1 and Ref2. The film Cov1 contained covalently linked PtTFPP (see M1 for details), while Ref1 and Ref2 contained physically embedded PtTFPP in PS. The average film thickness was 500 nm, which is well compatible with the set-up B (Fig. 25).

Sensor characteristics. Customized polydimethylsiloxane (PDMS) 1-well culture chambers (Fig. 27B) were assembled on the oxygen sensing plates, directly on the sensing film. The structure offered a sealed calibration chamber that can be filled with either gas or liquid, and its gas content can be controlled. The oxygen concentration of the chamber was varied at room temperature, and the sensor phase values were recorded.

The corresponding luminescence lifetime Stern-Volmer plots for set-up A, according to the eqs. (3.2) and (3.3), are shown in Fig. 37. In Fig. 37A, an oxygen-independent phase constant of ϕ_c = 16.50° between the excitation and the detector has been subtracted from the measured phase data. In Fig. 37B, separate best-fit phase constants have been applied to the data of each film. Interestingly, this

procedure results in relatively small changes in ϕ_c, but it nevertheless increases the linearity of the Stern-Volmer plots.

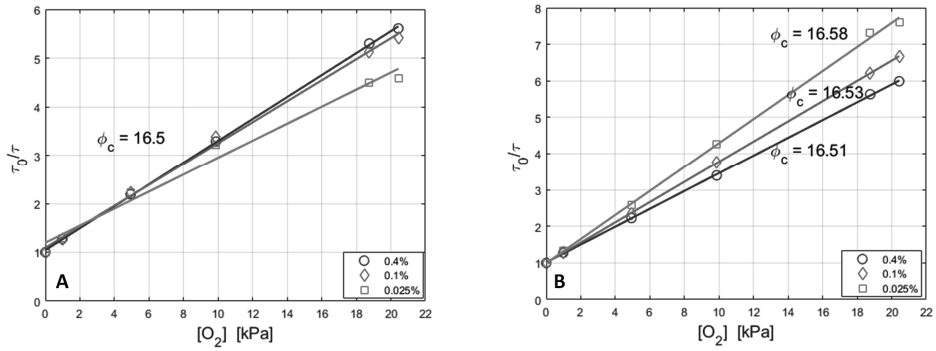

Figure 37. Set-up A: Lifetime Stern-Volmer plots with three different PtOEPK concentrations in polystyrene films. (A) each plot with the same phase constant ϕ_c = 16.50°; (B) each plot with a best-fit phase constant ϕ_c.

For calibration purposes, the Stern-Volmer equation (3.2) can also be rewritten, as in P4, as

$$\frac{\phi_0}{\phi} = 1 + K_{sv}\, pO_2 \qquad (4.1)$$

This is justified, as tanØ ≈ Ø for small Ø, and as the unquenched lifetime of approximately 60 μs for both PtOEPK and PtTFPP results in maximum phase values of approximately of π/5 at 2 kHz modulation frequency (Eq. 2.6). Fig. 38 shows the corresponding Stern-Volmer plots. The plots are very similar to the lifetime plots, thus illustrating the correctness of the (4.1). However, there is more variance in the best-fit phase constant values.

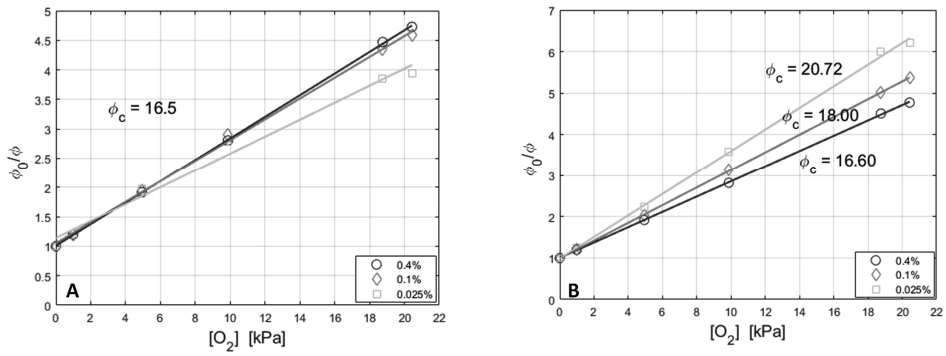

Figure 38. Set-up A: Stern-Volmer plots using the phase values. Responses with three different PtOEPK concentrations in polystyrene films. (A) with the same phase constant ϕ_c = 16.5°; (B) each plot with a best-fit phase constant ϕ_c. The figures are from P4.

Similar luminescence lifetime and phase-type Stern-Volmer plots for the set-up B are shown in Fig. 39. For the set-up B as well, the plots are well linearized by the best-fit phase constants.

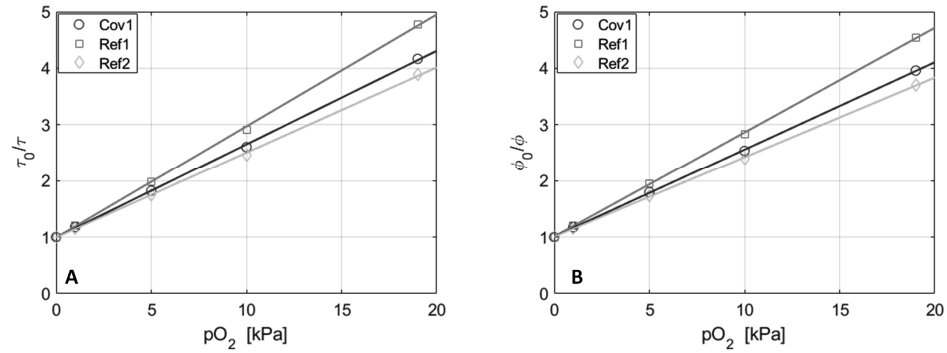

Figure 39. Set-up B: (A) Lifetime Stern-Volmer plots with three different PtTFPP-polystyrene oxygen sensing films (M1); (B) The corresponding Stern-Volmer plot using phase values.

The sensor characteristics for both set-ups with different sensing films are summarized in Table 5 (P4, M1). The variations in the Stern-Volmer constants stem from differences in oxygen diffusion constants, unquenched lifetimes and quantum yields - all affected by the indicator concentration and the polymer composition. The measured noise levels correlate inversely with the indicator concentration; higher concentration leads to higher signal levels and lower noise. Overall, the noise levels

are in the same range as the noise levels of some commercial devices[5], but accurate comparison is challenging, since the bandwidth information of the commercial devices is often unclear. However, the listed RMS phase noise values are already on or close to the limit of the 0.01° RMS phase noise of the used phase detection hardware.

Table 5. The oxygen sensor characteristics with different sensing films and optical set-ups. Measured at T = 25°C. Combined data of P4 and M1.

indicator	linked	[wt-%]	Set-up	K_{SV} [kPa^{-1}]	RMS phase noise [°] (at pO_2 = 5.0 kPa at 10 Hz data rate)
PtOEPK	no	0.400	A	0.185	0.0076
PtOEPK	no	0.100	A	0.215	0.019
PtOEPK	no	0.025	A	0.261	0.050
PtTFPP	no	0.5	B	0.151	0.010
PtTFPP	no	0.05	B	0.198	0.025
PtTFPP	yes	0.05	B	0.166	0.031

It should also be noted that the luminescence-based oxygen sensing is very sensitive to temperature variations, mainly due to the temperature sensitivity of oxygen diffusion in the matrix. In case of PtOEPK and PS, 0.1K temperature fluctuations can cause 0.01° phase fluctuations at kHz modulation (P4). Therefore, either a temperature compensation method must be applied (McDonagh et al. 2001), or a temperature control must be integrated into the system to ensure stable measurement conditions. In typical cell culturing set-ups, the temperature is well-controlled and compensation methods are not necessarily needed.

The long-term stability is another important feature of the oxygen sensor. Fig. 40 shows the sensor set-up B and the sensing film Cov1 with the covalently bound indicators in a week-long stability test (M1). Here, the calibration chamber was filled with DI water, and the oxygen partial pressure was changed stepwise between 19 kPa and 0 kPa. Especially the phase response (Fig. 40B) demonstrates a high degree of stability. The minor fluctuations in the responses are due to changes in the ambient temperature.

Overall, the achieved sensor characteristics are typical for luminescence lifetime-based sensor set-ups with Pt-porphyrins in PS-type polymers and well applicable to pO_2 measurements on physiological range. The integration of the developed set-ups into cell culture system is illustrated in the next section.

[5] See for example https://www.wpiinc.com/media/wysiwyg/pdf/DS/OxyMicro.pdf

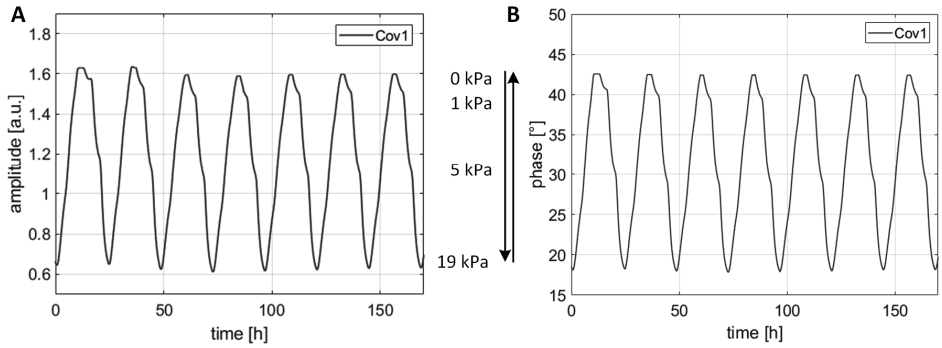

Figure 40. The amplitude (A) and phase (B) response of the oxygen sensor set-up B in a week-long continuous oxygen tension monitoring in water. The sensing film with covalently linked indicators (Cov1) is used. The oxygen partial pressure was varied according to the sequence [19, 10, 5, 1, 5, 10, 19, 10, 5, 1, …] kPa. The sensor response was measured four times a minute with a 1.5 s illumination. The figure is from (M1).

4.2.2 Cardiomyocytes in hypoxic conditions

CM cultures and cell models provide highly useful platforms for fundamental biomedical research (Chin et al. 2019), model development for heart diseases (Shah et al. 2019), toxicology and drug development (Sinnecker et al. 2014). From the measurement and observation point of view, the mechanobiological properties makes CMs especially attractive. Because of the relatively large size of CMs, not only CM clusters but also single CM cells can be monitored unobtrusively with standard phase microscopy, and tools for video-based analysis are available (Ahola 2019). In addition, MEAs, capable of detecting localized electric signals, provide another tool for analysis (Natarajan et al. 2011; Ryynänen et al. 2018).

Primary human CMs can be difficult to obtain. Therefore, hiPSC-derived CMs provide an excellent source of cells of human origin. The heart models based on cells of human origin avoid many research problems and the ethical concerns faced with animal cells. Moreover, as hiPSC-derived CMs can be collected both from healthy individuals and patients with genetic cardiac diseases, they provide tools for the development of personalized medicine applications (Karakikes et al. 2015).

Inadequate oxygen supply to heart muscles leads to a condition called myocardial ischemia, and a prolonged ischemia can lead to the irreversible death of CMS and myocardial infarction (Hafez et al. 2018). Similarly, hypoxic conditions disrupt the mitochondrial function of cell cultures and models.

In the following, preliminary experimental results are presented, where the developed sensors were applied to the monitoring of oxygen in hypoxia studies of hiPSC-derived CM cultures.

Experimental with set-up A (P4). CMs used in the study were differentiated from the hiPSC-line UTA.04602.WT (Lahti et al. 2012). Beating hiPSC-CM aggregates were plated on the sterilized culture wells mounted on the PS-PtOEPK oxygen sensing films spin-coated on glass substrates. After the plating, the aggregates were cultured in standard incubator conditions for 12 h for initial stabilization. For full details, see P4.

After the stabilization, the culture well was placed in the modular cell culturing platform (See Fig. 27 and P4 for full details). The baseline conditions – similar as in a standard incubator – were established by flushing the gas exchange chamber with a normoxic gas mixture containing 19% of O_2, 5% of CO_2 and 76% of N_2. As the conditions changed in the well relatively slowly, the oxygen partial pressure was recorded only six times an hour to minimize the disruptions to the CMs. The excitation power was kept as low as possible. A minute-long video was recorded once an hour. After the experiments, the videos were analyzed according to (Ahola et al. 2014). Fig. 41A shows the modular cell culturing system at the measurement laboratory, and Fig. 41B shows a still image from a typical video, where three hiPSC-derived CM clusters are beating.

Fig. 42A shows a typical oxygen tension curve during first two days of hypoxia testing. After 4 h hours of baseline recording in normoxia, the gas exchange chamber was flushed continuously with a hypoxic gas mixture containing 1% of O_2, 5% of CO_2 and 94% of N_2. Approximately in three hours, the system had reached oxygen tension close to 2 kPa. This tension is twice as much as the set-point of 1% should produce, which is probably due to the incomplete sealing of the system. After the tests, the post calibration data supported this assumption. The first hypoxic period had a duration of 12 h, and after a three hours recovery at oxygen tension of $pO_2 >$ 16 kPa, a second hypoxic period took place.

The video analysis generated time-dependent beating frequencies that were analyzed against the respective oxygen tension values. Fig. 42B shows the plot for the first hypoxic period. The data is relatively restricted, and it remains unclear whether there is a direct correlation between oxygen tension and beating frequency. However, subsequent tests of our group have confirmed that the hiPSC-derived CMs – at least from the used cell line – typically do react by decreasing their beating frequency.

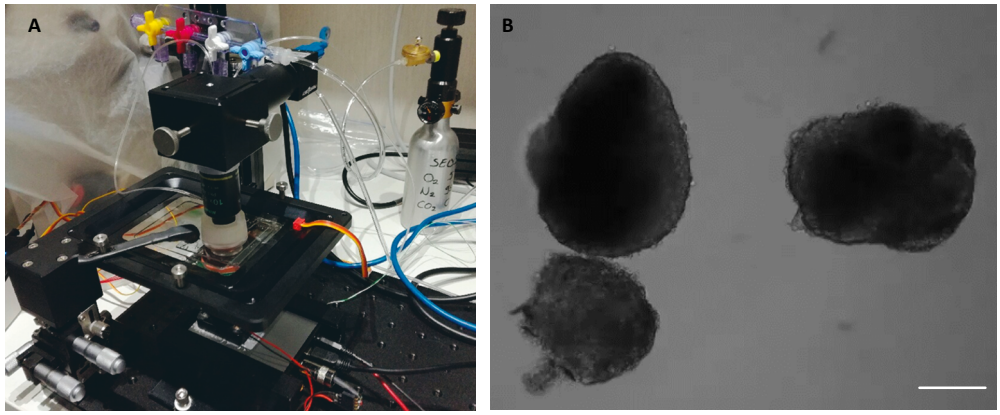

Figure 41. (A) The modular cell culturing system at the cell laboratory during the hypoxia tests with hiPSC-derived cardiomyocytes; (B) Still image of a video recording of three beating cardiomyocyte clusters. The white scale bar represents 200 µm. A sample of the data set supporting this claim is shown in the next subsection, where the biocompatibility test results of different oxygen sensing materials are presented.

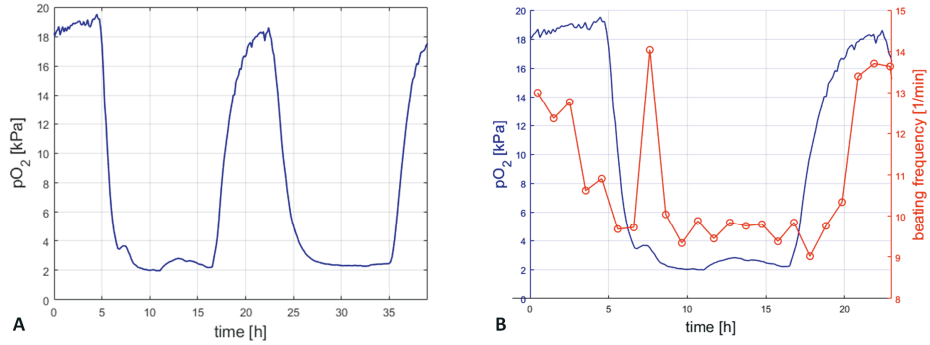

Figure 42. Oxygen sensor set-up A in oxygen monitoring. (A) Typical oxygen tension measurement during hypoxic testing of hiPSC-derived cardiomyocyte clusters; (B) The beating frequencies of the cluster and the oxygen partial pressure values during the first hypoxic period in (A). The figure is from P4.

4.2.3 Biocompatibility tests

While the hiPSC-derived CM clusters survived for days on the PtOEPK-PS surfaces in the experiments described above, the attachment and the morphology of the cells was poor. It became evident that a more biocompatible sensing layer is required, which led to the studies on covalently linked PtTFPP in PS (M1). In the following

we present the main results from the biocompatibility tests with hiPSC-derived neurons and CMs (M1).

The tested oxygen sensing materials are shown in Table 6. The material Cov1 is a polymer blend of PS (99.3%) and PPFS (0.7%), and PtTFPP has been linked to PPFS by thiol-mediated method (Koren et al. 2012). All other tests materials contain physically embedded indicators. For details, see M1.

Table 6. The oxygen sensor materials used in the biocompatibility tests with hiPSC derived neurons and cardiomyocytes (M1).

Code	polymer	Indicator	Type	concentration [wt-%]
Cov1	PS-PPFS blend	PtTFPP	Covalently linked	0.05
Ref1	PS	PtTFPP	Non-linked	0.05
Ref2	PS	PtTFPP	Non-linked	0.5
Ref3	PS	PtOEPK	Non-linked	0.05

hiPSC-derived neurons. The neurons were plated on the films Cov1, Ref1, Ref2 and Ref3, as well as on a plain PS film for a basic reference. The cells were cultured in the dark and followed up to seven days. One day after the cell plating, the cells displayed equal attachment, spreading and neuronal morphology (Fig. 43A). However, on day seven (D7), only the PS control and Cov1 films supported neuronal growth – the cells on the films Ref1, Ref2 and Ref3 had started to retract into aggregates. Images of the live-dead assays (D7) showed similar aggregate formation (Fig. 43B).

A small but statistically significant difference was present in the live cell coverage between the film Cov1 and PS control (Fig. 43D). The live cell coverage of Ref1 was lower compared to Cov1, but not statistically significantly. However, the live cell coverage on Ref2 and Ref3 were significantly lower than on Cov1. Images of the immunocytochemically stained wells (D7) showed similar nuclei counts between PS and Cov1 film (Fig. 43C), but the films Ref1, Ref2 and Ref3 supported cell growth only with a significantly lower rate (Fig. 43E). In addition, on PS control and Cov1 films, over 80% of cell population were β-tubulin-positive neurons, while the other films showed significantly lower percentages (Fig. 43E). In conclusion, the hiPSC-derived neuronal cells attached, spread and sustained their neuronal identity most efficiently the film with covalently linked indicators. Especially the biocompatibility of PtOEPK-based film (Ref3) was poor with hiPSC-derived neuronal cells.

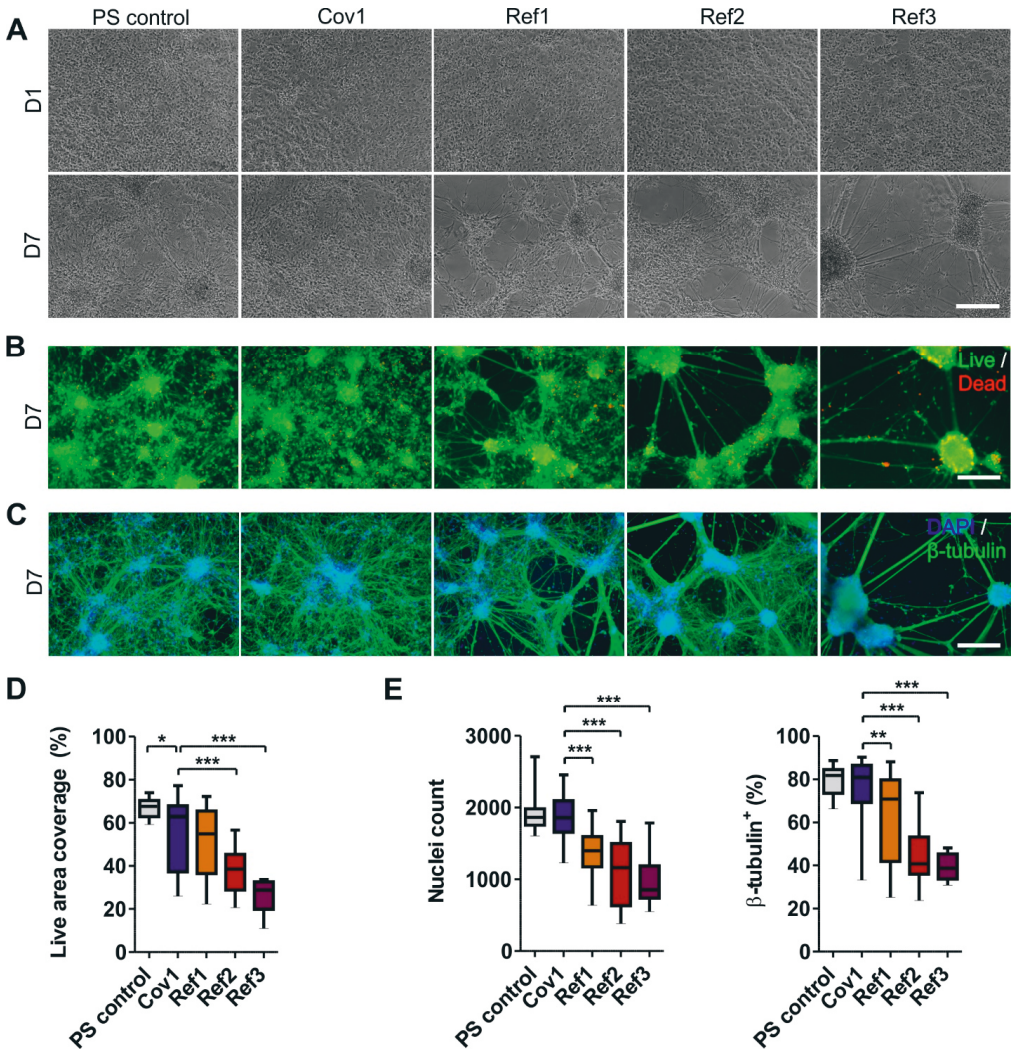

Figure 43. The viability and immunocytochemical characterization of the hiPSC-derived neuronal cells cultured on different oxygen sensing films and a plain PS control film. (A) Representative phase contrast images after on day one (D1) and seven (D7). (B) The Live/dead staining on D7. (C) The immunocytochemical staining of cell nuclei (DAPI) and neuronal cells (β-tubulin) on D7. Scale bar represents 200 µm. (D) The areal coverage of live cells. (E) The number of DAPI-positive cell nuclei and the percentage of β-tubulin-positive neurons. The data is presented as median and interquartile range with whiskers showing the minimum and maximum values. Statistical analysis according to Mann-Whitney U-test (two-tailed). Statistical significances are denoted as * $p < 0.05$; ** $p < 0.01$; *** $p < 0.001$. The figure is from M1.

hiPSC-derived cardiomyocytes. Biocompatibility tests with hiPSC-derived CM clusters showed a similar superiority of the oxygen sensing material with covalently linked indicators, although with a more restricted test set (details in M1). More recently, we have applied the sensing material Cov1 in numerous hypoxia tests with CMs. A sample of the data is shown in Fig. 44, where the phase contrast microscopy picture (A) shows the spread of CM clusters all over the sensing material after five days in an incubator, thus illustrating a high degree of biocompatibility (M1). Fig. 44.B shows the measured oxygen partial pressure and the video-analyzed beating frequency of a single cluster cultured on the modular cell culturing system. These curves show an evident correlation between the available oxygen concentration and beating frequency.

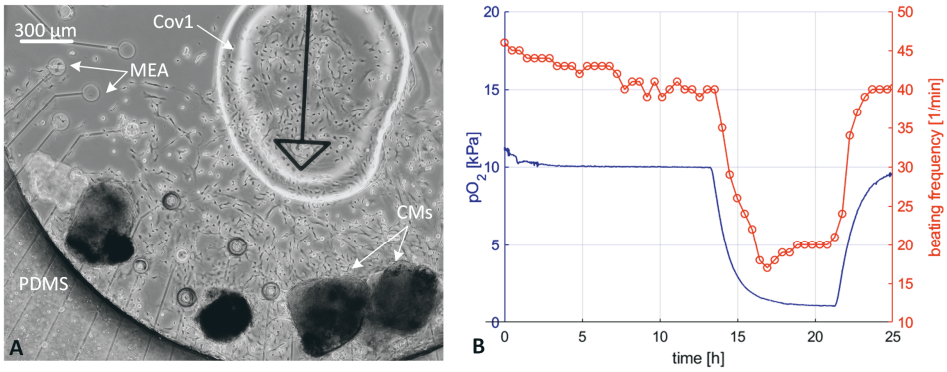

Figure 44. (A) hiPSC-derived CM clusters in hypoxic testing. Luminescent sensing material (Cov1) based on covalently linked PtTFPP in PS-based polymer is applied. (B) An example of the monitored pO2 condition (blue) and respective video-analyzed beating frequency (red). The figure is from M1.

4.2.4 Discussion on the oxygen sensing

In the previous chapters, we have presented and characterized two optical set-ups that can be applied in luminescence-based oxygen sensing in cell cultures. The essential feature of the set-ups is their optical design, which facilitates efficient luminescence detection and minimizes the excitation power radiated directly to culture, while integrating smoothly with the other instrumentation technologies of the modular cell culture system (Fig. 27). Especially when the luminescent sensing material is composed of covalently linked indicators, the set-ups provide means for

minimally invasive luminescence detection in sensitive cell cultures with low indicator concentration and excitation power.

However, the presented set-ups are single-spot pO_2 sensors, and as such, they can be applied only to the overall monitoring and control of oxygen tension in the culture. For localized pO_2 in 2D, scanning procedures can be applied. Mechanical xy-scanning with a motorized stage is possible, as the culture substrates can slide over the parabolic lens in a continuous, immersion oil-secured optical contact. However, more feasible options are provided by optical scanning technologies either based on the laser scanning (Jonkman and Brown 2015), or on a structural illumination through digital mirror device (DMD) technologies (Chao et al. 2007; Bednarkiewicz et al. 2008). Indeed, both simulations and experiments have shown that, depending on the design parameters of the parabolic lens, it is possible to shift the excitation focus 1-2 mm without a change in the measured luminescence lifetime. The DMD-based scanning technology is especially attractive, since

- the excitation areas can have any shape and size, within the limits of the geometrics
- DMD provides multi-wavelength excitation possibilities, thus facilitating multiparametric measurements
- DMD devices can be utilized in structural illumination purposes for optical microscopy
- DMD devices can be applied in optogenetic stimulation

One possible scheme for such combined DMD-based approach is shown in Fig. 45, where a special parabolic lens is shown with an additional facet that facilitates the scanning at the plane of the culturing substrate. The center part of the lens can be applied for optogenetic stimulation and structural illumination for optical microscopy. The luminescence emission is collected through the dichroic mirror as before. A device based on the shown scheme is under development in our group.

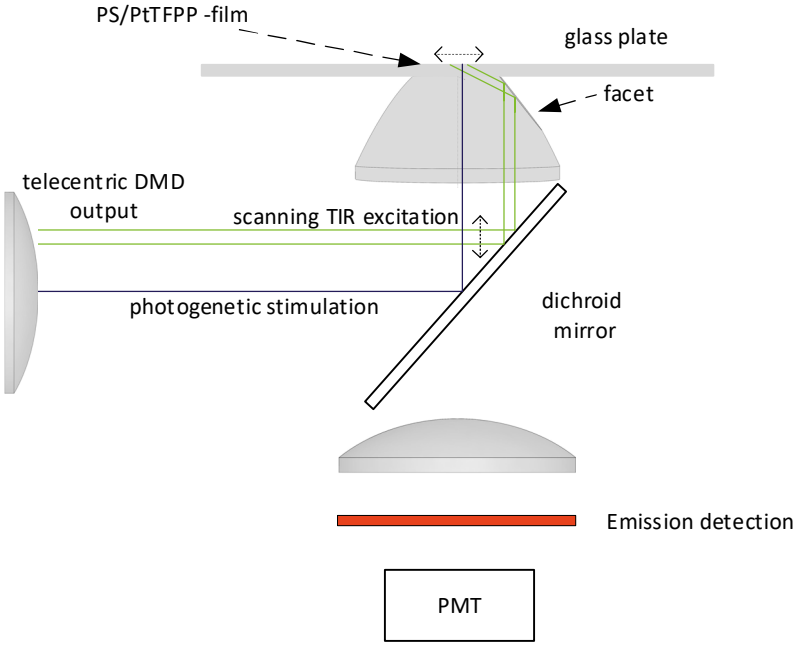

Figure 45. An optical oxygen sensor scheme utilizing a digital mirror device (DMD) for scanning. The output of the DMD is directed through a telecentric lens system to the dichroic mirror and the parabolic lens. The lens contains a facet that facilitates a scanning TIR luminescence excitation (green rays). The center part of the lens can be applied to optogenetic stimulation (blue ray) as well as for structural illumination for optical microscopy.

5 CONCLUSIONS AND FUTURE OUTLOOK

5.1 Conclusions

In the thesis, surface-selective luminescence methods were developed and utilized in immunoassays and chemical sensing in cell cultures. The conclusions can be summarized as follows:

Surface-selective luminescence methods in immunoassays

- An effective way to utilize surface-selective fluorescence methods in immunoassays is to simultaneously apply both total internal reflection excitation (TIR) and supercritical angle fluorescence (SAF) detection. Especially in applications where a maximal surface-selectivity is essential, this arrangement should be favored. Parabolic elements provide one effective means for platform designs.
- A measurement platform incorporating the above-mentioned methods has been constructed. The key component of platform is a parabolic lens, custom-manufactured from polystyrene, which facilitates the use of TIR and SAF. The platform is compatible with standard, flat bottom, polystyrene well plates. It has been demonstrated with a model immunoassay that the platform possesses a high collection efficiency and extreme surface-selectivity in the fluorescence detection.
- The high degree of surface-selectivity enables the monitoring of fluorescent binding processes in real time, even in samples containing high concentrations of free unbound detection molecules. This feature facilitates rapid immunoassays without any washing steps after the injection of the sample.

Rapid luminescence-based immunoassays for morphine and cocaine

- In the morphine immunoassay, the application of surface-selective methods enabled the transformation of the FRET-based homogeneous immunoassay into a heterogeneous form exploiting the real time monitoring of the binding processes. The achieved tests results showed,

albeit with a small sample size, that the transformation can increase the morphine assay sensitivity and reduce the test time from 2 two minutes to 30 sec. Morphine concentrations one decade below the recommended cutoff level could be detected below 30 sec in buffer solution with the developed platform.

- Displacement-type immunoassays for cocaine showed the power of the developed platform as well. Cocaine concentrations comparable to the recommended cutoff levels could be detected in saliva in 30 sec.

Surface-selective luminescence methods in chemical sensing in cell cultures

- Optical detection schemes similar to the suggested immunoassay platform are well-suited for the luminescence-based chemical sensing in cell cultures as well. Such surface-selective detection schemes enable efficient luminescence collection, including the peak radiation into supercritical angles.
- The efficient luminescence detection enables the use of low indicator concentration and excitation power without compromising the sensor performance; thus, providing means for minimally invasive luminescent sensing.

Luminescence-based oxygen sensing

- Oxygen sensor set-ups incorporating the above-mentioned methods have been constructed. The set-ups show sensor characteristics comparable to commercial devices, when used in connection with polystyrene based sensing films with low indicator concentrations.
- The oxygen sensor set-ups are shown to integrate smoothly into a system with other instrumentation such as microelectrode arrays, video microscopy, and temperature and gas control. Oxygen monitoring with the set-ups have been demonstrated in hiPSC-derived cardiomyocyte cultures.
- It has been shown that covalent linking of the oxygen indicators substantially increases the biocompatibility of the luminescent sensing material with hiPSC-derived neurons and cardiomyocytes.

5.2 Future outlook

Immunoassays. For the future work with the SAF-based immunoassays, there are many things to consider. As already discussed, the immunoassay performance – at least in terms of the assay speed – can probably be improved by removing most of the functionalized areas outside of the detection area (i.e. the area under the optical interrogation). Here, patterned functionalization procedures can be applied (Shuster et al. 2011). The other discussed methods to enhance the assay performance are also worth considering, such as site-directed immobilization techniques and controlled mixing procedures.

On-site and point-of-care (POC) devices. Studies related to the real on-site applicability of the platform are worth considering. Such studies should aim for a handheld, battery-powered device that is capable of testing or screening multiple analytes. A key component of such a device can be a sample cartridge with many integrated features, including fluid channels, excitation waveguide structures and emission front-end optics (Tappura et al. 2019). In addition, the shelf life and the stability of the functionalized sensing surfaces may prove critical factors in field conditions, and various functionalization methods should be rigorously studied with this respect. Here, according to our experiments, site-directed immobilization methods together with a hydrophilic polymer matrix can prove invaluable for improved shelf lives (Vikholm-Lundin 2005).

Morphine and cocaine. As at the time of (P2), the commercial immuno-chromatographic lateral flow tests are dominating the market of the saliva-based on-site screening of drugs today. In many countries, such tests are utilized by the authorities. While easy to use, the tests are still hampered by the lengthy testing times and significant number of false results, and the test results must be confirmed by laboratory methods. In a recent study, Gentili et al. (2016) studied the reliability of a widely applied commercial DrugWipe 5A test for five common drugs by collecting saliva samples from volunteering individuals and analyzing the samples both with the commercial test and GC-MS. According to the results, DrugWipe 5A generated false negative cocaine results for 8/24 samples and false positive cocaine results for 3/59 samples with a five-minute testing time. For the opiates, the numbers were slightly worse. Therefore, the need for more rapid and reliable drug screening methods has not disappeared, and the surface-selective luminescence methods may well be part of a future solution.

Interesting reports been recently published on novel biosensing solutions for morphine and cocaine. Aptamer-based biosensors with optical evanescent field transduction (Qiu et al. 2018) or polarization microscopy (Wang et. al 2019) have been used for the cocaine sensing. While the Qiu et al. achieved only a moderate LOD of 3.2 μg/mL in a buffer solution with a five-minute testing time, Wang et al. achieved an impressive LOD of 0.3 ng/mL in diluted urine, but the assay time remains unknown in this report. In addition, D'Aurelio et al. (2020) have reported in their study on molecularly imprinted nanoparticles of a LOD of 0.24 ng/mL for cocaine in buffer solutions after 30 minutes incubation. Cao et al. (2019) have reported on a novel competitive fluorescence immunoassay for morphine, where they achieved a LOD of 1 ng/mL in buffer with 2 hours incubation time. Evidently, in terms of LOD and assay time, the results achieved in the thesis have remained very competitive when comparing to the recent works.

The problem of false results in immunoassay-based drug screening stems at least partially from the challenges that the biological sample matrices generate for immunoassays. Therefore, the developments of the direct spectroscopic methods, such as surface enhanced Raman spectroscopy (SERS), should be followed closely as well. Recent reports on low-cost substrates and handheld devices for SERS provide an attractive alternative to immunoassays in biochemical analysis, as no immunochemistry is needed (Barnett and Rathmell 2015). Infrared attenuated total reflection spectroscopy represents another direct optical technique that may prove useful in the drug screening in the future (Hans et. al 2014). However, both spectroscopies should reduce the LODs 1-3 decades with handheld devices in order to compete with the immunoassay technology.

Oxygen sensing in cell cultures. For the future work with oxygen sensing in 2D cultures, the DMD-based illumination combined with surface-selective luminescence detection is an attractive option. DMD provides flexible scanning procedures and other interesting prospects, such as the optogenetical stimulation and structural optical illumination. In our group, a device based on the scheme in Fig. 45 is under development.

With regard to 2D chemical monitoring on MEA plates, the required patterning procedures of the spin-coated sensing films remained mere plans and discussions in this work. While the laser ablation and inkjet-printing in particular sound appropriate techniques for the task, probably many practical issues must be solved until a feasible patterning procedure is found. Especially the adhesion of the patterned films may prove to be an issue in long-term cultures.

Cell models in 3D are likely to become standard tools in future cell studies. Compelling evidence suggests that 2D models cultured on plastics or glass do not fully represent the cells residing in the complex microenvironment of a tissue, which can lead, for example, to failures in drug discoveries (Langhans 2018). The development of complex 3D cultures provides challenges for chemical sensing, and the application of distributed sensing beads or smart scaffolds structures (Jenkins et al. 2015) together with suitable microscopy technologies are feasible options. In particular, the combination of optical tomography and light sheet fluorescence microscopy, provide interesting prospects for 3D chemical imaging (Bassi et al. 2015).

REFERENCES

Ahola A, Kiviaho A, Larsson K, Honkanen M, Aalto-Setälä K, Hyttinen J (2014). Video image-based analysis of single human induced pluripotent stem cell derived cardiomyocyte beating dynamics using digital image correlation, Biomed. Eng. Online 13(39): 1–18.

Ahola A (2019). Quantification of Stem Cell Derived Cardiomyocyte Beating Mechanics using Video Microscopy Image Analysis, Tampere University Dissertations, No. 34. Tampere University.

Amao Y (2003). Probes and Polymers for Optical Sensing of Oxygen, Microchim. Acta 143: 1–12. DOI 10.1007/s00604-003-0037-x

Anfossi L, Di Nardo F, Cavalera S, Giovannoli C, Baggiani C (2019). Multiplex Lateral Flow Immunoassay: An Overview of Strategies towards High-throughput Point-of-Need Testing, Biosensors 9(1): 2 doi:10.3390/bios9010002

Armbuster DA and Pry T (2008). Limit of Blank, Limit of Detection and Limit of Quantitation, Clin Biochem Rev. 29(1): S49–S52.

Aslan K, Gryczynski I, Malicka J, Matveeva E, Lakowicz JR, Geddes CD (2005). Metal-enhanced fluorescence: an emerging tool in biotechnology, Current Opinion in Biotechnology 16(1): 55-62.

Astashkina A, Mann B, Grainger DW (2012). A critical evaluation of in vitro cell culture models for high-throughput drug screening and toxicity, Pharmacol Ther 134(1): 82-106. doi: 10.1016/j.pharmthera.2012.01.001.

Axelrod D, Burghardt TP, Thompson NL (1984). Total internal reflection fluorescence, Ann. Rev. Biophys. Bioeng 13: 247-268. https://doi.org/10.1146/annurev.bb.13.060184.001335.

Axelrod D (2001). Total InternalReflection Fluorescence Microscopy in Cell Biology, Traffic 2(11): 764-774. https://doi.org/10.1034/j.1600-0854.2001.21104.x

Axelrod D (2013). Evanescent Excitation and Emission in Fluorescence Microscopy, Biophysical Journal 104(10): 1401-1409. http://dx.doi.org/10.1016/j.bpj.2013.02.044.h

Bajar BT, Wang ES, Zhang S, Lin MZ, Chu J (2016). A Guide to Fluorescent Protein FRET Pairs, Sensors, 16(9): 1488. doi:10.3390/s16091488.

Baldini F, Carloni A, Giannetti A, Porro G, Trono C (2008). A new optical platform for biosensing based on fluorescence anisotropy, IEEE SENSORS JOURNAL 8(7): 1305-1309.

Baldini F, Carloni A, Giannetti A, Mencaglia A, Porro G, Tedeschi L, Trono C (2008). Optical PMMA Chip Suitable for Multianalyte Detection, Anal Bioanal Chem 391: 1837–1844. DOI 10.1007/s00216-008-1904-4.

Baldini F, Carloni A, Giannetti A, Porro G, Trono C (2009). An optical PMMA biochip based on fluorescence anisotropy: Application to C-reactive protein assay, Sensors and Actuators B Chemical 139(1): 64–68. DOI: 10.1016/j.snb.2008.08.027

Balsam J, Bruck AH, Raooly A (2013). Capilary array waveguide amplified fluorescence detector for mHealth, Sensor and Actuators B 186: 711-717. doi: 10.1016/j.snb.2013.06.030

Barnett N and Rathmell C (2015). Detecting Drugs in Saliva: Surface enhanced Raman spectroscopy enables rapid detection with non-invasive testing method, Optik & Photonik. 10(5), 31. doi.org/10.1002/opph.201500040

Basabe-Desmonds L, Reinhoudt DN, Crego-Calama M (2007). Desing of fluorescent materials for chemical sensing, Chem. Soc. Rev. 36: 993–1017.

Bassi A, Schmid B, Huisken J (2015). Optical tomography complements light sheet microscopy for in toto imaging of zebrafish development, Development 142: 1016-1020 doi:10.1242/dev.116970

Bednarkiewicz A, Bouhifd M, Whelan MP (2008). Digital micromirror device as a spatial illuminator for fluorescence lifetime and hyperspectral imaging, Applied Optics 47(9): 1193-1199. https://doi.org/10.1364/AO.47.001193

Benisty H, Stanley R, Mayer M (1998). Method of source terms for dipole emission modification in modes of arbitrary planar structures, J. Opt. Soc. Am. A 15(5): 1192.

Blue R, Kent N, Polerecky L, McEvoy H, Gray D, MacCraith BD (2005). Platform for enhanced detection efficiency in luminescence-based sensors, ELECTRONICS LETTERS, 41 (12): 682 – 68.

Booth M and Wilson T (2004). Low-cost, frequency-domain, fluorescence lifetime confocal microscopy, Journal of Microscopym 214: 36–42.

Bosker W and Huestis M (2009). Oral fluid testing for drugs of abuse, Clinical Chemistry 55(11): 1910-1931. doi: 10.1373/clinchem.2008.108670.

Burke CS, McGaughey O, Sabattie JM, Barry H, McEvoy AK, McDonagh C, MacCraith BD (2005). Development of an integrated optic oxygen sensor using a novel, generic platform, Analyst 130(1): 41-45. DOI: 10.1039/b409814p

Cao J, Chen X-Y, Zhao W-R (2019). Determination of Morphine in Human Urine by the Novel Competitive Fluorescence Immunoassay, Journal of Analytical Methods in Chemistry, 2019, Article ID 7826090, doi.org/10.1155/2019/7826090.

Carraway ER, Demás JN, DeGraff BA, Bacon JR (1991). Photophysics and Photochemistry of Oxygen Sensors Based on Luminescent Transition-Metal Complexes, Anal. Chem. 63(4): 337-342. https://doi.org/10.1021/ac00004a007

Carreau A, El Hafny-Rahbi B, Matejuk A, Grillon C, Kiedaa C (2011). Why is the partial oxygen pressure of human tissues a crucial parameter? Small molecules and hypoxia, J Cell Mol Med. 15(6): 1239–1253. doi: 10.1111/j.1582-4934.2011.01258.x

Chance RR, Prock A, Silbey R (1978). Molecular Fluorescence and Energy Transfer Near Interfaces, in Advances in Chemical Physics, I. Prigogine and S. R. Rice, eds. (Wiley, New York) 1– 65.

Chao S, Holl M, McQuaide S, Ren T, Gales S, Meldrum D (2007). Phosphorescence lifetime based oxygen microsensing using a digital micromirror device, Opt. Express 17(15): 10681–10689.

Chin IL, Hool L, Choi YS (2019). A Review of in vitro Platforms for Understanding Cardiomyocyte Mechanobiology, Front Bioeng Biotechnol. (7), 133. doi: 10.3389/fbioe.2019.00133.

Chiu ML, Lawi W, Snyder ST, Wong PK, Liao JC, Gau V (2010). Matrix Effects - A Challenge Toward Automation of Molecular Analysis, JALA 15:233–42. DOI:10.1016/j.jala.2010.02.001

Clark LC Jr (1956). Monitor and control of blood and tissue oxygen tension, Trans Am Soc Artif Intern Organs 2(1): 41-48.
Courtois JY, Courty JM, Mertz JC (1996). Internal dynamics of multilevel atoms near a vacuum-dielectric interface, Phys. Rev. A - At. Mol. Opt. Phys 53(3): 1862–1878.
Dahl TA (1993). Direct exposure of mammalian cells to pure exogenous singlet oxygen, Photochem Photobiol. 57(2):248-54.
Dams R, Choo RE, Lambert WE, Jones H, Huestis MA (2007). Oral fluid as an alternative matrix to monitor opiate and cocaine use in substance-abuse treatment patients. Drug Alcohol Depend 87:258–267.
D'Aurelio R, Chianella I, Goode JA, Tothill IE (2020). Molecularly Imprinted Nanoparticles Based Sensor for Cocaine Detection, Biosensors 10(3), 22. https://doi.org/10.3390/bios10030022
Drexhage KH (1970). Influence of a dielectric interface on fluorescence decay time, Journal of Luminescence 1(2): 693-701.
Ekins RP (1960). The estimation of thyroxine in human plasma by an electrophoretic technique. Clin Chim Acta 5:453–9.
Ekins RP (1998). Ligand assays: from electrophoresis to miniaturized microarrays. Clinical Chemistry 44(9): 2015-2030.
Enderlein J (1999). Fluorescence detection of single molecules near a solution/glass interface–an electrodynamic analysis, Chem. Phys. Lett. 308 (3,4): 263–266. https://doi.org/10.1016/S0009-2614(99)00595-3
Enderlein J, Ruckstuhl T, Seeger S (1999). Highly efficient optical detection of surface-generated fluorescence, Applied Optics 38(4): 724-732. https://doi.org/10.1364/AO.38.000724
Fogel R, Limson J, Seshia AA (2016). Acoustic Biosensors, Essays in Biochemicstry 60(1): 101-110. 10.1042/EBC20150011
Fort E and Grésillon S (2008). Surface enhanced fluorescence, J. Phys. D: Appl. Phys. 41(1): 013001.
Frisk T, Sandström N, Eng L, van der Wijngaart W, Månsson P, Stemme G (2008). An integrated QCM-based narcotics sensing microsystem, Lab Chip 8: 1648–1657. DOI: 10.1039/b800487k
Gandhi S, Suman P, Kumar A, Sharma P, Capalash N, Raman Suri C (2015). Recent advances in immunosensor for narcotic drug detection, BioImpacts, 5(4): 207-213.
Gentili S, Solimini R, Tittarelli R, Mannochi G, Busardo FP (2016). A Study on the Reliability of an On-Site Oral Fluid Drug Test in a Recreational Context, J Anal Methods Chem. 2016:1234581. doi:10.1155/2016/1234581
Gouin, JF, Doyle A, MacCraith BD (1998). Fluorescence capture by planar waveguide as platform for optical sensors, Electronics Lett. 34: 1685-1687.
Graf BW and Boppart SA (2010). Imaging and Analysis of Three-Dimensional Cell Culture Models, Methods Mol Biol. 591: 211–227. doi: 10.1007/978-1-60761-404-3_13
Grist SM, Chrostowski L, Cheung KC (2010). Optical oxygen sensors for applications in microfluidic cell culture, Sensors 10: 9286–9316. doi:10.3390/s101009286.
Grist SM, Oyunerdene N, Flueckiger J, Kim J, Wong PC, Chrostowski L, Cheung KC (2014). Fabrication and laser patterning of polystyrene optical oxygen sensor films for lab-on-a-chip applications, Analyst, 139: 5718–5727.
Gryczynski I, Malicka J, Gryczynski Z, Lakowicz JR (2004). Radiative decay engineering 4. Experimental studies of surface plasmon-coupled directional emission. Anal. Biochem. 324:170−182.

Gualda EJ, Simão D, Pinto C, Alves PM, Brito C (2014). Imaging of human differentiated 3D neural aggregates using light sheet fluorescence microscopy, Frontiers in Cellular Neuroscience 8:221

Gurwitz D (2016). Human iPSC-derived neurons and lymphoblastoid cells for personalized medicine research in neuropsychiatric disorders, Dialogues in Clinical Neuroscience 18(3): 267-276.

Hafez P, Chowdhury SR, Jose S, Law Xj, Ruszymah BHI, Ramzisham ARM, Ng MH (2018). Development of an In Vitro Cardiac Ischemic Model Using Primary Human Cardiomyocytes, Cardiovasc. Eng. Technol 9(3): 529-538. doi: 10.1007/s13239-018-0368-8

Hans KM, Müller S, Sigrist MW (2012). Infrared attenuated total reflection (IR-ATR) spectroscopy for detecting drugs in human saliva, Drug Test Anal. 4(6):420-429. doi:10.1002/dta.346

Hill D, McDonnell B, Hearty S, Basabe-Desmonts L, Blue R, Trnavsky M, McAtamney C, O'Kennedy R, MacCraith BD (2011). Novel disposable biochip platform employing supercritical angle fluorescence for enhanced fluorescence collection, Biomed. Microdevices 13(4): 759–767.

Hirschfeld TB (1965). Total reflection fluorescence, Can. J. Spectroscopy 10: 128.

Ho A.H-P, Wu S-Y, Kong SK, Zeng S, Yong K-T (2015) SPR Biosensors. In: Ho AP, Kim D, Somekh M. (eds) Handbook of Photonics for Biomedical Engineering. Springer, Dordrecht.

Holst G, Glud RN, Kuhl M, Klimant I (1997). A microoptode array for fine-scale measurement of oxygen distribution. Sens. Actuat. B-Chem 38(1-3): 122–129. https://doi.org/10.1016/S0925-4005(97)80181-5

Horvath P, Aulner N, Bickle M, Davies AM, Del Nery E, Ebner D, Montoya MC, Östling P, Pietiäinen V, Price LS, Shorte SL, Turcatti G (2016). Screening out irrelevant cell-based models of disease, Nature Reviews 15: 751-769.

Hung TQ, Sun Y, Poulsen CE, Linh-Quyen T, Chin WH, Bang DD, Wolff A (2015). Miniaturization of a micro-optics array for highly sensitive and parallel detection on an injection moulded lab-on-a-chip, Lab Chip 15(11): 2445-2451.

Hung TQ, Chin WH, Sun Y, Wolff A, Bang DD (2017). A novel lab-on-chip platform with integrated solid phase PCR and Supercritical Angle Fluorescence (SAF) microlens array for highly sensitive and multiplexed pathogen detection, Biosens. Bioelectron. 90: 217–223.

Jenkins J, Dmitriev RI, Morten K, McDermott KW Papkovsky DB (2015). Oxygen-sensing scaffolds for 3-dimensional cell and tissue culture, Acta Biomaterialia 16(1): 126-135. https://doi.org/10.1016/j.actbio.2015.01.032

Jonkman J and Brown CM (2015). Any Way You Slice It—A Comparison of Confocal Microscopy Techniques, J Biomol Tech. 26(2): 54–65.

Jun-ichi S, Noppavan J, Kunisuke N, TadaoT (1988). Production and characterization of high-affinity monoclonal antibodies against morphine, Molecular Immunology 25(9): 937-943. https://doi.org/10.1016/0161-5890(88)90133-2

Karakikes I, Ameen M, Termglinchan V, Wu J (2015). Human Induced Pluripotent Stem Cell-Derived Cardiomyocytes: Insights into Molecular, Cellular, and Functional Phenotypes, Circ Res. 117(1): 80–88. doi: 10.1161/CIRCRESAHA.117.305365.

Katsidis CC and Sipakas DI (2002). General transfer-matrix method for optical multilayer systems with coherent, partially coherent, and incoherent interference, Applied optics 41(19): 3978-3986.
Kieninger J, Weltin A, Flamm H and Urban GA (2018). Microsensor systems for cell metabolism – from 2D culture to organ-on-chip, Lab on a Chip 18: 1274-1291.
Kim JB, Stein R, O'Hare MJ (2004). Three-dimensional in vitro tissue culture models of breast cancer – a review, Breast Cancer Res. Treat. 85: 281-291. https://doi.org/10.1023/B:BREA.0000025418.88785.2b.
Kindt JT and Bailey RC (2013). Biomolecular analysis with microring resonators: applications in multiplexed diagnostics and interaction screening, Current Opinion in Chemical Biology. 17: 818−826.
Kindt JT, Luchansky MS, Qavi AJ, Lee S-H, Bailey RC (2013). Subpicogram Per Milliliter Detection of Interleukins Using Silicon Photonic Microring Resonators and an Enzymatic Signal Enhancement Strategy, Anal. Chem. 85: 10653−10657.
Koman VB, Santschi C, Martin OJ (2015). Multiscattering-enhanced optical biosensor: multiplexed, non-invasive and continuous measurements of cellular processes. Biomed Opt Express 6(7): 2353-65. doi: 10.1364/BOE.6.002353
Koren K, Borisov SM, Klimant I (2012). Stable optical oxygen sensing materials based on click-coupling of fluorinated platinum(II) and palladium(II) porphyrins - A convenient way to eliminate dye migration and leaching, Sensors Actuators, B Chem 169: 173–181. doi:10.1016/j.snb.2012.04.062
Kreutzer J, Ylä-outinen L, Kärnä P, Kaarela T, Mikkonen J (2012). Structured PDMS Chambers for Enhanced Human Neuronal Cell Activity on MEA Platforms, J. Bionic Eng. 9: 1–10. doi:10.1016/S1672-6529(11)60091-7.
Kreutzer J, Ylä-outinen L, Mäki A, Ristola M, Narkilahti S, Kallio P (2017). Cell culture chamber with gas supply for prolonged recording of human neuronal cells on microelectrode array, Journal of Neuroscience Methods 280: 27-35. https://doi.org/10.1016/j.jneumeth.2017.01.019
Krieg A, Laib S, Ruckstuhl T, Seeger S (2003). Real-time detection of nucleotide incorporation during complementary DNA strand synthesis, ChemBioChem 4(7): 589–592.
Krieg A, Laib S, Ruckstuhl T, Seeger S (2004). Fast detection of single nucleotide polymorphisms (SNPs) by primer elongation with monitoring of supercritical-angle fluorescence, ChemBioChem 5(12): 1680–1685.
Krieg A, Ruckstuhl T, Laib S, Seeger S (2004). Real-time detection of polymerase activity using supercritical angle fluorescence, Journal of Fluorescence, 14(1): 75–78.
Kronick MN and Little WA (1975). A new immunoassay based on fluorescence excitation by internal reflection spectroscopy, J. Immunol. Meth. 8: 235-240.
Kurzbuch D, Bakker J, Melin J, Jönsson C, Ruckstuhl T, MacCraith BD (2009). A biochip reader using super critical angle fluorescence, Sensors Actuators, B Chem. 137(1): 1–6.
Kurzbuch D, Somers M, McDonagh C (2013). High efficiency ring-lens supercritical angle fluorescence (SAF) detection for optimum bioassay performance, Opt. Express 21(19): 22070–22075.

Lahti AL, Kujala VJ, Chapman H, Koivisto A-P, Pekkanen-Mattila M, Kerkelä A, Hyttinen J, Kontula K, Swan H, Conklin BR, Yamanaka S, Silvennoinen O, Aalto-Setälä K (2012). Model for long QT syndrome type 2 using human iPS cells demonstrates arrhythmogenic characteristics in cell culture, Dis. Model. Mech. 5: 220-230. doi:10.1242/dmm.008409

Laib S, Krieg A, Rankl M, Seeger S (2006). Supercritical angle fluorescence biosensor for the detection of molecular interactions on cellulose-modified glass surfaces, Appl. Surf. Sci. 252(22): 7788–7793.

Lakowicz J (2006). Principles of Fluorescence Spectroscopy, 4th ed., Springer, US, New York.

Langel K, Gunnar T, Ariniemi K, Rajamäki O, Lillsunde P (2011). A validated method for the detection and quantitation of 50 drugs of abuse and medicinal drugs in oral fluid by gas chromatography–mass spectrometry, J. Chromatogr. B 879: 859-870.

Langhans SA (2018). Three-Dimensional in Vitro Cell Culture Models in Drug Discovery and Drug Repositioning, Frontiers in Pharmacology 9:6. DOI=10.3389/fphar.2018.00006

Lechuga LM, Lenferink TM, Kooyman RPH, Greve J (1995). Feasibility of evanescent wave interferometer immunosensors for pesticide detection: chemical aspects, Sensors and Actuators B 24(25): 762-765. https://doi.org/10.1016/0925-4005(95)85169-0.

Lehner P, Staudinger C, Borisov SM, Klimant I (2014). Ultra-sensitive optical oxygen sensors for characterization of nearly anoxic systems, Nature Communications 4:4460. DOI: 10.1038/ncomms5460.

Li K, Liu G, Wu Y, Hao P, Zhou W, Zhang Z (2014). Gold nanoparticle amplified optical microfiber evanescent wave absorption biosensor for cancer biomarker detection in serum, Talanta 120: 419-424.

Li Y, Zhang G, Mao X, Yang S, De Ruyck K, Wude Y (2018). High sensitivity immunoassays for small molecule compounds detection – Novel noncompetitive immunoassay designs, Trends in Analytical Chemistry 103: 198-208.

Liebsch G, Klimant I, Frank B, Holst G, Wolfbeis OS (2000). Luminescence Lifetime Imaging of Oxygen, pH, and Carbon Dioxide Distribution Using Optical Sensors, Applied Spectroscopy 54; 548-559.

Ligler FS, Breimer M, Golden JP,Nivens DA, Dodson JP, Green TM, Haders DP, Sadik OA (2002). Integrating Waveguide Biosensor, Anal. Chem. 74: 713-719.

Luan L, Sievert PR, Watkins B, Mu W, Hong Z, Ketterson JB (2006). Angular radiation pattern of electrci dipoles embedded in a thin film in the vicinity of a dielectric half-space, Applied Physics Letters 89:031119.

Lukosz W (1978). Light emission by magnetic and electric dipoles close to a plane dielectric interface. Ill. Radiation patterns of dipoles with arbitrary orientation, J. Opt. Soc. Am. 69(11): 1495-1503.

McDonagh C, Kolle C, McEvoy AK, Dowling DL, Cafolla AA, Cullen SJ, MacCraith BD (2001). Phase fluorometric dissolved oxygen sensor, Sensors and Actuators B 74 124-130.

McDonagh C, Burke C, MacCraith BD (2008). Optical Chemical Sensors, Chem. Rev. 108: 400-422.

MacCraith BD, McDonagh C (2002). Enhanced Fluorescence Sensing Using Sol-Gel Materials, Journal of Fluorescence 12(3/4): 333-342.

Mahmoudi P, Veladi H Pakdel FG (2017). Optogenetics, Tools and Applications in Neurobiology. J Med Signals Sens 7(2): 71–79.
Mannila R, Pulli T, Saari H, Tappura K, Tuppurainen J, Välimäki H, Niskanen A (2007). Fluorescence based fast diagnostics platform for the direct and indirect immunodiagnostic analysis methods. Progress in Biomedical Optics and Imaging - Proceedings of SPIE 6628.
Michl J, Park KC, Swietach P (2019). Evidence-based guidelines for controlling pH in mammalian live-cell culture systems, Commun. Biol 2:144. https://doi.org/10.1038/s42003-019-0393-7.
Mills A (1997). Optical Oxygen Sensors, Platin. Met. Rev. 41:115–127.
Modena MM, Chawla K, Misun PM, Hierlemann A (2018). Smart Cell-Culture Systems: Integration of Sensors and Actuators into Microphysiological Systems 13:1767-1784.
Mohyeldin A, Garzon-Muvdi T, Quinones-Hinojosa A (2010). Oxygen in stem cell biology: a critical component of the stem cell niche, Cell Stem Cell 7(6):150-161. DOI 10.1016/j.stem.2010.07.007
Moya A, Ortega-Ribera M, Guimerà X, Sowade E, Zea M, Illa X, Ramon E, Villa R, Gracia-Sancho J, Gabriel G (2018). Online oxygen monitoring using integrated inkjetprinted sensors in a liver-on-a-chip system, Lab Chip 18:2023–2035.
Mullet VM, Lai EP, Yeung JM (2000). Surface plasmon resonance-based immunoassays, Methods 22(1): 77-91. https://doi.org/10.1006/meth.2000.1039.
Mun J, Lee D, So S, Badloe T, Rho J (2019). Surface-enhanced spectroscopy: Toward practical analysis probe, Applied Spectroscopy Reviews 54(2): 142-175. DOI: 10.1080/05704928.2018.1467438
Mäki AJ, Verho J, Kreutzer J, Ryynänen T, Rajan D, Pekkanen-Mattila M, Ahola A, Hyttinen J, Aalto-Setälä K, Lekkala J, Kallio P (2018). A Portable Microscale Cell Culture System with Indirect Temperature Control, SLAS Technol. 23: 566-579. doi:10.1177/2472630318768710.
Natarajan A, Stancescu M, Dhir V, Armstrong C, Sommerhage F, Hickman JJ, Molnar P (2011). Patterned Cardiomyocytes on Microelectrode Arrays as a Functional, High Information Content Drug Screening Platform, Biomaterials 32(18): 4267–4274. doi:10.1016/j.biomaterials.2010.12.022.
Ngo TT (2007). Ligand Displacement Immunoassay, Anal. Lett. 38: 1057-1069. DOI: 10.1081/AL-200057190.
Nguyen H, Park J, Kang S, Kim M (2015). Surface Plasmon Resonance: A Versatile Technique for Biosensor Applications, Sensors 15(5): 10481–10510. doi:10.3390/s150510481.
Nock V, Blaikie R, David T (2008). Patterning, integration and characterisation of polymer optical oxygen sensors for microfluidic devices, Lab Chip 8: 1300–1307. DOI: 10.1039/b801879k
Nock V, Alkaisi M, Blaikie R (2010). Photolithographic patterning of polymer-encapsulated optical oxygen sensors, Microelectron. Eng. 87: 814–816.
Novotny L and Hecht B (2012). Principles of nano-optics. Cambridge University Press, 2nd edition. ISBN 978-1-107-00546-4.
O'Donovan C, Hynes J, Yashunskib D, Papkovsky DB (2005). Phosphorescent oxygen-sensitive materials for biological applications J. Mater. Chem. 5:2946–2951.

O'Driscoll S, McEvoy HM, McDonagh C, MacCraith BD (2012). Enhanced fluorescence-based optical sensor performance using a simple optical collection strategy, IEEE Photonics Technol. Lett. 24(6):425–427.

O'Mahony CC, Gubala V, Gandhiraman RP, Daniels S, Yuk JS, MacCraith BD, Williams DE (2012). Improving the sensitivity of immunoassays with PEG-COOH-like film prepared by plasma-based technique. J Biomed Mater Res Part A 2012:100A:230–235. https://doi.org/10.1002/jbm.a.33268

O'Riordan TC, Voraberger H, Kerry JP, Papkovsky DB (2005). Study of migration of active components of phosphorescent oxygen sensors for food packaging applications, Anal. Chim. Acta 530: 135-141.

Ogilby PR (2010). Singlet oxygen: there is indeed something new under the sun, Chem. Soc. Rev. 39: 3181-3209.

Olaru A, Bala C, Jaffrezic-Renault N, Aboul-Enein HY (2015). Surface plasmon resonance (SPR) biosensors in pharmaceutical analysis, Crit Rev Anal Chem. 45(2): 97-105. doi: 10.1080/10408347.2014.881250.

Owens GJ, Singh RK, Foroutan F, Alqaysi M, Han CM, Mahapatra C, Kim HW, Knowles JC (2016). Sol–gel based materials for biomedical applications, Progress in Materials Science 77: 1–79. https://doi.org/10.1016/j.pmatsci.2015.12.001

Ozturk SS. et al. (1997) Kinetics of Glucose Metabolism and Utilization of Lactate in Mammalian Cell Cultures. In: Carrondo M.J.T., Griffiths B., Moreira J.L.P. (eds), Animal Cell Technology. Springer, Dordrecht39/b926014p

Papkovsky DB and Dmitriev RI (2013). Biological detection by optical oxygen sensing, Chem. Soc. Rev. 42:8700–8732. doi:10.1039/c3cs60131e

Pfeiffer SA and Nagl S (2015). Microfluidic platforms employing integrated fluorescent or luminescent chemical sensors: a review of methods, scope and applications, Methods Appl. Fluoresc. 3: 034003. Doi: 10.1088/2050-6120/3/3/034003.

Polerecký L, Hamrle J, MacCraith BD (2000). Theory of the radiation of dipoles placed within a multilayer system, Appl. Opt. 39(22): 3968.

Pulli T, Höyhtyä M, Söderlund H, Takkinen K (2005). One-step homogeneous immunoassay for small analytes. Anal Chem 77:2637–2642.

Qiu Y, Tang Y, Li B, He M (2018). Rapid detection of cocaine using aptamer-based biosensor on an evanescent wave fibre platform. R. Soc. open sci. 5: 180821. http://dx.doi.org/10.1098/rsos.180821

Quaranta M, Borisov SM, Klimant I (2012). Indicators for optical oxygen sensors, Bioanal. Rev. 4: 115–157. doi:10.1007/s12566-012-0032-y.

Rajan DK, Patrikoski M, Verho J, Sivula J, Ihalainen H, Miettinen S, Lekkala J (2016). Optical non-contact pH measurement in cell culture with sterilizable, modular parts, Talanta 161:755-761.

Rajan DK, Kreutzer J, Välimäki H, Pekkanen-Mattila M, Ahola A, Skogberg A, Aalto-Setälä K, Ihalainen H, Kallio P, Lekkala J (2018). A portable live-cell imaging system with an invert-upright-convertible architecture and a mini-bioreactor for long-term simultaneous cell imaging, chemical sensing, and electrophysiological recording, IEEE Access. 6:11063-11075. doi:10.1109/ACCESS.2018.2804378.

Rodríguez-Pardo L, Rodríguez J, Gabrielli C, Perrot H, Brendel R (2005). Sensitivity, Noise, and Resolution in QCM Sensors in Liquid Media, IEEE SENSORS JOURNAL 5(6): 1251-1257.

Ruckstuhl T, Enderlein J, Jung S, Seeger S (2000). Forbidden light detection from single molecules, Anal. Chem. 72(9): 2117–2123.
Ruckstuhl T, Rankl M, Seeger S (2003). Highly sensitive biosensing using a supercritical angle fluorescence (SAF) instrument, Biosens. Bioelectron. 18(9): 1193–1199.
Ruckstuhl T and Verdes D (2004). Supercritical angle fluorescence (SAF) microscopy, OPTICS EXPRESS 12(18):4246–4254.
Ruckstuhl T, Winterflood CM, Seeger S (2011). Supercritical angle fluorescence immunoassay platform, Anal. Chem. 83(6): 2345–2350.
Ryynänen T, Pekkanen-Mattila M, Shah D, Kreutzer J, Kallio P, Lekkala J, Aalto-Setälä K (2018). Microelectrode array for noninvasive analysis of cardiomyocytes at the single-cell level, Japanese Journal of Applied Physics 57: 117001. https://doi.org/10.7567/JJ DOI: 10.3389/fnins.2019.00226AP.57.117001
Ryynänen T, Pelkonen A, Grigoras K, Ylivaara OME, Hyvärinen T, Ahopelto J, Prunnila M, Narkilahti S, Lekkala J (2019). Microelectrode Array With Transparent ALD TiN Electrodes, Frontiers in Neuroscience 13:226. DOI: 10.3389/fnins.2019.00226
Sandeau L, Vuillaume C, Contié S, Grinenval E, Belloni F, Rigneault H, Owens RM, Fournet MB (2015). Large area CMOS bio-pixel array for compact high sensitive multiplex biosensing, Lab Chip 15(3): 877–881.
Sapsford K, Charles PT, Patterson CH Jr., Ligler FS (2002). Demonstration of Four Immunoassay Formats Using the Array Biosensor, Anal. Chem. 74(5): 1061-1068.
Sapsford KE, Ligler FS (2004). TIRF Array Biosensor for Environmental Monitoring. In: Optical Sensors. Springer Series on Chemical Sensors and Biosensors (Methods and Applications), vol 1. Springer, Berlin, Heidelberg. https://doi.org/10.1007/978-3-662-09111-1_14
Schlachezki JCM, Saliba SW, de Oliveira ACP (2013). Studying neurogenerative diseases in culture models, Rev. Bras. Psiquitr. 35:S92-S100. Doi. 10.1590/1516-4446-2013-1159.
Shah D, Virtanen K, Prajapati C, Kiamehr M, Gullmets J, West G, Kreutzer J, Pekkanen-Mattila P, Heliö T, Kallio P, Taimen P, Aalto-Setälä K (2019). Modeling of LMNA-Related Dilated Cardiomyopathy Using Human Induced Pluripotent Stem Cells, Cells 8(6): 594.
Shuster MJ, Vaish A, Cao HH, Guttentag AI, McManigle JE, Gibb AL, Martinez MM, Nezarati RM, Hinds JM, Liao W-S, Weiss PS, Andrews AM (2011). Patterning small-molecule biocapture surfaces: microcontact insertion printing vs. photolithography, Chem. Commun.47: 10641-10643.
Singh G, Sridharan D, Khan M, Seshagir PB (2019). Mouse embryonic stem cell-derived cardiomyocytes cease to beat following exposure to monochromatic light: association with increased ROS and loss of calcium transients, Am J Physiol Cell Physiol 317:C725–C736. doi:10.1152/ajpcell.00188.2019
Sinkala E and Eddington DT (2010). Oxygen sensitive microwells, Lab on a Chip 10:3291–3295.
Sinnecker D, Laugwitz KL, Moretti A (2014). Induced pluripotent stem cell-derived cardiomyocytes for drug development and toxicity testing, Pharmacol Ther 143(2):246-52. doi: 10.1016/j.pharmthera.2014.03.004
Sommerfeld A (1909). Uber die Ausbreitung der Wellen in der drahtlosen Telegraphie, Ann. d. Physik 28:665–736.

Squires TM, Messinger R J, Manalis SR (2008). Making it stick: convection, reaction and diffusion in surface-based biosensors. Nat. Biotechnol. 26:417−426. doi: 10.1038/nbt1388.

Stano-Rossi S, Castrignano E, Anzillotti L, Serpelloni G, Mollica R, Tagliaro F, Pascali JP, di Stefano D, Sgalla R, Chiarotti M (2012). Evaluation of four oral fluid devices (DDS1, Drugtest 50001, Drugwipe 5+1 and RapidSTAT1) for on-site monitoring drugged driving in comparison with UHPLC–MS/MS analysis, Forensic Sci. Int 221:70-76.

Sun YS, Landry JP, Fei YY, Zhu XD, Luo JT, Wang XB, KS Lam (2008). Effect of Fluorescently Labeling Protein Probes on Kinetics of Protein-Ligand Reactions, Langmuir 24(23): 13399–13405. doi: 10.1021/la802097z.

Taitt CR, Anderson G, Ligler F (2005). Evanescent wave fluorescence biosensors, Biosens. Bioelectron. 20:2470-2487.

Taitt CR, Anderson G, Ligler F (2016). Evanescent wave fluorescence biosensors: Advances of the last decade, Biosens. Bioelectron. 76:103-112.

Tappura K, Vikholm-Lundin I, Albers M (2007). Lipoate-based imprinted self-assembled molecular thin films for biosensor applications, Biosensors& Bioelectronics 22:912-919.

Tappura K, Mäyrä A, Alamäki M, Kokkonen A, Aikio S, Hiltunen M (2019). Integration of fluidic channels and total internal reflection excitation with supercritical angle fluorescence detection, EPJ Web of Conferences 215, 15002. doi.org/10.1051/epjconf/201921515002

Teerinen T, Lappalainen T, Erho T (2014). A paper-based lateral flow assay for morphine, Anal Bioanal Chem 406: 5955–5965. DOI 10.1007/s00216-014-8001-7.

Thedinga E, Kob A, Holst H, Keuer A, Drechsler S, Niendorf R, Baumann W, Freund I, Lehmann M, Ehret R (2007). Online monitoring of cell metabolism for studying pharmacodynamic effects, Toxicology and Applied Pharmacology: 220 pp. 33–44.

Thomas PC, Halter M, Tona A, Raghavan SR, Plant AL, Forry SP (2009). A noninvasive thin film sensor for monitoring oxygen tension during in vitro cell culture, Anal. Chem. 81: 9239–9246. doi:10.1021/ac9013379.

Tian Y, Shumway BR, Meldrum DR (2010). A new cross-linkable oxygen sensor covalently bonded into poly(2-hydroxyethyl methacrylate)-co-polyacrylamide thin film for dissolved oxygen sensing, Chem. Mater. 22: 2069–2078. doi:10.1021/cm903361y.

Tian Y, Shumway BR, Gao W, Youngbull C, Holl MR, Johnson RH, Meldrum DR (2010). Influence of matrices on oxygen sensing of three sensing films with chemically conjugated platinum porphyrin probes and preliminary application for monitoring of oxygen consumption of Escherichia coli (E. coli), Sensors Actuators, B Chem 150: 579–587. doi:10.1016/j.snb.2010.08.036

Vikholm-Lundin I (2005), Immunosensing Based on Site-Directed Immobilization of Antibody Fragments and Polymers that Reduce Nonspecific Binding. Langmuir 21: 6473-6477. Doi; 10.1021/la046992u

Välimäki H, Lekkala J, Helle H (1997). Prediction ability of a lumped-element equivalent circuit model for thickness-shear mode resonators in liquids, Sensors and Actuators A 60:80.

Vashist SK and Luong JHT (eds.) 2018. Handbook of Immunoassay Technologies, Academic Press, Elsevier. ISBN 978-0-12-811762-0.

Voiculescua I and Nordin AN (2012), Acoustic wave based MEMS devices for biosensing applications, Biosens. Bioelectron. 33: 1-9.

Wang J (2008). Electrochemical Glucose Biosensors, Chem. Rev. 108: 814-825.
Wang L, Acosta MA, Leach JB, Carrier RL (2013). Spatially monitoring oxygen level in 3D microfabricated cell culture systems using optical oxygen sensing beads. Lab Chip. 13(8):1586-92. doi: 10.1039/c3lc41366g.
Wang, S, Zhang, G, Chen, Q, Zhou J, Wu Z (2019). Sensing of cocaine using polarized optical microscopy by exploiting the conformational changes of an aptamer at the water/liquid crystal interface, Microchim Acta 186, 724. https://doi.org/10.1007/s00604-019-3855-1
Wang XD, Wolfbeis OS, Meier RJ (2013). Luminescent probes and sensors for temperature. Chemical Society Reviews. 42:7834-69. DOI: 10.1039/c3cs60102a
Wang XD and Wolfbeis OS (2014). Optical methods for sensing and imaging oxygen: materials, spectroscopies and applications, Chem. Soc. Rev. 43:3666–3761. doi:10.1039/C4CS00039K.
Wang XD and Wolfbeis OS (2016). Fiber-Optic Chemical Sensors and Biosensors (2013−2015), Anal. Chem. 88: 203−227. DOI: 10.1021/acs.analchem.5b0429
Wang XH, Peng HS, Yang W, Di Ren Z, Liu YA (2016). Mitochondria-targeted theranostic nanoparticles for optical sensing of oxygen, photodynamic cancer therapy, and assessment of therapeutic efficacy, Microchim. Acta. 183: 2723–2731. doi:10.1007/s00604-016-1917-1.
Warsinke A, Benkert A, Scheller FW (2000). Electrochemical immunoassays, Fresenius J Anal Chem. 366(6-7):622-634.
Weigl BH, Wolfbeis OS (1994). Capillary Optical Sensors, Anal. Chem. 66: 3323-3327.
Welch NG (2017). Orientation and characterization of immobilized antibodies for improved immunoassays (Review), Biointerphases 12(2): 02D301.
Wencel D, Abel T, McDonagh C (2014). Optical Chemical pH Sensors, Anal. Chem. 86: 15−29 dx.doi.org/10.1021/ac4035168
Wilson DF (2008). Quantifying the role of oxygen pressure in tissue function, Am. J. Physiol. Heart Circ. Physiol. 294: H11–H13. doi:10.1152/ajpheart.01293.2007.
Winterflood CM, Ruckstuhl T, Verdes D, Seeger S (2010). Nanometer Axial Resolution by Three-Dimensional Supercritical Angle Fluorescence Microscopy, Phys Rev Lett 105(10):108103. DOI: 10.1103/PhysRevLett.105.108103
Winterflood CM, Ruckstuhl T, Seeger S (2013). Fast and sensitive interferon-γ assay using supercritical angle fluorescence, Biosensors 3(1): 108–115.
Wu A H B (2006). A selected history and future of immunoassay development and applications in clinical chemistry, Clinica Chimica Acta 369:119-124.
Wu J and Gu (2011). Microfluidic sensing: state of the art fabrication and detection techniques J. Biomed. Opt. 16 080901–12
Wolfbeis OS (2013). Probes, Sensors, and Labels: Why is Real Progress Slow? Angew. Chem. Int. Ed. 52: 9864-9865.
Wolfbeis OS (2015). Luminescent sensing and imaging of oxygen: Fierce competition to the Clark electrode, BioEssays 37:921–928. doi:10.1002/bies.201500002.
World Drug Report (2018) (United Nations publication, Sales No. E.18.XI.9). ISBN: 978-92-1-148304-8
Yalow RS and Berson SA (1959). Assay of plasma insulin in human subjects by immunological methods, Nature 184: 1648-1649.

PUBLICATIONS

PUBLICATION I

A novel platform for highly surface-sensitive fluorescent measurements applying simultaneous total internal reflection excitation and super critical angle detection

Hannu Välimäki and Kirsi Tappura

Chemical Physics Letters 473 (2009) 358–362
https://doi.org/10.1016/j.cplett.2009.04.010

Chemical Physics Letters 473 (2009) 358–362

Contents lists available at ScienceDirect

Chemical Physics Letters

journal homepage: www.elsevier.com/locate/cplett

A novel platform for highly surface-sensitive fluorescent measurements applying simultaneous total internal reflection excitation and super critical angle detection

Hannu Välimäki *, Kirsi Tappura

VTT Technical Research Centre of Finland, Molecular Sensors, P.O. Box 1300, FI-33101 Tampere, Finland

ARTICLE INFO

Article history:
Received 28 January 2009
In final form 7 April 2009
Available online 9 April 2009

ABSTRACT

A highly surface-sensitive fluorescent measurement platform for chemical and biochemical analysis is presented. The core component of the platform is a polystyrene parabolic lens that is utilised in simultaneous total internal reflection excitation and super critical angle fluorescence detection. Both the theoretical calculations and the experimental results of the immunological model assays show that the system is extremely sensitive to the surface bound fluorescence. The binding of analytes at concentrations down to 5 pmol/l has been detected in real time while the unbound fluorescent labels in the sample liquid did not show any response until at three decades higher concentrations.

1. Introduction

In many biochemical/immunological assays target molecules bind to receptor molecules that are immobilized on a surface. The binding process can be monitored with many different acoustical, electromechanical, electrochemical or optical detection methods of which one of the most sensitive and widely used is fluorescence. In fluorescence-based monitoring the target molecules themselves are fluorescent or, more typically, the binding (or dissociation) of secondary fluorescent trace molecules is utilised in the detection of the target molecules.

When monitoring molecular binding processes by fluorescence methods the essential task is to exclude the background fluorescence stemming from the unbound fluorescent molecules in the sample liquid. Basically, there are two ways to accomplish this: evanescent field fluorescence excitation and surface-restricted fluorescence detection. Depending on the optical properties of the interface different techniques apply. The idea to illuminate a dielectric interface with an evanescent field was first described by Hirschfeld over four decades ago [1] and since then it has evolved to a widely used technique in different total internal reflection fluorescence (TIRF) sensors and microscopy (TIRFM) devices. It is also known that the evanescent field can be enhanced by surface plasmon resonance (SPR) excitation [2]. This requires a thin metallic film deposited on the dielectric and the illumination of the interface from the glass side at an incident angle close to the angle of SPR. The idea to modify the emission properties of fluorescent molecules with an adjacent dielectric interface also dates back many decades [3]. This discovery provided the basis for a surface-restricted fluorescence detection called the super critical angle fluorescence (SAF) [4,5], which has become an alternative approach to TIRF sensors and microscopy. But as SAF is applicable only to dielectric interfaces, a technique called surface plasmon coupled emission (SPCE) applying to interfaces with thin metallic films has lately been in a focus of an intense research [6,7]. Moreover, many fluorescent assays have been enhanced by tailored metallic nanostructures [8].

All these techniques have both their advantages and shortcomings, and there is an ongoing discussion about the optimum method for the most surface-sensitive fluorescence detection, see for example [9]. Moreover, one should bear in mind that the properties of the interface do not influence only the fluorescence characteristics, but also the immobilisation of the receptor molecules [10]. This in turn may have an impact on the density, activity and stability of the receptor molecules, which all contribute to the measured fluorescence signal intensity.

In this Letter, we report on a study where dielectric interfaces are exploited in fluorescence measurements. The starting point comes from the works of Enderlein et al. [4] and Ruckstuhl et al. [5], where the design of the parabolic lens for SAF detection was first presented. We have combined the total internal reflection (TIR) excitation technique with this parabolic set-up and made the two techniques work in tandem, which should further enhance the surface sensitivity of the fluorescence measurements. A similar approach combining the two techniques has been suggested in a patent [11] and applied to fluorescence microscopy [12,13]. In the latter study an attoliter detection volume and single molecule sensitivity was experimentally achieved. Our focus, however, was more in the field of biosensors and diagnostic devices, which made us choose polystyrene as the material for the parabolic lens. Even though the optical quality of polystyrene is inferior to that of optical glass or quartz, the higher refractive index of polystyrene gives yet an advantage. It increases the frac-

* Corresponding author. Fax: +358 20 722 3498.
E-mail address: hannu.valimaki@vtt.fi (H. Välimäki).

0009-2614/$ - see front matter © 2009 Elsevier B.V. All rights reserved.
doi:10.1016/j.cplett.2009.04.010

tion of the surface fluorescence that is emitted into the lens side and, even more importantly, it decreases the penetration depth of both TIR excitation and SAF detection into the sample compared to the case where the lens is made of a standard optical glass or quartz. With the polystyrene lens the system is also compatible with standard micro titer plates, which makes the sample handling convenient.

2. Theory

In TIR excitation the dielectric interface between the lens material (refractive index n_1) and the sample liquid (refractive index $n_2 < n_1$) is exploited. The beam of excitation is directed to the interface from the side of the higher refractive index at an angle above the critical angle $\alpha_c = arcsin(n_2/n_1)$. This results in an exponentially decaying evanescent field intensity $I = I_0\, exp(-z/d)$ into the sample volume. Here I_0 denotes the intensity at the interface and z the distance from the interface. The penetration depth d of the field depends on the incident angle according to equation [14]

$$d = (\lambda/4\pi)(n_1^2 \sin^2 \alpha_i - n_2^2)^{-1/2}, \quad (1)$$

where λ is the excitation wavelength in vacuum and α_i the incident angle. The technique enables one to selectively excite only the fluorescent labels that are clearly closer the surface than the excitation wavelength. In Fig. 1a the relative excitation intensities are calculated for different incident angle values. The figure shows that with the incident angle value of $\alpha_i = 67°$ and the refractive index values $n_1 = 1.59$ and $n_2 = 1.33$, more than 90% of the excitation field intensity is attenuated when the distance from the surface exceeds 30% of the excitation wavelength (650 nm).

The SAF detection is based on the fact that the fluorescent labels in the vicinity of a dielectric interface emit light into a highly uneven spatial distribution [4,5]. The main part of the emission is towards the medium of higher refractive index and the intensity maximum is found in the direction of the critical angle. The distribution of the emission depends on the refractive indices of the system and on the distance of the molecule from the interface. The closer the fluorescent molecule is to the interface, the higher the part of fluorescence emitted into the medium of higher refractive index. But more importantly, the part of emission that is directed into super critical angles (the angles above the critical angle) decays very rapidly as the distance of the emitting molecule from the surface is increased. Therefore, by restricting the detection into a range of the super critical angles the fluorescence reading can be restricted into the very vicinity of the surface. The depth of the SAF detection into the sample volume depends on the refractive indices of the system and on the range of the collected super critical angles, but roughly speaking it is of the order of the penetration depth of TIR excitation.

We followed the modelling presented by Enderlein et al. [4] and calculated the SAF emission intensities for a randomly oriented electric dipole located near the polystyrene-water interface. In Fig. 1b, the relative emission intensity is presented for a set of different detection angles as a function of the distance of the fluorescence label from the interface. Note that since the range of the detection angles influences not only the surface sensitivity but also the overall emission intensity, the different curves are not normalised. The figure shows some interesting features. First, one can leave out the very largest angels from the detection without any significant loss in the detected intensity. This fact is illustrated with the first (A) and second (B) simulated curves: cutting of the largest nine degrees out of the detection does not essentially change the behaviour of the system. Second, the third curve (C) shows that detecting any amount of emission below the critical angle, $\alpha_c \approx 56.8°$, is clearly unfavourable. The detected intensity is increased, but the surface sensitivity is degraded due to the significantly increased emission component stemming from the fluorescent molecules far away from the surface. Third, the fourth curve (D) shows that the surface sensitivity can be further improved by increasing the lower limit of the detected angles. Cutting off 1.3° just above the critical angle makes the detected intensity decay within a noticeably shorter distance. But this leads to a

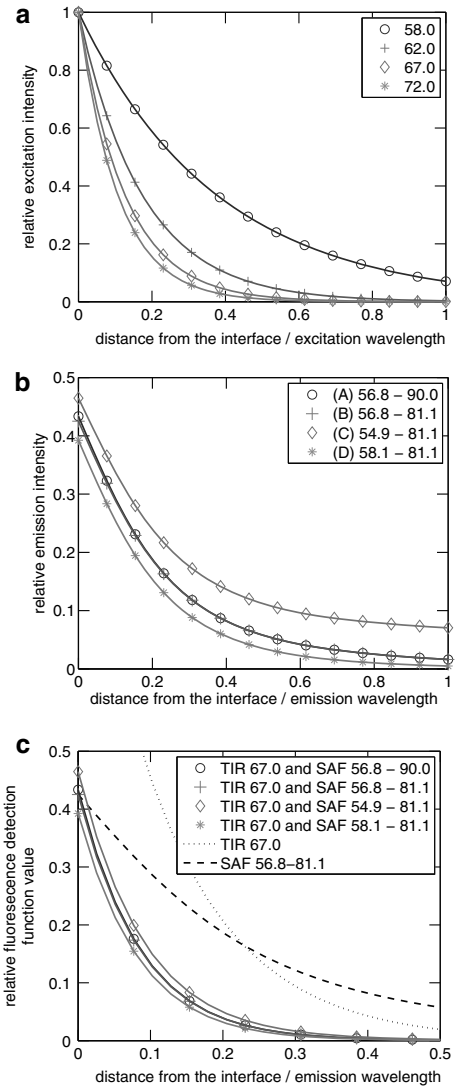

Fig. 1. (a) Relative TIR excitation intensities with different incident angle values, (b) relative SAF emission intensities with different detection angle values, and (c) the fluorescence detection function for simultaneous TIR excitation and SAF emission collection as a function of the distance of the fluorescent molecule from the surface. The refractive index values used in the calculations are $n_1 = 1.59$ (polystyrene) and $n_2 = 1.33$ (water), and the excitation and emission wavelengths 650 nm and 670 nm, respectively. The critical angle value is $\alpha_c = arcsin(n_2/n_1) \approx 56.8°$.

simultaneous decrease in the detected intensity and it is therefore not clear what is the optimum for the lower limit.

The surface sensitivity for simultaneous TIR excitation and SAF detection is illustrated in Fig. 1c, where the curves are calculated with the TIR excitation angle value of $\alpha_i = 67°$ and for the same set of the detection angles as in the previous figure. It is assumed that the emission wavelength (670 nm) is 3% greater than the excitation wavelength. The curves, referred to as fluorescence detection functions, are the products of the calculated emission intensities for the given detection angles and the calculated TIR excitation intensity distributions. One curve for a sole TIR excitation and sole SAF detection from the previous figures are shown for comparison. The figure shows that for all the sets of the detection angles the value of the detection function has dropped to values below 30% and 1% of the maximum when the distance from the surface exceeds 10% and 50% of the emission wavelength, respectively.

From the results of the calculations it can be concluded that if the surface sensitivity is the parameter to be maximised, then both the TIR excitation and SAF detection should be used simultaneously. This way the fluorescence measurements can be extremely effectively restricted to the very vicinity of the surface where the molecules of interest are bound.

3. Experimental

3.1. Instrumentation

The assembly of the polystyrene TIR-SAF-set-up is shown in Fig. 2a. A standard flat bottom polystyrene micro titter plate containing 96 sample wells (F96, 456537, type MaxiSorp from NUNC) is placed on the parabolic lens (manufactured by Jenoptik). The lens has a focal length of $f = 2.78$ mm and it is truncated so that the focal point of the lens is located exactly at the inner bottom surface of the sample well (1.00 mm above of the lens surface). The diameters of the narrow and the wide end of the lens are 13.00 and 24.90 mm, respectively. The optical contact between the plate and the lens is assured with immersion oil (Cargille Labs, custom made laser liquid type 5763 with refractive index $n = 1.59$).

The laser diode (650 nm, 0.8 mW, from Photonic Products) used for excitation is connected to an optical fibre (with 4 μm inner diameter) through a universal adaptor. The optical power of the laser is controlled with a WLD3393 Laser Diode Driver operating in a constant power mode. The fibre has a collimator at the output providing a collimated beam with the diameter of ~0.5 mm. The collimator is mounted to the system orthogonally with respect to the bottom surface of the parabolic lens. This arrangement takes advantage of the total internal reflection at the inner surface of the parabolic lens and results in an accurately adjusted excitation beam that hits to the centre of the inner surface of the sample well bottom. The incident angle of the excitation beam can be adjusted by adjusting the horizontal position of the collimator. If the surface sensitivity is to be maximised, then it is desirable to adjust the incident angle, α_i, to a value as large as possible, but at least to a value that is greater than the critical angle between water and polystyrene, i.e. $\alpha_i > \alpha_c = 56.8°$. For an excitation beam with an infinitely small diameter the geometry of the system would determine an upper limit of $\alpha_i = 81°$, but for the real beam with the diameter of 0.5 mm we had to accept the value $\alpha_i \approx 67°$ in order to avoid additional background signal stemming from the uncontrollable reflections at the edges of the lens. The direct reflection of the excitation beam is efficiently blocked by the mounting bar of the collimator.

The fluorescence emission is collected through the same polystyrene parabolic lens utilising again the total internal reflection taking place at the inner surface of the parabolic lens. At the wider end of the parabolic lens the reflected light is collimated. One can restrict the detection to an appropriate range of super critical angles by employing a cylindrical aperture blocker depicted in Fig. 2b. We decided to use a blocker with the open area diameters $d_1 = 13.0$ mm and $d_2 = 20.0$ mm, for the inner and outer dimensions, respectively. This corresponds approximately to a range of

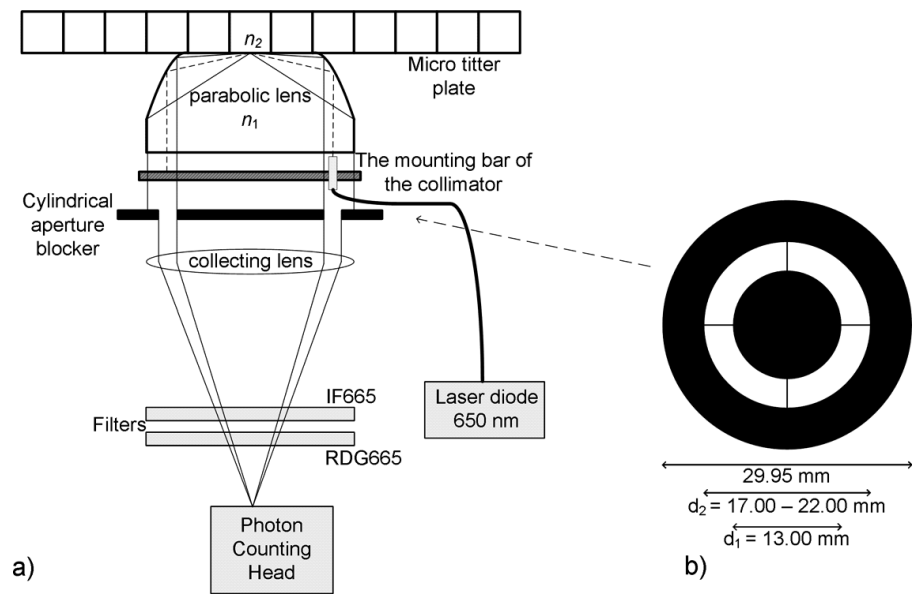

Fig. 2. (a) The assembly of the polystyrene fluorescent measurement platform utilising simultaneous TIR excitation and SAF detection. (b) The cylindrical aperture blocker used to select an appropriate range of super critical angels for surface generated fluorescence detection.

detection angles between 58.1° and 81.1°. The emission passing through the blocker is focused with a 80/21.4 mm plan-convex lens and filtered by two filters in cascade (IF665 from Edmund and RDG665 from Melles Griot). The filtered emission intensity is measured with a photon counting head, Hamamatsu 7421-40. The detection and excitation are controlled with a LabView program utilising a NI-USB-6251 hardware.

Because the system is designed to monitor molecular binding processes possibly taking hours to reach the equilibrium, it is desirable to use low excitation intensities and not to monitor the system unnecessarily often in order to avoid excessive photo bleaching. For this reason we adjusted the excitation intensity so that the pure PBS buffer containing no fluorescent molecules gave a response only 5–10 times higher than the dark counts of the photon counting head. Each individual measurement point corresponds to the number of photons counted during the single illumination time of 500 ms. The time interval T between individual measurements was set to $T = 60$ s for high concentrations (fast association processes) and $T = 180$ s for low concentrations (slow association processes).

3.2. Immobilisation

The micro titter wells were first coated with non-labelled anti-human IgG antibody Fab_2 fragments (Fc-specific) that were diluted in phosphate buffer PBS (15 mM, pH 7.4) to a concentration of 20 μg/ml. A volume of 100 μl was pipetted into each well and the plate was left in dark for incubation for 15 min at room temperature. Then the wells were emptied and 100 μl of 0.5% skimmed milk powder dissolved in PBS was pipetted in order to block the remaining free sites against non-specific binding. After the blocking (15 min in dark at room temperature) the wells were washed (5×200 μl) with the blocking solution containing 0.05% of Tween20.

The antibodies were from Jackson Immunoresearch. The labelling of the antibodies was carried out in our laboratory according to the instructions given in the Alexa-647 labelling kit.

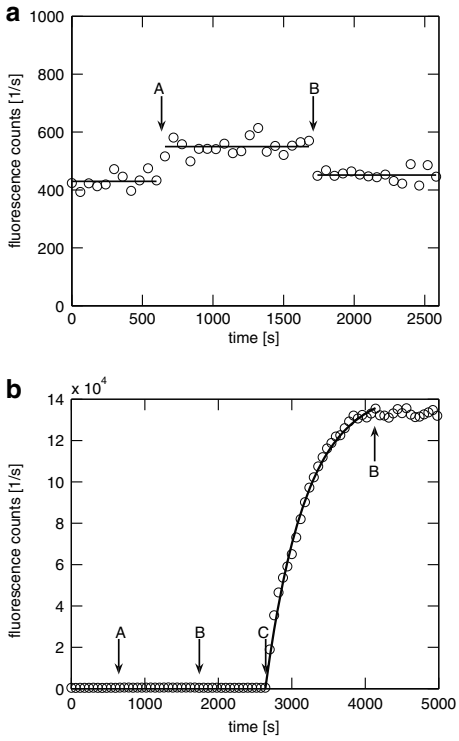

Fig. 3. The response of the system to (a) 20 nM of the non-specific analyte, (b) 20 nM of the specific analyte. The arrow A marks the time of the injection of the non-specific analyte; B the time of the rinsing with PBS-buffer; C the time of the injection of the specific analyte.

4. Results and discussion

To investigate the performance of the system based on the polystyrene parabolic lens and simultaneous TIR excitation and SAF detection, antibody–antigen binding was recorded in real time. For this purpose the wells of a micro titter plate were coated with non-labelled Fc-specific anti-human IgG antibody Fab_2 fragments as described above. Alexa 647 labelled Fab-specific anti-human IgG antibody Fab_2 fragments and Alexa 647 labelled whole human IgG molecules were used as the non-specific and the specific analytes (antigens) in the measurements, respectively.

4.1. Non-specific response

First the background fluorescence level of the system was recorded. When only PBS buffer was present in the well, the signal level was ~430 cts/s, as shown in Fig. 3a. Then at the time point $t = 600$ s, 40 μl of the non-specific analyte was pipetted into the well to a final concentration of 20 nM. As the figure shows, an instant shift in the signal to values around the level of 550 cts/s was recorded. The signal remained approximately constant at this level for about 17 min until the well was rinsed with the buffer at $t = 1680$ s. The rinsing immediately shifted the signal back close to the initial level. These shifts in the signal responses demonstrate two facts: (i) the blocking against the non-specific binding is efficient, since no creeping of the signal indicating an ongoing binding process can be seen; and (ii) the system is effectively able to restrict the fluorescence detection to the surface, since the relatively large free label concentration in the sample liquid caused only a just notable shift in signal level. Furthermore, the slight difference between the initial signal level and the level after the rinsing can be explained by a slight contamination of the surface.

4.2. Specific response

After rinsing the well with the buffer, 40 μl of the specific analyte were pipetted into to well to a final concentration of 20 nM at $t = 2640$ s, Fig. 3b. No constant shift was observed this time but the signal started to rise, presumably according to the kinetics of protein binding. About 25 min after the injection, the equilibrium level close to 1.4×10^5 cts/s was nearly reached and the surface was again rinsed with the buffer. The rinsing did not cause any significant change in the signal level. This suggests that the level of non-specific binding during the specific association process was low. This interpretation is further supported by the good fit (shown with the solid line in the figure) to the association model [15]

$$y = y_\infty(1 - e^{-kt})$$

with the parameter values $y_\infty = 1.45 \times 10^5$ cts/s; $k = 1.82 \times 10^{-3}$/s. The results indicate that the system is approximately 1200 times more sensitive to the specific analytes binding to the surface than to the unbound non-specific analytes in the sample liquid. This ratio between the signals stemming from the specific and non-specific analytes is over 20 times higher than what has been reported earlier

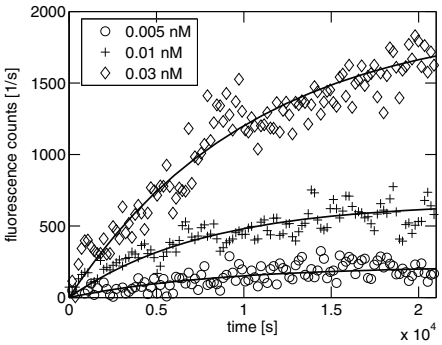

Fig. 4. The binding curves for three different specific analyte concentrations.

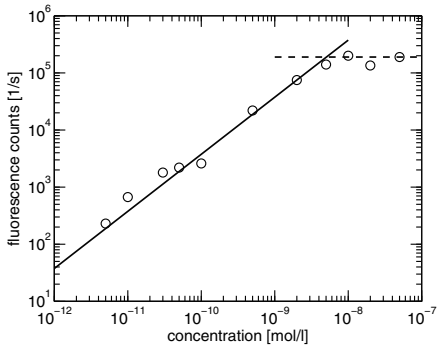

Fig. 5. The equilibrium fluorescence intensity levels (o) of the binding measurements plotted against the specific analyte concentrations. The solid line presents a linear fit and the dashed line the saturation level corresponding to the complete occupation of the binding sites on the surface.

for a same kind of parabolic lens utilised in SAF detection [5]. In that study, however, the excitation beam was directed perpendicularly to the interface, which can explain the difference in the results. While the perpendicular excitation may excite some labels throughout the sample liquid, the TIR-excitation restricts the excitation field to the vicinity of the interface and excites less likely any unbound labels.

To further investigate the sensitivity of the system, the binding kinetics of more diluted samples of the specific analyte was recorded. The time interval between individual measurements was now set to $T = 180$ s. In Fig. 4 the binding curves are presented for three different analyte concentrations. The initial background levels, measured when only buffer is present in the well, have been subtracted from the plots. The figure shows that the binding kinetics can be measured down to specific analyte concentrations below 5 pmol/l, which is close to the value of 2 pmol/l that was previously reached by Ruckstuhl et al. [5]. It is also noteworthy that the response to the specific analyte at 5 pmol/l is already higher than the response to the non-specific analyte at 4000 times higher concentration in the sample liquid (Figs. 3a and 4).

The final equilibrium levels of fluorescence intensity of different binding measurements (curves like the ones in Fig. 4) are plotted against the analyte concentration in Fig. 5. The figure shows a linear dependence in logarithmic scale between the low analyte concentration values and the corresponding final equilibrium levels. The linear range is approximately three decades, starting from 5 pmol/l and ending near 5 nmol/l. At higher analyte concentrations the saturation level ($\sim 1.7 \times 10^5$ cts/s) – corresponding to the complete occupation of the binding sites on the surface – is reached.

5. Conclusions

Extremely surface-sensitive fluorescence detection has been demonstrated by simultaneous TIR excitation and SAF emission collection. It has been shown that with a parabolic lens the set-up is realised conveniently. Polystyrene as the lens material provides additional benefits due to its higher refractive index compared to standard optical glass or quartz and to its compatibility with standard micro titter plates. With the presented platform the binding of analytes at concentrations down to 5×10^{-12} mol/l have been recorded in real time while the unbound non-specific analytes in the sample liquid did not show any response until at a three decades higher concentration.

Acknowledgements

We thank Prof. Jörg Enderlein for his helpful correspondence concerning the modelling of the SAF detection. We also thank our colleague Sanna Auer for the labelling of the antibodies and Dr. Inger Vikholm-Lundin for commenting on the manuscript. The Financial support by TEKES, the Finnish Funding Agency for Technology and Innovation, is gratefully acknowledged.

References

[1] T. Hirschfeld, Can. Spectrosc. 10 (1965) 128.
[2] T. Liebermann, W. Knoll, Colloids Surf. 171 (2000) 115.
[3] W. Lukosz, R.E. Kunz, J. Opt. Soc. Am. 67 (1977) 1607.
[4] J. Enderlein, T. Ruckstuhl, S. Seeger, Appl. Optics 38 (1999) 724.
[5] T. Ruckstuhl, M. Rankl, S. Seeger, Biosens. Bioelectron. 18 (2003) 1193.
[6] J.R. Lakowicz, Anal. Biochem. 324 (2004) 153.
[7] I. Gryczynski, J. Malicka, Z. Gryczynski, J.R. Lakowicz, Anal. Biochem. 324 (2004) 170.
[8] E. Fort, S. Grésillon, J. Phys. D: Appl. Phys. 41 (2008) 013001.
[9] J. Enderlein, T. Ruckstuhl, Opt. Exp. 13 (2005) 8855.
[10] I. Vikholm-Lundin, Langmuir 21 (2005) 6473.
[11] B. MacCraith, T. Ruckstuhl, US 20070262265A1.
[12] T. Ruckstuhl, S. Seeger, Appl. Optics 42 (2003) 3277.
[13] T. Ruckstuhl, S. Seeger, Optics Lett. 29 (2004) 569.
[14] M.V. Klein, T.E. Furtek, Optics, John Wiley & Sons, New York, 1986, 85.
[15] D.J. O'Shannessy, M. Brigham-Burke, K. Soneson, P. Hensley, I. Brooks, Anal. Biochem. 212 (1993) 457.

PUBLICATION II

Applying total tnternal teflection excitation and super critical angle fluorescence detection to a morphine assay

Hannu Välimäki, Timo Pulli and Kirsi Tappura

Journal of Fluorescence 20(2010) 1003–1008
doi: 10.1007/s10895-010-0647-8

J Fluoresc (2010) 20:1003–1008
DOI 10.1007/s10895-010-0647-8

ORIGINAL PAPER

Applying Total Internal Reflection Excitation and Super Critical Angle Fluorescence Detection to a Morphine Assay

Hannu S. Välimäki · Timo Pulli · Kirsi Tappura

Received: 8 September 2009 / Accepted: 23 March 2010 / Published online: 13 April 2010

Abstract A surface-sensitive fluorescence measurement platform is utilised in the detection of morphine. The platform is based on a polystyrene parabolic lens that enables the simultaneous application of total internal reflection excitation and supercritical angle fluorescence detection in the measurements. The molecular recognition of morphine is based on two antibodies, one against morphine and the other against the immune complex formed between the anti-morphine antibody and a morphine molecule. The antibodies are applied in a sandwich-like format in a one-step test, where the molecular binding onto a liquid-solid-interface is monitored in real time. Morphine concentrations between 0.6 and 18.2 ng/mL were reliably determined in 60 s, while concentrations down to 2.7 ng/mL were detected already in 20 s. With appropriate recognition molecules the technique is applicable also to other drugs and small analytes.

Keywords Fluoroimmunoassays · Total internal reflection fluorescence (TIRF) · Supercritical angle fluorescence (SAF) · Drug testing · Morphine

Introduction

Pharmaceuticals, drugs of abuse, steroids and toxins form a growing class of small analytes that need to be tested on different occasions by the authorities. For abused drugs, the available commercial diagnostic tests are typically lateral flow based competitive immunoassays. These tests, however, are usually relatively time-consuming to perform, their response-time can be several minutes, and due to their unspecific nature, they generate many false positive results [1]. Immunoassay tests for morphine and heroine, for example, typically cross-react with codeine that is a widely used substance in cough medicaments. Therefore, these tests are generally considered only as opiate-specific, and the positive test results must be confirmed using a more specific laboratory technique such as gas chromatography mass spectrometry.

In order to overcome the problem of the false positive test results and the long testing time, a one-step noncompetitive homogeneous immunoassay has been developed for small analytes using morphine as the model analyte [2]. The assay is based on a pair of engineered antibody Fab fragments, one against morphine (called M1) and the other against the immune complex (IC) formed between the anti-morphine antibody and a morphine molecule (called K11). In this assay, the presence of morphine molecules brings the two antibodies very close to each other. The antibodies are labelled with fluorophores forming a fluorescence resonance energy transfer (FRET) pair so that the close proximity of the antibodies leads to energy transfer from the donor to the acceptor fluorophore. The measured acceptor emission intensity corresponds to the morphine concentration. When tested with a commercial fluorometer, morphine concentrations down to 5 ng/mL were successfully detected within 2 min [2]. Compared to the recommend morphine cut-off concentrations of 40 ng/mL for drug testing [3], the achieved detection limit was very satisfactory.

Despite these achievements, there is still need for improvements, especially related to the speed of the test.

H. S. Välimäki (✉) · K. Tappura
VTT Technical Research Centre of Finland,
P.O.Box 1300, FI-33101 Tampere, Finland
e-mail: hannu.valimaki@vtt.fi

T. Pulli
VTT Technical Research Centre of Finland,
P.O.Box 1000, FI-02044 Espoo, Finland

In laboratory analysis or in the area of point-of-care diagnostics, the test duration of 2 min may be acceptable, but, for example, for a test to be used in the field, a testing time of 2 min is usually too long. An obvious way to further improve the assay speed and sensitivity is to further optimise the antibodies, the labelling ratio, the overall assay conditions as well as the signal to noise ratio in the fluorescence measurement. However, the optimisation of these parameters can improve the assay only to a certain degree. In order to take a more fundamental development step, a new scheme for the assay is proposed in this paper.

We have recently developed a novel fluorescence measurement platform based on a polystyrene parabolic lens [4]. This platform has its starting point in the works of Ruckstuhl et al. [5] and Enderlein at al. [6] and it utilises simultaneously both total internal reflection (TIR) excitation and supercritical angle fluorescence (SAF) detection principles, which makes the platform extremely sensitive to surface-bound fluorescence. The surface-sensitivity in the fluorescence detection provides means to transfer the morphine immunoassay from the pure liquid format into a sandwich-like format exploiting the binding processes occurring on a solid-liquid interface, but in such a way that it still remains essentially as a one-step assay. This new scheme is presented in Fig. 1, where the non-labelled anti-morphine antibody Fab fragments (M1) are immobilised onto a surface and the free sites are blocked against the non-specific binding before the labelled anti-IC antibody Fab fragments (K11) are set free in the sample liquid. The test is initiated by injecting the sample. If it contains morphine, the injection elicits the binding of the labelled K11 antibodies onto the surface. As it is schematically illustrated in the figure, the fluorescent detection can be restricted to the very vicinity of the surface so that no FRET interaction is needed to detect the mutual proximity of the antibodies. The morphine concentration is determined simply by monitoring the surface-bound fluorescence in real time.

The surface-bound assay scheme, where the extremely surface sensitive fluorescence monitoring is substituted for the FRET-interaction, results in some significant advantages. While FRET is a sophisticated method to study molecular interactions, it, as a coupling mechanism, inevitably creates losses, and thus, results in the attenuation of the detected signal. The efficiency of the energy transfer depends strongly ($1/r^6$) on the mutual distance of the fluorophores (r) that should generally not exceed 70 Å [7]. With two antibody Fab fragments we are close to this limit. Also the relative emission and absorption dipole orientations, which are typically out of control, influence the efficiency.

The other advantage of the surface-bound assay is the increased overall fluorescence detection efficiency. First, the molecules of interest are not distributed uniformly throughout the whole liquid volume, but are, due to the binding, concentrating at the interface where the detection is focused. Second, while the unbound fluorescent molecules in free space have an isotropic emission distribution, this is not the case when they are bound to a dielectric interface. The emission of the molecules located close to a dielectric interface is strongly directed towards the half-space of the higher refractive index, so that the usage of the SAF detection principle leads to significantly enhanced emission collection. Third, the evanescent field excitation leads to a decreased generation of background fluorescence in the sample liquid, which typically is one of the most limiting parameters in fluorescent assays. These facts, together with the absence of FRET and its demand for two different labels, are strong motives for transferring to the surface-bound assay scheme. In this paper, we report the first experimental results obtained in morphine detection.

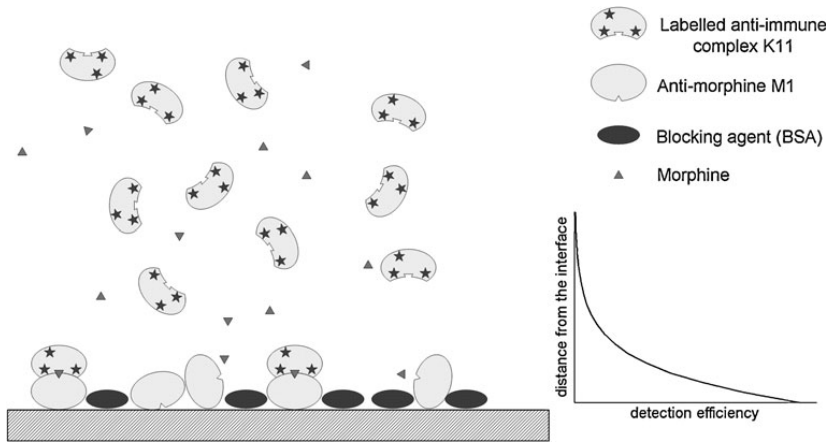

Fig. 1 The scheme of the surface-bound morphine immunoassay

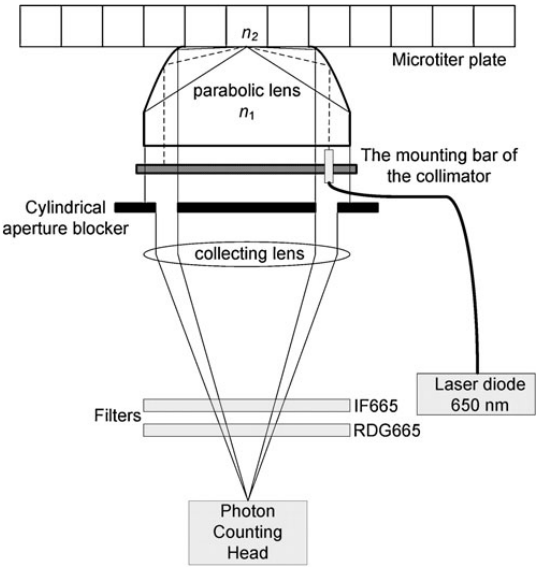

Fig. 2 The fluorescent measurement platform applying simultaneous total internal reflection (TIR) excitation and supercritical angle fluorescence (SAF) detection

Experimental

Antibodies

The antibody Fab fragments M1 and K11 were produced according to the methods described by Pulli et al. [2]. The antibody Fab fragments K11 were labelled with Alexa 647 fluorescence labels at our laboratory according to the instructions of the labelling kit.

Immobilisation

The microtiter wells were first coated with non-labelled anti-morphine antibody Fab fragments M1 that were diluted in phosphate buffer PBS (15 mM, pH 7.4) to a concentration of 10 μg/mL. A volume of 100 μl was pipetted into each well and the plate was left in dark for incubation for 90 min at room temperature. Then the wells were emptied and 100 μl of 0.5% skimmed milk powder dissolved in PBS was pipetted in order to block the remaining free sites against non-specific binding. After the blocking (90 min in dark at room temperature) the wells were washed (5×200 μL) with the blocking solution containing additional 0.05% of Tween20.

Fluorescence measurements

The fluorescence measurements were carried out with the system depicted in Fig. 2. A flat-bottom microtiter plate (F96, 456537, type MaxiSorp from NUNC) is placed on a polystyrene parabolic lens that is utilised in simultaneous TIR excitation and SAF detection. The set-up restricts the fluorescence read-out to the very vicinity (< 100 nm) of the surface so that the binding of the labelled antibodies onto the surface can be monitored in real time. The technical details and the system characteristics are described elsewhere [4]. In the present study, each individual measurement point corresponds to the number of photons counted during the single illumination time of 200 ms. The time interval T between individual measurements was set to T=10 s.

The injection procedure for morphine detection was as follows: First, the microtiter wells, coated with non-labelled M1 antibody fragments and the blocking agents as described above, were filled with 50 μL of PBS buffer. Then the fluorescence recording was started, and Alexa-647

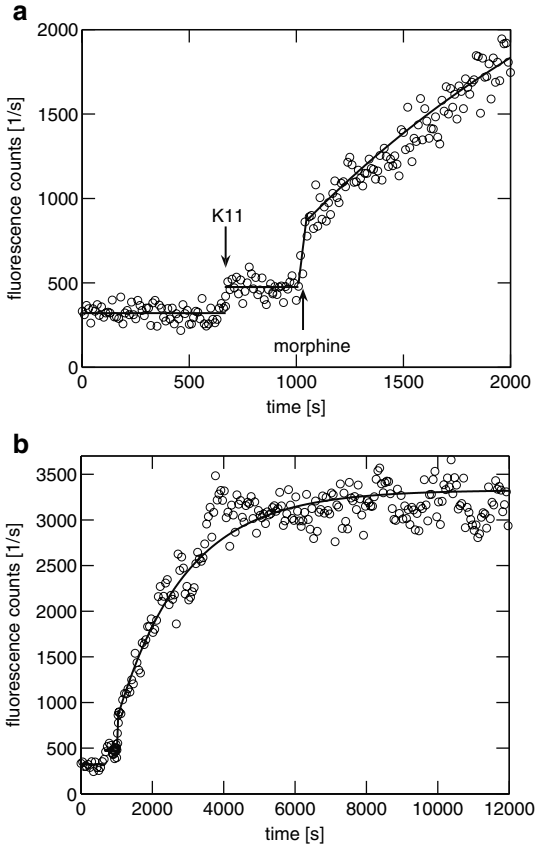

Fig. 3 (**a**) The first stages in morphine induced binding process: the injection of the Alexa-647 labelled K11 anti-IC antibodies into the final concentration of 5.0 μg/mL in 100 μL PBS, and the injection of morphine sample into the final concentration of 5.8 ng/mL in PBS. (**b**) The binding curve in its entire length. For the sake of clarity, only every fifth measurement point is shown. The *open circles* (o) represent the actual measurement points, the *solid lines* (-) the fits

labelled K11 antibody fragments, diluted in 50 μL of PBS, were injected into the well to the final concentration of 5 μg/mL. Finally, the morphine sample (10 μL in PBS) was injected into the well to obtain the desired final morphine concentration.

Results and discussion

A typical morphine measurement is shown in Fig. 3a and b, where the former figure presents the early phase of the measurement and the latter the entire recording. When only PBS buffer is present in the well (coated with M1 antibody fragments, as described above), the measured fluorescence intensity is shown to fluctuate around the value of 320 cst/s (Fig. 3a). Then at the timepoint t=670 s, Alexa-647 labelled K11 antibody fragments, diluted in 50 μL of PBS, are injected into the well to the final concentration of 5 μg/mL. This immediately shifts the measured intensity close to the level of 475 cts/s. It is noteworthy that the signal remains constant after the instant shift. This means that the blocking against non-specific binding is efficient, and that the shift corresponds only to the increased amount of the background signal stemming from the injected fluorescent labels in the sample liquid. Then at t=1,010 s, the morphine sample (volume 10 μL, concentration 64 ng/mL in PBS), is injected into the well leading to the final morphine concentration of 5.8 ng/mL. After the injection the signal starts to rise as the morphine molecules now bind to the M1 antibodies on the surface forming immune complexes that are capable to bind with the labelled K11 antibodies present in the sample liquid.

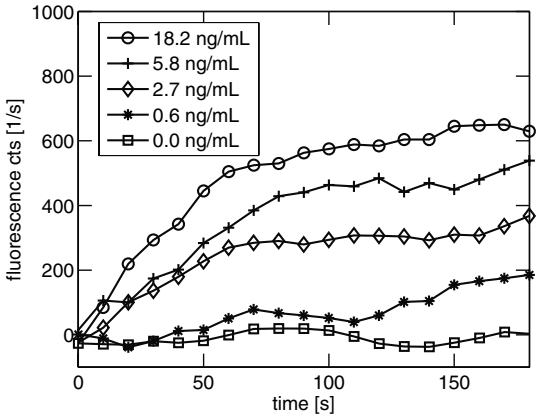

Fig. 5 A close-up of the responses of the Fig. 4 during the first 3 min of the measurements. The data is smoothed with a five-point moving average (backward)

The binding process of the K11 antibodies shows some peculiarities. First there is a brief phase (lasting 40–60 s) of rapid binding, and then a long phase (2–3 h) exhibiting a slower binding process. As a small molecule, morphine can quickly diffuse through the sample liquid, bind to M1 antibodies available at a high concentration in the early phase of the measurement, and thus very rapidly increase the amount of the available binding sites for the K11 antibodies, which, at the very beginning, are also available at a high concentration. These facts presumably induce the sharp initial rise in the response curve (marked as a straight,

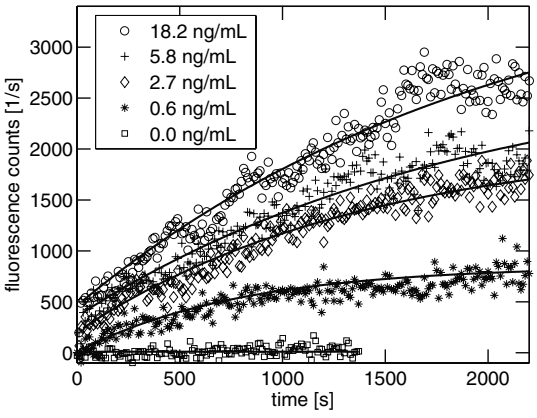

Fig. 4 The response of the system to different concentrations of morphine. The *markers* (o, +, ◦, *, ·) present the actual measurement points, and the *solid curves* (-) the fits. The background levels are subtracted from the data

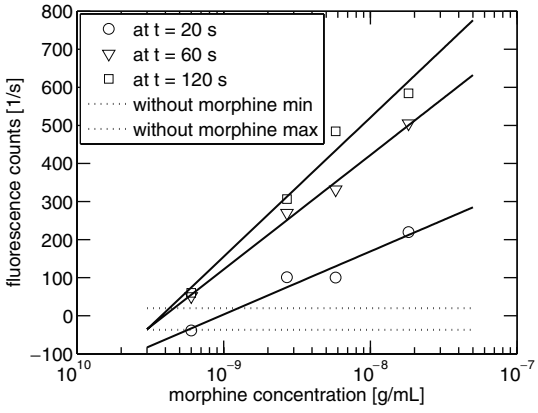

Fig. 6 The system response to different morphine concentrations at three timepoints after the morphine injection. The open markers denote the actual measurements, the *solid lines* (-) the fitted straight lines and the dashed lines the range of variation of the responses without morphine

almost vertical, solid line in the Fig. 3a). When the concentration of free morphine, as well as the concentration of the free morphine binding sites has decreased (and the number of the binding sites for K11 antibodies has started to saturate), and when the K11 antibodies closest to the surface are consumed, the binding rate of antibody K11 begins to slow down and show more a typical one-to-one binding kinetics. This assumption is supported by the good fit (shown as the solid line in Fig. 3b) of the one-to-one association model [8]

$$y = y_\infty\left(1 - e^{-kt}\right) \quad (1)$$

to the data starting at 40 s after the morphine injection. The best-fit parameter values are y_∞=2,456 cts/s and k=5.235×10^{-4} /s.

The response of the system to different concentrations of morphine is shown in Fig. 4. The background fluorescence level, measured after the injection of the K11 antibodies but before the injection of morphine, is subtracted from these curves. Together with the actual data points, also the best-fit curves of Eq. 1 are shown. The figure shows that both the initial rising velocity and the final equilibrium level depend logically on the morphine concentration, that is, the higher the morphine concentration, the higher are the rising velocity and the final equilibrium level.

Fig. 5 presents a close-up of the first 3 min of the response curves of Fig. 4, smoothed with a five-point moving average to the backward direction. The figure shows that the response curves differ logically from each other already in the very beginning of the measurements. To examine the early responses in more detail, the response values at three different time points, t=20 s; t=60 s; and t=120 s, extracted from Fig. 5, are plotted against the morphine concentration in Fig. 6. The actual data is presented with open markers and the fitted straight lines are plotted as solid lines. At all the time points, the dependence between the morphine concentration and the fluorescence intensity value is shown to be linear in the semilogarithmic scale, and the slope of the fit increases along with the time point value. The range of variation of the responses without morphine (describing the fluorescent background level) is shown for comparison with the dotted lines. The lowest measured concentration of 0.6 ng/mL gives a negative response at t=20 s that can not be distinguished from the background, but at the later time points all responses are strictly positive and differ clearly from the background. From these results it can be deduced that morphine concentrations at least down to 2.7 ng/mL can be detected already in 20 s, and that all the morphine concentrations studied (from 0.6 to 18.2 ng/mL) can reliably be predicted within 60 s.

Compared to the FRET-based assay reported earlier [2], we have now shown that the testing time can be reduced from 120 s to 20 s by transferring the molecular recognition from the sample liquid onto a liquid-solid interface and by applying both TIR excitation and SAF emission collection in the detection. In addition, more than eight times smaller morphine concentrations were reliably determined in 60 s with the new set-up. Furthermore, it should be noted that the concentrations of the K11 anti-IC antibodies were relatively small in the experiments presented above. With higher K11 concentrations also higher sensitivities are expected. Another way to obtain further enhancement in the response curves is to use site-directed immobilisation of M1 antibodies onto the surface with hydrophilic polymers with very low non-specific binding in between [9].

Conclusions

A very rapid and sensitive detection of morphine was realised with the surface-bound fluorescence immunoassay utilising simultaneous TIR excitation and SAF detection. The morphine concentrations between 0.6 and 18.2 ng/mL were reliably determined in 60 s, while the concentrations down to 2.7 ng/mL were shown to be detected already in 20 s. With appropriate recognition molecules the technique is applicable also to other drugs and small analytes.

Acknowledgements We thank Armi Boman for skilful technical assistance, Dr. Tarja Nevanen for commenting on the manuscript, and TEKES, the Finnish Funding Agency for Technology and Innovation, for financial support (40240/07).

References

1. Kerrigan S, Phillips WH (2001) Comparison of ELISAs for drugs-of-abuse testing. Jn Clin Chem 47:540–547
2. Pulli T, Höyhtyä M, Söderlund H, Takkinen K (2005) One-step homogeneous immunoassay for small analytes. Anal Chem 77:2637–2642
3. Dams R, Choo RE, Lambert WE, Jones H, Huestis MA (2007) Oral fluid as an alternative matrix to monitor opiate and cocaine use in substance-abuse treatment patients. Drug Alcohol Depend 87:258–267
4. Välimäki H, Tappura K (2009) A novel platform for highly surface-sensitive fluorescent measurements applying simultaneous total internal reflection excitation and super critical angle detection. Chem Phys Lett 473:358–362
5. Ruckstuhl T, Rankl M, Seeger S (2003) Highly sensitive biosensing using a supercritical angle fluorescence (SAF) instrument. Biosens Bioelectron 18:1193–1199
6. Enderlein J, Ruckstuhl T, Seeger S (1999) Highly efficient optical detection of surface-generated fluorescence. Appl Opt 38:724–732

7. Lakowicz JR (1999) Principles of fluorescence spectroscopy, 2nd edn. Kluwer Academic/Plenum Publishers, New York
8. O'Shannessy DJ, Brigham-Burke M, Soneson K, Hensley P, Brooks I (1993) Determination of rate equilibrium binding constants for macromolecular interactions using surface plasmon resonance: use of nonlinear least squares analysis Methods. Biochem Anal 212:457–468
9. Vikholm-Lundin I (2005) Immunosensing based on site-directed immobilization of antibody fragments and polymers that reduce nonspecific binding. Langmuir 21:6473–6477

PUBLICATION III

Applying a surface-sensitive fluorescence method to fast on-site detection of cocaine in saliva

Hannu Välimäki, Sanna Auer, Ann-Charlotte Hellgren and Kirsi Tappura

Procedia Engineering 25 (2011) 968 – 971
doi:10.1016/j.proeng.2011.12.238

Available online at www.sciencedirect.com

SciVerse ScienceDirect

Procedia Engineering 25 (2011) 968 – 971

Procedia Engineering

www.elsevier.com/locate/procedia

Proc. Eurosensors XXV, September 4-7, 2011, Athens, Greece

Applying a surface-sensitive fluorescence method to fast on-site detection of cocaine in saliva

Hannu Välimäki[a*], Sanna Auer[a], Ann-Charlotte Hellgren[b], Kirsi Tappura[a]

[a]*Molecular Sensors, VTT Technical Research Centre of Finland, Tampere, Finland*
[b]*Research and Development, Biosensors Applications AB, Solna, Sweden*

Abstract

Fast and sensitive detection of cocaine in saliva is realized utilizing a surface-sensitive fluorescence measurement platform. The platform is based on a polystyrene parabolic lens that enables the simultaneous application of total internal reflection excitation (TIR) and supercritical angle fluorescence detection (SAF), which results in extreme surface sensitivity in the measurements. The molecular recognition takes place in a scheme, where cocaine molecules to be detected generate a displacement of the labelled anti-cocaine antibodies from the cocaine-BSA-conjugate molecules immobilized on a surface. The results with untreated saliva spiked with cocaine demonstrate that by monitoring the dissociation process in real time, cocaine concentrations down to 1 ng/mL can be detected within 60 s.

Keywords: Surface sensitive fluorescence; TIR; SAF; on-site detection; drugs; cocaine; oral fluids; saliva; antibody displacement.

1. Introduction

Pharmaceuticals, drugs of abuse, steroids and toxins belong to a growing class of small analytes that need to be tested on different occasions by the authorities. For many drugs of abuse, oral fluids are very suitable test matrices [1], but the available commercial tests typically take several minutes to perform, which hinders their use in on-site screening [2].

In this paper, we present a potential test concept based on a recently developed fluorescence measurement platform [3, 4] and antibody displacement immunoassay. The platform has its starting point in the works of Ruckstuhl et al. [5] and Enderlein at al. [6] and it utilises simultaneously both total

* Corresponding autohor. Tel.: +358 20 722 3369 ; fax: +358 20 722 4398
Email address: hannu.valimaki@vtt.fi

1877-7058 © 2011 Published by Elsevier Ltd. Open access under CC BY-NC-ND license.
doi:10.1016/j.proeng.2011.12.238

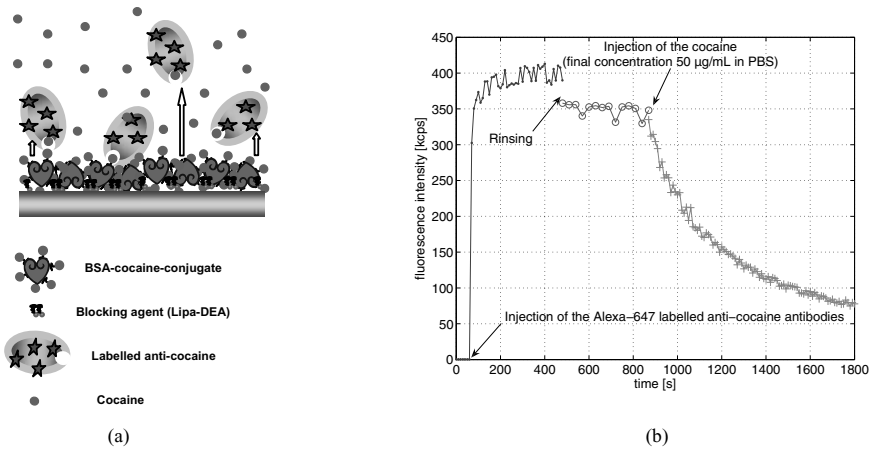

(a) (b)

Fig. 1. (a) The principle of the cocaine-induced displacement of antibodies; (b) Fluorescence intensity recordings during the final phase of surface functionalisation, and the effect of the injection of cocaine (in PBS buffer).

internal reflection (TIR) excitation and super critical angle fluorescence (SAF) detection principles, which makes the platform extremely sensitive to surface-bound fluorescence. This provides means to monitor the displacement of the antibodies from the functionalized surface with a high sensitivity in real time.

2. Materials and methods

For the detection of cocaine the scheme shown in Fig. 1a was applied. The surface was first functionalized with the BSA-cocaine-conjugate and diaminomethanol derivative of lipoic acid (Lipa-DEA) serving as a blocking agent [7]. Then the labelled anti-cocaine antibody was allowed to bind to the conjugate molecules. After rinsing, the test is initiated by injecting the saliva sample. The cocaine molecules in the sample generate a displacement of antibodies from the surface, which can be observed as instant fluorescence attenuation.

Anti-cocaine antibodies and BSA-conjugated cocaine were obtained from Biosensors Applications AB. The anti-cocaine antibodies were labelled with Alexa 647 fluorescence labels (from Molecular probes) at our laboratory according to the instructions of the labelling kit.

The flat bottom microtiter wells (F96, 456537, type MaxiSorp) were purchased from NUNC. The BSA-cocaine conjugate and Lipa-DEA were diluted in PBS buffer (15 mM, PH 7.4) to concentrations of 50 µg/mL and 200 µg/mL, respectively. A volume of 50 µL was added into each well and the plate was left in dark for 15 minutes at room temperature. The wells were rinsed with PBS (5 x 200 µL), and then the anti-cocaine antibodies diluted in PBS (50 µg/mL; 50 µL/well) were left to bind in dark for 15 minutes at room temperature. After the washing step (2 x 200 µL PBS; 2 x 200 µL PBS + 0.01% Tween 20; 1 x 200 µL PBS), 50 µL of saliva was added into each well. All saliva needed in the experiments was collected during the immobilization phase and used as such without any pre-treatment. The saliva content of the final samples was over 99.5%.

The fluorescence measurements were carried out with the platform described in details elsewhere [3]. The fluorescence intensity of the functionalized surface was recorded six times a minute by counting the photons during the illumination time of 500 ms. Before the injection of the cocaine sample (diluted in 50 µL of saliva) the baseline level was recorded for 60 s.

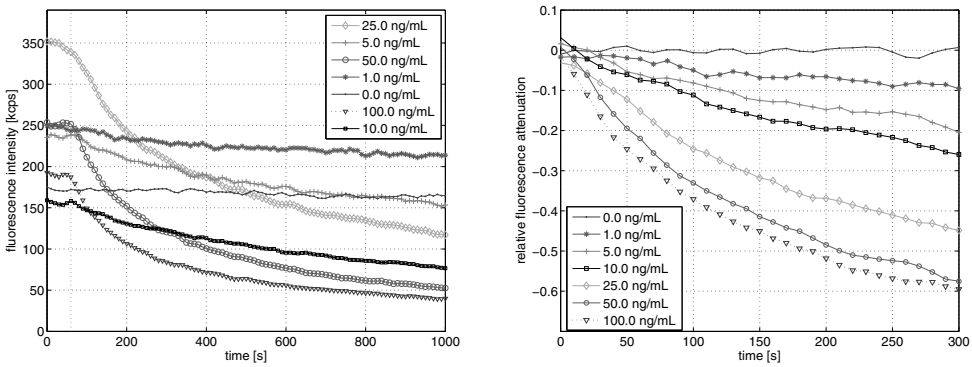

(a) b)

Fig. 2. (a) The fluorescence intensity recordings with different cocaine concentrations in untreated saliva; (b) The first 300 seconds of the data scaled with the baseline values and smoothed with a three point moving average.

To further illustrate the applied method, Fig. 1b shows the monitored fluorescence intensity during the final phase of the surface functionalisation and the effect of the injection of cocaine. When only PBS buffer is present in the well (coated with the BSA-conjugated cocaine and Lipa-DEA), the measured fluorescence intensity is about 0.35 kcps (kilo counts per second). Then Alexa-647 labelled anti-cocaine antibodies, diluted in 50 µL of PBS, are injected into the well to the final concentration of 50 µg/mL. The injection leads to rapidly increasing fluorescence intensity as the antibodies bind to the conjugate molecules at the surface. The binding process stabilizes in about eight minutes, and the well is then rinsed. After the rinsing the fluorescence signal has shifted from the level of 400 kcps to the level of 350 kcps/s, which suggest that about 15% of the antibodies were only loosely attached to the surface. During the next six minutes the signal remains stable. Then cocaine diluted in 50 µL of PBS is injected into the well (final concentration of 50 ng/mL). This leads to a rapidly decreasing signal as the anti-cocaine antibodies are now displaced from the surface. After 15 minutes the signal level has dropped below 80 kcps/s, which suggests that almost 80% of the antibodies have been displaced.

3. Results and discussion

Fluorescence intensity recordings with different cocaine concentrations in saliva are shown in Fig. 2a. The response before the sample injection at the time point t = 60 s serves as the baseline, which without exception is shown to be stable. After the sample injection the displacement of the antibodies is evident with all samples having cocaine, whereas no displacement can be seen with the control sample (no cocaine). It is noteworthy that the relative responses in saliva (Fig. 2a) and in PBS (Fig. 1b) are very similar. The cocaine concentration of 50 ng/mL causes a drop of 80% in fluorescence intensity in about 15 minutes both in saliva and PBS.

In Fig. 2b the relative changes during the first 300 s after the injection of the sample with respect to the baseline values are shown. The data is smoothed with a three-point moving average calculated backwards. The figure clearly illustrates that the relative changes are proportional to the cocaine concentrations, and that the concentration range of 1 – 100 ng/mL in saliva can be detected within tens of seconds.

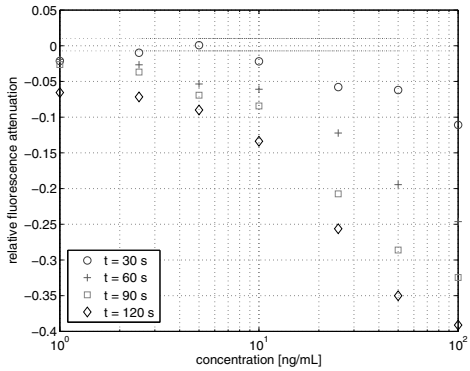

Fig. 3. The relative fluorescence attenuation at four different time points plotted against the cocaine concentration in saliva samples.

This fact is further illustrated in the Fig. 3, where the data points corresponding to the time points 30, 60, 90 and 120 seconds after the sample injection are plotted against the cocaine concentration. From this figure it can be deducted that cocaine concentrations down to 10 ng/mL or 1 ng/mL in untreated saliva can be detected in 60 s or 30 s, respectively. The current recommended oral fluid cut-offs for cocaine screening and confirmation varies between 8 and 20 ng/mL [1], so both in terms of sensitivity and speed the results are very satisfactory.

4. Conclusions

A very rapid and sensitive detection of cocaine in untreated saliva was realised utilising a surface-sensitive fluorescence measurement platform together with a displacement immunoassay. The cocaine concentrations down to 1 ng/mL were reliably determined in 60 s, while the concentrations down to 10 ng/mL were shown to be detected already in 30 s. The results suggests that a device based on the surface-sensitive fluorescence reading, realised in optical plastic like polystyrene, has a high potential for initial immunoassay screening of small molecules like drugs of abuse in untreated saliva at the site of collection. Also other demanding sample matrices like serum and whole blood may be applicable with the method.

References

[1] Bosker W, Huestis M. Oral fluid testing for drugs of abuse. *Clinical Chemistry* 2009;**55**:11 1910-3.
[2] Blencowe T, Pehrsson A, Lillsunde P(ed.).Analytical evaluation of oral fluid screening devices and preceding selection procedures. Driving under the Influence of Drugs, Alcohol and Medicines TREN-05-FP6TR-S07.61320-518404-DRUID 2010; D 3.2.2.
[3] Välimäki H, Tappura K. A novel platform for highly surface-sensitive fluorescent measurements applying simultaneous total internal reflection excitation and super critical angle detection. *Chemical Physics Letters* 2009;**473**:358-62.
[4] Välimäki H, Pulli T, Tappura K. Applying total internal reflection excitation and super critical angle fluorescence detection to a morphine assay. *Journal of Fluorescence* 2010; **20**:5 1003 – 8.
[5] Ruckstuhl T,Rankl M, Seeger S. Highly sensitive biosensing using a Supercritical Angle Fluorescence (SAF) instrument. *Biosensor s& Bioelectronics* 2003; **18**:1193-9.
[6] Enderlein J, Ruckstuhl T, Seeger S. Highly Efficient Optical Detection of Surface-Generated Fluorescence. *Applied Optics* 1999;**38:**724-32.
[7] Tappura K, Vikholm-Lundin I, Albers M. Lipoate-based imprinted self-assembled molecular thin films for biosensor applications. *Biosensors& Bioelectronics* 2007; **22**:912-9.

PUBLICATION IV

Fluorimetric oxygen sensor with an efficient optical read-out for *in vitro* cell models

Hannu Välimäki, Jarmo Verho, Joose Kreutzer, Dhanesh Kattipparambil Rajan, Tomi Ryynänen, Mari Pekkanen-Mattila, Antti Ahola, Kirsi Tappura, Pasi Kallio and Jukka Lekkala

Sensors and Actuators B 249 (2017) 738–746
http://dx.doi.org/10.1016/j.snb.2017.04.182

Sensors and Actuators B 249 (2017) 738–746

Contents lists available at ScienceDirect

Sensors and Actuators B: Chemical

journal homepage: www.elsevier.com/locate/snb

Fluorimetric oxygen sensor with an efficient optical read-out for *in vitro* cell models

Hannu Välimäki[a,*], Jarmo Verho[a], Joose Kreutzer[a], Dhanesh Kattipparambil Rajan[a], Tomi Ryynänen[a], Mari Pekkanen-Mattila[b], Antti Ahola[a], Kirsi Tappura[c], Pasi Kallio[a], Jukka Lekkala[a]

[a] *BioMediTech Institute and Faculty of Biomedical Sciences and Engineering, Tampere University of Technology, Korkeakoulunkatu 3, FI-33720 Tampere, Finland*
[b] *BioMediTech, Faculty of Medicine and Life Sciences, University of Tampere, FI-33014, Tampere, Finland*
[c] *VTT Technical Research Centre of Finland Ltd, Tekniikankatu 1, FI-33720 Tampere, Finland*

ARTICLE INFO

Article history:
Received 15 January 2017
Received in revised form 26 April 2017
Accepted 27 April 2017
Available online 28 April 2017

Keywords:
Fluorimetric oxygen sensor
Thin film fluorescence
Enhanced optical read-out
in vitro cell models
PtOEPK
Cardiac cells

ABSTRACT

This paper presents a phase fluorimetric sensor for the monitoring of the oxygen concentration in *in vitro* cell models. The sensing surface of the sensor consists of oxygen sensitive fluorescent dyes (platinum(II) octaethylporphyrinketone) embedded in a thin polystyrene film. In order to optimize the optical read-out scheme of the sensor, we carried out electromagnetic simulations of a fluorescently doped polystyrene film deposited on a glass-water interface. The simulation results showed highly anisotropic angular emission distribution with the maximum irradiance being at super critical angles, which attracts tailored optical designs to maximize the fluorescence collection efficiency. For this purpose, we applied an efficient optical read-out scheme based on an in-contact parabolic lens. The use of parabolic lens also facilitates confocal total internal reflection excitation from the substrate side. This makes the excitation effective and insensitive to biofouling or other optical changes in the sensing surface and, more importantly, greatly reduces the amount of excitation power radiated into the cell culture chamber. Experimental results show that when applied together with phase fluorimetric lifetime sensing, this optical scheme allows one to use thin films (<500 nm), dilute dye-polymer ratios (0.025%), low power LED excitation (<2 mW), and yet achieve over 40 dB signal-to-noise ratio at 10 Hz data rate at physiologically relevant oxygen concentrations. These features are important in cell studies, as the potential cytotoxicity of the dyes and the sensing method (i.e. the production of singlet oxygen) are mitigated by the low dye content and excitation power. In addition, thin and dilute polystyrene films are highly transparent and facilitate optical microscopy. We conclude the study by presenting experimental results where the device is applied together with on-line microscopy to an oxygen tension stress study of beating cardiomyocyte cultures.

1. Introduction

As the cellular oxygen level in mammalian tissues is highly regulated [1], a careful control of the oxygen tension is very important also in *in vitro* cell culturing and disease models. Ideally, when studying any cell model, one should be able to both maintain a stable oxygen tension, similar to the one in the corresponding tissue *in vivo,* and, if desired, generate timely changes in order to study the model responses.

The regulation of oxygen levels requires a reliable monitoring system, and especially in microfluidic cell cultures, this is a challenging task. Leaving out all the laboratory methods based on sampling (such as Winkler titration), or sophisticated, expensive and bulky instruments (such as functional Magnetic Resonance Imaging), one is left to make a choice between Clark-type O_2electrodes, and optical methods based on oxygen-dependent quenching of photoluminescence [2]. Clark-type O_2electrodes have been applied in microfluidic devices [3], but they consume oxygen and are easily contaminated by cell culture constituents, which can result in unstable sensor characteristics in long-term measurements [4]. On the other hand, optical methods do not consume oxygen, are non- or minimally invasive, quite easily miniaturized

* Corresponding author.
E-mail addresses: hannu.valimaki@tut.fi, hvalimaki@gmail.com (H. Välimäki).

http://dx.doi.org/10.1016/j.snb.2017.04.182
0925-4005/

and compatible with imaging set-ups [5], which makes them a very attractive choice. It is therefore no wonder that there has been a great progress in the development of optical oxygen probes, polymer matrix materials, and related measurement devices during recent decades. Today many commercial devices based on the oxygen-dependent quenching exist, and extensive technology reviews are available [2,4–6].

A typical sensor layout consists of a luminescent dye embedded in a polymer matrix deposited on a solid substrate such as glass, planar waveguide, well plate or optical fibre [6]. However, with some excellent exceptions [7–9], relatively little attention has been paid to the efficiency of the optical detection in the planar sensing scheme, and typically, the detector is placed directly under the substrate. However, when fluorescent oxygen detection is applied in cell cultures, the optical detection efficiency becomes important. Efficient detection scheme enables one to use lower dye/polymer ratios, thinner sensing films and less excitation power without significantly deteriorating the sensor characteristics. These features can greatly mitigate the potential cytotoxicity of the dyes and the sensing method i.e. the production of singlet oxygen [10].

In this paper, we aim at a design and demonstration of an improved optical detection scheme for luminescent oxygen sensing films. For this purpose, we start by presenting numerical simulations of the emission characteristics of thin, fluorescently doped polystyrene films deposited at a water-glass interface. The starting point for the simulations comes from the work of Lukos et al. [11] and, especially, from Frischeisen et al. [12] and Nowy et al. [13], who, in their work related to the organic LEDs, studied the effect of molecular dipole orientation in doped fluorescent organic thin films. Excellent work has also been carried out by Polerecky et al. [9], who theoretically studied the radiation characteristics of dipoles within an arbitrary planar multilayer system. After analysing the radiation pattern of a thin dye-polymer film, we present an efficient fluorescent detection scheme based on the works of Enderlein et al. [14], Kurtzbuch et al. [15] and Välimäki et al. [16], who all applied in-contact detection of super critical angle fluorescence to biosensing. In the experimental section, we first study the sensor characteristics of a phase fluorimetric device equipped with the suggested sensing scheme. Here, among the many possibilities for the oxygen sensitive dye and polymer matrix, we chose the combination of platinum(II) octaethylporphyrin-ketone (PtOEPK) and polystyrene (PS). Polystyrene was chosen, because it possesses many desired properties for the oxygen sensing surface in cell cultures. It has good optical and mechanical properties, and is a widely used a cell culture dish material. In addition, it is relatively gas permeable, and when mixed with a porphyrin dye like PtOEPK, it is very suitable for oxygen sensing at physiological oxygen ranges [5]. The phase fluorimetric detection principle was chosen, because it offers a relatively uncomplicated and cost-effective instrumentation for a single spot oxygen sensing, when compared to time-domain methods that typically require accurate gating and high-speed detectors, and have their advantage typically in direct imaging set-ups [6]. After studying the performance of the device and used collection optics, we conclude our paper by presenting and discussing the experimental results where the device is applied together with on-line microscopy in a pO_2 tension stress study of beating cardiomyocyte cultures.

2. Efficient optical read-out

2.1. Thin film fluorescence

Consider an ideal, polystyrene-PtOEPK film with thickness *d*, deposited on a glass-water interface (Fig. 1). Here we assume that the emitting PtOEPK molecules can be treated as oscillating electric

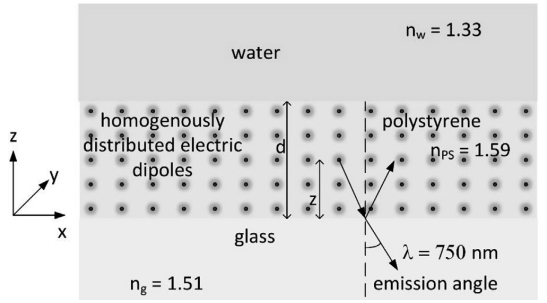

Fig. 1. The modelling scheme of the fluorescent molecules embedded homogenously in a thin polystyrene matrix at a glass-water interface.

dipoles ($\lambda = 750$ nm) that are homogenously distributed throughout the whole film thickness. As in typical state-of-the-art oxygen sensing films, we assume that the PtOEPK molecules are only physically entrapped in the polystyrene matrix [17], and have therefore completely random dipole orientation. To numerically simulate the emission distribution of such a film within the dielectric stack formed by the semi-infinite glass and water layers, we followed the methodology presented in [12,13] and simulated separately the contributions of vertically (p_z) and horizontally (p_x and p_y) oriented electric dipoles placed at a set of definite distances $z \in [0 \ldots d]$ from the polystyrene-glass interface and then summed up the contributions. Fig. 2a shows the simulated results for five homogenous films with thicknesses between 100 nm and 500 nm. The curves show that the actual distribution depends strongly on the film thickness, but also that in all cases the main part of the emission is towards the glass, and that the peak irradiance is found at or above the direction of the critical angle $\theta_c = sin^{-1}(n_w/n_g) = 61.7^\circ$ between water and glass (marked with dashed line). Note also that only a relatively moderate amount of power is radiated below the critical angle $\theta_c = 41.5^\circ$ between the glass and air (dotted line). This represents the part of the irradiation that maximally can be detected with non-contact optics.

Fig. 2b shows, as a function of the film thickness, the simulated relative irradiation (i.e. the power divided by the total radiated power) into the glass space (blue), the contribution of trapped light i.e. the part of the emission that cannot be detected with non-contact optics (red), and the amount that a non-contact lens with the numerical aperture of NA = 0.45, placed underneath the glass plate, could maximally collect (green). It is instructive to realize that with all the simulated film thickness values, only about 1/7 of the radiation emitted into the glass space (or about 1/10 of the total emitted power) can reach the detector when such a typical non-contact sensing scheme is applied.

2.2. Optical read-out

An efficient way to collect the trapped light is to apply a parabolic lens [14–16] or other kind of refractive and reflective structures [7,8] in optical contact with the substrate, which guide the trapped light to the detector. Here we apply the arrangement shown in Fig. 3a, where the parabolic lens is truncated so that the focal point of the lens is at the glass-water interface, similarly as in a previous set-up targeted to surface sensitive biosensing [16]. The parabolic lens used in the set-up has a focal length of f = 2.78 mm, and the upper and lower diameters of 13.00 mm and 24.90 mm, respectively. With this geometry, the fluorescent emission radiated into the angles between 48.1° and 81.2° can be collected. As Fig. 3b shows, this range fits especially well when the film thick-

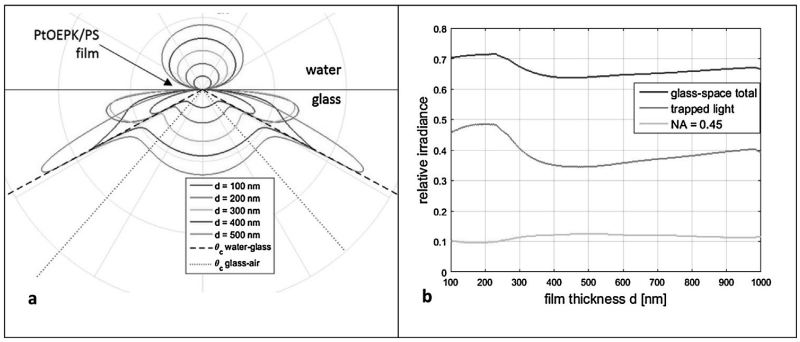

Fig. 2. (a) The angular emission distribution of polystyrene films with varying thickness d, doped with fluorescent dyes emitting at 750 nm; (b) the relative irradiance towards glass-space (blue), the amount of trapped light (red) and the collection efficiency of a lens with NA = 0.45 (green) as a function of film thickness d. (For interpretation of the references to colour in this figure legend, the reader is referred to the web version of this article.)

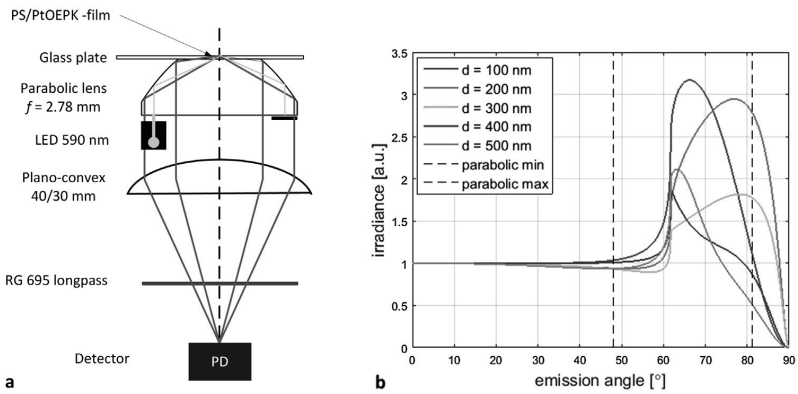

Fig. 3. (a) The optical set-up based on a truncated parabolic lens; (b) The relative emission irradiance (scaled by power emitted directly downwards) vs emission angle with varying film thickness d. The minimum and maximum detectable supercritical angles with the used parabolic lens are marked with dashed lines. (For interpretation of the references to colour in this figure legend, the reader is referred to the web version of this article.)

ness d = 100, 400 or 500 nm, that is, when the peak irradiance is in the center of the angular detection range.

If the emission collection efficiency is the parameter to be maximized, then both the direct radiation and trapped light should be collected. A sophisticated way to accomplish this would be to manufacture an integrated lens structure in the center of the bottom surface of the parabolic lens. With an integrated convex surface, the emission that enters into the paraboloid but is not reflected at the parabolic surface could be collected with greater efficiency. As a first small angle approximation, a convex surface with the radius of curvature of $R = L(n_g - 1)/n_g$, where L is the distance between the polystyrene film and the lower surface of the parabolic lens, could be used [18]. We, however, wanted to use the central area of the parabolic lens for microscopy illumination and left this option out.

In the scheme, the parabolic lens is also used for the total internal reflection excitation. The parabolic surface – again through the total internal reflection – focuses the parallel output beam of the excitation LED to the focal point of the parabolic lens. This makes the excitation effective and insensitive to biofouling or other optical changes in the sensing surface. The totally reflected excitation beam is blocked with a plastic blocker below the parabolic lens, which prevents any long wavelength tail of the excitation LED to enter the detector. The total internal reflection excitation arrangement significantly reduces the excitation power radiated into the culture chamber, which diminishes both the direct illumination stress and the possibility of generating singlet oxygen by unintentionally exciting the dyes that could have migrated from the polymer matrix closer to cell membranes. Finally, as both the excitation and the main part of read-out are strictly focused on sensing film, the arrangement is insensitive to autofluorescence and other background signals stemming from the sample side.

When it comes to the fluorimetric oxygen sensing, fluorescence lifetime based methods – being insensitive to variations in excitation power, dye concentration, photo bleaching, and other gain-type factors – are preferable to direct irradiance-based methods [19]. By modulating the excitation amplitude and measuring the phase between the excitation and emission signals one can make a lifetime-based oxygen sensing scheme that is well described by the Stern-Volmer equation

$$\frac{\phi_0}{\phi} = 1 + K_{sv} pO_2 \tag{1}$$

where ϕ_0 and ϕ; are the measured phase values in the absence and presence of oxygen, respectively; K_{sv} is Stern-Volmer constant and pO_2 is the oxygen partial pressure.

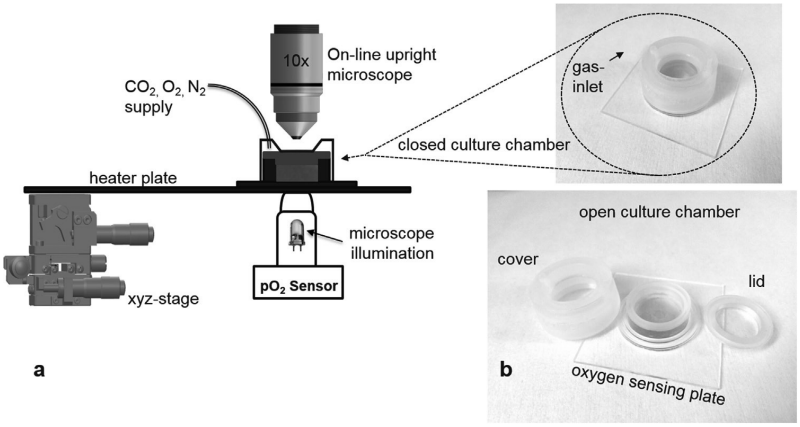

Fig. 4. (a) The scheme of the tailored cell culturing system; (b) the parts of the cell culture chamber.

3. Materials and methods

3.1. Oxygen sensing plates

Polystyrene pellets (m_w = 200 000, from Sigma, St. Louis, USA) were dissolved in toluene (4.0% w/w), and platinum(II) octaethylporphyrinketone (PtOEPK, from Frontier Scientific, Logan, USA) were added to the solution in variable proportions (from 0.025% to 0.4% w/w with respect to PS). Glass plates (49 mm × 49 mm × 1 mm) were cleaned with a sequence of 2 min ultrasonic baths in acetone and isopropanol, rinsed with deionized (DI) water and dried with nitrogen flow. PS/PtOEPK films were then fabricated by spincoating first 200 μL of hexamethyldisilazane (HMDS), and immediately after that 200 μL of PS/PtOEPK-toluene solution, both at 3000 rpm for 60 s under cleanroom conditions. The HMDS pre-treatment was found to increase significantly the adhesion between glass and PS films. Immediately after spin coating the plates were placed on a hot plate (T = 100 °C) for 10 min, and then left for overnight drying. This coating procedure resulted in films with the average thickness of 480 nm (measured with Bruker Dektak XT contact profilometer), which is in the same range as the reported spin coated PS and PS-PtOEPK film thicknesses in [20,21]. Before any use, the sensing plates were bathed in DIwater for 48 h at room temperature to ensure the stable film adhesion.

3.2. Optical set-up of the sensor

The lenses, filters and LED (LED591E, 590 nm, 2 mW) needed in the set-up shown in Fig. 2a were from Thorlabs, Germany. The parabolic lens was manufactured by Jenoptik, Germany, and made of polystyrene, which caused some additional aberrations at the glass plate – polystyrene lens interface that are neglected in the analysis. Optical contact between the glass plate and the parabolic lens was assured with immersion oil (n = 1.51).

The oxygen-induced changes in the fluorescence lifetime were measured by a quadrature synchronous detection with a tailored hardware. The excitation LED was driven using 2 kHz square wave current (20 mA peak-to-peak), and the fluorescent emission was detected with a photodiode (S1226-18BQ). The synchronous detector had a bandwidth of 23 Hz and its I/Q outputs were sampled to produce phase angle measurements at a data rate of 10 Hz. The LED excitation signal was used as a phase reference.

3.3. Sensor calibration

Sodium sulfite (Na_2SO_3, from Merck, Germany) was used as chemical deoxygenator (1 g Na_2SO_3 dissolved in 100 mL of DI water) in some calibration measurements.

3.4. Set-up in cell experiments

The set-up used in the experiments with the cardio myocytes is schemed in Fig. 4a. A tailored PDMS 1-well culture chamber with a volume of 1 mL (Fig. 4b, see also [22,23]) is mounted directly on the sensing film (film thickness 480 nm, PtOEPK/PS ratio 0.1%) on the oxygen sensing plate. The bottom of the culture chamber has a round opening (diameter 3.5 mm), operating as a cell area, where the cells can be plated. The culture chamber is closed with a transparent polycarbonate lid, and the structure is covered with a 3D-printed cover made of UV curable acrylic plastic. This arrangement creates a small volume gas environment around the PDMS structure, which enables one to control the gas content of the culture medium. In addition, the cover is equipped with a glass window so that on-line microscopy is possible from the top. The glass plate containing the PDMS culture well is placed on a commercial transparent ITO heater plate (Okolab 401, glass thickness 0.5 mm) and the pO_2 sensor optics is placed in contact with the heater plate. Optical contacts in both sides of the heater plate are assured with the immersion oil (n = 1.51). For the on-line microscopy, we used upright configuration with a Nikon 10x objective. For microscopy illumination purposes, a green LED (532 nm) and 3 × 3 x 1 mm glass diffuser are mounted inside the pO_2sensor head, on the optical axis of the system, just underneath the parabolic lens. This arrangement results in some losses in fluorescence collection efficiency, but as the most of the emission power is radiated into the supercritical angles and therefore collected through the outer parts of the parabolic lens, it is not critical. Finally, the heater plate is fixed in a tailored metallic frame mounted in a xyz-stage enabling accurate adjustments. The illumination control, video recording and pO_2 sensor recording is controlled through a Matlab-interface.

3.5. PS-cardiomyocyte culture

Cardiomyocytes (CM) were derived from human iPS-cell line UTA.04602.WT as previously described in [24]. For sterilization, the oxygen sensing plates were immersed in 70% ethanol for 2 h and dried under sterilized conditions. PDMS 1-well culture chambers

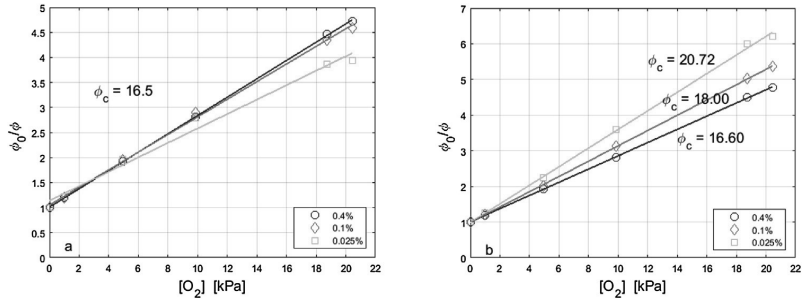

Fig. 5. Stern-Volmer plots with three different PtOEPK/polystyrene ratios. (a) with the same phase constant; (b) with best-fit phase-constants.

were mounted on the sterilized plates, directly on the PtOEPK/PS films. Beating iPS-CM aggregates were plated on the cell well bottom, which was first hydrophilized with FBS and then coated with 0.1% gelatin type A (Sigma-Aldrich, St Louis, MO, USA). The iPS-CMs were cultured in KO-DMEM-media (Lonza, Basel, Switzerland) with 20% FBS (Lonza), 1% non-essential amino acids (NEAA) (Cambrex, East Rutherford, NJ), 2 mM Glutamax (Invitrogen, Carlsbad, CA), 50 U/ml penicillin/streptomycin (Lonza). For each cell well, 3–4 iPS-CM aggregates were plated. After plating, the iPS-CM aggregates were cultured in an incubator (T = 37 °C, 5% CO2, 19% O2, 76% N2) for initial stabilization for 12 h.

4. Results and discussion

4.1. Sensor performance

In order to reveal the presence of any autofluorescence from the glass substrate, the polystyrene film itself or from the LED, the response of the respective samples without PtOEPK were measured. With the maximum available excitation power in our system (100 mA led-current at 2 kHz), no emission signal ($\lambda > 695$ nm) could be seen in the detector. Then the excitation power was adjusted to 20 mA at 2 kHz, and the sensor performance with three PtOEPK/PS films having the same average thickness of d ~480 nm but different dye/polymer ratios, was investigated. The sensing surface of the oxygen sensing plate was flushed with a gas containing a variable concentration of O_2 at room temperature and atmospheric pressure, and the sensor phase responses were recorded. Fig. 5 shows the corresponding Stern-Volmer plots, generated according to Eq. (1), for three different PtOEPK/PS ratios. In Fig. 5a, a separately measured constant phase lag $\phi_c = 16.5°$ between the LED excitation and photodiode amplifier signal, has been subtracted from all phase values before the division in Eq. (1). The figure shows very similar linear Stern-Volmer characteristics for the two highest PtOEPK/PS ratios, but the film with the lowest PtOEPK/PS ratio has a clearly less linear response. However, our phase detection hardware is not totally immune against to the change in overall signal level, which takes place when the film with the lowest concentration is used. This is demonstrated in Fig. 5b, where we have used a separate best-fit value of ϕ_c for each film. This procedure improves the performance in all cases, and almost perfectly linearizes the Stern-Volmer characteristics also for the film with the lowest PtOEPK/PS ratio, where now only a minor deviation at high oxygen concentrations can be seen. The sensor characteristics, as well as the used best-fit values of ϕ_c, are summarized in Table 1. The presented sensitivity values are calculated by solving (1) for ϕ; and taking the derivative with respect to pO_2.

The noise values shown in the table are measured at $pO_2 = 5$ kPa. It is well-known that the noise-level of an oxygen sensor based on oxygen dependent fluorescence quenching is pO_2 dependent: the lower the pO_2 the less quenching takes place, which results in higher signal amplitudes and the lower noise levels also in phase detection. Overall, the noise levels of our device are clearly comparable with commercial devices [25,26], but accurate comparison of signal-to-noise ratio is difficult since the bandwidth information of the commercial devices is often unclear.

In order to study in more details the emission characteristics of the used PtOEPK/PS films, and the performance of the proposed collection optics, we replaced the photodiode in the optics scheme in Fig. 3a with a monochrome camera (Point Grey Grashopper3 GS3-U3-91S6M). The distance between the parabolic lens bottom and the collection lens was adjusted to 145 mm, so that the complete parabolic bottom surface could be imagined. All structures between the parabolic lens and the collection lens were removed, and a focused excitation beam (beam waist ~1.1 mm) was directed to the PS/PtOEPK film (d ~480 nm) through an excitation filter (FGL38) from above in a 45° angle. To make the results comparable with the simulations, the sensing film was covered with a 1 mm layer of water. Fig. 6a shows an image of the measured fluorescence emission. In the central area, we can see the contribution of the direct radiation that could be detected with non-contact optics. The large ring-like structure, in turn, is formed by the super critical angle emission that is being internally reflected by the parabolic part of the lens between the flat upper and lower surfaces of the lens (marked as red dashed lines in the picture). The picture demonstrates how the peak irradiance lies within the range of supercritical angles, and that the total signal collected over the supercritical range of angles exceeds many times the signal that can be collected in the middle area. In more details, the data shown in Fig. 6a is used first for the calculation of a co-centric mean irradiance distribution (in 0.0985 mm steps) as a function of the distance from the center of the excitation beam. Due to the geometry, within the range of angles that are reflected by the parabolic edge, every co-centric ring of irradiance corresponds to a single emission angle from the polystyrene film to the glass substrate. This calculation results in the angular emission distribution shown as blue line in Fig. 6b. The angular radiation distribution of the direct radiation in the middle area is shown as a red line, where the instant drop of the level is exaggerated by the large distance of the collecting lens. Comparing the measured super critical angle distribution with the simulated distributions in Fig. 3b, one can notice how closely the shape of the measured distribution resembles the shape of the simulated ones for 400 nm and 500 nm films. In the measurements, however, the maximum value is shifted about five degrees to the direction of smaller angles, which can be explained by the refractive index mismatch between the glass substrate and the polystyrene parabolic lens. Due to this mismatch, all super critical emission angles at the glass substrate/polystyrene lens interface are refracted more towards the optical axis, which results in a shift towards larger distances from the axis and, therefore, in smaller calculated emission

Table 1
Oxygen sensor characteristics with different PtOEPK/polystyrene – ratios.

PtOEPK/PS [%]	ϕ_c [°]	K_{SV} [kPa^{-1}]	Sensitivity [°/kPa] (at pO_2 = 5.0 kPa)	Phase noise [° rms] (at pO_2 = 5.0 kPa at 10 Hz data rate)	pO_2 noise [kPa rms] (at pO_2 = 5.0 kPa at 10 Hz data rate)
0.400	16.60	0.185	−1.97	0.0076	0.0039
0.100	18.00	0.215	−1.87	0.019	0.010
0.025	20.72	0.261	−1.66	0.050	0.030

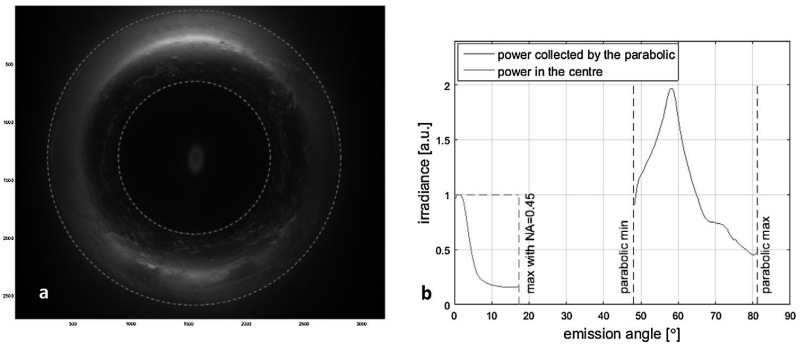

Fig. 6. (a) A picture of the fluorescence emission distribution under the parabolic lens. The locations of the upper (in contact with the sensing plate) and lower surfaces of the lens are marked as red dashed lines; (b) The calculated co-centric mean irradiance as a function of the emission angle from the polystyrene film into the glass. (For interpretation of the references to colour in this figure legend, the reader is referred to the web version of this article.)

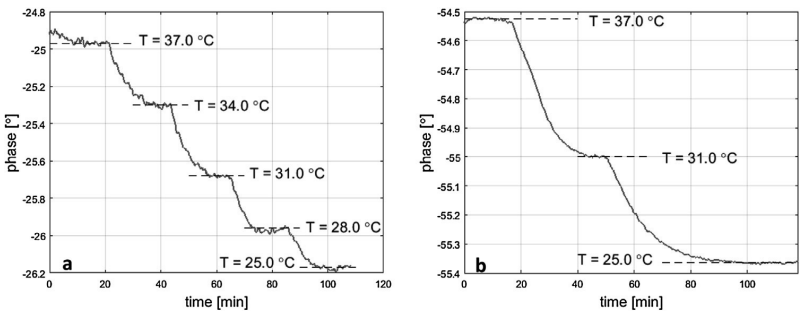

Fig. 7. The phase response of the pO_2 sensor at different temperatures in water (a) and in de-oxygenated water (b).

angles in Fig. 6b. Another way to interpret this shift is to recall that the simulations with d = 400 and d = 500 m resulted in peak irradiance at the critical angle between water and the substrate. As the glass thickness is 1 mm and the polystyrene parabolic lens thickness is 12.1 mm, the substrate can be seen as mainly polystyrene, so the peak irradiance should be found close to the critical angle between water and polystyrene $\theta_c = 56.8°$, which is good agreement with the measurements. It is also noteworthy that the measured ratio (∼2) of the peak irradiance to the irradiance in the middle is in agreement with the simulations.

Finally, we can estimate (overestimate) that the absolute maximum power detectable with NA = 0.45 non-contact optics under a glass substrate is the power measured in the middle over the whole range of detectable emission angles (from polystyrene into glass) up to 17.2°, where the upper limit comes from the geometry and refractive indices of glass and air (marked with the dashed red line). Here, this estimation results in a power ratio of ∼2.0 between the detected supercritical angle power and the estimated absolute maximum power detectable with NA = 0.45. Taking into account that for the d = 500 nm films, our parabolic lens can collect 83% of the trapped light, also this estimated power ratio is in approximate agreement with the calculations in Fig. 2b.

Although these results are clearly supportive to the simulation results and the suggested optical read-out, it should be emphasized that a more detailed analysis and more rigorous experimental verification of the emission distribution would require a more suitable set-up, such as used with LED development in [12]. However, the construction of such a different set-up is out of the scope of this paper. Instead, we proceed to show some preliminary results when the device is applied to the pO_2 monitoring of cardiomyocyte cultures, which highlights some additional advantages of the system.

4.2. Cell experiments

While in the characterization measurements the substrate thickness was 1.0 mm, in cell experiment set-up the heating plate contributes with additional 0.5 mm glass thickness (Fig. 4). This results in diminished performance as the used parabolic lens is tuned for 1.0 mm substrates. We mitigated this to some extent by grinding additional 0.5 mm away from the upper surface of the lens.

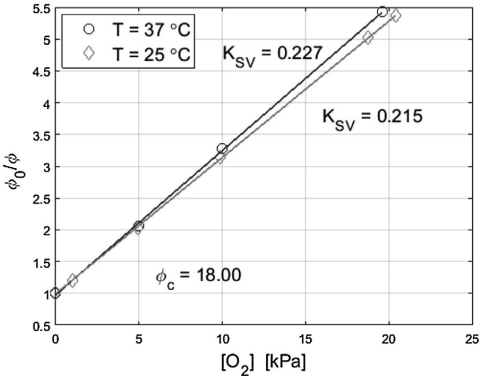

Fig. 8. The Stern-Volmer plots at T = 25 °C and T = 37 °C.

4.2.1. Calibration at T = 37 °C

Fig. 7 shows the phase response of the oxygen sensor, in the cell experiment set-up, at different temperatures in water, and in water deoxygeneated with Na_2SO_3. According to the measurements in water (Fig. 7a), the phase difference decreases 1.20° as the temperature increases from T = 25 °C to T = 37 °C. At the used 2 kHz modulation frequency, this corresponds to decrease of 1.67 μs in the fluorescence lifetime, or 0.54% per 1 °C if we assume τ = 26 μs for the PtOEPK fluorescence lifetime in PS in air-saturated water [27].The shortening of the lifetime is induced by the increased thermal quenching and faster oxygen diffusion in PS [17]. In addition, the temperature dependence of the read-out electronics contributes to the change, but as the electronics closure is separated from the heater plate, the contribution is negligible.

In deoxygenated water (Fig. 7b) the corresponding change is 1.17 μs or 0.16% per 1 °C, where the unquenched lifetime τ_0 = 60 μs have been used as reference [27]. Here, as the oxygen diffusion does not have an impact in deoxygenated conditions, the decrease in the lifetime is probably mainly due thermal quenching. The value of 0.16% per 1 °C is in agreement with previous findings for Pt(II) metalloporphyrins [5].

Fig. 8 shows the Stern-Volmer plot at T = 37 °C, where two additional points (at 5.0 and 10.0 kPa) have been generated by directing a constant flow of pre-heated gas mixture of known oxygen content to the preheated oxygen sensing plate. For comparison, the Stern-Volmer plot for the same plate type (0.1% PtOEPK/PS) at T = 25 °C is also shown. The phase lag constant is held as ϕ_c = 18.0 in both plots, as it corresponds to the unchanging basic phase lag value between the LED excitation and photodiode signal. The change in the Stern-Volmer plots between T = 25 °C and T = 37 °C is relatively small, and the increase in Stern-Volmer constant with increasing temperature is in agreement with the arguments above and [19].

4.2.3. Monitoring cardiomyocytes

After the iPS-CMs were plated in the PDMS culture chamber, mounted on an oxygen sensing plate as described earlier, the iPS-CMs were cultured first in an incubator (T = 37 °C, 5% CO2, 19% O2, 76% N2) for 12 h. Then the culture chamber was closed with the lid and the cover, and the plate was placed on the heater plate, calibrated for T = 37 °C. The baseline oxygen conditions were established by flushing the gas environment around the culture chamber with a constant flow (5 $mLmin^{-1}$) of a gas mixture containing 19% of O_2, 5% CO_2, and 76% of N_2. Oxygen recordings were carried out every 10 min and a one-minute long video at 40 frames per second (PointGrey FL3-U3-13E4M-C) was recorded once an hour. These videos were later analysed according to methods described in [28].

Fig. 9a shows the induced oxygen tension during 40 h of such a test. After 4 h of baseline recording, the system was set towards hypoxic conditions by switching into a gas mixture containing 1% of O_2, 5% of CO_2 and 94% of N_2. In about 3 h, the system had reached a stage close to the oxygen condition of pO_2 = 2 kPa. This is slightly more than what the set point of 1% should yield, which is probably due to some leakage in the sealing of the system. The essentially unchanged post-calibration after the completed tests (data not shown) supported this hypothesis. The first hypoxic period lasted 12 h, and then the system was returned to the baseline conditions for a short time until a second hypoxic period took place.

In Fig. 9b, the average beating frequencies, analysed from the videos as in [28], are plotted together with the respective pO_2 sensor output during the first hypoxic period. According to this small data set, it remains questionable whether there exists a direct correlation between the pO_2 tension and the beating frequency. A slight indication of a correlation can be seen, as well as some interesting anomalies. Especially at 7.6 h, the beating frequency has a great deviation, and interestingly this happens at the same time when there is also an anomaly in the pO_2 sensor output. In principle, a rise in the temperature could cause both deviations, but a closer analysis in the pO_2 sensor data reveals that this would indicate approximately a 6 °C rise in the temperature for about 1 h, which would have been lethal for the cells. However, as the temperature sensor recording failed during the first 24 h, the possibility of a period of elevated temperatures cannot be absolutely excluded.

4.3. Discussion

The presented results with cardiac cells are only very preliminary. They serve here as exemplary experiments highlighting the

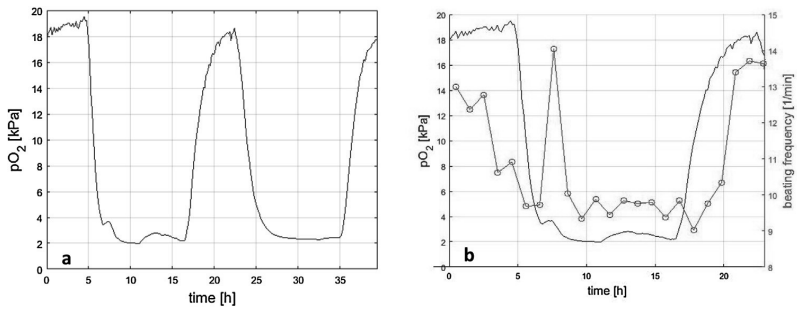

Fig. 9. Applying the oxygen sensor into the pO_2 control of beating cardiomyocyte cultures. (a) The pO_2 output of the sensor; (b) The pO_2 output together with the beating frequency of the followed cluster during the first hypoxic period.

performance and the features of the developed oxygen sensor. More tests, repetitions, and further equipment development and tuning are needed for achieving rigorous results from the point of view of cell research. However, in our tests, the cardiac cell aggregates from the used cell line could endure the sensing surface with PtOEPK/PS ratio of 0.1% more than five days (three repetitions in total). This means that for the many coming tests with these cells, it is probable that no additional biocompatible shielding layer is needed.

As such, the reported device is only a single-spot pO_2 sensor, but it could be turned into an imaging or a multi-spot sensor by integrating a scanning mechanism in the device. We have found that with the current geometry, a glass plate with the spin-coated PtOEPK-PS film can be moved in the xy-plane over 1 mm without any change in the measured phase difference. For the scanning purposes a digital mirror device could be a good option [29]. However, even in a single-spot sensing, the presented detection scheme can have a justified use in applications such as the oxygen control of cell cultures, where the biocompatibility issues are very important and the dye concentrations and the excitation power radiated into the cell chamber must be minimized. In addition, the geometry of the detection scheme gives freedom to integrate other instruments, such as microscope illumination devices, temperature sensors, microelectrode arrays (MEAs) the center of the cell area.

5. Conclusions

Based on electromagnetic simulations, and on an optical detection scheme utilising an in-contact parabolic lens, an efficient way for collecting the fluorescence stemming from a thin dye-polymer film deposited on a glass-water interface has been demonstrated. It has been shown how the use of parabolic lens also facilitates a confocal total internal reflection excitation from the substrate side. This makes the excitation effective, and importantly, greatly reduces the amount of excitation power radiated to the cell culture chamber. As both the excitation and the main part of read-out are strictly focused on sensing film, the arrangement is insensitive to autofluorescence and other background signals stemming from the sample side. This feature is further emphasized if the direct radiation in the center of the sensing are is excluded from the fluorescence detection. The experimental results with a phase fluorimetric oxygen sensor, taking advantage of the developed optical read-out, and 480 nm PtOEPK/PS films having 0.025% dye/polymer ratio, showed sensor characteristics comparable to commercial devices. The set-up can be especially useful when the biocompatibility issues are important, and the dye concentration and the excitation power must be minimized. In addition, it has been shown how the optical arrangement leaves space for other instrumentation such us microscopy illumination in the center of the sensing area and how the arrangement can be integrated together with an ITO heating plate in an *in vitro* cell monitoring system. Finally, it has been demonstrated how the developed sensor system can be applied to an on-line cell culture monitoring, such as on-line video analysis of beating cardiomyocytes under pO_2 stress.

Acknowledgement

The Financial support by TEKES, the Finnish Funding Agency for Technology and Innovation, is gratefully acknowledged.

References

[1] D.F. Wilson, Quantifying the role of oxygen pressure in tissue function, Am. J. Physiol.: Heart Circ. Physiol. 294 (2008) H11–H113.
[2] D. Papkovsky, R. Dmitriev, Biological detection by optical oxygen sensing, Chem. Soc. Rev. 42 (2013) 8700–8732.
[3] C. Wu, T. Yasukawa, H. Shiku, T. Matsue, Fabrication of miniature Clark oxygen sensor integrated with microstructure, Sens. Actuators B 110 (2005) 324–349.
[4] S. Grist, L. Chrostowski, K. Cheung, Optical oxygen sensors for applications in microfluidic cell culture, Sensors 10 (2010) 9286–9316.
[5] M. Quaranta, S. Borisov, I. Klimant, Indicators for optical oxygen sensors, Bioanal. Rev. 4 (2012) 115–157.
[6] X.-D. Wang, O. Wolfbeis, Optical methods for sensing and imaging oxygen: materials: spectroscopies and applications, Chem. Soc. Rev. 43 (2014) 3666–3761.
[7] S. O'Driscoll, C. McEvoy, B. McDonagh, Enhanced fluorescence-Based optical sensor performance using a simple optical collection strategy, IEEE Photonics Technol. Lett. 6 (24) (2012).
[8] R. Blue, N. Kent, L. Polerecky, H. McEvoy, D. Gray, B.D. MacCraith, Platform for enhanced detection efficiency in luminescence-based sensors, Electron. Lett. 12 (41) (2005).
[9] L. Polereckyí, J. Hamrle, B.D. MacCraith, Theory of the radiation of dipoles placed within a multilayer system, Appl. Opt. 38 (2000) 3968–3977.
[10] P. Ceroni, A. Lebedev, E. Marchi, M. Yan, T. Esipova, G. Bergamini, D. Wilson, T. Busch, S. Vinogradov, Evaluation of dentritic porphyrin-based phosphorescent oxygen probes: an *in vitro* study, Photochem. Photobiol. Sci. 10 (6) (2011) 1056–1065.
[11] W. Lukosz, R.E. Kunz, Light emission by magnetic and electric dipoles close to a planar interface. I. Total radiated power, J. Opt. Soc. Am. 67 (1977) 1607–1615.
[12] J. Frischeisen, D. Yokoyama, C. Adachi, W. Brütting, Determination of molecular dipole orientation in doped fluorescent organic thin films by photoluminescence measurements, Appl. Phys. Lett. 96 (2010) 073302.
[13] S. Nowy, B.C. Krummacher, J. Frischeisen, N.A. Reinke, W. Brütting, Light extraction and optical loss mechanisms in organic light-emitting diodes: influence of the emitter quantum efficiency, J. Appl. Phys. 104 (2008) 123109.
[14] J. Enderlein, T. Ruckstuhl, S. Seeger, Highly efficient optical detection of surface-generated fluorescence, Appl. Opt. 38 (1999) 724–732.
[15] D. Kurzbuch, J. Bakker, J. Melin, C. Jönsson, T. Ruckstuhl, B.D. MacCraith, A biochip reader using super critical angle fluorescence, Sens. Actuators B 137 (2009) 1–6.
[16] H. Välimäki, K. Tappura, A novel platform for highly surface-sensitive fluorescence measurements applying simultaneous total internal reflection excitation and super critical angle detection, Chem. Phys. Lett. 473 (2009) 358–362.
[17] K. Koren, S. Borisov, I. Klimant, Stable optical oxygen sensing materials based on click-coupling of fluorinated platinum(II) and palladium(II) porphyrins – a convenient way to eliminate dye migration and leaching, Sens. Actuators B 169 (2012) 173–181.
[18] E. Hecht, Optics, 4th ed., Addison Wesley, San Francisco, 2002.
[19] J. Lakowicz, Principles of Fluorescence Spectroscopy, 4th ed., Springer, US, New York, 2006.
[20] V. Nock, R. Blaikie, T. David, Patterning: integration and characterisation of polymer optical oxygen sensors for microfluidic devices, Lab Chip 8 (2008) 1300–1307.
[21] D. Hall, P. Underhill, J. Torkelson, Spin coating of thin and ultrathin polymer films, Polym. Eng. Sci. 8 (12) (1998) 2039–2045.
[22] J. Kreutzer, K. Rantanen, H. Välimäki, J. Lekkala, P. Jaakkola, P. Kallio, Mini-incubator for prolonged cell culture and hypoxia studies outside an incubator. front. neurosci. conference abstract: MEA meeting, 10th International Meeting on Substrate-Integrated Electrode Arrays (2016), http://dx.doi.org/10.3389/conf.fnins.2016.93.00043.
[23] J. Kreutzer, L. Ylä-Outinen, A. Mäki, M. Ristola, S. Narkilahti, P. Kallio, Cell culture chamber with gas supply for prolonged recording of human neuronal cells on microelectrode array, J. Neurosci. Methods 280 (2017) 27–35.
[24] A. Lahti, V. Kujala, H. Chapman, A. Koivisto, M. Pekkanen-Mattila, E. Kerkelä, J. Hyttinen, K. Kontula, H. Swan, B. Conklin, S. Yamanaka, O. Silvennoinen, K. Aalto-Setälä, Model for long QT syndrome type 2 using human iPS cells demonstrates arrhythmogenic characteristics in cell culture, Dis Model Mech. 5 (2) (2012) 220–230.
[25] https://www.presens.de/fileadmin/user_upload/brochures/Web_Presens_O2_Broschuere_08-16.pdf, 14.1.2017.
[26] https://www.wpiinc.com/clientuploads/pdf/DS/OxyMicro.pdf, 14.1.2017.
[27] C. O'Donovan, J. Hynes, D. Yashunski, D. Papkovsky, Phosphorescent oxygen-sensitive materials for biological applications, J. Mater. Chem. 15 (2005) 2946–2951.
[28] A. Ahola, A. Kiviaho, K. Larsson, M. Honkanen, K. Aalto-Setälä, J. Hyttinen, Video image-based analysis of single human induced pluripotent stem cell derived cardiomyocyte beating dynamics using digital image correlation, Biomed. Eng. Online 13 (39) (2014) 1–18.
[29] S. Chao, M. Holl, S. McQuaide, T. Ren, S. Gales, D. Meldrum, Phosphorescence lifetime based oxygen microsensing using a digital micromirror device, Opt. Express 17 (15) (2007) 10681–10689.

Biographies

Hannu Välimäki received the M.Sc. degree in electrical engineering from the Tampere University of Technology (TUT), Tampere, Finland, in 1996. He worked as a Research Scientist in the field of acoustical and optical sensors at the VTT Technical Research Centre of Finland, Tampere, until 2013. Currently he works at BioMediTech

Institute and Faculty of Biomedical Sciences and Engineering (TUT), where he develops optical sensing technologies for cell culturing applications.

Jarmo Verho is working as a research assistant at BioMediTech Institute and Faculty of Biomedical Sciences and Engineering, Tampere University of Technology. He is specialized in low-noise electronics design and embedded systems. His other research interests include sensor networks, radio networks, short range inductive links and capacitive sensing techniques.

Joose Kreutzer received the B.Eng. degree in electrical and electronic engineering from the University of Sunderland, Sunderland, U.K., in 2003, and the M.Sc. degree in electrical engineering from the Tampere University of Technology (TUT), Tampere, Finland, in 2005. He works currently as a Research Scientist with the Micro- and Nanosystems Research Group at BioMediTech Institute and Faculty of Biomedical Sciences and Engineering (TUT). His current research interests include microfabrication, microfluidics, and their applications in biomedical engineering, especially for stem cell-based bioengineering.

Dhanesh Kattipparambil Rajan received his M.Sc. degree (Tech.) in Biomedical Engineering from Tampere University of Technology (TUT), Finland, in 2008. Currently he is pursuing PhD at BioMediTech Institute and Faculty of Biomedical Sciences and Engineering, (TUT). His research interests include optical sensors, modular-compact microscopy and sensor systems. Prior to his current PhD studies, he worked for four years in the microfabrication and lithography facility.

Tomi Ryynänen received his M.Sc. degree in applied physics from the University of Jyväskylä in 2000. After a couple of years in optoelectronics and software industry, he has been working at Tampere University of Technology since 2005. In addition to doctoral studies he has been responsible for developing the cleanroom laboratories and microfabrication activities. His research is focused on microelectrode arrays (MEAs) and other microsensors for cell culturing applications.

Mari Pekkanen-Mattila received her PhD in stem cell and tissue engineering from the University of Tampere, Finland, in 2011. Her research has focused on human induced pluripotent stem cells, cell differentiation and disease modelling of human genetic cardiac diseases

Antti Ahola graduated with a Master's degree in Biomedical Engineering from Tampere University of Technology, Finland, in 2010. His research interests include cardiomyocyte biomechanics, video microscopy and image analysis. Currently, he is finalizing his D.Sc studies in this field.

Kirsi Tappura received the M.Sc. (Tech.), Lic.Sc. (Tech.), and D.Sc. (Tech.) degrees in technical physics from the Tampere University of Technology (TUT), Tampere, Finland, in 1990, 1992, and 1993, respectively. She continued her research on semiconductor physics and optoelectronics at TUT as a Research Scientists and a Postdoctoral Research Fellow of the Academy of Finland until joined the Nokia Research Center, where she was a Senior Research Scientist involved with novel electronic displays. Currently she is a Principal Scientist at the VTT Technical Research Centre of Finland, Espoo/Tampere. Since 1999, she has also been a Docent of Physics with TUT. Her research interests include the optical (including plasmonic), electronic and thermal properties of various sensing, detector/imaging and energy harvesting devices with an emphasis on computational physics.

Pasi Kallio received the M.S. degree in electrical engineering and the D.Tech. degree in automation engineering from the Tampere University of Technology (TUT), Tampere, Finland, in 1994 and 2002, respectively. Since 2008, he has been a Professor of Automation Engineering at TUT. He is an author of more than 120 articles, and more than ten patent applications. His current research interests include microrobotics, microfluidics, and their automation in cell and tissue engineering, medical diagnostics, and soft material testing applications. Prof. Kallio was the Chair of the IEEE Finland Section from 2012 to 2013. He was a recipient of the Finnish Automation Society Award in 2009.

Jukka Lekkala received the M.Sc. degree in electronics and the D.Sc. (Tech.) degree in biomedical engineering from the Tampere University of Technology (TUT), Tampere, Finland, in 1979 and 1984, respectively. Since 1991, he has been a Docent of Bioelectronics at the University of Oulu, Oulu, Finland, and a Docent of Biomedical Engineering at TUT. He is currently a Professor of Automation Technology at the Faculty of Biomedical Sciences and Engineering (TUT). His current research interests include sensors, measurement systems, and biosensing.

MANUSCRIPT
I

Covalently linked indicators enhance the biocompatibility of the luminescent oxygen sensing material with hiPSC-derived neurons and cardiomyocytes

Hannu Välimäki, Tanja Hyvärinen, Joni Leivo, Haider Iftikhar, Mari Pekkanen-Mattila, Dhanesh Kattipparambil Raja, Jarmo Verho, Joose Kreutzer, Tomi Ryynänen, Jonatan Pirhonen, Katriina Aalto-Setälä, Pasi Kallio, Susanna Narkilahti and Jukka Lekkala

Unpublished manuscript[1]

[1] A revised version of the manuscript is published under the title "Covalent immobilization of luminescent oxygen indicators reduces cytotoxicity", Biomedical Microdevices (2020) 22:41 https://doi.org/10.1007/s10544-020-00495-3

Covalently linked indicators enhance the biocompatibility of the luminescent oxygen sensing material with hiPSC-derived neurons and cardiomyocytes

Hannu Välimäki[a,1], Tanja Hyvärinen[b], Joni Leivo[a], Haider Iftikhar[a,2], Mari Pekkanen-Mattila[b], Dhanesh Kattipparambil Rajan[a], Jarmo Verho[a], Joose Kreutzer[a], Tomi Ryynänen[a], Jonatan Pirhonen[b], Katriina Aalto-Setälä[b], Pasi Kallio[a], Susanna Narkilahti[b], Jukka Lekkala[a]

[a]*Faculty of Medicine and Health Technology, Tampere University, Korkeakoulunkatu 3, 33720 Tampere, Finland*
[b]*Faculty of Medicine and Health Technology, Tampere University, Arvo Ylpön katu 34, 33520 Tampere, Finland*

[1] Corresponding author. Tel. +358405511695.
E-mail addresses: hannu.valimaki@tuni.fi, tanja.hyvarinen@tuni.fi, joni.leivo@tuni.fi, haider.iftikhar@aalto.fi, mari.pekkanen-mattila@tuni.fi, dhanesh.kr@tuni.fi,jarmo.verho@tuni.fi, joose.kreutzer@tuni.fi, tomi.ryynanen@tuni.fi, jonatan.pirhonen@tuni.fi, katriina.aalto-setala@tuni.fi, pasi.kallio@tuni.fi, susanna.narkilahti@tuni.fi, jukka.lekkala@tuni.fi
[2] Present address: Department of Bioproducts and Biosystems, Aalto University, 02150 Espoo, Finland

Abstract. *Luminescence-based oxygen sensing is a widely used tool in cell culture applications. In a typical configuration, the luminescent oxygen indicators are embedded in a solid, oxygen-permeable matrix in contact with the culture medium. However, in sensitive cell cultures the biocompatibility of such a sensing material is crucial, and the leaching of the indicators often becomes an issue. One way to prevent the leaching is to link the indicators covalently into the supporting matrix. In this article, we report on a method, where platinum(II)-5,10,15,20-tetrakis-(2,3,4,5,6-pentafluorphenyl)-porphyrin (PtTFPP) oxygen indicators are covalently linked into the polymer matrix consisting of polystyrene and poly(pentafluorostyrene). We study how the linking of the indicators influences the biocompatibility of the sensing material with human induced pluripotent stem cell-derived (hiPSC-derived) neurons and cardiomyocytes by 1-2 week culturing experiments and various viability analyses. In addition, we study the effect of the linking on the chemical stability and the oxygen sensing properties of the material. The results show that the covalently linked indicators substantially enhance both the chemical stability and the biocompatibility of the oxygen sensing material, while the influence on the oxygen sensing properties remains small or nonexistent.*

INTRODUCTION

Molecular oxygen has a large impact on the viability and functioning of cells and tissues, thus requiring careful monitoring and control in cell cultures [1,2]. Today, a widely applied technique for oxygen monitoring is based on the use of luminescent indicators, which is replacing Clark's electrodes in many fields [3]. The luminescence-based technique is sensitive, and it provides a large set of sensing schemes and modalities, including sensing spots, fiber-optic set-ups, planar films, smart scaffolds as well sensing beads for 3D oxygen imaging [4]. In addition, the sensitivity and measurement range can be tuned with appropriate choice of indicators and matrix materials [5,6]. Moreover, the luminescent technique does not consume oxygen and integrates well into many systems, which are important features in microfluidic or miniaturized cell cultures [7-9].

The luminescent oxygen indicators are typically embedded in a solid, oxygen-permeable matrix, most often in a suitable polymer in cell culture applications. However, when monitoring sensitive cultures, it is important that the indicators do not leach out of the matrix, as they can be cytotoxic and hamper the cells even in minute concentrations. In addition, the leached indicators may prove fatal through the phototoxic effects – the effect that is utilized in photodynamic cancer therapy [10].

The indicator leaching can be mitigated in various ways. Firstly, the sensing material can be covered with an indicator-free but oxygen-permeable shielding layer. This approach adds to the complexity of the system but can be effective against both the cytotoxic and phototoxic effects [11]. Ideally, the shielding layer can also affect favorably on the hydrophilicity of the sensing material and make it more attractive to cells [12]. On the other hand, a separate layer may create new adhesion problems and, due to the increased diffusion distance, increase the response time as well. Moreover, the layer can generate calibration problems due to the migration of the indicators [13].

Another way to prevent the indicator leaching is to link the indicators covalently into the matrix. The technique requires both suitable indicators and matrix constituents with carefully chosen chemical functionalities. Porphyrins with pentafluorophenyl groups, such as platinum(II)-5,10,15,20-tetrakis-(2,3,4,5,6-pentafluorphenyl)-porphyrin (PtTFPP), are excellent in this respect, and they have been covalently linked in many matrices, including polystyrene (PS), PHEMA [14,15], silica gel [16], poly(styrene-co-pentafluorostyrene) and ormosil [17]. In addition, nanoparticles based on covalently linked metalloporphyrins and conjugated polymer antennas have been prepared for oxygen imaging in cells and 3D tissue models [18].

Our group has recently developed a modular platform for cell culturing [19]. The platform incorporates numerous sensing functionalities, including microelectrode arrays (MEAs), optical microscopy and luminescence-based oxygen sensing, and it has been applied for temperature [20] and hypoxia [21] studies of human induced pluripotent stem cell-derived (hiPSC-derived) cardiomyocytes (CMs). In the hypoxia study, we used Pt(II) octaethyl-porphyrinketone (PtOEPK) embedded non-covalently in PS matrix for the oxygen monitoring, as reports exist on the biocompatibility of such a sensing material with mammalian cells [22]. In our studies, however, it became evident that the biocompatibility of physically embedded PtOEPK in PS is not sufficient with hiPSC-derived cells, at least for longer culturing times. Therefore, the reports of PS with covalently linked metalloporphyrins evoked our interest, even though these reports typically either lacked biocompatibility tests [17], or the tests covered only relatively short (24 hours) culturing of bacteria [14] or cancer cells [16].

This paper studies the effect of covalent linking on the biocompatibility of the luminescent oxygen sensing material. In particular, the study focuses on materials based on PtTFPP and PtOEPK in PS and on their biocompatibility with hiPSC-derived neurons and CMs. For the covalent linking of PtTFPP, we apply the thiol-mediated method [17] with some modifications. Briefly, a polymer blend of PS and poly(pentafluorostyrene) (PPFS) is created, and PtTFPP is linked to PPFS. PtOEPK cannot be linked with the method, but a non-linked PtOEPK-PS reference material is included in the biocompatibility tests because of its popularity [5,8]. We start the report by characterizing and comparing PtTFPP-based oxygen sensing materials with linked and non-linked indicators in terms of the oxygen sensing performance. Then we apply the sensing materials to the biocompatibility studies with hiPSC-derived neurons or CMs. After the biocompatibility tests, we study how the covalent linking influences the chemical stability of the material. Finally, we discuss the results.

RESULTS AND DISCUSSION

Different experimental set-ups were used to study the effect of the covalent linked indicators on the properties of the sensing material in terms of the oxygen sensing performance, biocompatibility with hiPSC-derived neurons and CMs and chemical stability.

PS-based oxygen sensing materials were manufactured as follows: Cov1 (containing 0.05% w/w PtTFPP, covalently linked in PS-PPFS blend); Ref1 (0.05% w/w PtTFPP non-linked in PS); Ref2 (0.5% w/w PtTFPP non-linked in PS); Ref3 (0.05% w/w of PtOEPK non-linked in PS). The PS-PPFS blend contained approximately 0.6% w/w of PPFS and 99.4% w/w PS. The materials were used in the comparative oxygen sensing studies as spin-coated sensing films. In the biocompatibility tests, either spin-coated sensing films (neurons) or distinct sensing spots (CMs) were used.

Oxygen sensing properties. The covalent linking of the indicators had no significant effects on the spectral properties of the sensing material. The absorption maximum was at 397 nm and the emission maximum at 650 nm for both the linked and non-linked PtTFPP (Fig. S1 in the Supporting Information).

A calibration chamber was mounted on the oxygen sensing films. The oxygen concentration of the chamber was controlled, and the sensor amplitude and phase responses were recorded. The corresponding luminescence lifetime-type Stern-Volmer plots [23] are shown for the PtTFPP-based films in Fig. 1A. The Stern-Volmer constants of the films are in the same range, and the relatively small differences in the values presumably stem from differences in oxygen diffusion constants, unquenched lifetimes and quantum yields - all affected by the indicator concentration and the polymer composition. Fig. 1B summarizes the oxygen sensing characteristics of the sensing films. For completeness, the table also includes typical values for the PtOEPK-based films.

A

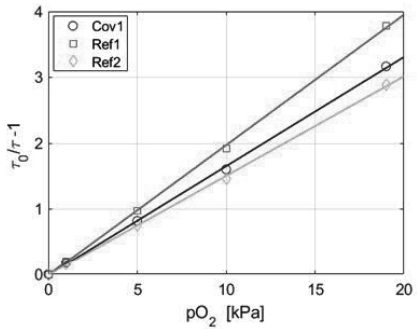

B

Code	Type	Indicator	Indicator concentration [% w/w]	abs λmax [nm]	em λmax [nm]
Cov1	Linked	PtTFPP	0.05	397, 509, 542	650
Ref1	Non-linked	PtTFPP	0.05	397, 509, 542	650
Ref2	Non-linked	PtTFPP	0.5	397, 509, 542	650
Ref3	Non-linked	PtOEPK	0.05	398, 592[1]	759[1]

Code	τ_0 [µs][2]	K_{sv} [1/kPa]	rms noise [°]
Cov1	61	0.202	0.031
Ref1	64	0.244	0.025
Ref2	58	0.182	0.010
Ref3	61	0.239[3]	0.028[3]

[1]values from [24]; [2]estimated with a fitted monoexponential decay curve at pO_2 = 0.0 kPa; [3]measured with the set-up as in [21]

Fig 1. (**A**) Stern-Volmer plots of different PtTFPP-polystyrene oxygen sensing films. (**B**) A table summarizing the oxygen sensing characteristics of the films.

Biocompatibility with hiPSC-derived neurons. hiPSC-derived neurons were plated on different sensing films and followed up to seven days in an incubator. In addition to the films listed in Fig. 1B, a film containing only PS (PS control) was used as a basic reference. First, the morphology and spreading of the neuronal cells were evaluated with phase contrast images. One day (D1) after the cell plating, all groups showed equal cell attachment, spreading and neuronal morphology (Fig. 2A). On day seven (D7), both the PS control and Cov1 still supported neuronal growth. However, on the films Ref1, Ref2 and Ref3 the cells started to retract into cell aggregates (Fig. 2A).

Live-dead staining was performed on D7. Some live-dead images showed similar retraction into aggregates as the phase contrast images (Fig. 2B). Very few dead cells were spread among living cells (Fig. 2B). We quantified the coverage of the live cells in the image area (Fig. 2D). There was a small but statistically significant difference between Cov1 and PS control (medians 63% and 68%, $p < 0.05$). On Ref1, the live cell coverage was lower (median 55%), but not significantly, compared to Cov1. However, the live cell coverage on Ref2 and Ref3 were significantly lower than on Cov1 (medians 38% and 29%, $p < 0.001$).

Immunocytochemical staining was performed on D7 to quantify the total cell count and the cells positive for the neuronal marker β-tubulin (Fig. 2C). Similar nuclei counts (DAPI staining) were observed for the PS control and Cov1 films (medians 1862 and 1945, Fig. 2E). However, the films Ref1, Ref2 and Ref3 did not support cell growth as well as Cov1 (medians 1397, 1163 and 853, in all $p < 0.001$). On the PS control and Cov1, over 80% of cell population expressed β-tubulin neuronal marker (Fig. 2E). However, on Ref1 the percentage of neurons was significantly lower (median 71%, $p < 0.01$), and both Ref2 and Ref3 showed only poor support for the neuronal identity (medians 41% and 39%, $p < 0.001$).

In conclusion, the hiPSC-derived neuronal cells attached, spread and sustained their neuronal identity most efficiently on the film Cov1 containing covalently linked PtTFPP. Non-linked PtTFPP (Ref1) or PtOEPK (Ref3), as well as an increased indicator concentration (Ref2) lowered the spreading of the live cells, decreased the total number of the attached cells, and failed to support the neuronal phenotype.

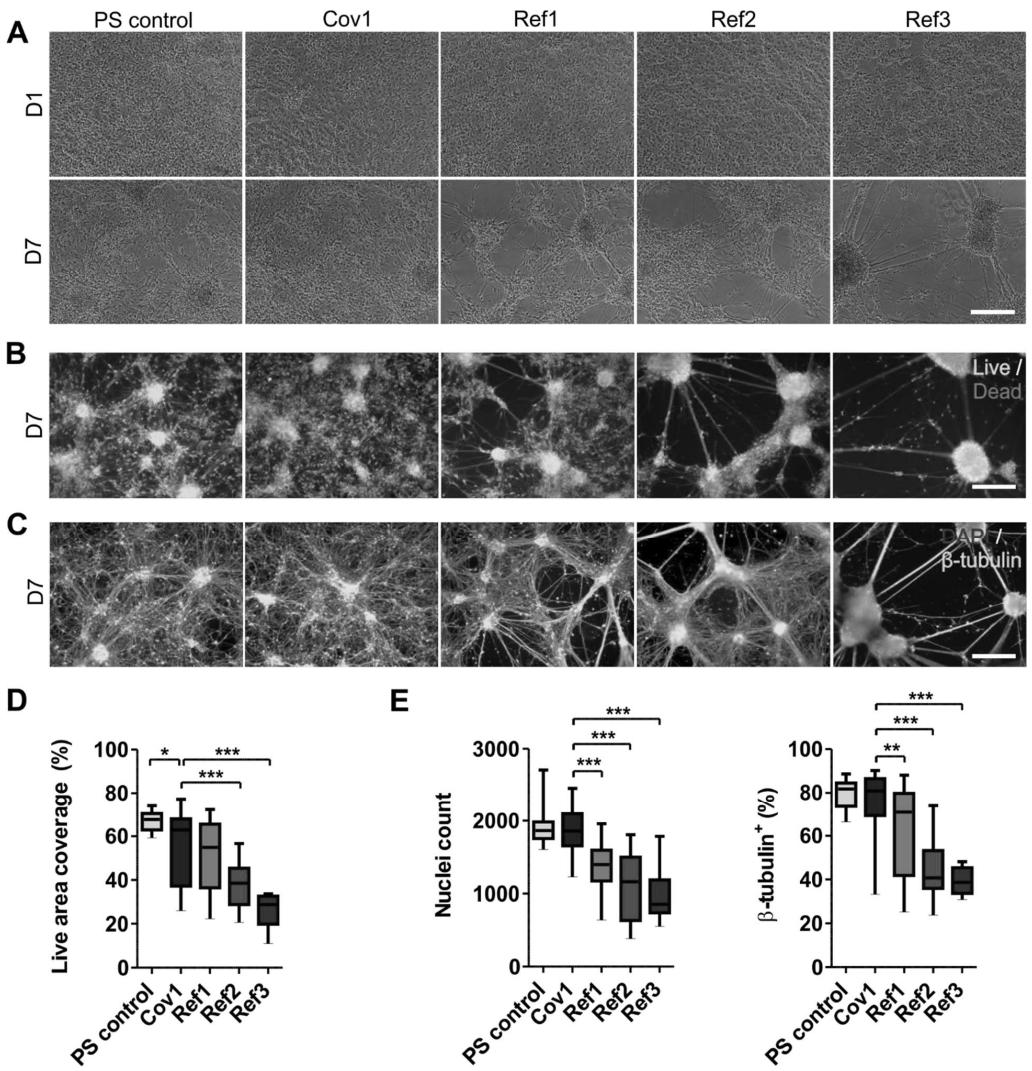

Fig. 2. The viability and immunocytochemical characterization of the hiPSC-derived neuronal cells cultured on different oxygen sensing films and a plain PS control film. **(A)** Representative phase contrast images after one (D1) and seven days (D7) in culture. **(B)** The Live/dead staining at D7. **(C)** The immunocytochemical staining of cell nuclei (DAPI) and neuronal cells (β-tubulin) at D7. Scale bar represents 200 µm in all images. **(D)** The areal coverage of live cells. **(E)** The number of DAPI-positive cell nuclei and the percentage of β-tubulin-positive neurons. For all quantifications, n=9-37 derived from 1-2 experiments (Table S1 in the Supporting Information), and the data is presented as median and interquartile range with whiskers showing the minimum and maximum values. Statistical analysis according to Mann-Whitney U-test (two-tailed). Statistical significances are denoted as * $p < 0.05$; ** $p < 0.01$; *** $p < 0.001$.

Biocompatibility with hiPSC-derived cardiomyocytes. In the biocompatibility tests with hiPSC-derived CMs, oxygen sensing spots were used instead of spin-coated sensing films. Adherent cells typically prefer areas outside the sensing material [7]; therefore, the separate spots provided an opportunity to study possible regional preferences of hiPSC-CM clusters with different sensing materials. Such preferences could be utilized, for example, for guiding the growth of the cells.

Oxygen sensing spots were manufactured on the bottom of 18 cell wells (Cov1 x 10, Ref1 x 4, Ref3 x 4). Six wells without sensing spots were used as glass controls (GC). The CMs were plated and followed up to 13 days in an incubator. However, the size of the data set decreased significantly after the first week of test, when the optical evaluation revealed that the sensor spots had disappeared from four wells, probably during the medium change that took place on day five. The decrease in the data size necessitated reorganization of the data. Therefore, the statistical analysis were performed on day 13 (D13) with following three data sets: i) Cov1 (9 wells); ii) all non-linked materials combined into a single reference set denoted as Ref (1 x Ref1 wells and 4 x Ref3 wells); (iii) control (6 wells) (details summarized in Table S2 in the Supporting Information).

Fig. 3 shows representative images of the CM clusters in different wells on D13. In Fig. 3A, a poorly attached (and non-beating) cluster is located next to the sensing spot manufactured of the non-linked material (Ref3), and a close-up of the same cluster is shown in Fig. 3B. The cluster differs morphologically from the cluster in the control well, shown in Fig. 3D. On the other hand, the well attached (and strongly beating) cluster in Fig. 3C, located very close to the sensing spot manufactured of the covalently linked material (Cov1), resembles morphologically the cluster in the control well (Fig. 3D). In addition, many clusters close to the Cov1 material were partly attached and spread over the spot itself; thus, indicating good biocompatibility of the sensor material Cov1 (Fig. 8C).

Fig. 8E summarizes the attachment and beating score values on D13. The values demonstrate the superiority of the sensing material with covalently linked indicators. Indeed, the difference between the Cov1 and Ref is evident, while the difference between Cov1 and GC is small. These facts are supported by the Mann-Whitney test showing a statistically significant difference between Ref and Cov1 ($p < 0.05$) as well as between Ref and GC ($p < 0.05$).

Monitoring pO_2 in hiPSC-derived CM cultures. In order to study only the effects of different chemistries, the biocompatibility tests were carried out in the dark of the incubator. In real applications, however, the photoexcitation of the indicator can generate, as an unwanted byproduct, a certain amount of singlet oxygen $^1O_2$. Exposure to $^1O_2$ can be irreversibly damaging or even lethally toxic to cells [25]. Fortunately, the lifetime ($\tau \approx 3.5$ µs) and mean diffusion distance (of order 200 nm for 5τ) of $^1O_2$ are very limited in aqueous solutions [26]. Thus, to make damage, $^1O_2$ should be produced inside, or at least very close to the cell membrane. Therefore, preventing the indicator leaching, applying low excitation power and preferably avoiding direct illumination of the cells should generally strongly mitigate against phototoxic issues in oxygen sensing.

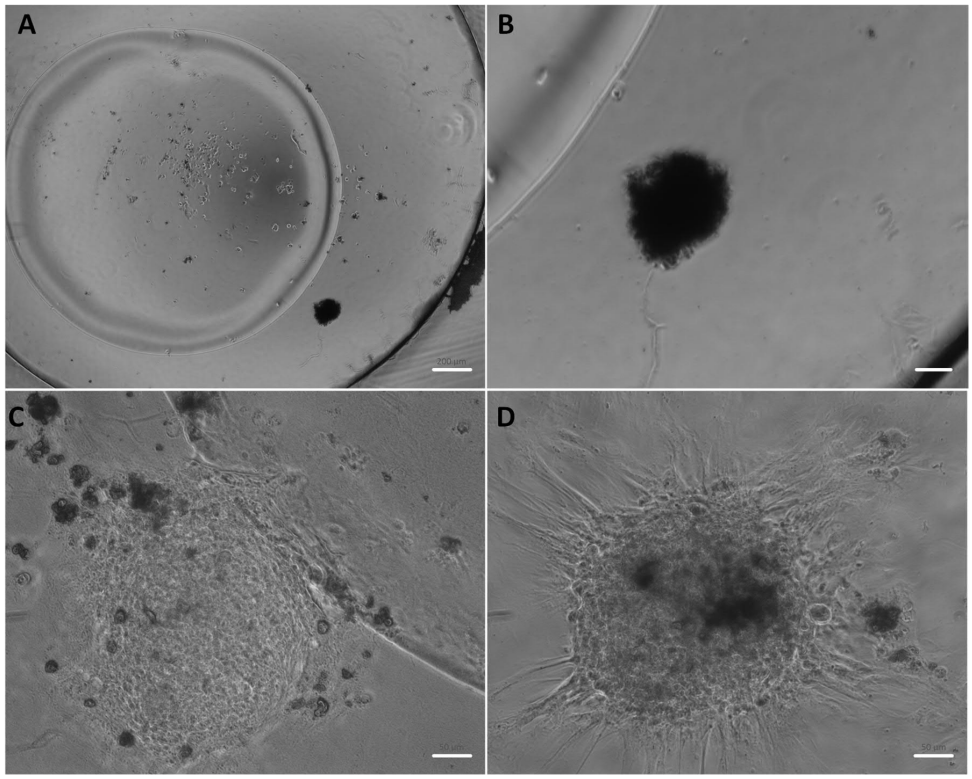

E score	Cov1 (linked)	Ref (non-linked)	GC (glass)
0 (non-beating and non-attached)	2	3	1
1 (either beating but non-attached or non-beating but well-attached)	-	1	-
2 (beating and well-attached)	7	1	5
	*	*	

Fig. 3. Representative phase contrast images and the classification of the cultured hiPSC-derived CM clusters on day 13. (**A**) Score 0; a non-beating and non-attached CM cluster next to a non-linked (Ref3) spot. (**B**) A close-up of the cluster in (**A**). (**C**) Score 2; a well-attached and strongly beating cluster in the edge of the cross-linked (Cov1) spot. (**D**) Score 2; a well-attached and strongly beating cluster on the control well (GC). Scale bar 200 µm (**A**); 50 µm (**B, C, D**). (**E**) The summary of the scores. Statistical analysis according to Mann-Whitney U-test (two-tailed). Statistical significances are denoted as * $p < 0.05$; ** $p < 0.01$; *** $p < 0.001$.

We applied oxygen sensing material Cov1 together with the reported sensing set-up (Fig. S5 in the Supporting Information) in hypoxia studies of hiPSC-derived CMs. Fig. 6A displays a phase contrast image of four CM clusters in the study. The clusters were cultured on a customized MEA substrate [27], inside a 1-well culture chamber with surrounding gas-control structures [21], and the environmental conditions were monitored and controlled by the modular cell-culturing system [19]. The morphology of the cells again indicates the biocompatibility of the material Cov1. The oxygen sensor response was recorded once a minute with a three second illumination time. The measured oxygen partial pressure and the beating frequency for one cluster are shown in Fig. 6B. The beating frequencies were calculated from the recorded videos according to methods described by Ahola et al. [28], and they display clear correlation with the measured oxygen partial pressure. During numerous similar experiments, the oxygen measurements have not been observed to have a harmful effect on the CM clusters.

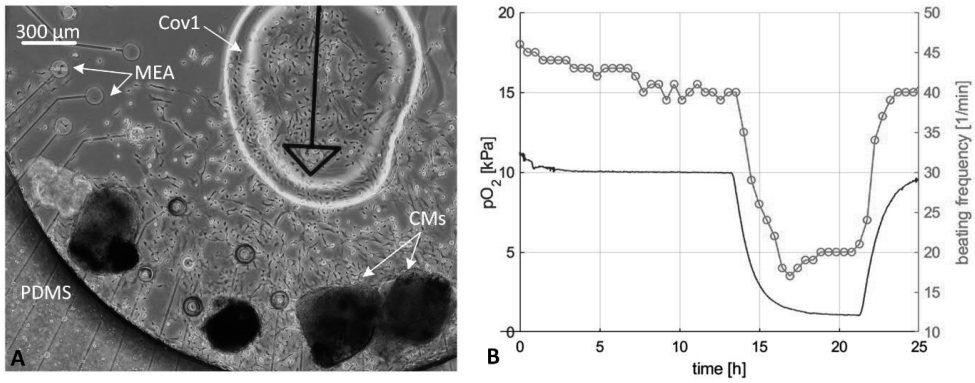

Fig. 6. (A) A phase contrast image of four hiPSC-derived cardiomyocyte clusters during hypoxia studies. (B) The measured oxygen partial pressure and video-based beating frequency analysis of one cluster.

Chemical stability. The biocompatibility test results are presumably directly related to the chemical stability of the material, that is, to the extent the material can limit the indicator leaching. However, with the tested materials, it is challenging to assess the leaching in aqueous solutions used in cell culturing. Indeed, the leaching of non-linked PtTFPP and PtOEPK out of polystyrene in aqueous solutions, as well as in 95% EtOH, can remain as undetectable for weeks [13]. Therefore, we decided to apply acetone as a test solvent. Short acetone treatments can be expected to generate detectable differences between the sensor materials, as acetone is known to dissolve PtTFPP and to some extent PPFS [29], but does not immediately dissolve PS [30].

Glass plates with spin-coated films, containing either covalently linked (Cov1) or non-linked (Ref2) PtTFPP, were immersed halfway in acetone for 20 s. The short acetone treatment turned film Cov1 into a less transparent, slightly white-colored film, probably due to a partial dissolution of PPFS. On the other hand, the mild red appearance in Ref2 film vanished in the treatment, thus indicating that the most of the non-linked PtTFPP has been leached out of the film (Fig. S2 in the Supporting Information).

Fig. 4 shows the influence of the acetone treatment on the oxygen sensing performance. The amplitude responses (Fig. 4A) reveal that the emission of Ref2 is almost completely vanished after the treatment, thus indicating a strong leakage of PtTFPP. On the other hand, the same treatment only halves the emission power of Cov1, despite the substantially decreased transparency of the film. The difference

between the films is further illustrated in Fig. 4B, where the phase responses are shown. Due to the lost emission power, the noise in the phase signal of Ref2 is increased, and the absolute phase change is significantly reduced. However, the phase response of Cov1 is only slightly shifted, presumably due to the increased optical losses and modified oxygen diffusion rate. Indeed, the oxygen sensing performance of Cov1 remains almost the same. These results evidently suggest that the covalent linking substantially increases the chemical stability of the material.

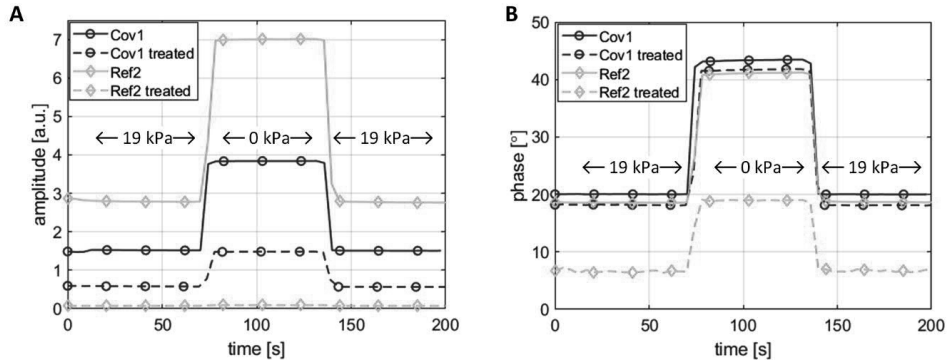

Fig. 4. Oxygen sensing responses of the sensing films with covalently linked (Cov1) and non-linked (Ref2) indicators on the non-treated sides (solid) and acetone-treated sides (dashed). The treated sides have been immersed in acetone for 20 s. (**A**) amplitude and (**B**) phase responses at pO_2 = 19 kPa and pO_2 = 0 kPa.

The stability of the material Cov1 was further studied in a week-long experiment, where the calibration chamber was filled with de-ionized water, and the oxygen partial pressure was changed step-wise between 19 kPa and 0 kPa. The luminescence responses were recorded four times a minute, and the results are shown in Fig. 5. The recorded responses demonstrate a solid luminescence intensity (Fig. 5A) and, in particular, luminescence lifetime stability (Fig. 5B). The minor fluctuations in the responses are due to changes in the ambient temperature.

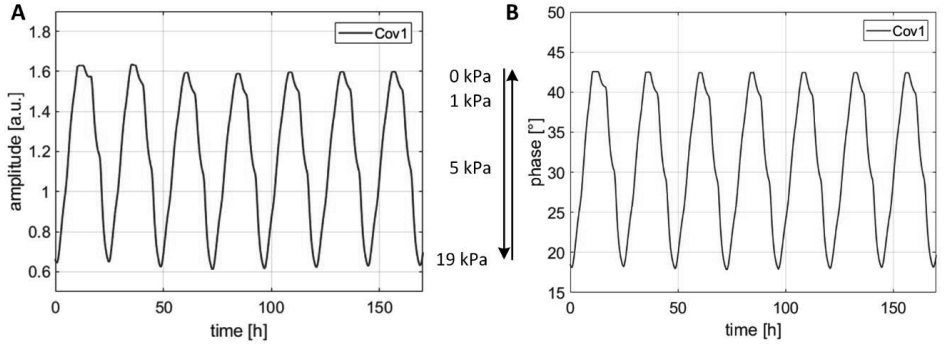

Fig. 5. The luminescence amplitude (**A**) and phase (**B**) response in oxygen tension monitoring in de-ionized water. Sensing film with covalently linked indicators (Cov1) was used. The oxygen partial pressure was varied according to the sequence [19, 10, 5, 1, 5, 10, 19, 10, 5, 1, …] kPa.

Finally, we compared the photostability of the materials Cov1 and Ref1. As PtTFPP is known for excellent photostability properties [31], we utilized a high-power UV curing spot light device and recorded the sensor responses after a sequence of powerful UV exposures (see Fig. S3 in the Supporting Information). The UV process resulted in a low negative phase change for both films indicating a minor shortening of the luminescence lifetimes, and the effect was slightly more pronounced for the film Cov1 than for Ref1. However, the differences between the films were small, and it is evident that the covalent linking of PtTFPP generates no serious effects on the oxygen sensing performance in terms of sensitivity, noise level or photostability.

Discussion. This paper studied the influence of the covalent linking of PtTFPP on different properties of the PS-based oxygen sensing material. As the main result, the material with covalently linked PtTFPP showed significantly enhanced biocompatibility with the hiPSC-derived neurons and CMs, compared to reference materials with non-linked indicators. The results also suggest that the enhanced biocompatibility is due to the enhanced chemical stability of the material, which significantly limits the leaching of the indicators. Moreover, the experimental data, albeit small within this paper, suggests that phototoxicy is not on issue as long as the indicators are not leaching and the excitation power low.

There are relatively few reports on luminescence-based oxygen sensing with hiPSC-derived cultures, and the studies typically rely on commercial plates and devices [32,33]. However, such devices are challenging to integrate into other systems, such as the modular cell culturing system with many simultaneous functionalities [19]. For such systems, the manufacturing method described in this paper can be applied when preparing PtTFPP-based oxygen sensing films, spots or beads. Moreover, the method may apply to other host polymers than PS as well.

MATERIALS AND METHODS

Reagents. PtTFPP and PtOEPK were from Livchem Logistics.. PS pellets, PPFS powder and the solvents were from Sigma.

Preparation of the polymer blend with covalently linked indicators. The preparation was carried out according to Koren et al. [17] with some modifications. Briefly, 1.00 g of PS and 6.3 mg of PPFS were dissolved in 20 ml of dimethylformamide (DMF) at 60°C. Then 300 µl of 1,3-propanedithiol (PDT) cross-linker and 500 µl of triethylamine (TEA) were added to the solution at 75°C. The solution was stirred at 75°C for six hours. The precipitates were washed with methanol (MeOH) and ethanol (EtOH) and dried at 60°C for 18 hours. Next, 500 mg of the precipitate was dissolved in 20 ml of DMF and stirred at 75°C overnight. In a separate vessel, 50 mg of PtTFPP was dissolved in 25 ml of DMF and 250 µl of TEA at 75°C, and then added into the polymer blend solution. After six hours at 75°C, the solution was washed with MeOH and EtOH to remove excess TEA and unbound PtTFPP. The resulting precipitate, a blend of PS and PPFS with covalently linked PtTFPP, was dried on a hot plate at 60°C overnight. Finally, the precipitate was dissolved in toluene to produce a 4.0% w/w solution for the manufacturing of the sensing films and spots. The PtTFPP concentration of the prepared material, denoted as Cov1, was estimated with optical absorbance measurements. Typically, the absorbance spectrum of Cov1 in toluene was similar to the absorbance of a reference material containing 0.05% w/w of non-linked PtTFPP (see Fig. S4 in the Supporting Information)

Preparation of the reference polymers with non-linked indicators. Briefly, PS pellets were dissolved in toluene (4.0% w/w), and PtTFPP was added into the solution in two concentrations: material Ref1 contained 0.05% w/w (same as Cov1) and Ref2 0.5% w/w of PtTFPP with respect to PS. Finally, a PS solution with non-linked PtOEPK (0.05% w/w) was prepared as an additional reference material (Ref3).

Preparation of the oxygen sensing films and spots. Glass plates (49 mm × 49 mm × 1 mm; n = 1.5171; Gerhard Menzel GmbH) were sonicated in acetone and isopropanol, rinsed with deionized (DI) water and dried with nitrogen. The plates were treated with oxygen plasma for five minutes and pre-coated with hexamethyldisilazane (HMDS) in vacuum at 150°C (Hotplate HMDS-OPTIhot SVT20). Oxygen sensing films were manufactured by spin coating the prepared polymer solutions with a speed of 3000 rpm, resulting in a film thickness of approximately 500 nm [21,34]. The plates were placed on a hot plate at 100°C for ten minutes, and then left to dry for 12 h.

Alternatively, oxygen sensing spots were manufactured by pipetting 0.2 – 0.3 µL drops of the polymer solution with a small glass capillary on the sonicated and pre-coated glass plates and letting the spots dry in cleanroom conditions for 12 h. The resulting sensor spots had a diameter between 1.5 mm and 2.0 mm and a thickness between 3 µm and 10 µm at the center.

Oxygen sensing. To characterize the oxygen sensing properties of the prepared sensing films, the optical set-up reported earlier [21] was applied with some modifications (see Fig. S5 in the Supporting Information). Tailored polydimethylsiloxane (PDMS) 1-well culture chambers with surrounding gas-control structures were utilized as calibration chambers [21]. The chambers were mounted directly on the oxygen sensing films.

Biocompatibility tests. Cells were derived from human induced pluripotent stem cells (hiPSC) with standard techniques. Ethical approval was obtained from the ethics committee of Pirkanmaa Hospital District for the derivation, culture, and differentiation of hiPSCs (R08070).

Neuronal cells. Neuronal cells were derived from the hiPSC-line 10212.EURCCs. The hiPSCs were maintained on top of a human feeder cell layer according to [35], and before differentiation expanded in a feeder-free culture [36]. The cortical neural differentiation was based on [37] with some modifications. Neuronal cells were differentiated in neural maintenance medium consisting of 1:1 D-MEM/F12 with Glutamax and Neurobasal, 0.5% N2, 1% B27 with Retinoic Acid, 0.5 mM GlutaMAX, 0.5% NEEA, 50 µM 2-mercaptoethanol (all from Thermo Fisher Scientific), 2.5 µg/ml Insulin (Sigma) and 0.1% penicillin/streptomycin (Thermo Fisher Scientific). For neural induction, the culture dishes were coated with Matrigel (Corning) and neural maintenance medium supplemented with 100 nM LDN193189 and 10 µM SB431542 (both from Sigma) for 12 days. After neural induction, the culture dishes were coated with 100 µg/ml poly-L-ornithine (PO, Sigma) in borate buffer and 15 µg/ml mouse laminin (Sigma) in PBS. From day 13 to day 25, the neural progenitor cells were expanded in neural maintenance medium supplemented with 20 ng/ml fibroblast growth factor-2 (FGF2) (R&D Systems). From day 26 onwards, neural maintenance medium was supplemented with 20 ng/ml brain-derived neurotrophic factor (BDNF, R&D Systems), 10 ng/ml glial-derived neurotrophic factor (GDNF, R&D Systems), 500 µM dibutyryl-cyclicAMP (db-cAMP, Sigma) and 200 µM ascorbic acid (AA, Sigma) for neuronal maturation.

The oxygen sensing films were sterilized using 70% ethanol. Custom-made PDMS rings were bonded to oxygen sensing films in order to create six separate cell culture areas [38]. These cell culture areas were coated with 100 µM/ml PO for one hour at 37°C and washed three times with sterile H_2O and left to dry at room temperature. Double coating was finished with 50 µg/ml mouse laminin overnight at 4°C. The cells were plated at density of 290 000/cm^2 on the day 32 of the differentiation. Mediums were refreshed three times a week, and cultures were followed for seven days before cell characterizations.

The viability of the neurons on D7 was studied using a LIVE/DEAD® Viability/Cytotoxicity Kit for mammalian cells (Thermo Fisher Scientific) [39]. Briefly, cultures were incubated for 30 minutes in a dye solution containing 0.1 µM calcein-AM for the detection of the live cells and 0.5 µM ethidium homodimer-1 live for the detection of the dead cells. Samples were imaged with Olympus IX51 microscope. The CellProfiler software [40] was used to quantitate the area covered by the cells.

The number of the cells and the percentage of neurons were evaluated with immunocytochemical staining on D7 [41]. Nuclei were stained with 4',6-diamidino-2-phenylindole (DAPI), and neurons with a primary antibody β-tubulin$_{III}$ (1:500; T8660, Sigma-Aldrich) and secondary antibody Alexa Fluor 488 (1:400; A21202, Thermo-Fisher). Imaging as above, and the number of the nuclei and the percentage of the β-tubulin-positive cells were determined with the CellProfiler and CellProfiler Analyst [42] software.

Cardiomyocytes. CMs were differentiated from the hiPSC-line UTA.04602.WT [43]. The differentiation was carried out by co-culturing hiPSCs with mouse visceral endodermal-like (END-2) cells [44]. The beating hiPSC-CM clusters were mechanically excised from the differentiation cultures 20-30 days after the differentiation initiation.

PDMS rings, similar to those used with neuronal cells, were bonded to the glass plates. An oxygen sensing spot with a diameter between 1.5 and 2.0 mm was manufactured on the center of each cell culture area (diameter of 3.0 mm) The structures were sterilized with 70% ethanol. The cell culture areas were hydrophilized with fetal bovine serum (FBS) (Lonza) for five minutes and coated with 0.1% gelatin type A (Sigma-Aldrich) for one hour at room temperature. For each well, 1-3 beating hiPSC-CM clusters were plated. The CMs were plated and cultured in KnockOut Dulbecco's Modified Eagle Medium (KO-DMEM) (Lonza) with 20% FBS (Lonza), 1% non-essential amino acids (NEAA) (Cambrex), 2 mM Glutamax (Invitrogen) and 50 U/ml penicillin/streptomycin (Lonza). The medium was refreshed twice a week.

The viability of the CM clusters was assessed with phase microscopy on D7 and D13. The clusters in each well were evaluated in terms of the attachment and beating. If the CM cluster in the well was both well-attached and beating, the cluster was given a score of 2. If the cluster was neither well-attached nor beating, it was given the score of 0. The well-attached but non-beating as well as poorly-attached but beating clusters were evaluated as the score of 1.

Statistical tests. The non-parametric Mann-Whitney U-test (two-tailed) was applied in statistical analysis. A value of $p < 0.05$ was considered as statistically significant. All the statistical tests were performed with SPSS Statistics software v25.0.

Monitoring pO_2 in hiPSC-derived CM cultures. The hiPSC-derived CM clusters were derived as above. A glass substrate with a customized single-cell MEA structure was used [27]. The MEA structure contained an electrode free area, where the oxygen sensing spot with a diameter of approximately 1.5 mm was manually manufactured. A PDMS 1-well culture chamber [21] was bonded to the substrate. Cell plating as above, and the cultures were placed in a standard incubator for five days for initial stabilization. The medium was refreshed on D4. After the initial stabilization, the culture was moved to the modular system [19], where the temperature was stabilized at T=37°C and the gas content of the culture was controlled. The baseline conditions (O_2 10%, CO_2 5%, N_2 85%) continued for 13 h until the hypoxic conditions (O_2 1%, CO_2 5%, N_2 94%) were set. After 8 h, the baseline conditions were restored.

Photostability. To assess the photostability of the prepared oxygen sensing films, an UV curing spot light device (Dymax BlueWave 50 AS) was applied. The fiber output of the device (beam diameter 5.0 mm, 3 000 mWcm^{-2} at 320 nm – 440 nm) was directed to the sensing films at 1.0 mm distance. Short exposures followed with luminescence measurements were carried out in controlled oxygen conditions.

ACKNOWLEDGEMENTS

We thank Dr. E. Vuorimaa-Laukkanen for her help in the spectral measurements, and Tampere Imaging Facility for the microscopy equipment. The Financial support by Business Finland (former TEKES, the Finnish Funding Agency for Technology and Innovation, decision number 40332/14) and by the Academy of Finland (decision No. 311017, 311021 and 311022) are gratefully acknowledged.

REFERENCES

[1] Wilson, D. F. (**2008**) Quantifying the role of oxygen pressure in tissue function. *Am. J. Physiol. Heart Circ. Physiol. 294*, H11–H13, doi:10.1152/ajpheart.01293.2007

[2] Bunn, H. F. and Poyton, R. O. (**1996**) Oxygen sensing and molecular adaptation to hypoxia. *Physiol. Rev. 76*, 839–885, doi:10.1152/physrev.1996.76.3.839

[3] Wolfbeis, O. S. (**2015**) Luminescent sensing and imaging of oxygen: Fierce competition to the Clark electrode, *BioEssays 37*, 921–928, doi:10.1002/bies.201500002

[4] Wang, X. and Wolfbeis, O. S. (**2014**) Optical methods for sensing and imaging oxygen: materials, spectroscopies and applications. *Chem. Soc. Rev. 43*, 3666–3761. doi:10.1039/C4CS00039K

[5] Quaranta, M., Borisov S. M. and Klimant I. (**2012**) Indicators for optical oxygen sensors. *Bioanal. Rev. 4*, 115–157, doi:10.1007/s12566-012-0032-y

[6] Mills, A. (**1997**) Optical Oxygen Sensors. *Platin. Met. Rev. 41*, 115–127.

[7] Papkovsky, D. B. and Dmitriev R. I. (**2013**) Biological detection by optical oxygen sensing. *Chem. Soc. Rev. 42*, 8700–8732, doi:10.1039/c3cs60131e

[8] Grist, S. M., Chrostowski L. and Cheung, K. C. (**2010**) Optical oxygen sensors for applications in microfluidic cell culture. *Sensors 10*, 9286–9316, doi:10.3390/s101009286

[9] Pfeiffer, S.A. and Nagl, S. (**2015**) Microfluidic platforms employing integrated fluorescent or luminescent chemical sensors: a review of methods, scope and applications. *Methods Appl. Fluoresc. 3*, 034003, Doi: 10.1088/2050-6120/3/3/034003

[10] Agostinis, P., Berg, K., Cengel, K., Foster, T. H., Girotti, A. W., Gollnick, S. O., Hahn, S. M., Hamblin, M.R., Juzeniene, A., Kessel, D., Korbelik, M., Moan, J., Mroz P., Nowis, D., Piette J., Wilson, B. C. and Golab, J. (**2011**) Photodynamic therapy of cancer: an update. *CA. Cancer J. Clin. 61*, 250-281, doi:10.3322/caac.20114

[11] Thomas, P. C., Halter, M., Tona, A., Raghavan, S.R., Plant, A. L. and Forry, S. P. (**2009**) A noninvasive thin film sensor for monitoring oxygen tension during in vitro cell culture. *Anal. Chem. 81*, 9239–9246, doi:10.1021/ac9013379.

[12] Xue, R., Behera, P., Xu, J., Viapiano, M. S. and Lannutti, J. J. (**2014**) Chemical Polydimethylsiloxane core – polycaprolactone shell nanofibers as biocompatible , real-time oxygen sensors. *Sensors Actuators B. Chem. 192*, 697–707, doi:10.1016/j.snb.2013.10.084

[13] O'Riordan, T. C., Voraberger, H., Kerry, J. P. and Papkovsky, D. B. (**2005**) Study of migration of active components of phosphorescent oxygen sensors for food packaging applications. *Anal. Chim. Acta 530*, 135-141, doi:10.1016/j.aca.2004.08.075

[14] Tian Y., Shumway, B. R. and Meldrum, D. R. (**2010**) A new cross-linkable oxygen sensor covalently bonded into poly(2-hydroxyethyl methacrylate)-co-polyacrylamide thin film for dissolved oxygen sensing. *Chem. Mater. 22*, 2069–2078, doi:10.1021/cm903361y

[15] Wu, Sh., Wu, Si., Yi, Z., Zeng, F., Wu, W., Qiao, Y., Zhao, X., Cheng, X. and Tian Y. (**2018**) Hydrogel-based fluorescent dual pH and oxygen sensors loaded in 96-well plates for high-throughput cell metabolism studies. *Sensors 18,* 564, doi:10.3390/s18020564

[16] Tian, Y., Shumway, B. R., Gao, W., Youngbull, C., Holl, M. R., Johnson, R. H., and Meldrum, D. R. (**2010**) Influence of matrices on oxygen sensing of three sensing films with chemically conjugated platinum porphyrin probes and preliminary application for monitoring of oxygen consumption of Escherichia coli (E. coli). *Sensors Actuators, B Chem. 150,* 579–587, doi:10.1016/j.snb.2010.08.036

[17] Koren, K., Borisov, S. M. and Klimant, I. (**2012**) Stable optical oxygen sensing materials based on click-coupling of fluorinated platinum(II) and palladium(II) porphyrins - A convenient way to eliminate dye migration and leaching, *Sensors Actuators, B Chem. 169*, 173–181, doi:10.1016/j.snb.2012.04.062

[18] Dmitriev, R. I., Borisov, S. M., Düssmann, H., Sun, S., Müller, B. J., Prehn, J., Baklaushev, V.P., Klimant, I. and Papkovsky, D. B. (**2015**) Versatile conjugated polymer nanoparticles for high-resolution O_2 imaging in cells and 3D tissue models*, ACS Nano. 9,* 5275–5288, doi:10.1021/acsnano.5b00771

[19] Rajan, D. K., Kreutzer, J., Välimäki, H., Pekkanen-Mattila, M., Ahola, A., Skogberg, A., Aalto-Setälä, K., Ihalainen, H., Kallio, P. and Lekkala, J. (**2018**) A portable live-cell imaging system with an invert-upright-convertible architecture and a mini-bioreactor for long-term simultaneous cell imaging, chemical sensing, and electrophysiological recording. *IEEE Access. 6*, 11063-11075, doi:10.1109/ACCESS.2018.2804378

[20] Mäki, A. J., Verho, J., Kreutzer, J., Ryynänen, T., Rajan, D., Pekkanen-Mattila, M., Ahola, A., Hyttinen, J., Aalto-Setälä, K., Lekkala, J. and Kallio, P. (**2018**) A Portable Microscale Cell Culture System with Indirect Temperature Control. *SLAS Technol. 23*, 566-579, doi:10.1177/2472630318768710

[21] Välimäki, H., Verho, J., Kreutzer, J., Kattipparambil Rajan, D., Ryynänen T., Pekkanen-Mattila, M., Ahola, A., Tappura, K., Kallio, P. and Lekkala, J. (**2017**) Fluorimetric oxygen sensor with an efficient optical read-out for in vitro cell models, *Sensors Actuators, B Chem. 249*, 738-746, doi:10.1016/j.snb.2017.04.182

[22] Sinkala, E. and Eddington, D. T. (**2010**) Oxygen sensitive microwells*, Lab on a Chip 10*, 3291–3295, DOI: 10.1039/C0LC00244E

[23] Lakowicz, J. R. (**2006**) Principles of Fluorescence Spectroscopy, 4th ed., Springer, US, New York.

[24] Papkovsky, D. B., Ponomarev, G. V., Trettnak W. and O'Leary P. (**1995**). Phosphorescent Complexes of Porphyrin Ketones:Optical Properties and Application to Oxygen Sensing, *Anal. Chem. 67*, 4112-4117.

[25] Dahl, T. A. (**1993**). Direct exposure of mammalian cells to pure exogenous singlet oxygen. *Photochem Photobiol. 57*(2), 248-54

[26] Ogilby, P. R. (**2010**) Singlet oxygen : there is indeed something new under the sun. *Chem. Soc. Rev. 39*, 3181-3209, doi:10.1039/b926014p

[27] Ryynänen, T., Pekkanen-Mattila, P., Shah, D., Kreutzer, J., Kallio, P., Lekkala, J. and Aalto-Setälä, K. (**2018**) Microelectrode array for noninvasive analysis of cardiomyocytes at the single-cell level. *Japanese Journal of Applied Physics 57*, 117001.

[28] Ahola, A., Kiviaho, A., Larsson, K., Honkanen, M., Aalto-Setälä, K. and Hyttinen, J. (**2014**) Video image-based analysis of single human induced pluripotent stem cell derived cardiomyocyte beating dynamics using digital image correlation. *Biomed. Eng. Online 13 (39)*, 1–18, DOI: 10.1186/1475-925X-13-39

[29] Paz-Pazos, M. and Pugh, C. (**2005**) Synthesis, isolation, and thermal behavior of polybutadiene grafted with poly(2,3,4,5,6-pentafluorostyrene). *J. Polym. Sci. Part A Polym. Chem. 43,* 2874–2891. doi:10.1002/pola.20765.

[30] Mark, J. (**1999**) Polymer Data Handbook, second ed., Oxford University Press.

[31] Amao, Y. (**2003**) Probes and Polymers for Optical Sensing of Oxygen. *Microchim. Acta. 143*, 1–12. doi:10.1007/s00604-003-0037-x.

[32] Kusuma, S., Peijnenburg, E., Patel, P. and Gerecht, S. (**2014**) Low oxygen tension enhances endothelial fate of human pluripotent stem cells. *Arterioscler. Thromb. Vasc. Biol. 34*, 913-920. doi: 10.1161/ATVBAHA.114.303274.

[33] Abaci, H. E., Truitt, R., Luong, E., Drazer, G. and Gerecht, S. (**2010**) Adaptation to oxygen deprivation in cultures of human pluripotent stem cells, endothelial progenitor cells, and umbilical vein endothelial cells. *Am. J. Physiol. Physiol. 29*8, C1527–C1537, doi:10.1152/ajpcell.00484.2009

[34] Hall, D. B., Underhill, P. and Torkelson, J. M. (**1998**) Spin coating of thin and ultrathin polymer films. *Polym. Eng. Sci. 38(12)*, 2039–2045

[35] Rajala, K., Hakala, H., Panula, S., Aivio, S., Pihlajamäki, H., Suuronen, R., Hovatta, O. and Skottman, H. (**2007**) Testing of nine different xeno-free culture media for human embryonic stem cell cultures. *Hum. Reprod. 22,* 1231-1238, doi:10.1093/humrep/del523

[36] Hongisto, H., Ilmarinen, T., Vattulainen, M., Mikhailova, A. and Skottman H. (**2017**) Xeno- and feeder-free differentiation of human pluripotent stem cells to two distinct ocular epithelial cell types using simple modifications of one method. *Stem Cell Res. Ther. 8*, 291, doi:10.1186/s13287-017-0738-4

[37] Shi, Y., Kirwan, P., Smith, J., Robinson, H. P. C. and Livesey, F. J. (**2012**) Human cerebral cortex development from pluripotent stem cells to functional excitatory synapses. *Nat. Neurosci. 15*, 477-486, doi:10.1038/nn.3041

[38] Kreutzer, J., Ylä-Outinen, L., Kärnä, P., Kaarela, T. and Mikkonen, J. (**2012**) Structured PDMS Chambers for Enhanced Human Neuronal Cell Activity on MEA Platforms. *J. Bionic Eng. 9*, 1–10. doi:10.1016/S1672-6529(11)60091-7.

[39] Ylä-Outinen, L., Joki, T., Varjola, M., Skottman, H., and Narkilahti, S. (**2014**) Three-dimensional growth matrix for human embryonic stem cell-derived neuronal cells. *J. Tissue Eng. Regen. Med. 8*, 186-194, doi:10.1002/term.1512.

[40] Carpenter, A. E., Jones, T. R., Lamprecht, M. R., Clarke, C., Kang, I. H., Friman, O., Guertin, D. A., Chang, J. A., Lindquist, R. A., Moffat, J., Golland, P. and Sabatini, D. M. (**2006**) CellProfiler: Image analysis software for identifying and quantifying cell phenotypes. *Genome Biol. 7*, R100, doi:10.1186/gb-2006-7-10-r100

[41] Lappalainen, R. S., Salomäki, M., Ylä-Outinen, L., Heikkilä, T. J., Hyttinen, J. A., Pihlajamäki, H., Suuronen, R., Skottman, H.and Narkilahti, S. (**2010**) Similarly derived and cultured hESC lines show variation in their developmental potential towards neuronal cells in long-term culture. *Regen. Med. 5*, 749-762, doi:10.2217/rme.10.58.

[42] Jones, T. R., Kang, I. H., Wheeler, D. B., Lindquist, R. A., Papallo, A., Sabatini, D. M., Golland, P. and Carpenter, A. E. (**2008**) CellProfiler Analyst: Data exploration and analysis software for complex image-based screens. *BMC Bioinformatics 9*, 482, doi:10.1186/1471-2105-9-482

[43] Lahti, A. L., Kujala, V. J., Chapman, H., Koivisto, A.-P., Pekkanen-Mattila, M., Kerkelä, E., Hyttinen, J., Kontula, K., Swan, H., Conklin, B .R.,Yamanaka, S., Silvennoinen, O. and Aalto-Setälä, K. (**2012**) Model for long QT syndrome type 2 using human iPS cells demonstrates arrhythmogenic characteristics in cell culture. *Dis. Model. Mech. 5,* 220-230, doi:10.1242/dmm.008409

[44] Mummery, C. L., Zhang, J., Ng, E. S., Elliott, D. A., Elefanty, A. G. and Kamp, T. J. (**2012**) Differentiation of human embryonic stem cells and induced pluripotent stem cells to cardiomyocytes: A methods overview. *Circ. Res. 111*, 344-358, doi:10.1161/CIRCRESAHA.110.227512